The ThF^+ eEDM experiment: concept, design, and characterization

by

Kia Boon Ng

B.A., National University of Singapore, 2015

M.S., University of Colorado, Boulder, 2018

A thesis submitted to the

Faculty of the Graduate School of the

University of Colorado in partial fulfillment

of the requirements for the degree of

Doctor of Philosophy

Department of Physics

2024

Committee Members:

Eric A. Cornell, Chair

Jun Ye

James Thompson

John Bohn

Marco Nicotra

Ng, Kia Boon (Ph.D., Physics)

The ThF^+ eEDM experiment: concept, design, and characterization

Thesis directed by Prof. Eric A. Cornell

The Standard Model of particle physics is one of the most successful models that we have to describe the universe at a fundamental level. However, the Standard Model is known to be incomplete. For instance, the Standard Model does not explain the degree of abundance of matter over anti-matter. When theorists make extensions to the Standard Model through new physics models, their models usually make predictions on the value of the electric dipole moment of the electron (eEDM). By measuring (or placing improved limits on) the eEDM, we can place constraints on these new theories. The eEDM experiments at JILA use molecular ions to measure the eEDM. Molecular ions are good for two main reasons: (i) our molecules give us enhanced sensitivity to the eEDM, and (ii) trapped ions allow us to take advantage of the long coherence times of the eEDM-sensitive states. The Generation II JILA eEDM experiment using HfF^+ concluded in November 2022 by setting the world's best limit. In our Generation III project, we seek to further improve upon our limit by switching over to ThF^+, which promises enhanced sensitivity to the eEDM. Herein, I present (i) spectroscopy work performed on ThF^+ to allow us to control the molecule in both the external and internal degrees of freedom, (ii) design and characterization of a prototype of a multiplexed ion trap.

Acknowledgements

Rating: ★★★★☆

Comment: 5-star experience in JILA and CU Boulder. Many thanks to the whole JILA community, and staff in the Department of Physics. Special thanks to Bosses, lab mates, support staff, and collaborators, who have made my learning journey fruitful and exciting. Special mention to all my friends and family members who have kept me sane and emotionally healthy. One star deducted because of disappointing food choices in Boulder (within graduate student budget).

Recommendation: Would strongly recommend to friends and family.

Contents

Chapter

Tables

Table

Figures

Figure

Chapter 1

Introduction

1.1 Background of the eEDM

An improved or non-zero measurement of the electron's electric dipole moment (eEDM, d_e) would have huge implications for our understanding of the universe [1–4]. Our current understanding is nicely encapsulated at a fundamental level by the Standard Model of particle physics, but many observations hint that the Standard Model is incomplete. This problem is being addressed by numerous works on the theoretical front to introduce new physics through extensions of Standard Model [5, 6]. These new physics models come in many different classes, and each class makes a different prediction of the value of the eEDM [7–12]. Hence, a measurement (or a null-measurement) of the eEDM would place constraints on these new theories, and guide us towards a better understanding of the universe.

There are many ongoing works trying to measure the eEDM [13–20], and in recent years the effort has been switched from atoms to molecules because of molecular enhancement factors and robust systematic error rejection [21–27] that are available only to molecules because of their rich internal structures. There are several proposals that seek to exploit the rich internal structures even further to realize exotic ways to measure the eEDM [28, 29]. Figure 1.1 is a compilation of published upper bounds of the eEDM.

The richness of the molecular internal structure provides additional tools for diagnostics and eEDM sensitivity enhancements, but it proves to be a double-edged sword, as non-diagonal Franck-Condon factors and rotational branching increase the complexity of compressing the Hilbert space into the states that we care about. This additional complexity complicates state preparation, and also makes standard AMO practices

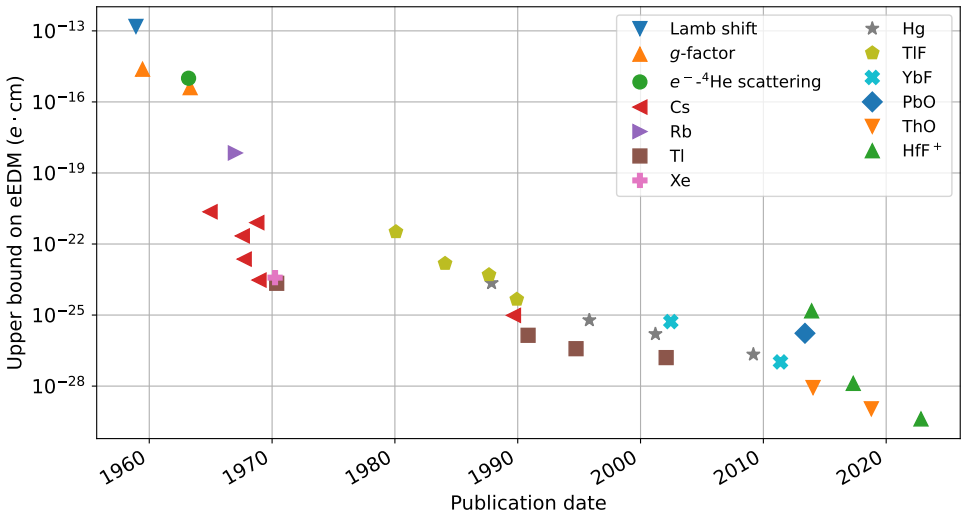

Figure 1.1: **Upper bounds on the eEDM set by experiments over the years.** Adapted from Paul Hess's thesis from the Gabrielse Group. Bounds are plotted at 90% confidence level.

like laser cooling and state detection through cycling transitions less applicable to molecules. Incidentally, there are groups trying to get around this limitation by working with polyatomic molecules [30–32] to marry favorable photon cycling properties of the heavy metal atom in the molecule to the advantages that come with the rich internal structures of a molecule. Although these groups are in the very early stages of their spectroscopy ground work, much related work [33, 34] is showing promising signs for future work.

The eEDM experiment here at JILA uses diatomic molecular ions. The statistical sensitivity to the eEDM depends on three main factors in the experiment: (i) effective electric field strength that couples to the eEDM, (ii) interrogation time of the eEDM-sensitive state, and (iii) total number of counts in the experiment for statistics. The first two generations of the JILA eEDM experiment [14, 35, 36] take advantage of the long ion trapping times to tap the long coherence times of the eEDM-sensitive state. The following sections give brief introductions to the JILA eEDM experiment with HfF^+ and ThF^+.

1.2 eEDM measurement with molecular ions

1.2.1 JILA eEDM experiment with HfF^+

The determination to measure the eEDM with molecular ions was first written in stone in the JILA 2011 paper [25], which addressed many concerns that skeptics in the AMO community had regarding performing a precision metrology experiment with trapped ions with a rotating electric field. Fast forward to 2017, the first generation measurement (Gen. I) from JILA using trapped HfF^+ convinced the last of the skeptics by placing an upper bound on the eEDM at $|d_e| < 1.3 \times 10^{-28}\, e\,\mathrm{cm}$ (90% confidence) [14], falling just slightly behind the world's best record set by ACME at that time at $|d_e| < 8.7 \times 10^{-29}\, e\,\mathrm{cm}$ (90% confidence) [37]. Since then, there has been friendly competition between JILA, ACME, and Imperial College [13] to see who can set the best limits on the eEDM, or even measure the eEDM itself. Soon after, ACME published an improved limit at $|d_e| < 9.6 \times 10^{-30}\, e\,\mathrm{cm}$ (90% confidence) [15] to spice up the game. In the meantime, JILA has made improvements to various aspects of the experiment, culminating in a second generation measurement (Gen. II, unblinded in November 2022) [35, 36], and is now the world's best limit at $|d_e| < 4.1 \times 10^{-30}\, e\,\mathrm{cm}$.

Some of the major improvements made in the Gen. II experiment include (i) better designed ion trap for field homogeneity, (ii) trapping more ions for better statistics, and (iii) new state preparation and detection techniques to reduce measurement noise. The details of upgrades pertaining to the Gen. II measurement can be found in numerous papers [38, 39] and theses from the JILA eEDM group (e.g. William Cairncross and Tanya Roussy) and shall be omitted here to save the spotlight for ThF^+.

1.2.2 JILA eEDM experiment with ThF^+

At the time of this writing, JILA has the world's best upper bound on the eEDM. The race is still on, however, so we need ideas on how to improve on this result. Small epsilon upgrades typically take about five years from conception to fruition; big overhauls can take up to fifteen years, but our competitors are certainly not patient enough to wait fifteen years for our big overhaul before resuming the competition. To

get a head start for the third generation experiment, we used[1] the time machine called *foresight* to go back in time to 2008 to start laying the foundations for a third generation experiment (Gen. III).

During the early days of the HfF^+ experiment, the JILA eEDM team learnt about a new molecule ThF^+ that can potentially help them get/stay ahead in the race [40–42]. The level of sensitivity to the eEDM (δd_e) depends on three main factors:

$$\delta d_e \sim \frac{1}{\mathcal{E}_{\text{eff}} \tau \sqrt{N_{\text{single}} \cdot f_{\text{rep.}} \cdot T_{\text{tot.}}}}, \tag{1.1}$$

Effective electric field, $\mathcal{E}_{\text{eff}}$. Relativistic effects allow for a non-zero electric field to couple to the EDM of the electron, despite having net zero time-averaged electric field inside the molecule. The effective electric field is molecular species dependent, and it turns out that ThF^+ has a slightly larger $\mathcal{E}_{\text{eff}} = 35$ GV/cm [22, 41] than HfF^+ at $\mathcal{E}_{\text{eff}} = 23$ GV/cm [24, 25]

Coherence time, τ. A longer coherence time is in general a good thing to have. In the context of the eEDM precision metrology experiment, which is a Ramsey spectroscopy measurement, a long coherence time allows for long Ramsey fringes to be taken. A longer Ramsey fringe translates to a more precise determination of the Ramsey frequency. The coherence time can be affected by, say, less than perfect control over the ions or fields (T_2^* type losses), and even if we have full control over the whole experiment, the coherence time of the eEDM sensitive states is bounded by the natural decay lifetime of the states (T_1 type losses). The eEDM sensitive states in HfF^+ have natural decay lifetimes of about 2 s. However, the eEDM sensitive states in ThF^+ are shown to be the ground rovibronic state [43], so the coherence times in ThF^+ can be much longer than 2 s.

Number statistics, $\sqrt{N_{\text{single}} \cdot f_{\text{rep.}} \cdot T_{\text{tot.}}}$, where N_{single}, $f_{\text{rep.}}$, and $T_{\text{tot.}}$ are the total number of ions counted in a single shot of the experiment, the repetition rate of the experiment, and the total time for which the graduate students are willing to take data, respectively. In the Gen. II experiment, the dead time of the experiment is short compared to a single Ramsey integration time, which in turn is limited by the coherence time. Hence the repetition rate is $f_{\text{rep.}} \approx 1/\tau$. As we shall see

[1] It is not immediately obvious to the author, who does not major in the English language, what tense to use when time travel is involved.

in later sections, we have tricks up our sleeves that allow us to work with $f_{\text{rep.}} \gg 1/\tau$ that we will implement in our eEDM experiment with ThF^+.

Despite the successes we have in measuring the eEDM with HfF^+ [14, 35, 36], it is not immediately obvious if the same experimental techniques (i.e. state preparation and readout) used on HfF^+ can be transferred over to ThF^+. For instance, the laser transitions required to address states in ThF^+ may be entirely different from those of HfF^+. Are the relevant transitions covered by lasers that are readily available? Are the internal quantum states easy to understand given that thorium, a heavy metal that is even heavier than hafnium, may break all the usual rules that we use for state assignments? How do we even create thorium monofluoride ions? Someone has to turn knobs in the laboratory to answer these questions. That someone, for the past eight years, happens to be me.

1.2.3 How an eEDM experiment is done at JILA

This thesis is a build up to a precision measurement of the eEDM in ThF^+, involving a lot of spectroscopy, design, and characterization of both the molecule and the setup. To understand why we do these in certain ways, mostly guided by our experience with the experiment using HfF^+, we need to understand how the eEDM experiment is done at JILA. This has already been covered in numerous theses before mine (e.g. Huanqian Loh, Kevin Cossel, Matt Grau, Daniel Gresh, William Cairncross, and Tanya Roussy), but I will present a brief summary in the context of ThF^+ (first time this is done) to make this thesis more self-contained. The ideas in this section serve only as a "quick start guide", and will be further developed throughout this thesis.

The first step to understanding how we perform an eEDM experiment at JILA involves knowing the energy landscape of the molecule. Figure 1.2 shows the most important features of the energy landscape of ThF^+. A diatomic molecule like ThF^+ has a very rich internal structure. Much like atoms, our molecules have electronic states. Unlike atoms, however, the electronic states are further split into vibrational manifolds, which are then further split into rotational manifolds, and finally within each rotational manifold, we have the hyperfine structure and parity doublets. The states that we choose to perform our eEDM measurement in are the $X\,^3\Delta_1(v = 0, J = 1, F = 3/2, m_F = \pm 3/2)$ states. Much must be done to compress internal

population of our molecule into just these four states alone. We do this through optical (and microwave) pumping.

The second step to understanding how we perform an eEDM experiment at JILA involves knowing how optical pumping works in our molecule. Figure 1.3 shows the basic idea behind optical pumping. These are standard techniques used in the AMO community. Further explanation in the captions.

The last piece of information we need to understand how we perform an eEDM experiment at JILA is what we are measuring that tells us about the eEDM. Figure 1.4 shows the energy level diagrams for the eEDM-sensitive states, and introduces the frequencies f_0 (the frequency offset that we intentionally introduce), f^{u} (frequency difference of the upper Stark doublet), and f^{l} (frequency difference of the lower Stark doublet). At the end of the day, all efforts discussed in this thesis are aimed at measuring f^{u} and f^{l} to the best of our abilities. Further explanation in the captions.

1.3 Thesis Layout

This thesis is a culmination of two main efforts: (i) various spectroscopy work on ThF and ThF^+, and (ii) design work on a prototypical multiplexed ion trap to take full advantage of the long coherence time of ThF^+. It serves as a guide on how to use ThF^+ to measure the eEDM, albeit an incomplete one, one that is a work in progress. Correspondingly, this thesis is split into the two parts:

(1) Part I: controlling the internal states of ThF^+

   (a) Preparing ThF^+ ions (Chapter 2): how do we create ions state selectively;

   (b) State readout of ThF^+ (Chapter 3): how do we use action spectroscopy to readout the quantum states of our ions;

   (c) Quantum control of ThF^+ (Chapter 4): how do we usher the ions into the desired quantum state through optical and microwave pumping;

(2) Part II: the JILA proposal for how we want to use ThF^+

   (a) Interlude (Chapter 5): can we do something more with ThF^+ than what we are already doing with HfF^+, formally introducing a multiplexed ion trap (the Bucket Brigade);

(b) Ion cloud & decoherence (Chapter 6): the dynamics of an ion cloud and its consequences on the design of the multiplex ion trap;

(c) Electric fields in the Bucket Brigade (Chapter 7): the design of the electrodes of a multiplexed ion trap;

(d) Generating f_0 in the Bucket Brigade (Chapter 8): exploration on various ways to turn bugs (sources of systematic errors) into features (let them work for us);

(e) Control system (Chapter 9): an introduction to our upgraded control system;

(f) Cryogenics (Chapter 10): using cryogenics to take full advantage of the long coherence time in ThF^+.

So turn over to the next chapter, and we shall begin the story of how to perform an eEDM experiment with ThF^+ starting with the first step: how to create ThF^+ ions.

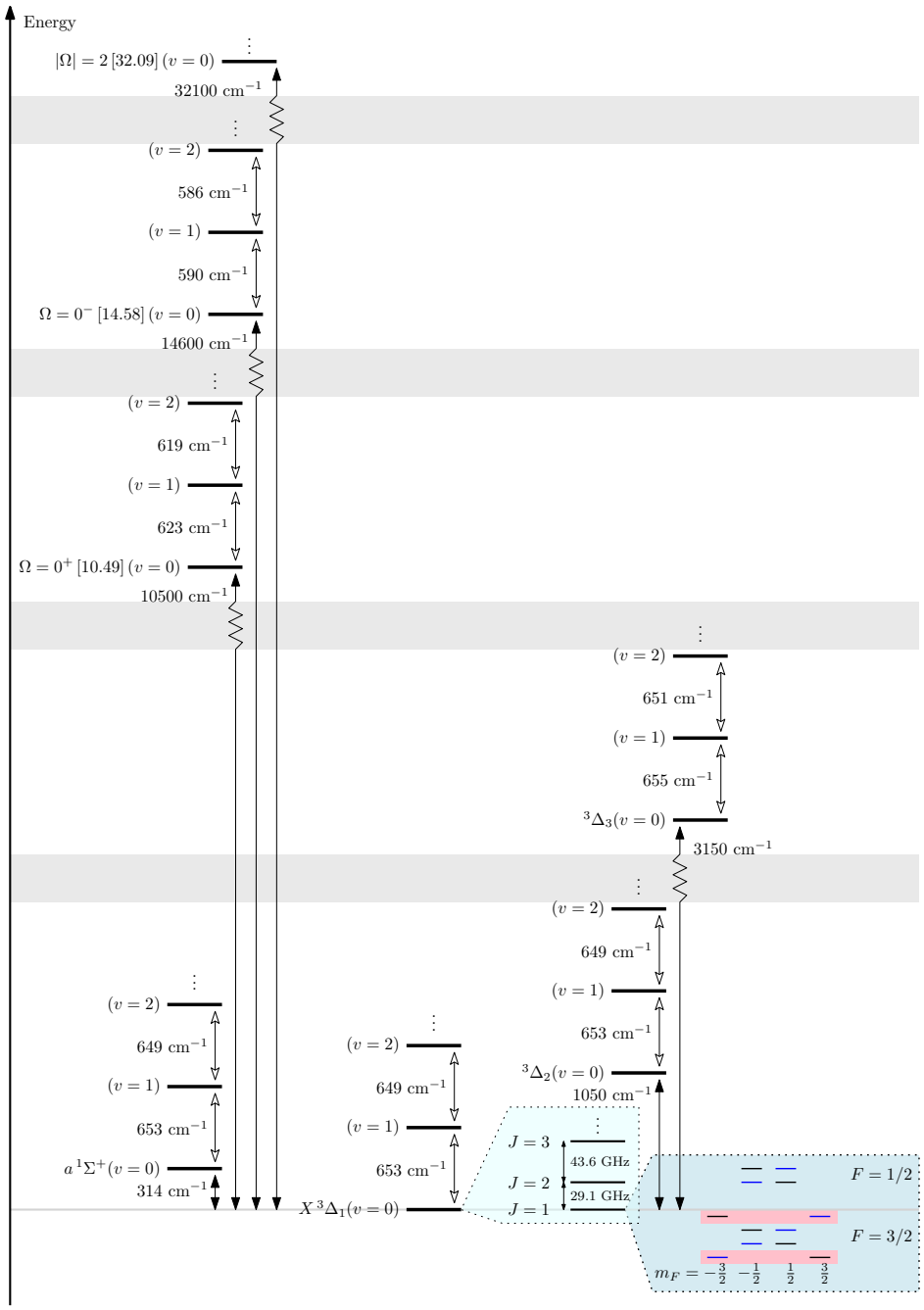

Figure 1.2: **Energy landscape of a molecular ion like ThF$^+$.** Not drawn to scale. 1 cm^{-1} $\approx$ 30 GHz. The electronic ground state is the $X\,^3\Delta_1$. Within each electronic state, there are vibrational manifolds, labelled by quantum number v. Within each vibrational level, there are rotational manifolds, labelled by quantum number J (Hund's case (c)). Within each rotational state, there are hyperfine manifolds (labelled by quantum number F), parity doublets (labelled by quantum number Ω; $\Omega = \pm 1$ are color coded black and blue, respectively), and Zeeman sublevels (labelled by quantum number m_F). This diagram shows a compilation of (i) the few lowest lying electronic states ($^3\Delta_1$, $^1\Sigma^+$, $^3\Delta_2$, and $^3\Delta_3$), (ii) higher lying states used for optical pumping ($\Omega = 0^+$ and $\Omega = 0^-$), and a high lying state available for photodissociation ($|\Omega| = 2$). The grey horizontal boxes indicate breaks in the vertical (energy) axis. The two pairs of states highlighted in pink are those used for the the eEDM measurement.

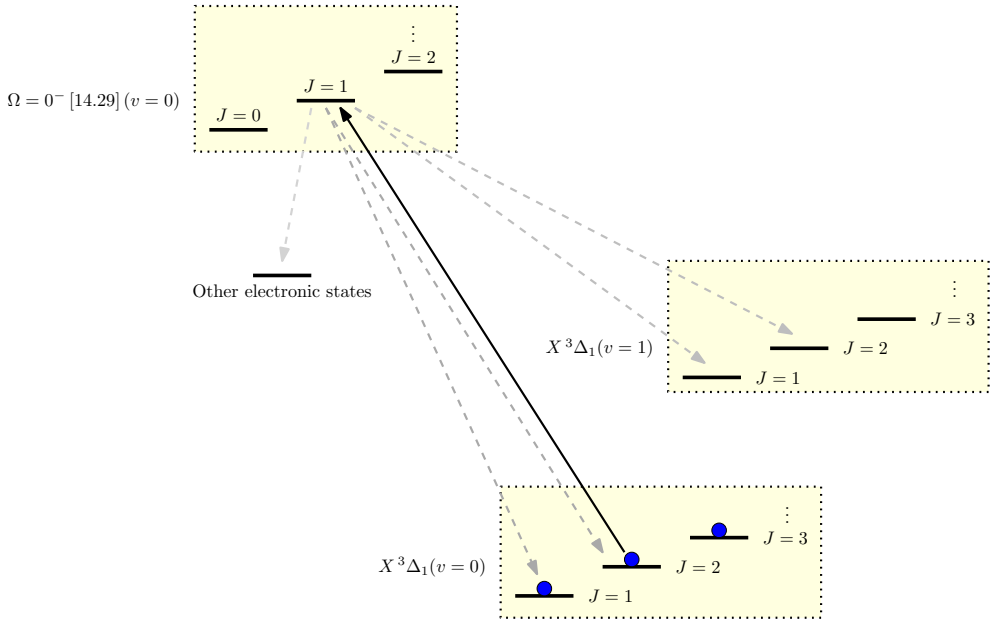

Figure 1.3: **Basic idea behind optical pumping.** Only the relevant states from Figure 1.2 are shown here. We start with population distributed among several rotational states in the $X\,^3\Delta_1(v = 0)$ vibronic manifold (blue shaded circles). A laser incoherently pumps population out of the $J = 2$ rotational state into the $\Omega = 0^- [14.29] (v = 0, J = 1)$ state (solid black arrow).

Population pumped to the excited state then decays into lower lying states (grey dashed arrows). The decay is subjected to selection rules ($\Delta J = 0, \pm 1$). Hence, molecules can fall back to the $J = 1, 2$ rotational states. Population that fall back to the $X\,^2\Delta_1(v = 0, J = 2)$ state can be pumped up again by the laser. Population that fall back to the $X\,^2\Delta_1(v = 0, J = 1)$ state will remain dark to the laser, but this also happens to be where we want the molecules to be for the eEDM measurement. This basic pattern (using the resonance selectivity of excitations plus the "selection rule" selectivity of spontaneous decay) is used (i) to deplete population from where we do not want it, or (ii) to accumulate population where we do, or (iii) sometimes both. The entropy associated with the internal state distribution is transferred to the dissipated photons from the spontaneous emission.

Population in the $X\,^2\Delta_1(v = 0, J = 3)$ state do not move in this partial scheme, but as we will see in Chapter 4, we can use microwaves to couple the $J = 2$ and 3 to pump population from $J = 3$. Non-diagonal Franck-Condon factors (vibrational wavefunction overlap between the electronic states $X\,^3\Delta_1$ and $\Omega = 0^- [14.29] (v = 0)$) allow for decay into higher vibrational manifolds in $X\,^3\Delta_1$. These molecules will decay to the $v = 0$ manifold after about 200 ms. We could also speed up the process by using vibrational repumps: lasers that connect to the $\Omega = 0^- [14.29]$ state from the $v > 0$ vibrational manifolds.

In general, molecules in in excited states can decay to multiple electronic states. In ThF^+, however, the branching ratio from $\Omega = 0^- [14.29]$ back to $X\,^3\Delta_1$ is very close to unity. Therefore, to close the optical pumping cycle, we only need vibrational repump lasers.

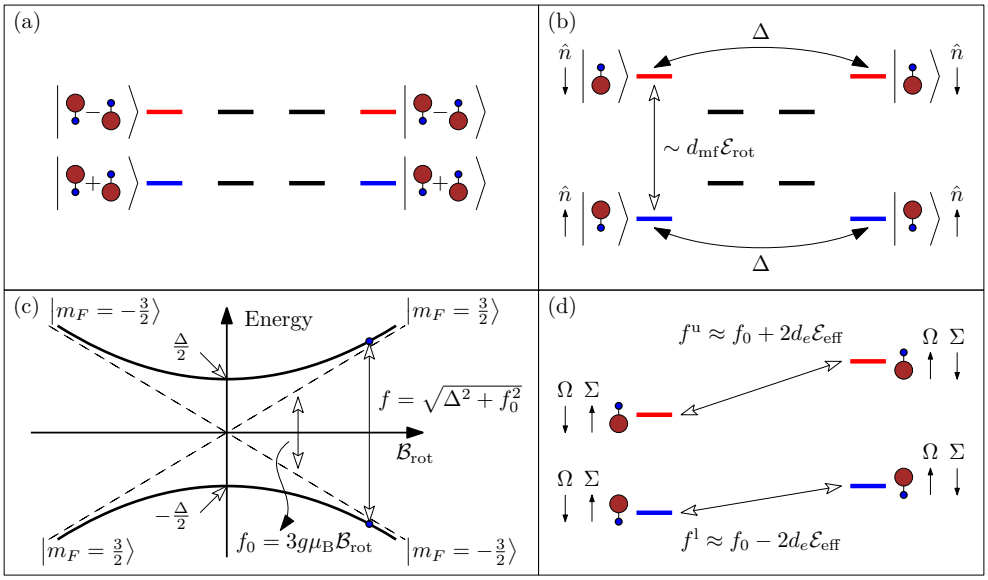

Figure 1.4: **Energy level diagrams of the eEDM-sensitive states.** Only the $X\,^3\Delta_1(v = 0, J = 1, F = 3/2)$ states are shown. Refer to Figure 1.2 for the bigger overview.

(a) In the absence of external fields, the eigenstates are states of good parity. The molecule does not have a preferred orientation. We assume that the positive parity state has the lower eigenenergy in this schematic. We did not determine the energy ordering of the parity states in our experiments.

(b) When we apply an external electric field, we get Stark shifts that scale with the molecular dipole moment d_{mf} and the applied electric field $\mathcal{E}_{\mathrm{rot}}$. The parity states mix and produce states of good orientation. The internuclear axis unit vector $\hat{n}$ points from the lighter anion to the heavy cation. To polarize our molecular ions with an external electric field without ejecting them out of the ion trap, we apply a rotating electric field, with rotation frequency f_{rot} that is fast compared to typical ion motion in the trap, but adiabatic compared to typical energy scales in the molecule. As a result, we work in the rotating frame of the molecules. In the absence of external magnetic fields, the $m_F = \pm 3/2$ states mix from the non-inertial-frame term in the rotating frame. The coupling strength is Δ.

(c) Without the non-inertial-frame term, the energy levels of the $m_F = \pm 3/2$ states within either the upper or lower Stark doublet follow the dashed lines. The energy difference f_0 is just the Zeeman splitting between them. In the presence of the non-inertial-frame term, we get an avoided crossing with splitting Δ. The net frequency difference between the $m_F = \pm 3/2$ states is the quadratic sum of Δ and f_0. Note that f_0 is of a Zeeman nature in this schematic diagram, but as we will see in Chapter 8, it can also come from Berry's phase. The only purpose of f_0 is to lift the degeneracy of the $m_F = \pm 3/2$ states. For our eEDM measurements, we park at an $f_0 \gg \Delta$, where $|m_F = \pm 3/2\rangle$ are good eigenstates of the system. To perform our $\pi/2$ pulse to prepare a superposition of the $m_F = \pm 3/2$ states for our Ramsey sequence, we ramp our fields so that $f_0 \ll \Delta$ and allow the new eigenstates (almost equal superposition of $m_F = \pm 3/2$) to evolve for a time τ, such that $2\pi \cdot \Delta \cdot \tau = \pi/2$, before restoring our fields to the $f_0 \gg \Delta$ setting.

(d) We measure the eEDM in both the upper (red) and lower (blue) Stark doublets. The energy level of each state goes as $E \sim E_{\mathrm{Stark}} + E_{\mathrm{Zeeman}} + E_{\mathrm{EDM}}$. We measure the energy difference within each Stark doublet, so the Stark term drops out. The eEDM term is $E_{\mathrm{EDM}} = -d_e\mathcal{E}_{\mathrm{eff}}$, where $\mathbf{d}_e || \Sigma \cdot \hat{n}$ and $\vec{\mathcal{E}_{\mathrm{eff}}} || -\hat{n}$. We take the difference between f^{u} and f^{l} to extract E_{EDM}. Higher order corrections like slight differences in the g-factors and the Δ coupling between the upper and lower Stark doublets are ignored here for simplicity.

Chapter 2

Preparing ThF^+ ions

2.1 Introduction

Following the footsteps of the experiments with HfF^+, the first step in performing an eEDM experiment with ThF^+ involves creating neutral ThF. These neutral ThF will then be ionized state selectively through resonance-enhanced multi-photon ionization (REMPI) to produce ThF^+ in the eEDM-sensitive state with high preparation efficiency. This process involves exciting ThF to a pre-ionization state, which is higher in energy than the ground state of ThF^+, whereupon it sheds energy by giving up an electron and falls into a lower energy state in ThF^+. To perform this state selective REMPI, we first need to perform survey spectroscopy of the excited states of ThF to find the appropriate intermediate state for REMPI.

Previous work on ThF [44, 45] were laser-induced fluorescence (LIF) spectroscopy in a very limited range slightly below 21500 cm^{-1} above the ground state $X\,^2\Delta_{3/2}$, which is less than half of the ionization energy (IE = 51585(50) cm^{-1} [44]). This is not the most optimum state for state selective REMPI because of the following:

- The second photon of a $1 + 1'$ REMPI usually requires more pulse energy than the first, so that the transition from the intermediate state to the final state can be saturated.
- Since the laser pulse of the second photon is of higher energy, it is more likely to drive a one-color multi-photon (off-resonant) transition than the first photon, because this process is a strong function of the peak laser intensity. If the second photon has more energy than IE/2, then it could drive its own $1' + 1'$ multi-photon ionization, and create ions with undesired internal states.

- Therefore, it is better to have a first photon that is bluer in wavelength than the second, i.e. the first photon should be more than IE/2. In ThF, the first photon should have a wavelength of less than 387 nm.

To find a state that fulfils all the above criteria for state-selective ion creation, we perform laser-induced fluorescence (LIF) spectroscopy on ThF. This chapter is structured as follows. We first begin with an introduction to the setup of the experiment in Section 2.2. Then we take a look at a sample of the results of the scan in Section 2.3. A simple explanation of how we extract the spectroscopic constants is shown in Section 2.4 and 2.5. Finally we conclude with further discussions of the LIF results and their relation to the eEDM experiment with ThF^+ in Section 2.6. The following sections will be paraphrases of our publication Ref. [46].

2.2 Setup

A schematic of the setup is shown in Figure 2.1. The control system and data acquisition systems we use are similar to those used in the HfF^+ experiment, and shall be omitted here for brevity. The interested reader can refer to theses of earlier members of the group (e.g. Huanqian Loh and Matt Grau) for more details.

We use a tunable pulsed dye laser (Sirah Cobra-Stretch, 1800 grooves/mm single grating, 0.06 cm^{-1} linewidth at 600 nm) to perform the LIF spectroscopy. The wavelength of the laser is monitored continuously by a wavemeter (Bristol 871B) during the scan. We reference the wavemeter to a stabilized He-Ne laser with $\sim$50 MHz absolute accuracy. We note that there are vibronic bands that overlap with each other, such that they cannot be rotationally resolved by the pulsed dye laser, especially in the deep ultraviolet region. To resolve these lines, we use a narrow-band pulsed laser system, which consists of a tunable cw-ring dye laser (Sirah, Matisse DR2) and a pulsed dye amplifier (Radiant Dye Amp, 150 MHz linewidth). The wavelength of the seeding laser is monitored by a high resolution wavemeter (High Finesse, WS7), which is referenced to an external-cavity diode laser locked to a ^{87}Rb transition at 384.227982 THz. Lastly, to reduce noise due to laser scattering (e.g. from the ablation laser), a fast switch gates the PMT on 10 ns after the excitation

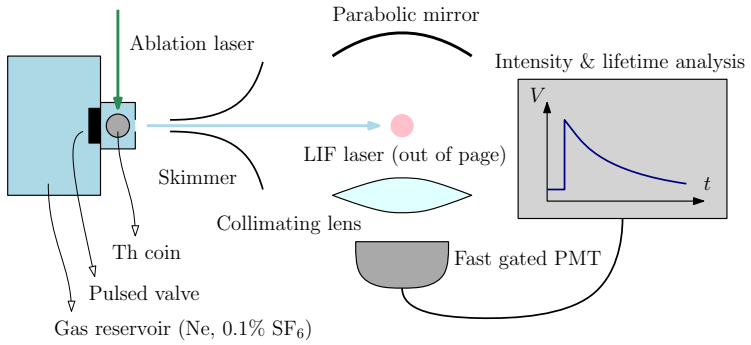

Figure 2.1: **Schematic diagram of the LIF experimental setup.** The LIF spectroscopy consists of the following steps:

(1) A plume of Th plasma is created through the ablation of a Th metal with a 532 nm laser focused down to a beam waist of about 150 µm with about 2 mJ per 5 ns pulse from a Q-switched Nd:YAG laser. The Th metal is mounted on an electronically controlled movable stage to give a fresh surface for each ablation.

(2) The nozzle lets out a buffer gas of Ne at room temperature seeded with SF_6 from a stagnant 100 PSI reservoir. SF_6 reacts with the Th plasma to give ThF, which gets entrained in the supersonic expansion of Ne to form a molecular beam of ThF and cools ThF down to about 10 K in translational and rotational degrees of freedom.

(3) A tunable laser intercepts the molecular beam in a cross-beam setup. If the laser frequency is resonant with a transition in ThF, the molecule is excited to the excited state, and relaxes through fluorescence, which is collected with optics and a photomultiplier tube (PMT). The signal from the PMT goes to an oscilloscope, where the amplitudes and decay time of the trace are recorded and analyzed.

(4) Repeat the experiment with different excitation wavelengths.

laser pulse is fired to extract the long-lived fluorescence signals (> 50 ns).

2.3 Sample of results

We record survey scans over the ranges of 13000 to 16000 cm^{-1}, 18000 to 20000 cm^{-1}, and 26000 to 44000 cm^{-1} using multiple laser dyes (LDS 698, DCM, Coumarin 540A, Coumarin 503, Coumarin 480 and Coumarin 460), and as necessary, frequency-doubled with a BBO crystal. 345 previously unreported vibronic bands of ThF are recorded. The tables of quantum numbers of all the 345 vibronic bands span 15 pages in the paper, and shall not be included in this thesis for brevity. I would refer the interested reader to our publication [46] for the fitted transitions. Specific vibronic bands that are interesting will be reproduced here for discussion. A compressed plot of all the bands found and fitted in our spectroscopy is shown in

Figure 2.2.

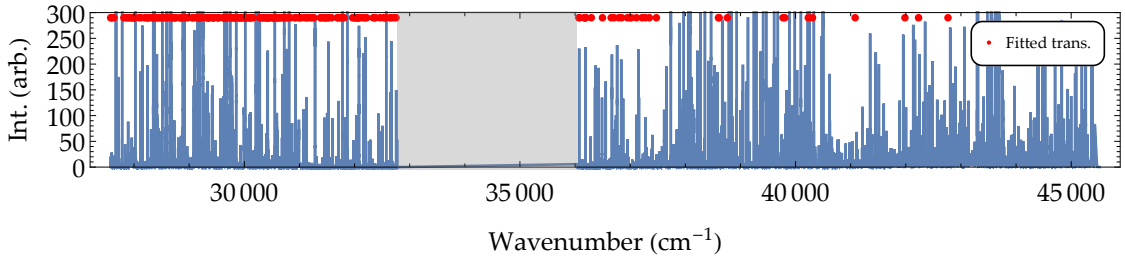

Figure 2.2: **Compressed spectra of all bands found (blue trace) and fitted (red dots above traces) in our LIF survey spectroscopy.** The grey region in the center indicates the region that we did not scan. The area of interest lies to the right of the grey region because of the "above IE/2" requirement mentioned in the introduction of this chapter.

Plotting the LIF amplitudes against the frequencies of the laser gives rotational structures as shown in Figure 2.3.

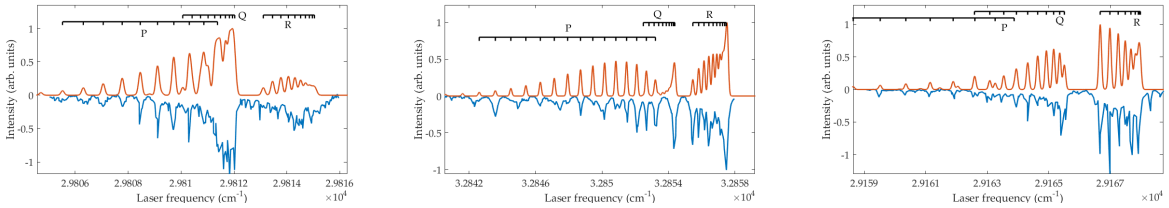

(a) $\Omega' = 1/2$ (b) $\Omega' = 3/2$ (c) $\Omega' = 5/2$

Figure 2.3: **Samples of rotational bands obtained from the LIF survey spectroscopy.** The quantum number Ω (Section 2.4) is listed for each of the three sample plots shown. The blue inverted traces are data points from experiment, while the red traces are profiles of the simulated fits.

Interpretation of these bands and assignment of quantum numbers require knowledge of allowed transitions through selection rules. We shall cover this in the next section.

2.4 Spectroscopic constants, energy scales, and fitting form

The Hamiltonian governing a diatomic molecule is highly non-trivial. I would refer the interested reader to textbooks (e.g. Ref. [47]) for a complete treatment of the full Hamiltonian and the selection rules that come from it. Here, I shall only attempt to describe very specific cases, and lay out the spectroscopic constants and quantum numbers relevant to selection rules that apply to most of the bands found in this LIF survey spectroscopy:

Rotational constant, B. Inversely proportional to the moment of inertia of our diatomic molecule modelled as a rigid rotor. Usually reported in units of cm^{-1}.

Origin of vibronic band, ν_0. Usually reported in units of cm^{-1}.

Rotational quantum number, J. The quantum number J comes from the total angular momentum operator $\mathbf{J} = \mathbf{L}+\mathbf{S}+\mathbf{R} = \mathbf{J}_a+\mathbf{R}$, where $\mathbf{L}$, $\mathbf{S}$, $\mathbf{J}_a$ and $\mathbf{R}$ are the electronic orbital angular momentum, electronic spin angular momentum, total electronic angular momentum, and rotational angular momentum of the nuclei, respectively. Selection rules for E1 (electric dipole; single photon) transitions only allow for transitions between states with $\Delta J = -1, 0, +1$, which, in spectroscopy literature, correspond to P, Q, and R transitions, respectively. The P, Q, and R transitions give rise to distinctive P, Q, and R branches, which can be seen from the marked ticks in Figure 2.3. The relative intensities of the P, Q, and R branches are determined by Hönl-London factors, which are detailed below.

Projection of total angular momentum onto internuclear axis, Ω. The quantum number Ω takes values from $-J_a$ to J_a (in integral steps). It is formally defined as $\mathbf{J}_a \cdot \mathbf{n}$, where $\mathbf{n}$ is the internuclear axis vector pointing towards the cation. The quantum number Ω reported for the LIF spectroscopy are the absolute values $|\Omega|$ since our setup is not sensitive to the sign of Ω. Selection rules for E1 transitions only allow for transitions between states with $\Delta\Omega = 0, \pm 1$.

For completeness, the projections of $\mathbf{L}$ and $\mathbf{S}$ onto the internuclear axis are denoted as $\mathbf{L}\cdot\mathbf{n} =: \Lambda$ and $\mathbf{S}\cdot\mathbf{n} =: \Sigma$. Some combination of all the above quantum numbers are used in the molecular term symbol: ${}^{2S+1}\Lambda_\Omega$ to

label the molecular quantum states, much like the Russel-Saunders term symbol for atomic states. These term symbols are strictly only valid for states that fall under Hund's case (a), because quantum numbers like Λ may no longer be good quantum numbers for states belonging to other Hund's cases. While more information on Hund's cases can be found in many textbooks (e.g. Brown et al. [47]), Figure 2.4 provides a quick summary of three Hund's cases relevant to this thesis.

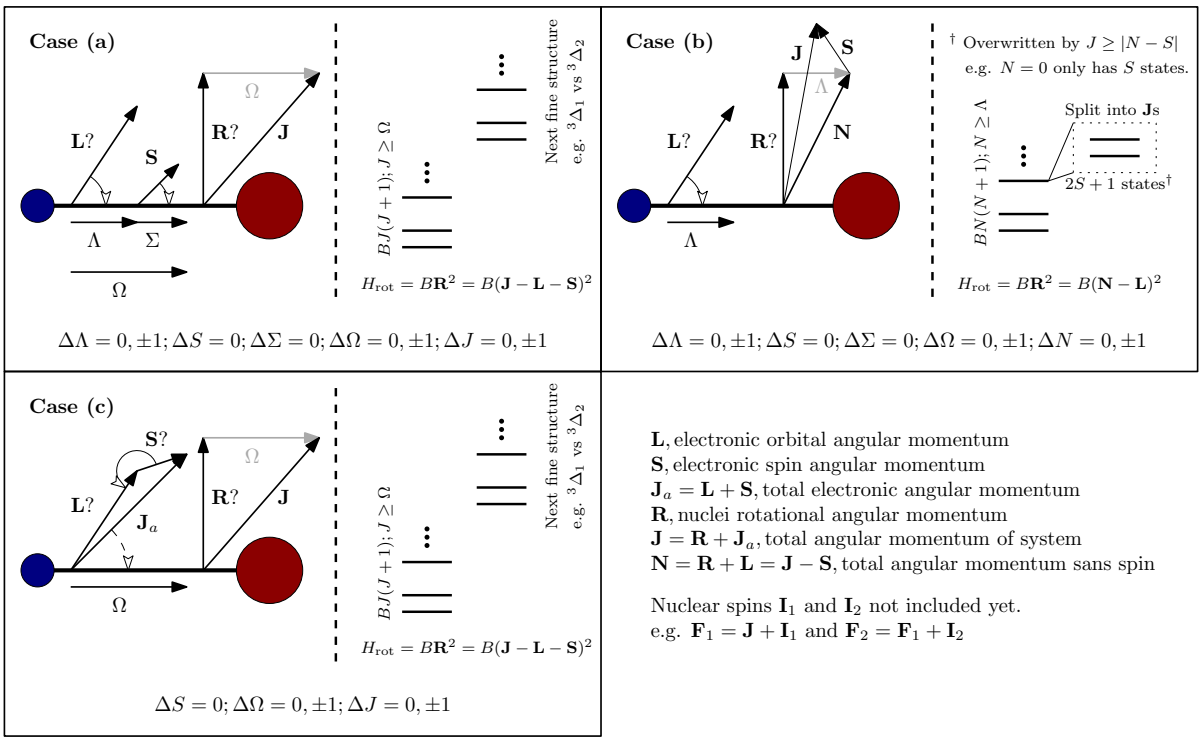

Figure 2.4: **Quick summary of Hund's cases (a), (b), and (c).** Adapted from Ref. [47]. Hund's cases (d) and (e) are not relevant to this thesis. Solid filled arrows indicate angular momenta or their projections onto the internuclear axis. Unfilled arrows indicate couplings between angular momenta or the internuclear axis; solid unfilled arrows imply a stronger coupling than dashed unfilled arrows. Quantum numbers with "?" indicate not-a-good quantum number. Selection rules are also indicated at the bottom of each box. Examples of the relevant rotational energy level structure are also shown in each box.

The transitions between the ground state in ThF and excited states have energies of the following form:

$$\nu = \nu_0 + E'(J') - E''(J''), \tag{2.1}$$

where $E(J)$ can take on several forms depending on which Hund's case the relevant states fall under. We managed to fit our transitions to three main classes, and these are the forms of $E(J)$ relevant to our LIF

spectroscopy:

Hund's case (c). **L** and **S** couple strongly together, and their resultant angular momentum then couples to the internuclear axis to give Ω. This situation arises in heavy molecules. We expect most electronic states in ThF to fall under this category because of the heavy thorium atom. This is especially true when J is small. This will give:

$$E(J) = BJ(J+1). \tag{2.2a}$$

The ground electronic state of ThF ($X\,^2\Delta_{3/2}$) is well described by Hund's case (c). Good quantum numbers are J and Ω. The observed Ω-doubling is much smaller than the linewidth of our laser, and shall be neglected in our fitting model. Hönl-London factor is given by:

$$\mathrm{HL}_{\Omega',J',\Omega'',J''} = (1+\delta_{\Omega',0}+\delta_{\Omega'',0}-2\delta_{\Omega',0}\delta_{\Omega'',0})\,(2J'+1)\,(2J''+1)\times \begin{pmatrix} J' & 1 & J'' \\ -\Omega' & (\Omega'-\Omega'') & \Omega'' \end{pmatrix}^2, \tag{2.2b}$$

where $\delta_{i,j}$ is the Kronecker delta function, and the last term is the Wigner $3j$ symbol. Single- (double-) primed quantum numbers correspond to those of the excited (ground) state. Samples of bands in Hund's case (c) are shown in Figure 2.3.

Hund's case (b). This is the case where $\Lambda = 0$, e.g. when **L** precesses around the internuclear axis, but is fully orthogonal to it. In this case, spin-orbit coupling vanishes, and **S** decouples from the internuclear axis. One consequence of this is that Ω is now ill-defined; the good quantum number to use now is N, where N is the quantum number for the total angular momentum excluding spin $\mathbf{N} = \mathbf{J} - \mathbf{S}$. Another consequence is that there will multiple sets of PQR branches corresponding to the multiplicity of the spin. For the case of $S = 1/2$, we have two sets of PQR branches with:

$$E_{a/b}(N) = BN(N+1) - \frac{\gamma}{2}\left(N + \frac{1 \pm s}{2}\right), \tag{2.3a}$$

where $\{a, b\}$ denote the doublets, γ is the spin-rotation constant, and $s = \pm 1$ corresponds to the a

and b doublets, respectively. The PQR branches are determined by the following selection rules:

$$\mathrm{P}_{a/b} : \left(N' \mp \frac{1}{2}\right) - J'' = -1,$$
$$\mathrm{Q}_{a/b} : \left(N' \mp \frac{1}{2}\right) - J'' = 0,$$
$$\mathrm{R}_{a/b} : \left(N' \mp \frac{1}{2}\right) - J'' = 1,$$

where the upper (lower) sign corresponds to the a (b) state, and once again single- and double-primed variables denote the excited and ground states involved in the transitions, respectively. The Hönl-London factors for a Hund's case (c) (the ground state) to a Hund's case (b) transition is:

$$\mathrm{HL}_{\Lambda' J' N', \Omega'' J''} = \left| \sum_{\Sigma', \Omega'} \sqrt{2N'+1}\,(-1)^{J'+\Omega'} \sqrt{\mathrm{HL}_{\Omega', J', \Omega'', J''}} \begin{pmatrix} S & N' & J' \\ \Sigma' & \Lambda' & -\Omega' \end{pmatrix} \right|^2, \tag{2.3b}$$

where $\mathrm{HL}_{\Omega', J', \Omega'', J''}$ is the Hönl-London factor for a Hund's case (c) to case (c) transition, as shown in equation 2.2b. A sample of a rotational band under Hund's case (b) in the LIF spectroscopy is shown in Figure 2.5.

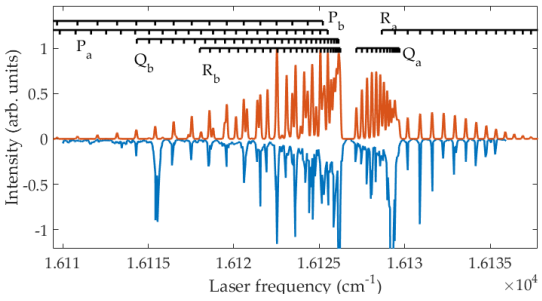

Figure 2.5: **Sample of a Hund's case (b) rotational band obtained from the LIF survey spectroscopy.** The blue inverted traces are data points from experiment, while the red traces are profiles of the simulated fits.

$^2\Pi$ states The last class of transitions involve excited $^2\Pi$ states. These states have significant Λ-doubling. Since we do not have enough spectroscopic resolution to resolve the e/f symmetry components of the lower state of the transition, we cannot determine the absolute parities of the upper states. Following the convention used in Loh *et al.* [48], we label related Λ-doubling pairs as a/b instead of

e/f. The upper state can be modeled by:

$$E_{a/b}(J) = B'J(J+1) \mp \frac{1}{2}(p+2q)\left(J+\frac{1}{2}\right), \tag{2.4}$$

where $(p+2q)/2$ is the Λ-doubling constant. The upper (lower) sign corresponds to the a (b) symmetry component. An example of a band with resolvable Λ doubling is shown in Figure 2.6.

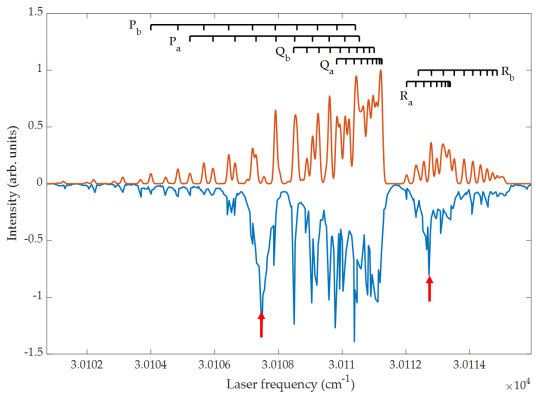

Figure 2.6: **Sample of a band with resolvable Λ-doubling.** Red arrows indicate strong thorium atomic transitions (from NIST Atomic Spectra Database [49]). The blue inverted traces are data points from experiment, while the red traces are profiles of the simulated fits.

2.5 Vibrational progression

All of the ThF transitions that we have assigned seem to have the $X\,^2\Delta_{3/2}$ ground electronic state as the lower level. The first excited state of ThF is $^2\Delta_{5/2}$, which is 2500 cm^{-1} higher in energy and has not been observed in our experiments [44]. However, there are finer structures within the ground electronic states, e.g. vibrational. During the molecule production, some of the molecules are created in excited vibrational states within the ground electronic manifold. The vibrational spacing of the ground state is about 600 cm^{-1} (1 cm^{-1} $\approx$ 30 GHz). Given favorable Franck-Condon factors, different vibrational states from the ground electronic manifold can couple to the same excited vibronic state, giving rise to a vibrational progression of transitions separated by the vibrational spacing of the ground electronic manifold. Likewise, the same lower vibronic state can couple to vibrational progressions of the excited electronic state.

Using a combination difference analysis, we tentatively group vibronic bands that share the same upper and lower electronic states, but different vibrational levels, into sets of vibrational progressions. The

combination differences of the lower states are known from previous work [44, 45]. The criteria for extracting combination differences for the upper states are: (i) vibronic bands that belong to the same electronic state should have similar rotational constants; and (ii) vibrational constants should agree with *ab initio* calculations within a reasonable range ($500 < \omega_e < 700$ cm^{-1}, $0 < \omega_e\chi_e < 10$ cm^{-1}, similar radiative lifetime).

For transitions that we associate with a vibrational progression, we redo the fit to the vibronic band using the rotational constant ($B_{v''}$) for the relevant vibrational quantum number (v'') of the lower state in the transition. From these fits, we extract the molecular constants ν_e, B_e, α_e, ω_e, and $\omega_e\chi_e$. These constants are related to the fitting constants (ν_0, B_v, and v, which are defined in previous sections) as such:

$$\nu_0 = \nu_e + \omega_e'\left(v' + \frac{1}{2}\right) - \omega_e'\chi_e\left(v' + \frac{1}{2}\right)^2 - \omega_e''\left(v'' + \frac{1}{2}\right) + \omega_e''\chi_e\left(v'' + \frac{1}{2}\right)^2, \tag{2.5a}$$

$$B_v = B_e - \alpha_e\left(v + \frac{1}{2}\right). \tag{2.5b}$$

We extract the molecular constants of the ground state with global fit to all the transitions involved in vibrational progressions, and the result is summarized in Table 2.1.

	This work (exp.)	Barker *et al.* [44]	Theory
ω_e (cm^{-1})	601.00(2)	605(15)	598.8
$\omega_e\chi_e$ (cm^{-1})	2.07(3)	-	2.1
B_e (cm^{-1})	0.2339(2)	0.237(5)	0.2325
α_e (cm^{-1})	0.0014(3)	-	-
r_e (Å)	2.026(3)	2.01(3)	2.032

Table 2.1: Comparison of molecular constants of the $X\,^2\Delta_{3/2}$ ground state of ThF in experiment and theory. 90% confidence intervals are quoted in parentheses. The parameter r_e is the equilibrium internuclear distance, and the other molecular constants are defined in equation 2.5. We collaborated with Prof. Lan Cheng from Johns Hopkins University for the theoretical calculations [46].

A comprehensive list of the upper state vibrational progressions that we have tentatively assigned is shown in Table 2.2.

For progressions with only two different v', e.g. $v' = 0$ and $v' = 1$, we conventionally set $\omega_e\chi_e$ to zero so that ω_e is just the splitting between the relevant rotational band origins of the upper state. 90% confidence intervals, which come from a convolution of fitting uncertainties and vibrational progression fitting uncertainties, are quoted in parentheses in Table 2.2.

Since the bands in our data set have relatively low resolution and high state density, there is a risk that

	ν_e	B_e	α_e	ω_e	$\omega_e\chi_e$	$\frac{p+2q}{2}$
$\Omega = 3/2$ [14.09]	14093.80(3)	0.2276(5)	-	557.25(2)	-	-
$\Omega = 3/2$ [15.18]	15180.19(1)	0.2221(9)	-	584.00(4)	-	-
$\Omega = 3/2$ [18.62]	18616.19(2)	0.2179(5)	0.0013(2)	517.54(3)	2.00(1)	-
$\Omega = 3/2$ [19.98]	19978.19(3)	0.2172(4)	0.0007(3)	533.05(3)	-	-
$\Omega = 3/2$ [20.40]	20397.40(2)	0.2126(3)	-	569.47(2)	-	-
$^2\Pi_{1/2}$ [27.98]	27977.94(4)	0.2173(8)	-	563.13(4)	-	0.009(6)
$\Omega = 3/2$ [28.37]	28370.52(3)	0.2138(5)	-	577.59(3)	-	-
$^2\Pi_{1/2}$ [29.22]	29223.19(6)	0.2175(3)	-	580.5(1)	3.80(8)	0.022(3)

Table 2.2: **Comprehensive list of tentative assignments of vibrational progressions.** Vibrational progressions are groups of transitions which share the same upper and lower electronic states, but different vibrational levels. Units for all the above constants are quoted in cm^{-1}. 90% confidence intervals, which come from a convolution of spectroscopic fitting uncertainties and vibrational progression fitting uncertainties, are quoted in parentheses. Large fitting uncertainties for the rest of the vibrational progressions prevent us from extracting their corresponding α_e, so α_e is set to zero for our fitting purposes.

transitions are incorrectly grouped, and that apparent progressions occur only due to coincidence. Hence, more experiments are required to confirm these preliminary assignments, and we leave this as a challenge to our fellow spectroscopists.

The aforementioned analysis allows us to group most of the vibronic bands found in the visible region into vibrational progressions. In the ultraviolet region, however, we are unable to identify any definite vibrational progressions. Missing transitions in vibrational progressions could be explained by perturbations of these high energy levels, which will be discussed in Section 2.6.2.

2.6 Further discussion

2.6.1 Search for the s^2l state in ThF

The ground electronic state of ThF has an s^2d structure for its valence electrons. A one-photon transition can bring the configuration to *spd*, s^2p, or s^2f. We started the LIF experiment hoping to find an s^2f Rydberg state, where we can excite it with more photons to bring it to a pre-ionization state with s^2l configuration, where $l \geq 4$. States with s^2l configurations are known as core-nonpenetrating Rydberg states, where the orbital angular momentum of the Rydberg electron prevents the electron from having significant spatial overlap with the rest of the molecule. This molecule can then autoionize by shedding energy from the s^2 ion core to the Rydberg electron and preserve its s^2 nature.

An ionization process like this would prepare all the ions in the $J = 0$ state. In principle, this can give a much higher state preparation efficiency as compared to the one we settled on (Section 2.6.3), where the molecule autoionizes into a distribution of J states within the ground vibronic manifold of ThF^+ $X\,^3\Delta_1(v = 0, J = 1\,\text{to}\,5)$.

Working with our theorist collaborator Prof. Lan Cheng, we know that s^2l states are high-lying states and have B constants that are close to that of ThF^+ (0.243 cm^{-1} [43]) because of their similarities in electronic structures. However, all the B constants of the transitions that we find are smaller than the ground state (0.233 cm^{-1}), which is consistent with the fact that excited states usually have longer internuclear separation of the nuclei, resulting in smaller $B = \frac{\hbar^2}{2\mu r_e^2}$ (where μ is the reduced mass). Disappointingly, these states with B smaller than that of the ground state are probably *spd* states.

Moreover, the spectra obtained at high energy levels (deep ultraviolet region) in our LIF spectroscopy exhibit characteristics of strong perturbations (lack of regular rotational band structure), which make identifying the states very hard with the resolution that we have. Hence, we ended up with an extensive database of transitions but not the one we started out to search for. Nevertheless, we managed to find a suitable state to use as our intermediate state for REMPI (Section 2.6.3), but before we move on to that we shall address the problem with perturbations in the deep ultraviolet region in the next section for completeness.

2.6.2 Perturbations in the deep ultraviolet region

One explanation for the lack of regular rotational band structures in the deep ultraviolet region is the result of perturbations between the s^2f states and *spd* states. In contrast to the region where only *spd* states exist, i.e. low lying states, the diabatic potential curves of both types of states cross very frequently at high energy levels (Figure 2.7), because of the significant difference in their internuclear distances (different rotational constants of *spd* and s^2f). In this region, interactions could give rise to many avoided crossings, and profoundly distort the molecular potentials for both the s^2f and *spd* states. The crossings of these potential curves would redistribute the oscillator strength of a vibrational level in a potential curve to many other vibrational levels of other potentials, hence making the transitions very weak and come with irregular vibrational patterns.

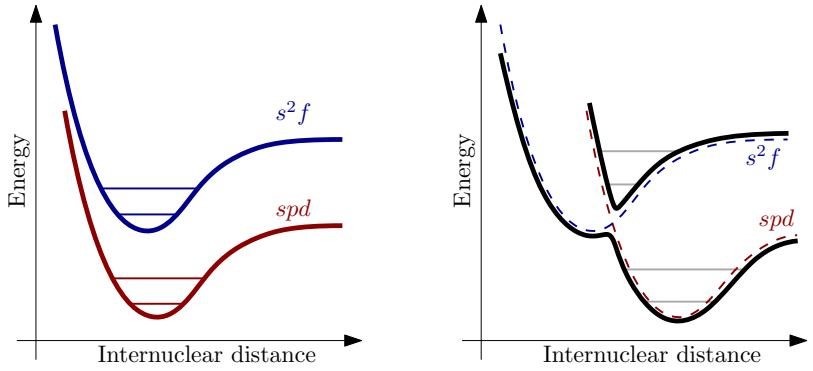

(a) Similar internuclear distances. (b) Different internuclear distances.

Figure 2.7: **Crossings of diabatic potential curves of *spd* and s^2l states distort the potential curves.** The horizontal lines represent the vibrational levels. Left: low lying *spd* and s^2f states have similar internuclear distances, so their potential curves do not cross each other. Right: high lying *spd* and s^2f states have different internuclear distances, so their potential curves (dashed) cross each other and mix, giving rise to very different adiabatic potential curves (solid).

2.6.3 Auto-ionization into the ground vibronic state of ThF^+

We choose the $\Omega = 3/2$ [32.85] state as the intermediate state for the creation of ThF^+ in the $X\,^3\Delta_1(v = 0)$ state through REMPI. This choice is motivated by several considerations:

(1) This chosen intermediate state lies above IE/2, and so non-resonant ionization from ground state of ThF by the more intense second photon is greatly suppressed.

(2) The transition from the ground state to the $\Omega = 3/2$ [32.85] state is a relatively strong transition in a wavelength region that is easily accessible.

(3) A convenient 532 nm photon (from the second harmonic of Nd:YAG laser) can be used as the second photon, which excites the neutral molecule into a broad autoionizing resonance that lies only 62 cm^{-1} above the ionization potential for decay into the $X\,^3\Delta_1(v = 0)$ state in ThF^+. Since the next vibronic state $a\,^1\Sigma^+(v = 0)$ lies 314 cm^{-1} above the ground state, energy considerations restrict all ions formed to be in the ground vibronic state, which coincidentally is the preferred eEDM-sensitive state.

We verify the formation of ions in the ThF^+ ground vibronic state by state-selective resonance-

enhanced multi-photon dissociation (REMPD). The details of the dissociation technique will be described in Chapter 3. Using the dissociation readout technique, we also show that the distribution of the ion population across the different J^+ levels depends on the J' quantum number of the intermediate state used in the REMPI process (the + superscript indicates quantum numbers of the ThF^+ to distinguish it from those of ThF). The J^+-distributions of the ions created with different J' intermediate states are shown in Figure 2.8.

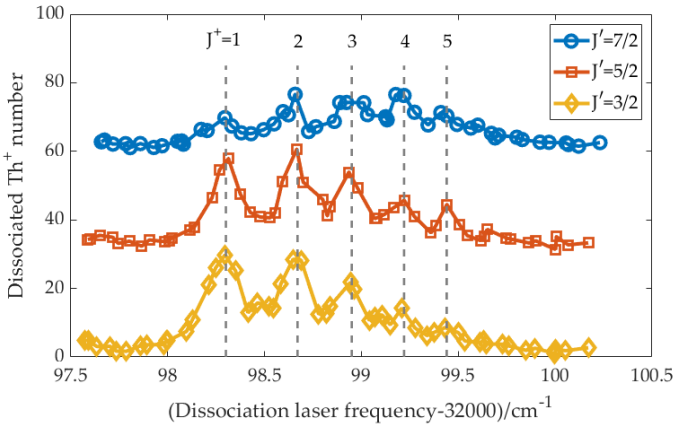

Figure 2.8: **J^+-distributions of ThF^+ ions created from different intermediate J' states of ThF.** The rotational distribution of the ThF^+ ions shifts toward higher J^+ states as the J' value of the intermediate state is increased. For easy comparison purposes, the red and blue traces are offset upward from zero by 30 and 60, respectively. These traces are scans of the R branch of the dissociated intermediate state used in the resonance-enhanced multi-photon dissociation spectrum.

Figure 2.8 shows that the rotational distribution of the ions shifts toward higher J^+ states when a higher J' intermediate state is used. Since the electron that is lost during the ionization process carries a fixed range of angular momenta, we expect to see a higher final angular momentum distribution for the ions when an intermediate state of higher angular momentum is used, and *vice versa* [50]. Since the eEDM sensitive state is the lowest rotational state ($J^+ = 1$), we use the $J' = 3/2$ state as our intermediate state for the REMPI process, which results in 30% of the ions being produced in the desired $J^+ = 1$ state.

Before we move on to talk about spectroscopy experiments performed on ThF^+ created with this new-found intermediate state, we shall have some closing remarks on the LIF experiment.

2.6.4 Closing remarks

2.6.4.1 Contamination from other species and REMPI TOF-MS

The LIF experiment on ThF has been plagued by contamination from other species created during the molecule creation stage. Performing a REMPI time-of-flight mass spectrometry (TOF-MS) on our molecular beam shows contamination by species like ThO and ThF_2. The TOF-MS is performed by kicking the molecular beam with electric fields towards a microchannel plate (MCP) after they are ionized by the REMPI lasers. The kick imparts the same momentum to all the ions (of the same charge), resulting in spatial separation of species with different masses as they fly towards the MCP, giving rise to different arrival times at the MCP. A sample of the trace from the REMPI TOF-MS is shown in Figure 2.9

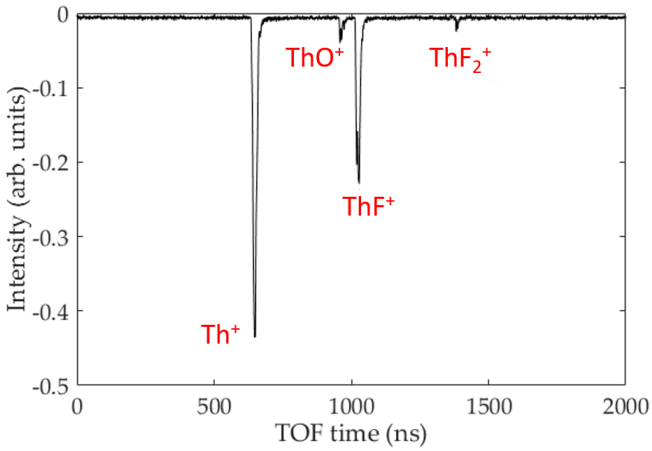

Figure 2.9: **Typical traces of the REMPI TOF-MS experiments.** The separation of species by mass in the REMPI TOF-MS trace allows us to distinguish the ion species to separate the ThF signals from the rest. Our mass resolution is sufficiently high to separate ThO^+ from ThF^+.

One possible reason for seeing ThO signals in our LIF is that ThO is created during the ablation stage where residual oxygen from air that is mixed into our buffer gas reservoir reacts with the thorium plasma to create ThO.

2.6.4.2 Current status of ion creation

In Section 2.6.3, we saw that we can create ions with 30% of them in the $J^+ = 1$ rotational manifold by addressing the $\Omega = 3/2\,[32.85]\,(v' = 0, J' = 3/2)$ intermediate state. Having a lot of ions created in the $J^+ = 1$ rotational manifold is desirable because that is the eEDM-sensitive manifold in our experiment, and ions in the rest of the rotational manifolds only contribute to decoherence through ion-ion collisions in our ion trap.

We can go through the $\Omega = 3/2\,[32.85]\,(v' = 0, J' = 3/2)$ intermediate state by addressing the ground state of our neutral ThF molecule with a laser tuned to the P(5/2) or a Q(3/2) line as the first photon of our REMPI process. However, as we shall see in Chapter 4, we have the ability to move ion population in the $J^+ > 1$ rotational manifolds into the $J^+ = 1$ manifold with optical and microwave pumping. Hence, there is no pressing need for us to stick to the $J' = 3/2$ intermediate state to maximize our yield of useful ThF^+ ions. In fact, we now illuminate our ions with our dye laser parked at the Q branch, addressing the Q(3/2), Q(5/2), and Q(7/2) lines simultaneously (incoherently) with the broad linewidth of our pulsed dye laser. The ions created no longer have a population peak at $J^+ = 1$, but we now have many more ions because the Q lines address the molecules in the $X\,^2\Delta_{3/2}(v'' = 0, J'' = 3/2\,\text{to}\,7/2)$ vibronic manifold instead of only the $J'' = 3/2$ with the Q(3/2) line only. Ions spread out across the rotational manifolds can then be ushered into the $J^+ = 1$ rotational manifold with techniques to be introduced in Chapter 4.

Understanding how we usher ions to our desired quantum states involve knowing how to perform state readout of our ions first. So we shall be patient and first look at how we read out the quantum states of our ions using photodissociation in the next chapter. Note that from here on, we will only be talking about the ThF^+ ion, so we shall drop the + superscript from the quantum numbers.

Chapter 3

State readout of ThF^+

3.1 Introduction

The previous chapter taught us how to prepare ThF^+ ions. Using techniques to be discussed in this chapter, we managed to verify that the ions are prepared in the ground vibronic state of ThF^+. Similar to its ionization counterpart, REMPI, we use resonance-enhanced multi-photon dissociation (REMPD) to dissociate our molecule state selectively to perform our quantum state readout. Our pulsed dye laser (Sirah Cobra-Stretch) has a linewidth that is narrow enough ($\sim$ 6 GHz after doubling with BBO) to distinguish between rotational lines ($\sim$ 10 GHz), but not structures like hyperfine, Stark, parity doublets, and Zeeman sublevels within each rotational manifold. To discern ion population within the finer structures, we use cw lasers to shelf ions in higher rotational or vibrational states (see Chapter 4) before dissociating everything that is left in that rotational manifold. Upon dissociation, the molecules in the targeted rotational state will turn into Th^+ ions and neutral F atoms, and the ions (both the dissociated Th^+ and the undissociated ThF^+) are ejected towards our microchannel plate (MCP) assembly for detection (see Figure 3.1). The time of flight is long enough for the ions of different species to separate by their masses. This has been the basis of state readout in the Gen. I experiment. With this technique, we can read out the ion population in a single selected rotational manifold with each shot of our experiment.

In the Gen. II experiment, in collaboration with Prof. Tanya Zelevinsky from Columbia University, we managed to squeeze more out of our dissociation technique to give us two-state detection, instead of just one state, with each destructive measurement with our action spectroscopy [38]. In short, this upgrade makes

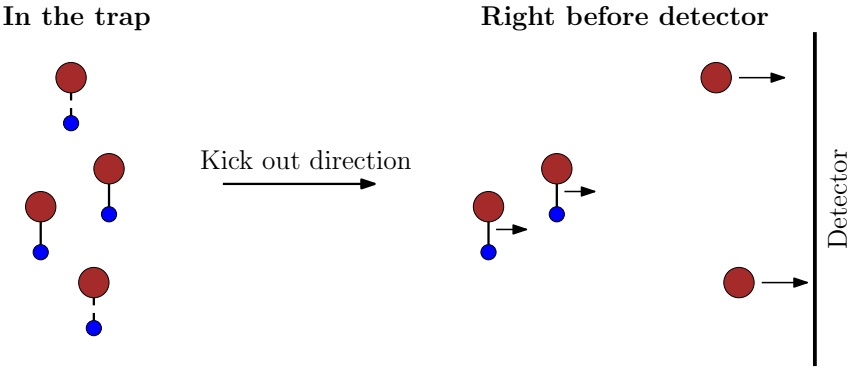

Figure 3.1: **Schematic diagram showing state readout using state-selective REMPD.** On the left we have the ions right after dissociation; molecules in the targeted state are dissociated (indicated with dashed lines connecting the blue fluorine atom and the red thorium ion), and those in the wrong state remain intact as molecules (indicated with solid lines). Right after dissociation, the ions are ejected out of the trap (rightwards in the diagram) towards the ion detector. The Th^+ ions are separated from the ThF^+ ions by their difference in masses, and they reach the detector first. By counting the number of Th^+ ions, we can deduce how many ions are in the targeted state right before dissociation.

use of the fact that the photofragments can be ejected out of the molecule with an angular dependence on the state of the molecule before dissociation. By choosing the intermediate state used for REMPD carefully, we can have the photofragments ejected in largely opposite directions for the two different states that we wish to detect. This also relies on the fact that our molecules have well defined orientations in our trap along the direction of the electric field ($\mathcal{E}_{\text{rot}}$) that we use to polarize our molecules. The physics behind this angle-resolved photofragments technique is quite involved, but it is mentioned in many sources (see Ref. [38, 51–53], and William Cairncross's thesis) so I shall only state the expression of the angular distribution here:

$$
\begin{aligned}
I(\theta,\phi) &\propto \sum_{\Omega_f} \left| \sum_{J_f,(m_J)_f} \sqrt{2J_f+1} \left(\mathcal{D}^{J_f}_{(m_J)_f,\Omega_f}(\phi,\theta,0)\right)^* \langle \phi^{\text{cont.}}_{J_f,(m_J)_f,\Omega_f,E} | \boldsymbol{\mu}\cdot\boldsymbol{\epsilon} | \phi' \rangle \right|^2 \\
&= \sum_{\Omega_f} \left| \sum_{J_f,(m_J)_f} \sqrt{2J_f+1} \left(\mathcal{D}^{J_f}_{(m_J)_f,\Omega_f}(\phi,\theta,0)\right)^* \right. \\
&\qquad \times \sum_{p,q} (-1)^{p+(m_J)_f-\Omega_f} \sqrt{(2J_f+1)(2J'+1)} \\
&\qquad \left. \times \begin{pmatrix} J_f & 1 & J' \\ -(m_J)_f & -p & m'_J \end{pmatrix} \begin{pmatrix} J_f & 1 & J' \\ -\Omega_f & q & \Omega' \end{pmatrix} \boldsymbol{\mu}_{q,\{J_f,(m_J)_f,\Omega_f,E\}} \boldsymbol{\epsilon}_p \right|^2 ,
\end{aligned}
\tag{3.1}
$$

where $\mathcal{D}$ is the Wigner D-matrix; $\boldsymbol{\mu}_q$ is the q^{th} (spherical tensor) component of the transition dipole moment;

$\boldsymbol{\epsilon}_p$ is the p^{th} (spherical tensor) component of the (second REMPD) photon polarization; primed variables belong to the state that we are dissociating from (the intermediate state in our $1+1'$ scheme); variables with the subscript f indicate those for the predissociation state. By E1 selection rules (or properties of the Wigner 3-j symbol), we demand that $(m_J)_f = m'_J - p$ and $\Omega_f = \Omega' + q$. The sum is coherent in $\{J_f, (m_J)_f\}$ but incoherent in Ω_f. Caveat: this necessarily assumes that predissociation states of different Ω_f are well separated in energies.

The question now is whether we can also implement this upgraded detection scheme on ThF^+. The rest of this chapter will proceed as follows. We will begin with the rule of thumb (Section 3.2) for choosing the intermediate state that will give us the best angle-resolved photofragment resolution. We will then look at results from our spectroscopy (Section 3.3). Finally we will discuss how we can further optimize this technique on ThF^+ (Section 3.4).

3.2 Rule of thumb for two-state detection using angle-resolved photofragments

There are two main things[1] that we care about in performing two-state detection using angle-resolved photofragments: (i) angular distribution of photofragments, and (ii) energy of ejected photofragments.

3.2.1 Angular distribution of photofragments

We want the angular distribution to be asymmetric about the equator, and as polar as possible. It turns out that the angular distribution depends on both the intermediate and the predissociation states that we address. There is no hard and fast rule on what dissociation pathway we should take to get the most directed angular distribution, a polar one in an ideal case, but here is a rule of thumb on how to choose the intermediate state.

Dissociate from states with $\Omega' \neq 0$. States with $\Omega' = 0$ are not polarized, i.e. the molecule does not have a preferred orientation w.r.t. our polarizing $\mathcal{E}_{\text{rot}} = 60$ V/cm at the current field strength applied. Our $\mathcal{E}_{\text{rot}}$ is not strong to couple states of opposite parity for states with $\Omega' = 0$; the closest state of opposite parity in an $\Omega' = 0$ state is the next rotational state, but the Stark coupling is small compared to the rotational splitting ($d_{\text{mf}}\mathcal{E}_{\text{rot}} \sim 100$ MHz vs rotational splitting ~ 30 GHz)[2] . Since states with $\Omega' = 0$ are not polarized, the photofragments will be ejected equally likely in both hemispheres, thus rendering the two-state detection through angular resolution of photofragments ineffective.

Dissociate from states with $m'_J \neq 0$. Molecules in the $m'_J = 0$ state have the J' vectors precessing on the plane perpendicular to the quantization axis. We do not expect highly polar angular distributions when dissociating from such states.

The first REMPD photon: $J' = 2$. Our first REMPD photon takes us from our eEDM-sensitive state $X\,^3\Delta_1(v = 0, J = 1, m_J = 1, |\Omega| = 1)$ to an intermediate state $(J', m'_J, |\Omega'|)$.[3] We choose to work

[1] There is a third. We want to have high dissociation efficiency. We will talk about this more in Section 3.4.2.
[2] For the $|\Omega'| > 0$ states, states of opposite parities are separated only by the Ω-doubling splitting ~ 10 MHz
[3] Our eEDM-sensitive states are in the $m_F = \pm 3/2$ stretched Zeeman states, so they correspond to the $m_J = \pm 1$ states. We will be switching between these two languages for the bulk of this section.

with $J' = 2$ because the linewidth of our pulsed dye lasers are not narrow enough to resolve the Q lines to dissociate only the $X\,^3\Delta_1(v = 0, J = 1)$ rotational manifold, so we park on the R(1) line instead. The quantum number m'_J depends on the polarization of the photon used, e.g. $m'_J = 2$ if we use a σ^+ photon, and $m'_J = 1$ if we use a π photon. Our molecule decides what $|\Omega'|$ is at the wavelength of the first photon used, but we get to decide which wavelength to use.

One could simulate the angular distributions of all possible dissociation pathways from our eEDM-sensitive state, assuming that the transitions exist. One can then see what intermediate states are available to us from our spectroscopy, and decide on a REMPD scheme that gives the most polar angular distribution. All the constraints above limit us to only ten possible outcomes: four for $|\Omega_f| = 1$, and six for $|\Omega_f| = 2$. There is no reason not to look at all of them, shown in Figures 3.3 and 3.4.

The first thing we noticed from Figure 3.3 is that the directedness of the photofragments do not look impressively polar for the cases of $|\Omega_f| = 1$. One reason is that when $\Omega' < J'$ for a fixed m'_J, the internuclear axis of the molecule is not as aligned with the polarization axis (see Figure 3.2).

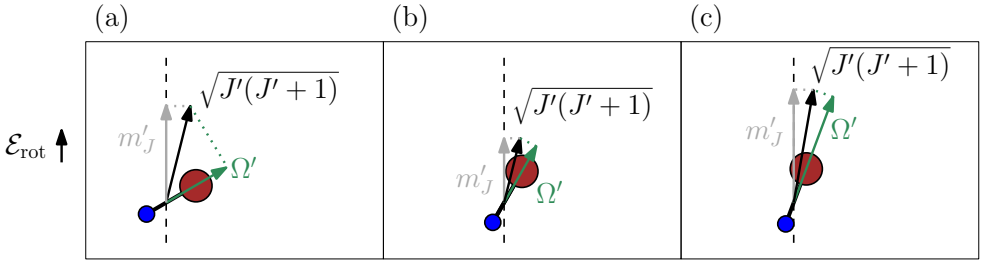

Figure 3.2: **Semiclassical picture of molecule alignment with polarizing field.** The dashed line indicates the direction of our polarizing axis defined by our applied electric field $\mathcal{E}_{\text{rot}}$. (a) The quantum numbers m'_J and Ω' are the projections of J' onto the quantization axis and internuclear axis, respectively. The internuclear axis precesses and nutates around the polarizing axis to preserve the quantum numbers. The configuration in (a) shows the situation where $|m'_J| \neq |\Omega'|$: the internuclear axis is not well aligned with the quantization axis. (b) Situation where $J' = |m'_J| = |\Omega'|$; the internuclear axis is better aligned with the polarizing axis, giving more directed photofragments towards the pole. (c) Having a large $J' = |m'_J| = |\Omega'|$ makes the J' vector precess even closer to the internuclear axis as compared to (b), giving even more directed photofragments towards the pole.

Furthermore, we only have access to $|\Omega_f| = 0, 1, 2$ if we start from the $|\Omega'| = 1$ intermediate state by the E1 selection rules. Throwing $\Omega_f = 0$ out of our list of choices for aforementioned reasons, we are limited to only four choices. Only the σ^+ plot in Figure 3.3b looks promising, but there is no promise that we will

end up with an $|\Omega_f| = 2$ predissociation state. Fortunately, the directedness of the photofragments do look much more polar if $|\Omega'| = 2$. We shall take a look at this next.

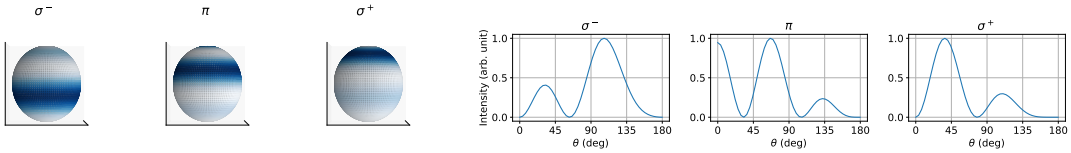

(a) From $J' = 2, m'_J = 1, \Omega' = 1$ to $\Omega_f = 1$. Transition strength: (0.102, 0.158, 0.188)

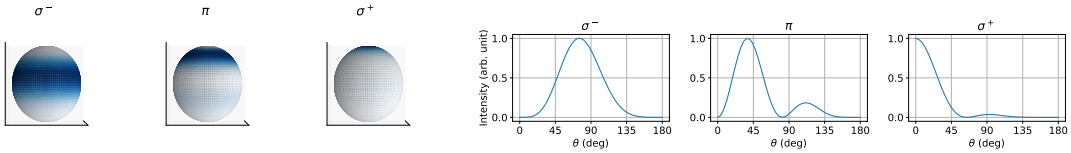

(b) From $J' = 2, m'_J = 1, \Omega' = 1$ to $\Omega_f = 2$. Transition strength: (0.102, 0.145, 0.249)

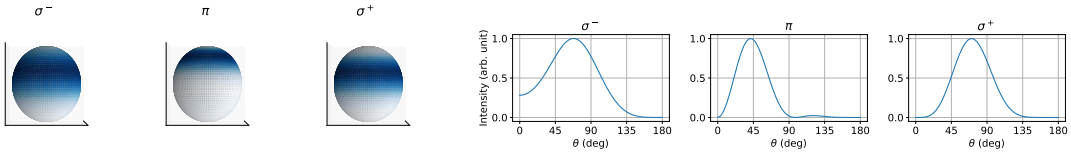

(c) From $J' = 2, m'_J = 2, \Omega' = 1$ to $\Omega_f = 1$. Transition strength: (0.200, 0.116, 0.381)

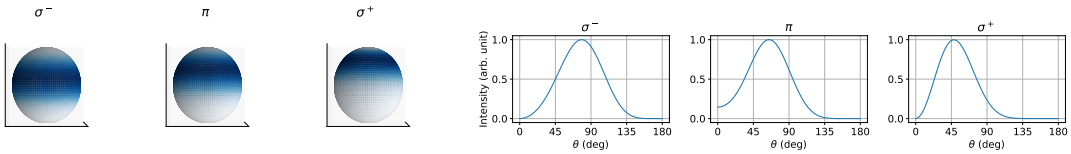

(d) From $J' = 2, m'_J = 2, \Omega' = 1$ to $\Omega_f = 2$. Transition strength: (0.0392, 0.201, 0.476)

Figure 3.3: **Simulated angular distribution of photofragments $I(\theta, \phi)$ for $\Omega' = 1$.** Left column: Newton sphere plots. The Newton sphere plots should be interpreted this way: (i) imagine the molecule to be at the center of the sphere, oriented with the Th side pointing upwards; (ii) upon dissociation, the Th^+ ion is ejected from the molecule, and it hits the inside surface of the sphere, painting it blue. To effect a two-state detection with the anisotropic angular distribution of photofragments, we demand the blue (photofragments) to be as concentrated at the poles as possible, so that the overlap of photofragments from molecules with the opposite orientation is minimized for maximum distinguishability. In each subfigure, there are three Newton spheres, corresponding to the result of using different polarizations of the dissociating photon (second REMPD photon in our case). Right column: number density along the polar angle (θ) direction. In other words, the total number of photofragments within a solid angle spanned by $\mathrm{d}\theta\,\mathrm{d}\phi\,\sin\theta$ at (θ, ϕ) is $I(\theta, \phi)\sin\theta\,\mathrm{d}\theta\,\mathrm{d}\phi$, and I have plotted out $\int I(\theta, \phi)\,\mathrm{d}\phi$. The dissociation efficiencies are shown in order of the cases $(\sigma^-, \pi, \sigma^+)$. The strengths shown are evaluated from $\frac{1}{4\pi}\int I(\theta, \phi)\,\mathrm{d}\Omega_{s.a.}$ with $\boldsymbol{\mu}$ in Equation 3.1 given only by the relevant Clebsch-Gordan coefficients, and $\Omega_{\mathrm{s.a.}}$ the solid angle, not to be confused with quantum number Ω. More discussion of the plots in main text.

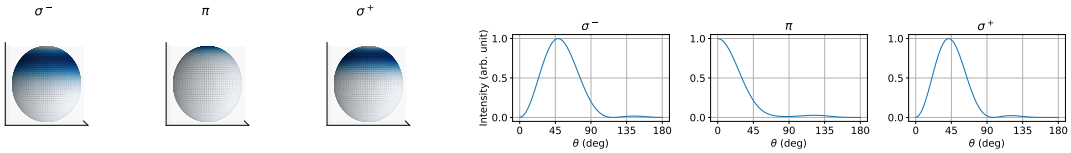

(a) From $J' = 2, m'_J = 1, \Omega' = 2$ to $\Omega_f = 1$. Transition strength: (0.175, 0.113, 0.0582)

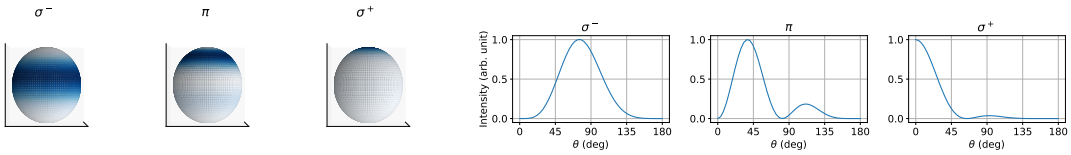

(b) From $J' = 2, m'_J = 1, \Omega' = 2$ to $\Omega_f = 2$. Transition strength: (0.176, 0.0862, 0.180)

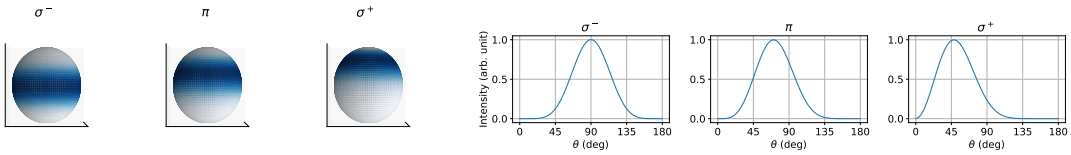

(c) From $J' = 2, m'_J = 1, \Omega' = 2$ to $\Omega_f = 3$. Transition strength: (0.0286, 0.203, 0.317)

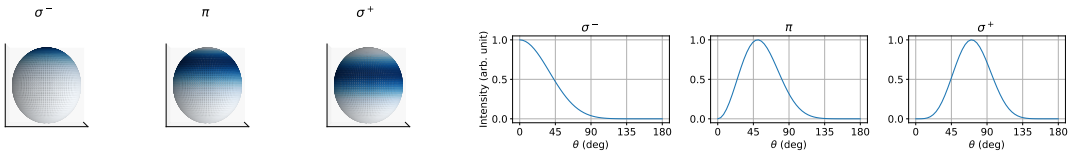

(d) From $J' = 2, m'_J = 2, \Omega' = 2$ to $\Omega_f = 1$. Transition strength: (0.397, 0.153, 0.0476)

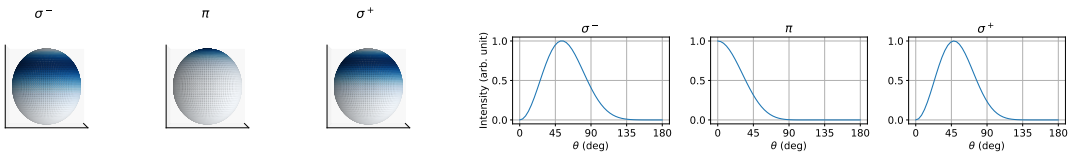

(e) From $J' = 2, m'_J = 2, \Omega' = 2$ to $\Omega_f = 2$. Transition strength: (0.0751, 0.322, 0.238)

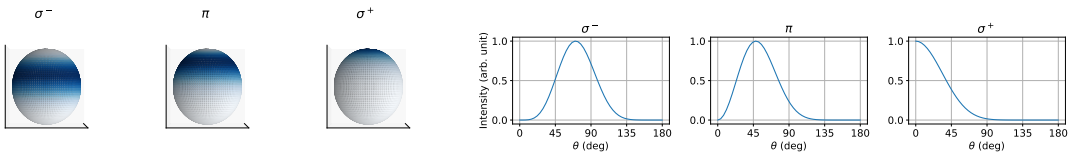

(f) From $J' = 2, m'_J = 2, \Omega' = 2$ to $\Omega_f = 3$. Transition strength: (0.00317, 0.0794, 0.713)

Figure 3.4: **Simulated angular distribution of photofragments $I(\theta, \phi)$ for $\Omega' = 2$.** Left column: Newton sphere plots. See caption of Figure 3.3 on the interpretation of the Newton sphere plots. Right column: number density along the polar angle (θ) direction. In other words, the total number of photofragments within a solid angle spanned by $\mathrm{d}\theta\,\mathrm{d}\phi\,\sin\theta$ at (θ, ϕ) is $I(\theta, \phi)\sin\theta\,\mathrm{d}\theta\,\mathrm{d}\phi$, and I have plotted out $\int I(\theta, \phi)\,\mathrm{d}\phi$. The transition strengths are shown in order of the cases $(\sigma^-, \pi, \sigma^+)$. The strengths shown are evaluated from $\frac{1}{4\pi}\int I(\theta, \phi)\,\mathrm{d}\Omega_{s.a.}$ with $\boldsymbol{\mu}$ in Equation 3.1 given only by the relevant Clebsch-Gordan coefficients, and $\Omega_{\mathrm{s.a.}}$ the solid angle, not to be confused with quantum number Ω. More discussion of the plots in main text.

We shall use the results in Figure 3.4 to make a few comments:

Choice of second REMPD photon polarization. Let me draw your attention to the last three rows of Figure 3.4. These correspond to angular distributions of photofragments with the same intermediate state (with a σ^+-polarized first REMPD photon), but different $|\Omega_f|$. The thing to note is that depending on what $|\Omega_f|$ is, one has to choose the appropriate polarization of the second REMPD photon to maximize the directedness of the angular distribution of photofragments, i.e. σ^--, π-, and σ^+-polarized second REMPD photon for $|\Omega_f| = 1$, 2, and 3, respectively.

How can we know what $|\Omega_f|$ is? We could just scan the whole photon polarization parameter space to find out, but let me suggest an approach that is more guided from an experimental standpoint. We still focus on the last three rows of Figure 3.4. We can compare the contrast of the angular distribution of the case where the second REMPD photon is σ^+ against that of σ^-. If they look very similar, chances are the predissociation state has a very strong $|\Omega_f| = 2$ character (see Figure 3.4e).

To verify the $|\Omega_f| = 2$ character, one would have the switch either the first photon (Figure 3.4b) or the second photon (Figure 3.4e) to π-polarization, and see an improvement in contrast.

If the contrasts look very different with the handedness of the circular polarization for the second photon, one can switch both REMPD photon polarizations to π, and see if we end up with Figures 3.4a or 3.4c.

What should we do for the different cases of $|\Omega_f|$? If $|\Omega_f| = 3$, we just need to use a σ^+-polarized first photon, and a σ^+-polarized second photon. This is as good as it gets for $|\Omega_f| = 3$.

If $|\Omega_f| = 2$, we have a choice. Comparing Figures 3.4b and 3.4f, one may think that the σ^+ plot in former gives a more polar angular distribution than the π plot in the latter, because the part above the equator is more concentrated at the pole in the former. However, the former has some structure on the other side of the equator from the pole, while the latter decreases monotonically from the pole. The differences are small, but the latter is cleaner in principle. Nevertheless, the best doublet angle-resolved scheme for an $|\Omega_f| = 2$ predissociation state will involve one σ^+ photon and one π

photon. This has to be a cross-beam setup, where the two photons will have to come in through different windows at the trap.

For the $|\Omega_f| = 1$ case, a similar comparison to the $|\Omega_f| = 2$ case holds for the π plot in Figure 3.4a and the σ^- plot in Figure 3.4d. We either do a π first photon and π second photon (for the former), or a σ^+ first photon and a σ^- second photon (for the latter). In either case, both photons can come in through the same window at the trap.

What should we make of the transition strengths reported in the figures? The net dissociation efficiency depends on a few factors: (i) the strength of the transitions, (ii) the intensities of the dissociation lasers, and (iii) the potential energy landscape past the dissociation threshold.

For a weak transition, e.g. the σ^- transition from Figure 3.4e, one can increase the overall dissociation efficiency by overwhelming the transition with a very intense laser. Jumping ahead to data shown in Figure 3.12, which we believe to be a case of Figure 3.4e, it is then interesting to see that the σ^- and σ^+ transitions result in similar dissociated Th^+ numbers. This suggests that the second dissociation photon is saturating the transitions for both transitions. This could result in the two transitions having the same overall dissociation efficiencies, despite having vastly different predicted transition strengths. The puzzle now, then, is why would the overall dissociation efficiency be so low (around 10%) for those transitions. Our guess right now is that the second photon could be connecting to a predissociation curve that has non-trivial crossings with other predissociation curves much like those shown in Figure 2.7. It could also be that the first photon is not saturating the bound-to-bound transition. However, we are seeing signs of power broadening of the first photon at the current laser intensity that we are using, so this is likely not the case.

These rules are by no means rigorous, and it depends on the structure of the predissociation potential landscape. The plots in Figures 3.3 and 3.4 are generated assuming that (i) we connect to only one predissociation state and that it comes with a definite Ω_f, (ii) there are no potential crossings with other predissociation potential curves, and (iii) we can sum contributions from all allowed J_f coherently with amplitudes given by the Clebsch-Gordan coefficients. We have no reason *a priori* to believe that all these

assumptions hold. We make these assumptions only to simplify the model for understanding. In fact, we see in the Gen. II eEDM experiment with HfF^+ that the REMPD protocol used resulted in two radial bands of photofragments, corresponding to the dissociated ions going through two different pathways ending up with different $KE_{dissoc.}$ (see William Cairncross's and Tanya Roussy's theses, and also the section below). Interpret the results of Figures 3.3 and 3.4 qualitatively and with a teaspoon of soy sauce; they only serve to guide the general direction of the experiment design, not to claim full understanding of the angular distributions seen in the experiments like those in Section 3.3.

3.2.2 Energy of ejected photofragments

Right before dissociation, the ThF^+ molecules have a spatial extent in our ion trap. The molecules also have a thermal velocity distribution. Upon dissociation, the Th^+ ions inherit the positions and velocities of their parent molecules. In addition to the kinetic energy ($KE_{therm.}$) that the Th^+ ions inherit from their ThF^+ parents, they can also gain additional kinetic energy ($KE_{dissoc.}$) from the dissociation (see Figure 3.5).

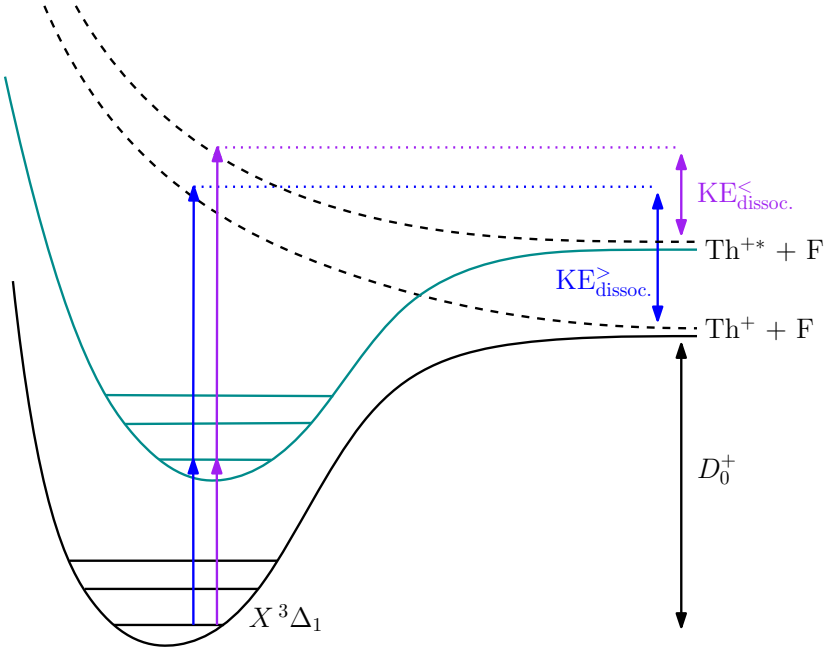

Figure 3.5: **Schematic diagram of molecular potential curves.** Not drawn to scale. The horizontal axis indicates the internuclear distance of our molecule, and the vertical axis indicates potential energy. The horizontal lines indicate various vibrational manifolds for each potential curve. D_0^+ indicates the minimum energy required to dissociate our molecule from the ground state. In our 1+1′ REMPD scheme, the first photon is a bound-to-bound transition bringing our molecules from $X\,^3\Delta_1$ (in black) to an intermediate state (in green), and the second photon brings our molecules into the predissociation state (indicated by the dashed lines). Upon dissociation, the photofragments can acquire an additional kinetic energy by moving down the potential curves of the predissociation molecular potentials. One would naïvely think that we can impart more kinetic energy to our photofragments through using REMPD photons of shorter wavelength so that we end up with more energy above the dissociation threshold. This is wishful thinking, because $KE_{dissoc.}$ depends on which predissociation potential the second photon connects to: the purple second photon is more energetic than the blue second photon in the figure, but connects to a predissociation potential curve that relaxes to an excited state of Th^+, imparting an overall lower kinetic energy to the photofragment.

In the limit of $KE_{dissoc.} \ll KE_{therm.}$ and in the velocity mapping regime (because we have a very long time of flight compared to the ratio of our ion cloud size and thermal velocities of our ions), the angular

distribution of ejected photofragments on our ion detector will be smeared out by the initial distribution of ThF^+ thermal velocities. This is unfavorable for two-state detection.

We want the other limit of $KE_{dissoc.} \gg KE_{therm.}$ for us to see the effect of angular distribution of the photofragments on our ion detector. Working with typical ion cloud temperatures of 10 to 200 K, corresponding to ion speeds of 20 to 80 m/s, we need to find a REMPD process that will give our Th^+ ions additional kinetic energy corresponding to more than 80 m/s in speeds. Figure 3.6 gives a visual comparison of the two limits.

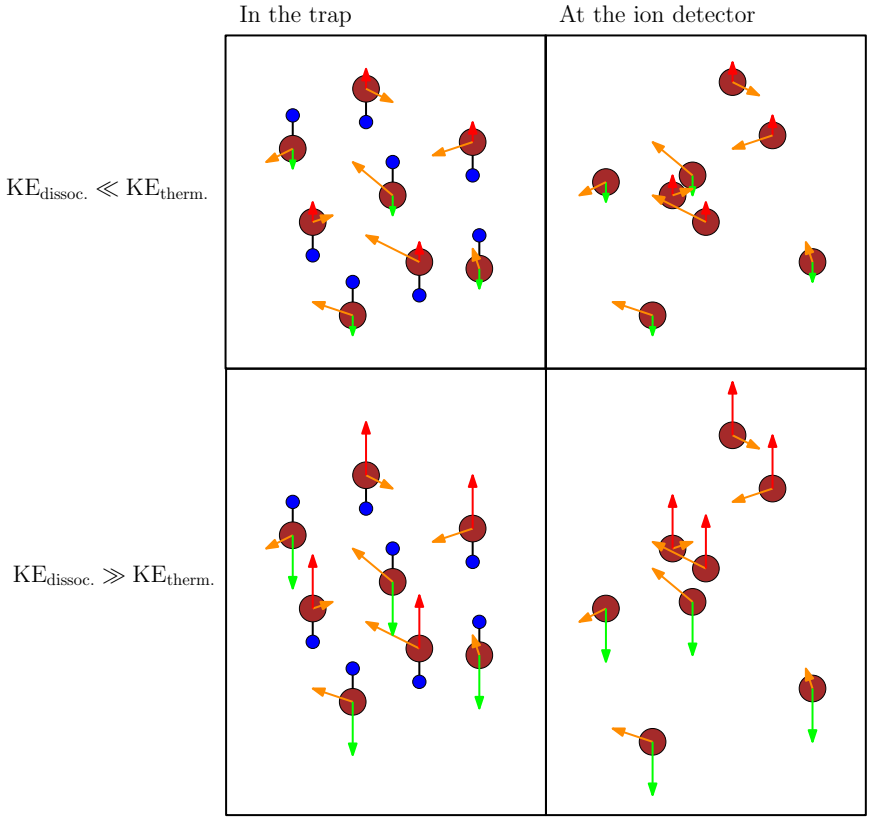

Figure 3.6: **Schematic diagram comparing the effects of $KE_{dissoc.}$ w.r.t. $KE_{therm.}$.** The left column corresponds to the molecule positions right after dissociation, while the right column corresponds to those at the ion detector after the ions are kicked out of the trap. The orange arrows indicate thermal velocity. The red and green arrows indicate additional kinetic energy gained from dissociation; they are color coded red and green to guide the eye to the dissociation ejection direction. The top row shows the case where $KE_{dissoc.} \ll KE_{therm.}$: one can see that the Th^+ moving upwards are not well separated in position from those going downwards; the ion positions are dominated by the thermal velocities. The bottom row shows the other limit of $KE_{dissoc.} \gg KE_{therm.}$: one can see that all the Th^+ ions moving upwards are on the top half of the detector, while those moving downwards are on the bottom half; the ion positions correlate very strongly to the dissociation ejection directions, allowing us to effect a two-state detection with each shot of the experiment.

Unfortunately, unlike choosing an intermediate state with the right quantum numbers, there is no knob for us to turn to control $\mathrm{KE}_{\mathrm{dissoc.}}$ directly. We can only scan the wavelength of our lasers to look for strong transitions with the right quantum numbers, and hope that they have enough $\mathrm{KE}_{\mathrm{dissoc.}}$. Fortunately, at least one such transition exists, as we shall see in the next section.

3.3 Angle-resolved photofragments in ThF^+

The setup used to look for good REMPD intermediate states is similar to that used in the LIF experiment, and a schematic diagram is shown in Figure 3.7.

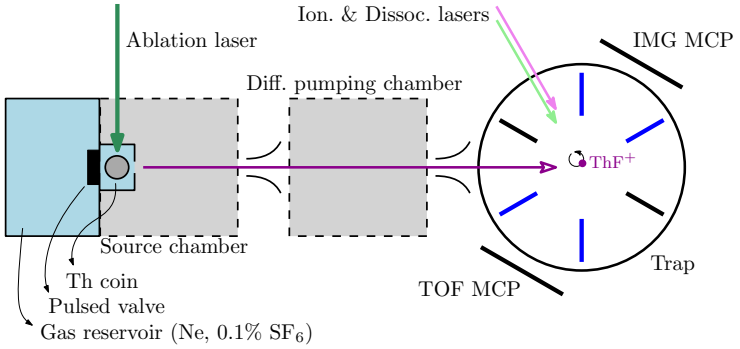

Figure 3.7: **Schematic diagram of the REMPD experimental setup.** The REMPD spectroscopy consists of the following steps:

(1) A molecular beam of ThF is created in a similar manner as the LIF experiment.

(2) The molecules are ionized into the ground vibronic state of ThF^+ with REMPI lasers at the center of ion trap, and the ions are loaded into the trap.

(3) We have an option of populating the $X\,^3\Delta_1(v=1)$ or the $a\,^1\Sigma^+(v=0)$ vibronic states by depleting the $X\,^3\Delta_1(v=0)$ states with a laser into an excited state found in previous work [43], and allowing the states to decay back down to one of the aforementioned states through selection rules. As such, we will see excited states of ThF^+ that couple to the aforementioned states, allowing for state readout of those states, which will prove to be very useful in later chapters.

(4) Another set of lasers consisting of (i) a tunable laser, and (ii) a second UV laser excites the ions in the trap. The sum of the energies of the two photons is greater than the dissociation energy of ThF^+. If the first photon is resonant with a transition between the ground vibronic state and an excited state, the ions will be excited to the intermediate state where it gets further excited to a pre-dissociation state by the second photon. The ion then dissociates into Th^+ and F. To ensure that the signal is real, we take four scans: (i) with no REMPD laser, (ii) with only the first photon, (iii) with only the second photon, and (iv) with both REMPD photons.

(5) The resulting mix of ThF^+ and Th^+ ions are kicked out towards one of the two MCPs, where we can read out ion numbers of both species through TOF-MS (Section 2.6.4.1).

(6) Repeat the experiment with different excitation wavelengths.

The ion trap used in the setup is the 6-fin Paul trap from the setup used in the Gen. I experiment [14]. At some point, we switched the 6-fin Paul trap to the baby Bucket Brigade (which is also a Paul trap, see Section 7.4), but the general workings of both traps are the same. The workings of the 6-fin Paul trap and trap electronics are detailed in theses of previous group members (e.g. Huanqian Loh and Matt Grau) and

shall be omitted here for brevity. A simple description of how a Paul trap works is summarized in Appendix A.

We began on the spectroscopy to search for the intermediate state for REMPD before we knew about angle-resolved photofragments, so we did not pay attention to the polarization of the REMPD lasers during the early days of the spectroscopy. Still feeling hurt from the disappointment in the results of our LIF spectroscopy, we decided to start the REMPD spectroscopy using a convenient dye with the widest tuning range: DCM in ethanol. This dye allows us access to 602 nm to 660 nm with a peak wavelength at 627 nm. We doubled the output from our dye laser with a BBO and found a few transitions. The transition with the strongest strength is the [32.09]+266 nm combination.

3.3.1 The [32.09]+266 nm transition

After we learnt about angle-resolved photofragments from Prof. Tanya Zelevinsky, and saw that it can be used for two-state detection in HfF^+, we decided to implement it in ThF^+. We chased our tails for some time in the optimization of our REMPD process,[4] but to cut the chase short, Figures 3.8 and 3.9 show the experimental proof of principle results of angle-resolved photofragments with ThF^+.

Figure 3.10 shows a typical two-state detection characterization plot on the Gen. II JILA eEDM experiment setup using HfF^+. Comparing Figures 3.9 and 3.10 shows that the quality of our two-state detection scheme for ThF^+ is on par with that for HfF^+.

In Figures 3.8 and 3.9, we present the positions of the ions on the ion detector for two combinations of the experimental parameters: keeping the polarizations of the REMPD photons fixed, we prepared our ions in the $m_F = 3/2$ or $-3/2$ Zeeman states. The "relative sign" of the Zeeman state chosen during state preparation and the helicities of the REMPD photons matter for the separation of the doublets on the ion detector as we shall see in the next section.

[4] For example, we first started to look for angle-resolved photofragments along the time-of-flight axis instead of the transverse imaging plane [38] because we were limited by the relative orientations of our laser beams and ion detectors.

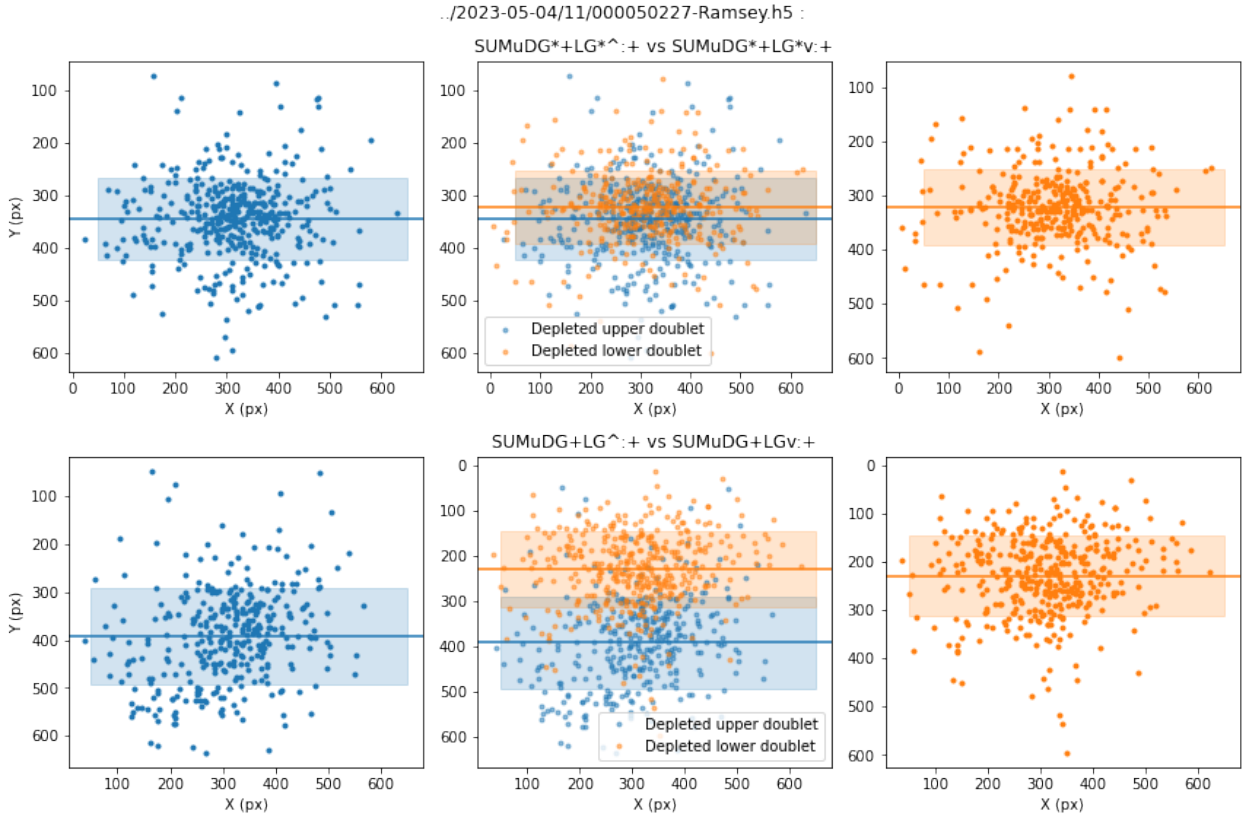

Figure 3.8: **Scatter plot of the Th^+ ion positions at the ion detector (same data as that used in Figure 3.9).** Each plot shows the ions from a sum of five shots of the experiments. The two rows correspond to two slightly different experiment conditions: the polarizations of the REMPD photons were kept the same across the two rows, but we prepare the molecules in the $(J = 1, m_J = -1)$ state for the top row, and $(J = 1, m_J = 1)$ for the bottom row. The first REMPD photon increases the m_J quantum number by 1, and brings the molecules in the top (bottom) row to $m'_J = 0$ ($m'_J = 1$). The horizontal lines in each plot corresponds to the mean position of the ions (of the corresponding color), while the shaded area corresponds to the 1σ spread of the ion locations in the Y direction. The middle column is an overlay of the left and right columns. There is clear evidence of angle-resolved photofragments in the bottom row, where the ions in the upper doublet end up on the upper side of the detector, while those in the lower doublet end up on the lower side.

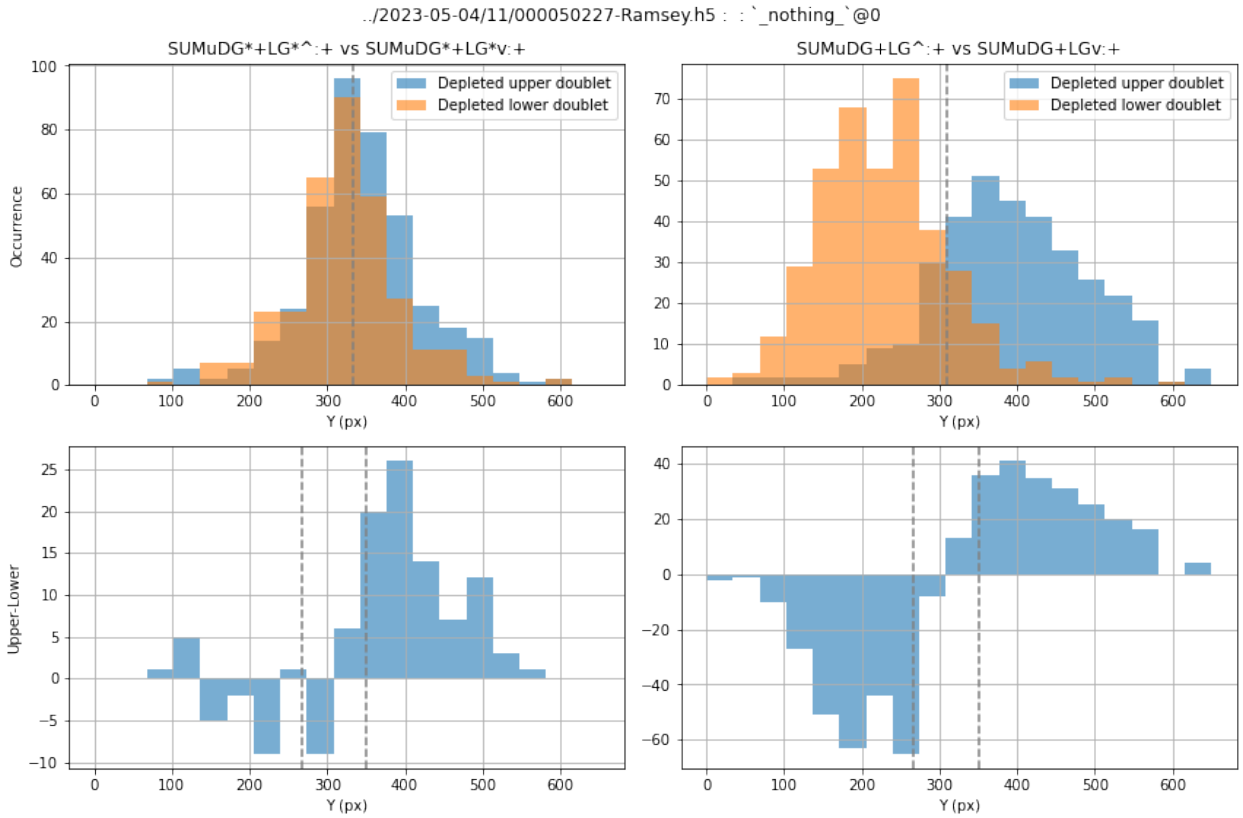

Figure 3.9: **Histograms of the Th^+ ion positions, integrated over the X direction, at the ion detector (same data as that used in Figure 3.8).** The two columns correspond to two slightly different experiment conditions: the polarizations of the REMPD photons were kept the same across the two columns, but we prepare the molecules in the $(J = 1, m_J = -1)$ state for the left column, and $(J = 1, m_J = 1)$ for the right column. The first REMPD photon increases the m_J quantum number by 1, and brings the molecules in the left (right) column to $m'_J = 0$ ($m'_J = 1$). The top row shows the overlay of the ion distribution in the Y direction from both doublets. The grey dashed line indicates the mean of the mean positions of ions in both doublets. The bottom row takes the difference between the two doublets. The grey dashed lines indicate the region of the "swatch" — the region where we do not count ions to either doublet for our two-state detection protocol, and we associate ions to the left (right) of the swatch with the upper (lower) doublet.

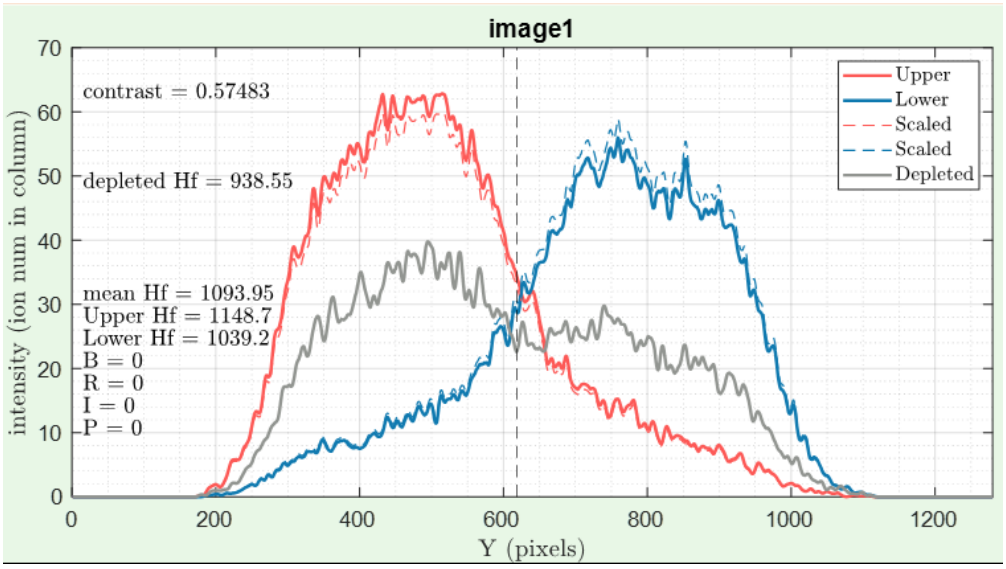

Figure 3.10: **Histograms of the Hf^+ ion positions, integrated over the X direction, at the ion detector.** Courtesy of the group members who worked Gen. II experiment. Comparing this with the top-right plot in Figure 3.9 indicates that the quality of our two-state detection for ThF^+ is on par with that for HfF^+.

3.3.2 Photon polarization combination

Depending on the "relative sign" of the Zeeman state chosen during state preparation and the helicities of the REMPD photons, the molecules could take a different pathway to dissociation. Figure 3.11 shows the various pathways the molecules can take.

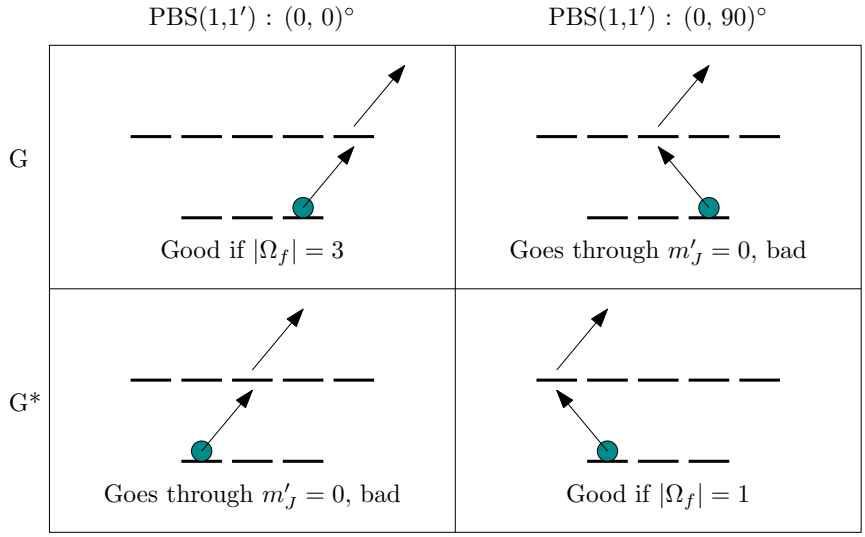

Figure 3.11: **Pathway taken by molecules to during dissociation with various combinations of photon polarizations.** The three lower (five upper) horizontal lines correspond to the m_J sublevels in the $J = 1$ from the eEDM-sensitive state ($J' = 2$ in the intermediate state). The arrows indicate the REMPD photons. The REMPD photons nominally go through a PBS each, exiting horizontally polarized, and they go through the same QWP (after being combined through a dichroic mirror) to have the same circularity handedness. This configuration is represented by the "PBS(1,1′):(0,0)°" notation, and it corresponds to the first column. We change the handedness of the first photon by rotating the PBS of the first photon by 90° to make it go through the QWP vertically polarized; this configuration corresponds to the second column. The first row, denoted by "G" is where we prepare the ions in the $m_F = 3/2$ Zeeman state, while "G*" corresponds to preparing the ions in the $m_F = -3/2$ Zeeman state. Molecules that take pathways that go through $m'_J = 0$ lose their directedness, so they should be avoided. Only the top left and bottom right pathways can be good, but the quality of each depends on the $|\Omega_f|$ that we connect to with the second photon in REMPD.

We went through the combinations and obtained results shown in Figure 3.12 for the [32.09] intermediate state, and Figure 3.13 for the [32.50] intermediate state. Common to both intermediate states, we see that the combinations on the off-diagonal axis show poor doublet separation, agreeing with the model we have in Figure 3.11. Using combinations along the diagonal axis, we also saw that the [32.50] intermediate state exhibits inferior doublet separation than the [32.09] one. This could be because the [32.50]+266 nm combination imparts the dissociated Th^+ ions with less energy than the [32.09]+266 nm combination.

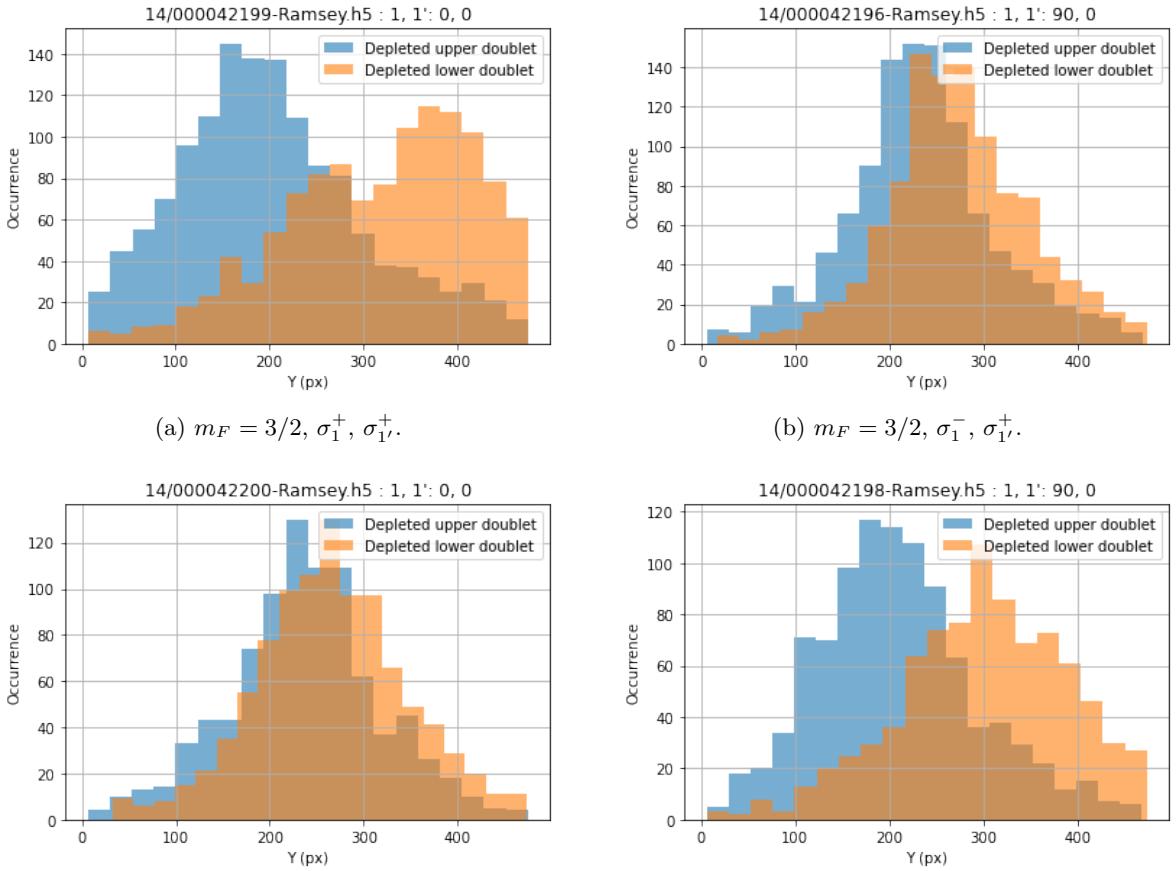

(a) $m_F = 3/2$, σ_1^+, $\sigma_{1'}^+$.

(b) $m_F = 3/2$, σ_1^-, $\sigma_{1'}^+$.

(c) $m_F = -3/2$, σ_1^+, $\sigma_{1'}^+$.

(d) $m_F = -3/2$, σ_1^-, $\sigma_{1'}^+$.

Figure 3.12: **Distribution of ions along the Y axis on the ion detector with various combinations of photon polarizations for the [32.09] intermediate state.** Top (bottom) row: we prepare the ions in the $m_F = 3/2$ ($m_F = -3/2$) state. Left (right) column: the first REMPD photon has the same (opposite) circular polarization as the second photon. Note that the combination used in the top left plot gives the best separation of doublets. Having similar quality of doublet separation in (a) and (d) suggests that the second photon connects to a predissociation state that has a predominant $|\Omega_f| = 2$ nature (compare with Figure 3.4e). Assuming that the predissociation state is predominantly $|\Omega_f| = 2$, the fact that we get similar dissociated Th^+ numbers in (a) and (d) suggests that our second REMPD photon is saturating (c.f. Figure 3.4e). See the discussion on dissociation efficiencies on Page 35.

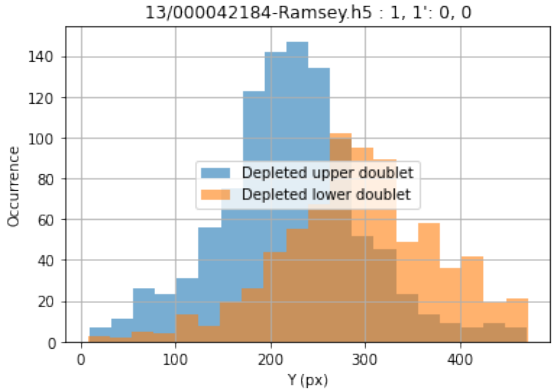

(a) $m_F = 3/2$, σ_1^+, $\sigma_{1'}^+$.

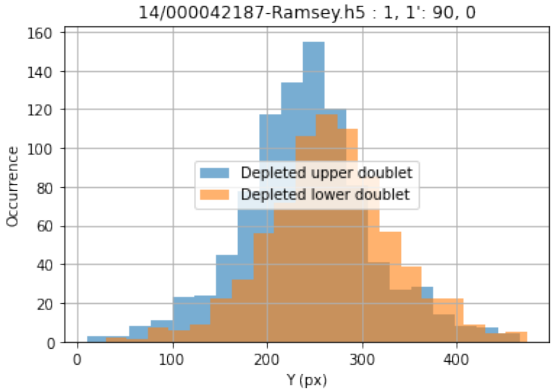

(b) $m_F = 3/2$, σ_1^-, $\sigma_{1'}^+$.

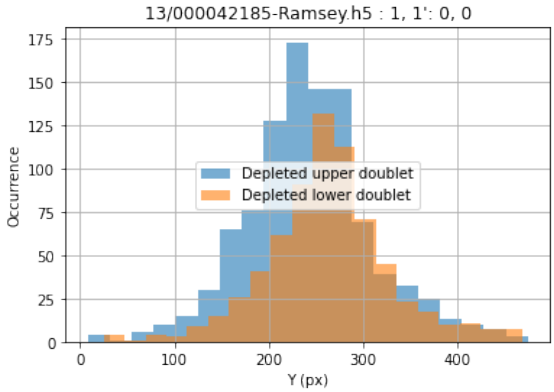

(c) $m_F = -3/2$, σ_1^+, $\sigma_{1'}^+$.

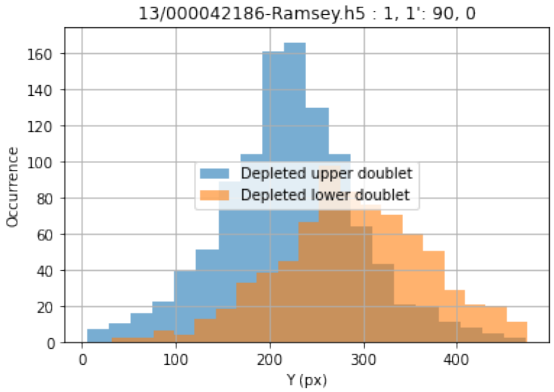

(d) $m_F = -3/2$, σ_1^-, $\sigma_{1'}^+$.

Figure 3.13: **Distribution of ions along the Y axis on the ion detector with various combinations of photon polarizations for the [32.50] intermediate state.** Top (bottom) row: we prepare the ions in the $m_F = 3/2$ ($m_F = -3/2$) state. Left (right) column: the first REMPD photon has the same (opposite) circular polarization as the second photon. Even though there is some separation of doublets in some of the plots shown here, they are not as good as those using [32.09] as the intermediate state (see Figure 3.12a), indicating that perhaps the [32.50]+266 nm combination imparts a lower dissociation kinetic energy to the Th^+ ions than the [32.09]+266 nm combination.

3.4 Further discussion

In the previous sections, we have seen that we can perform two-state detection with each destructive shot of our action spectroscopy on ThF^+. Before we close this chapter, we shall address a few points: (i) other important REMPD intermediate states, and (ii) possible future directions to make the two-state detection scheme better.

3.4.1 Other important transitions

Table 3.1 shows a list of transitions that we found in our REMPD spectroscopy with doubled frequency using the DCM dye. We performed the scan once with 266 nm as the second photon, and once with 355 nm as the second photon. Given the same first photon, we noticed that the choice of the wavelength of the second photon can affect the degree of doublet separation. This is probably because the combination of the first and second photon energies address a different dissociation potential depending on which second photon is used, resulting in different dissociation kinetic energies (see Section 3.2.2). Switching between 266 nm and 355 nm is not an easy task — we have to change the optics within the Nd:YAG laser, and all the downstream optics between the laser and the trap — this is not an easy knob to turn.

As of this writing, we typically perform dissocation from the following lines:

32097. Our main dissociation line for the $X\,^3\Delta_1(v=0)$ manifold. We characterized angle-resolved photofragments on this line. With 266 nm as our second photon, this puts us about 16500 cm^{-1} above the dissociation threshold.

31973. Our main dissociation line for the $X\,^3\Delta_1(v=1)$ manifold for diagnostics.

31201. Our main dissociation line for the $X\,^3\Delta_1(v=2)$ manifold for diagnostics.

$X\,^3\Delta_1(v=0)$	$X\,^3\Delta_1(v=1)$	$a\,^1\Sigma^+(v=0)$	Ω
30799	-	-	2 (?)
30857	-	-	1 (?)
30934	-	-	0 (?)
31030 (*)	-	-	1
31073	-	30759	-
31144	-	30830	0 (?)
31210	-	30896	0 (?)
31230	-	30916	1
31242	-	-	2 (?)
31312	-	30998	1 (?)
31355	-	-	-
31392	-	-	2 (?)
31450	30796	-	0
31461	30808	-	0 (?)
31572	30919	-	1 (?)
31619	30966	31305	1 (?)
31662	31009	-	0 (?)
31723	31070	31409	-
31751	31097	31436	1 (?)
31780	31126	-	-
31825	31171	31511	-
31922	31269	-	2 (?)
31957	31304	31643	1 (?)
31984	31331	31670	1 (?)
32097 (*)	-	-	2
32171	31518	31857	-
32179	31526	-	-
32269	31616	-	-
32449	31796	32135	-
32504 (*)	31851	-	2
-	31973 (*)	-	2

Table 3.1: **Relevant parameters of fitted transitions in the REMPD spectroscopy of ThF^+.** The first three columns indicate the transition frequencies in cm^{-1} connecting the same upper state to the corresponding lower state stated for each column; dashed entries indicate transitions not found. The column for Ω indicate the fitted values of the quantum number Ω for the transitions; entries marked with (?) indicate a crude fit due to the low signal to noise ratio of the scans, while those without the mark have very good fits; dashed entries indicate that Ω was not fit for that transition. The transitions marked with (*) are ones that we frequently use. The scanning range of the DCM dye was not enough for us to classify bands into vibrational progressions like that in Section 2.5. We associate certain bands together in this table through (i) similar B' for the upper state, and (ii) reasonable energy difference between the transitions, corresponding to the vibrational spacing of the $X\,^3\Delta_1$ electronic state.

3.4.2 Possible future directions

We note that 266 nm is more energetic than our first photon at around 311 nm. This means that 266 nm can induce a one-color two-photon dissociation by itself. For a resonant two-photon process, one would rather have a more energetic first photon than the second photon, and in the ideal situation the first photon should exceed half of the dissociation energy. This allows the first photon to be much weaker than the second photon, so that the first photon would not induce its own one-color two-photon process, while the stronger but less energetic second photon will not be able to induce a one-color two-photon dissociation by energy considerations. A possible future direction will be to use a first photon that exceeds half of our dissociation threshold ($D_0^+ = 53230$ cm^{-1} from Ref. [44]). This would require survey spectroscopy on the Pyrromethene 597 or Coumarin 153 dyes; these dyes are chosen such that we can use the convenient 532 nm laser as the second photon.

Things to look out for in the survey spectroscopy include:

Kinetic energy of photofragments upon dissociation. We want this to be as high as possible to overwhelm the original ion cloud temperature for good angle-resolved photofragments. We just need to make sure that the photofragments do not have so much energy that they miss the ion detector, but this can be easily solved by transverse focusing using some ion optics.

$|\Omega'|$ of the intermediate state. We want $|\Omega'| = 2$ (see Section 3.2). The absence of a P(2) line in the band would indicate such a state.

B' of the intermediate state. The rotational constant of the intermediate state determines the spacing between the R lines. We want this spacing to be large compared to our laser linewidth so that we dissociate only one J manifold. We want a large B'.

$|\Omega_f|$ of the predissociation state. This would determine what photon polarizations we want to use for each of the two photons in the REMPD scheme (see Figure 3.4).

Unwanted one-color multi-photon dissociation in a $1 + 1'$ scheme. We want the first photon to address only the bound-to-bound transition, and the second photon to saturate the bound-to-continuum

transition. We do not want the first photon to excite a bound-to-continuum transition; we also do not want the second photon to address off-resonant bound-to-bound transitions. We can always achieve this by reducing the energies of the laser pulses, but we also want to have as high a dissociation efficiency as possible, which requires laser pulses with high energies. Hence we want to find an intermediate state such that there are no accidental resonances that could enhance one-color multi-photon transitions.

One-color two-photon dissociation with good angle-resolved photofragments. If it turns out that the first photon can also act as a second photon, hitting a pre-dissociation state that gives us very high $KE_{dissoc.}$, there would be no reason not to use this 1+1 REMPD transition.

Dissociation efficiency. We have conveniently left out dissociation efficiency in all our previous discussions, but dissociation efficiency is also a very important factor. Only the dissociated Th^+ ions contribute to our statistics, and the rest of the ions only contribute to decoherence in our ion trap. The [32.09]+266 nm scheme currently gives us 10% dissociation efficiency. We determined the efficiency in two ways, both giving consistent results:

(1) All our ions are in the ground vibronic state, spread across a few rotational states. With our usual experiment parameters (i.e. laser powers and ion numbers), we scanned the R branch for the intermediate state [32.09] to count the number of dissociated Th^+ ions. We then compare the total number (accounting for the Hönl-London factors for the R lines) to the total ThF^+ number. The latter is inferred through a calibrated area under the curve on the capacitively coupled output from our microchannel plate assembly.

(2) Alternatively, we could compare the areas under the curve for both Th^+ and ThF^+ from the capacitively coupled output from our microchannel plate assembly. We would need to increase our total ThF^+ ion numbers for the Th^+ ions to have an appreciable signal on the capacitively coupled output.

In the Gen. II experiment, the dissociation efficiency is at least 20%. The lower bound comes from not having full control/knowledge of the Hilbert space spanned by all the HfF^+ ions in the trap. It

would be great if we can find a new intermediate state (with the relevant second photon) that can give us higher dissociation efficiency.

The above can be very tedious work with no promised returns, and the quality of our angle-resolved photofragments is already good enough for most practical purposes. Let me suggest possible optimization routes and consequences, arranged in increasing order of tediousness.

Current configuration. We are currently using the [32.09]+266 nm scheme, both circularly polarized with the same handedness. These photons go through the same windows on our vacuum chamber, and lies perpendicular to the axis of the molecular beam source. The vacuum chamber has eight flanges arranged in an octagon. The molecular beam comes in through one of the flanges horizontally. The REMPD beams go up windows vertically. The rest of the windows are used for other lasers and microwaves. See part (a) of Figure 3.14.

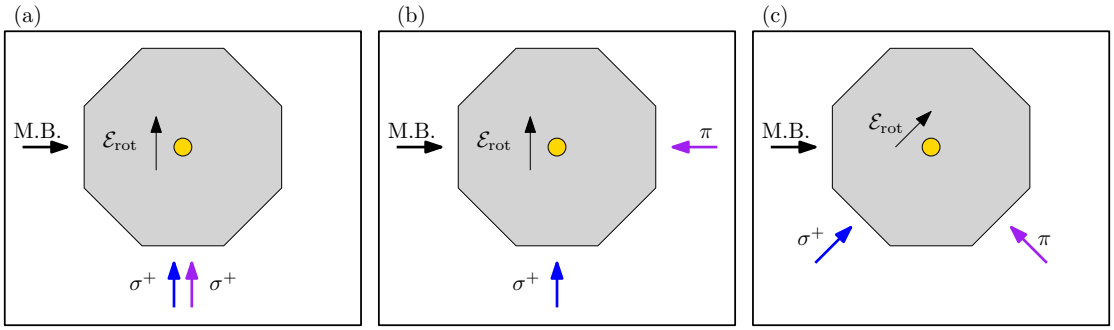

Figure 3.14: **Various configurations of REMPD beams.** M.B. stands for molecular beam. The grey octagon represents our vacuum chamber with eight flanges (2.75″ CF). The into-page and out-of-page directions are 10″ CF flanges that are not meant for optics, see Figure 7.9. (a) Current configuration. (b) Naïve implementation of Route 1. This does not work because the π photon will be hitting the skimmers and molecular beam source. (c) One will have to move the beams around like this to implement Route 1.

Route 1: switching to π-polarized photon when $|\Omega_f| = 2$. We saw in Section 3.2 that we can increase the directedness of the angular distribution of photofragments if $|\Omega_f| = 2$ by switching either of the REMPD photons to π-polarization. This can be done in a cross-beam setup, where the REMPD photons go into the trap perpendicularly. The polarization axis will be aligned with the k-vector of the circularly polarized photon. We will have to move the beams around from the current configuration to avoid hitting the molecular beam source with our lasers (see parts (b) and (c) in Figure

3.14). Using four windows instead of two for the high pulse energy lasers also means fewer windows for the cw lasers for state preparation and detection. This may be a little tricky given the number of cw lasers we need.

Furthermore, it turns out that in our current trap setup (see Figure 7.9 and Section 7.4), the positions of our ions at our ion detector is velocity (position) dominated in the vertical (horizontal) direction. This means that we may lose some contrast if the molecules are dissociated at 45° w.r.t. the vertical (part (c) of Figure 3.14). We will need to understand the ion lensing effects during the flight between the trap and the detector, and turn both vertical and horizontal directions to be velocity map imaging.

Route 2: changing the second photon in the [32.09]+266 nm scheme. We can change the second photon to 355 nm, or any arbitrary wavelength with a tunable dye laser. Doing so can change the $|\Omega_f|$ of the predissociation state, and also the dissociation kinetic energy imparted to Th^+. We can keep the current laser beam configuration if we find address an $|\Omega_f| = 1, 3$ predissociation state. We would have to ensure that the dissociation efficiency and kinetic energy are still high enough. This would involve (i) changing the downstream optics from those of 266 nm to 355 nm, or (ii) introducing an additional dye laser and doubling optics.

Route 3: changing both photons to get a [?]+532 nm scheme. In this scheme, the second photon is below half of the dissociation energy. This means that it will be much harder for the second photon to induce one-color multi-photon dissociation. One will need to switch the dye used to generate the first photon, and perform survey spectroscopy. The group will have to look out for intermediate states with all the properties mentioned at the start of this section.

Route 4: changing both photons to get a [?]+(≈532 nm) scheme. If the above is too easy, or if the [?]+532 nm scheme results in (i) lower dissociation efficiency, (ii) lower dissociation kinetic energy, or (iii) an undesirable $|\Omega_f|$, then one might want to tune the 532 nm photon. Route 4 is a combination of Routes 2 and 3.

I shall leave the decision of whether to perform this survey spectroscopy in the good hands of the

group members that stay on after me. In the meantime, we have answered the question of how to detect the internal states of our ions, so we shall now move on to discuss how we can perform quantum control of the states inside ThF^+.

Chapter 4

Quantum control of ThF^+

Now that we know how to create ThF^+ ions (Chapter 2), and how we can perform state readout (Chapter 3), we are now ready to look at how we can perform quantum control of ThF^+. We intend to use lasers and microwaves to do this, so we need to know the frequencies of these transitions required for state preparation and detection. Fortunately, some of the laser part of the spectroscopy has already been done before I joined the group (see Daniel Gresh's thesis and Ref. [43]), but the microwaves part still needs to be done, and we also need to decide on which of the transitions that Gresh *et al.* found is suitable for our needs. Furthermore, we have been emphasizing how ThF^+ can give us better statistical sensitivity than HfF^+, but we also need to understand systematic effects in using ThF^+ to measure the eEDM. This requires knowing how the $X\,^3\Delta_1$ electronic state responds to external electric and magnetic fields. We thus need to determine certain spectroscopic constants in the effective Hamiltonian governing our system. Much of this chapter is directly lifted from our publication [54].

The layout of this chapter is as follows. We first show results of our spectroscopy on the eEDM-sensitive states of ThF^+ in Section 4.1. We then go on to discuss in Section 4.2 a possible mechanism limiting coherence time in ThF^+ despite having a ground state for the eEDM-sensitive state, and how we intend to overcome it. Finally, we discuss an experiment sequence that we can use to obtain Ramsey fringes in the eEDM-sensitive state in ThF^+ in Section 4.3.

4.1 Spectroscopic constants of ThF^+

The following sections detail the spectroscopy process to extract the spectroscopic constants crucial to the eEDM experiment. We begin with an overview of the state preparation process in Section 4.1.1, then we touch on the details of the measurement of the hyperfine coupling constant (Section 4.1.2), molecular frame electric dipole moment (Section 4.1.2), and the magnetic g-factor (Section 4.1.3). Finally we present a summary of the results in Section 4.1.4.

4.1.1 State preparation and readout for eEDM-sensitive state spectroscopy

The energy level of a diatomic molecule like ThF^+ has nested progressively finer structure (see Figure 1.2). The eEDM-sensitive states are labeled by the quantum numbers $X\,^3\Delta_1(v=0, J=1, F=3/2, m_F=\pm 3/2)$, which correspond to the electronic, vibrational, rotational, hyperfine, and Zeeman manifolds, respectively, with increasing fineness in their structures. We first prepare ThF^+ in the $X\,^3\Delta_1(v=0)$ vibrational manifold through REMPI of neutral ThF [46] (Chapter 2), and usher them into the finer energy structures with optical pumping via an excited electronic state $\Omega = 0^-$ [14.59] (Figure 4.1). The $\Omega = 0^-$ electronic state lies approximately 14600 cm^{-1} above $X\,^3\Delta_1$ [43]. The full process to prepare our ions in the $X\,^3\Delta_1(v=0, J=1, F=3/2, m_F=-3/2, \Omega=1)$ is illustrated in Figure 4.1, where Ω is the quantum number for the Ω-doublets.

State preparation involves two pulsed lasers at 304 nm and 532 nm for REMPI, multiple cw lasers at 685 nm for optical pumping [Figures 4.1(a-c)], a cw repump laser at 717 nm [Figure 4.1(a)], and microwave channels at 29.1 GHz and 43.6 GHz [Figure 4.1(b,d)].

We perform our state readout by dissociating our molecular ions state-selectively with methods used in our previous work [38, 46, 55] and detailed in Chapter 3.

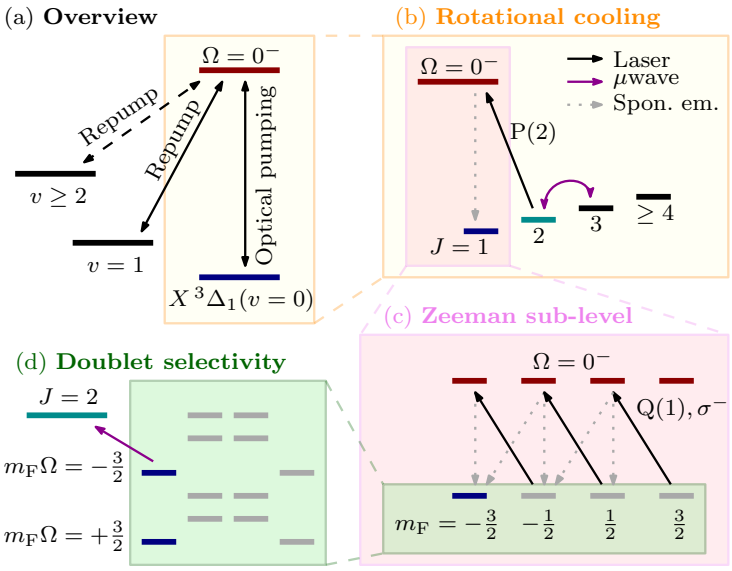

Figure 4.1: **State preparation sequence (not to scale).** The state preparation process is shown as a sequence of steps for clarity, but all the steps involved occur at the same time in our experiment.

(a) All our optical pumping lasers connect from the $X\,^3\Delta_1(v = 0)$ vibronic manifold to the $\Omega = 0^-(v = 0)$ vibrational manifold [43]. We have vibrational repump lasers from the higher vibrational manifolds. For some of the spectroscopy shown in the following sections, we only have the vibrational repump laser from the $(v = 1)$ manifold. We added more vibrational repump lasers as time progressed.

(b) Within the $X\,^3\Delta_1(v = 0)$ vibronic manifold, we perform rotational cooling by optically pumping the $J = 2$ state through the $\Omega = 0^-$ state. We use microwaves to couple the $J = 2$ and $J = 3$ states together to transfer $J = 3$ population eventually into $J = 1$.

(c) Within the $J = 1$ manifold, we pump all the ions into a single Zeeman m_F state using circularly polarized light on the Q(1) line. We also introduce a magnetic field to prevent the Zeeman levels from mixing through rotation coupling (refer to Section 4.1.3). We show only one lower state for each m_F value (in the grey box), but there are in fact two or four levels at each m_F value; compare with (d).

(d) Ω-doubling gives rise to two closely spaced states with the same m_F number. We can deplete one of these states by coupling it with microwaves to $J = 2$.

4.1.2 Microwave spectroscopy on the $J = 1$ to $J = 2$ transition; Hyperfine coupling constant and molecular electric dipole moment

A schematic diagram of the energy levels of the $J = 1$ and $J = 2$ rotational states in $X\,^3\Delta_1(v = 0)$ is shown in Figure 4.2. We use state preparation steps shown up to panel (b) in Figure 4.1 to prepare our ions into $X\,^3\Delta_1(v = 0, J = 1)$. We then perform microwave spectroscopy on the detailed structure of the $J = 1$ to $J = 2$ rotational transition. Our observable is the appearance of population in the $J = 2$ state, detected by state-selective photodissociation. No external magnetic fields are applied for the microwave spectroscopy experiments in this section.

At near-zero external electric field, selection rules and energy degeneracies result in just six distinct resonant frequencies (refer to Figures 4.2 and 4.3), from which we perform a fit to the spectroscopic constants $A_{||}$ (hyperfine coupling constant) and ω_{ef} (Ω-doubling splitting constant). We are able to extract $4B = 29.09733(4)$ GHz (see Equation 2.2a), which is roughly the $J = 1$ to $J = 2$ separation. This number is consistent with 29.093(9) GHz obtained in our previous work [43]. Figure 4.2 illustrates how the spectroscopic constants fit into the energy level structure.

By repeating the above experiment with a non-zero external electric field strength, we can see the Stark shifts in the spectral lines (illustrated in Figure 4.2), shifts which depend on m_F and d_{mf} (molecular frame electric dipole moment). To enhance signal-to-noise ratio for the extraction of d_{mf}, we prepare all the ions into $X\,^3\Delta_1(v = 0, J = 1, F = 3/2, m_F = -3/2)$ with state preparation sequence up to panel (c) in Figure 4.1. This allows us to suppress all lines coming from the $m_F = \pm 1/2$ states to obtain a much cleaner spectrum to extract d_{mf}. We search for the lines corresponding to the (L) and (U) transitions shown in Figure 4.2. The spectroscopy of these two lines are shown in Figure 4.4. These two lines were used for the measurement of d_{mf} because of their strong intensities. The (L) and (U) lines will be used to perform doublet depletion [preparation step (d) of Figure 4.1] in subsequent sections.

Before we end off this section we shall look at some diagrams to give us a better understanding of the energy level structure of ThF^+. Figure 4.5 shows transitions that are allowed between $J = 1$ and 2 in $v = 0$, intensity-coded for the relative strengths. Figures 4.6 and 4.7 show the corresponding eigenstates and

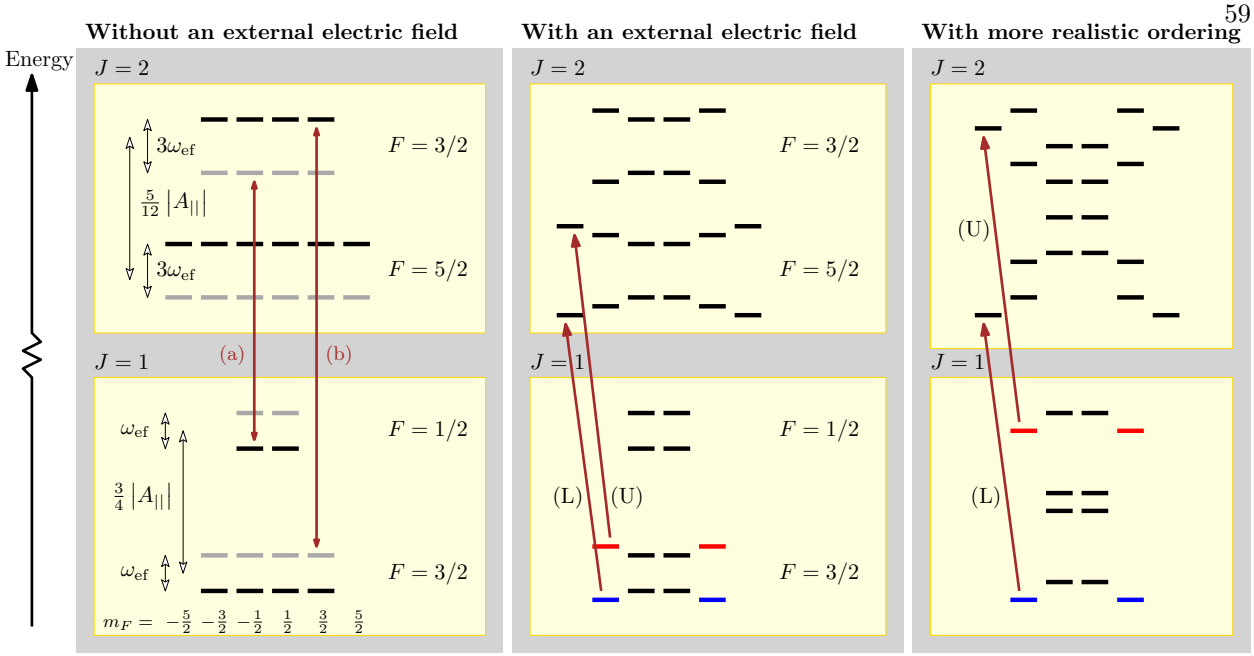

Figure 4.2: **Energy landscape (not to scale) of the neighborhood of the eEDM-sensitive state $X\,^3\Delta_1(v = 0)$, showing only the first two rotational levels.** See Figure 1.2 for the bigger picture involving the other states.

In the absence of external electric field, the eigenstates are states of good parity. The energy levels with e (f) parity are denoted by black (grey) lines in the energy level diagram on the left.

Selection rules for E1 transitions only allow for transitions connecting states of opposite parities, $\Delta F = 0, \pm 1$, and $\Delta m_F = 0, \pm 1$, thus resulting in only six distinct frequencies for resonant transitions connecting the $J = 1$ to $J = 2$ rotational manifold in the absence of an external magnetic field. For example, the transitions with the highest and lowest frequencies are labelled (a) and (b), respectively, here and also in Figure 4.3.

In the presence of an external electric field, states of opposite parities mix. The parity selection rule is now replaced by the $\Delta\Omega = 0, \pm 1$ selection rule. The red arrows in the middle panel labeled (L) and (U) correspond to the stretched-to-stretched transitions used to determine the Stark shift in our microwave spectroscopy. The Stark shift depends on m_F and d_{mf}. The eEDM-sensitive states used for the eEDM measurement are the upper (red) and lower (blue) doublets.

To reduce clutter in the left and middle diagrams, the states drawn do not reflect the true nature of the states in three aspects: (i) the states are drawn with an artificially large $A_{||}$ in comparison to ω_{ef} for well separated hyperfine levels in the diagram; (ii) the Stark shifts in the diagram are portrayed proportionally smaller than those in the actual experiment, where Stark shifts are large enough to allow some states in the lower hyperfine level to be more energetic than the upper; and (iii) F is no longer a good quantum number in the presence of a strong external electric field, except for the most stretched Zeeman states in each rotational manifold. Hence, in the presence of an external electric field, the only selection rule remaining on the $J = 1$ to $J = 2$ transition is $\Delta m_F = 0, \pm 1$. The panel on the right shows a more realistic ordering of the energy levels.

energy level diagram to scale. In the figures, we make use of the result of the g-factor from the next section.

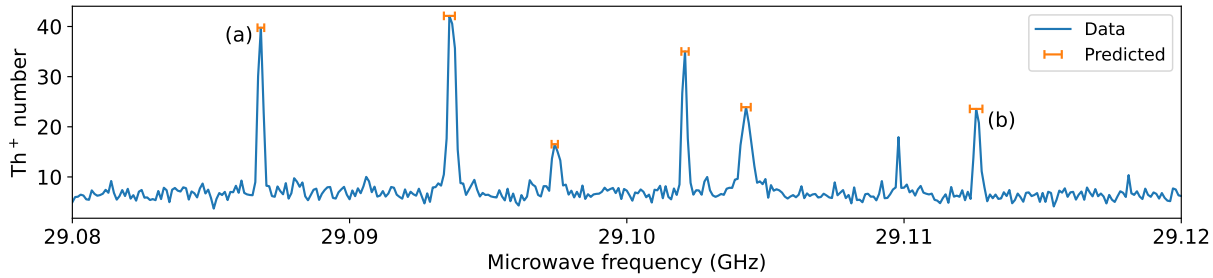

Figure 4.3: **Microwave scan at zero net external electric field.** The blue peaks and yellow markers correspond to the actual measurement and simulated position of the peaks, respectively. The unexpected peak at 29.11 GHz is most likely due to a spike in the experimental noise. Error bars from the simulation are propagated from the values shown in Table 4.1. The uncertainty of the Th^+ numbers in our data is typically around 5 ions. The lines labelled (a) and (b) are the corresponding transitions labelled in Figure 4.2.

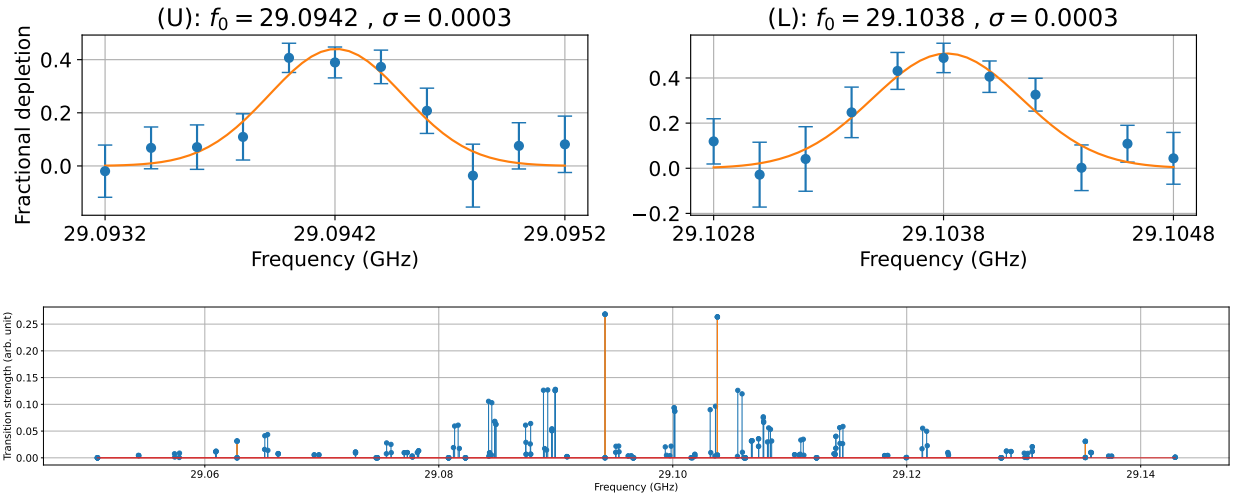

Figure 4.4: **Microwave transitions between the $X\,^3\Delta_1(v = 0, J = 1, m_F = -3/2)$ and $J = 2$ states at an applied electric field strength of 24 V/cm.** The top two plots show the transition lines corresponding to (U) and (L) of Figure 4.2. Error bars show the estimated 1σ error in the signal. The bottom plot shows a simulation of the microwave spectrum across a wider frequency range. The left and right peaks highlighted in yellow correspond to (U) and (L), respectively. The intensities are evaluated from Clebsch-Gordan coefficients. In the limit of $d_{\mathrm{mf}}\mathcal{E} \gg \omega_{\mathrm{ef}}$, where $\mathcal{E}$ is the applied electric field, the splitting between (U) and (L) is given by $d_{\mathrm{mf}}\mathcal{E}/3$. At $\mathcal{E} = 24$ V/cm, $d_{\mathrm{mf}}\mathcal{E}$ is roughly 8 times larger than ω_{ef}.

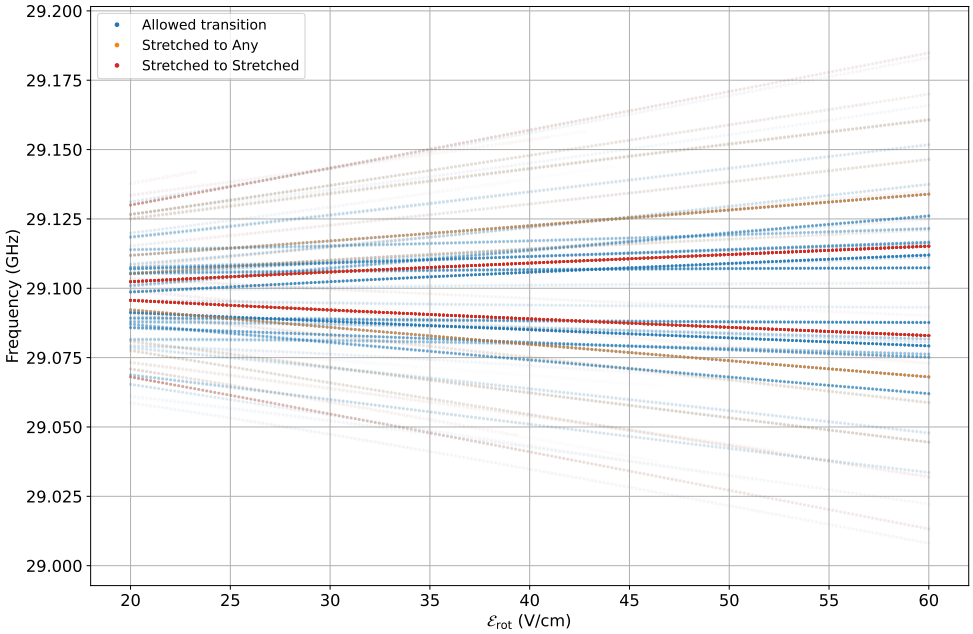

(a) Zoomed out view.

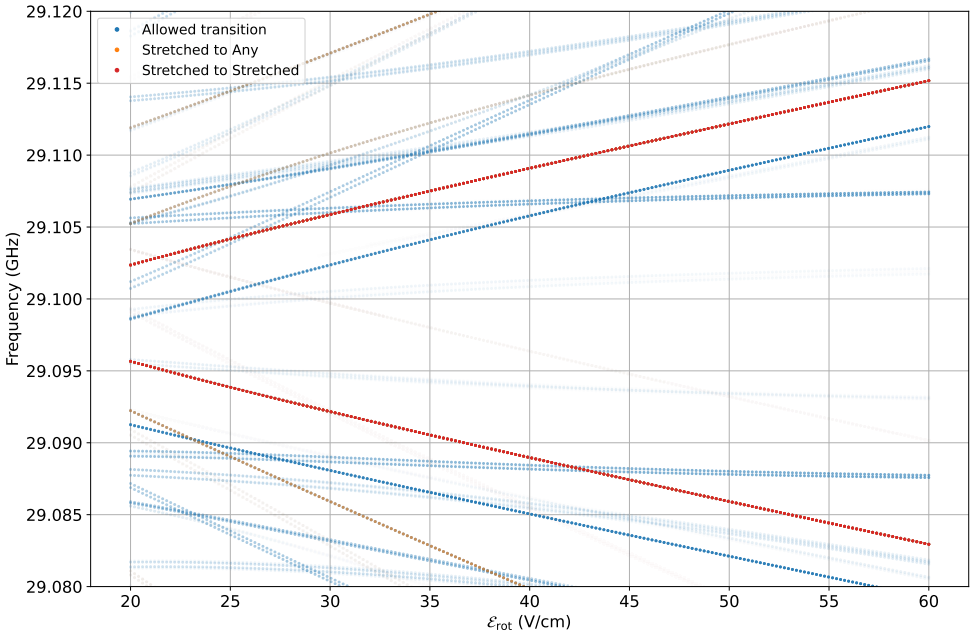

(b) Zoomed in view.

Figure 4.5: **Allowed transitions between $J = 1$ and $J = 2$ in $X\,^3\Delta_1(v = 0)$.** The (L) and (U) transitions (stretched to stretched) are colored red. We want to operate at an $\mathcal{E}_{\text{rot}}$ such that these red lines are not crossing any other line. There is another pair of stretched to stretched transition (also colored red) that is weakly allowed by Ω-doubling in the $J = 2$ manifold. Transitions connecting the stretched states, i.e. the doublets, in the $v = 0$ manifold are colored yellow.

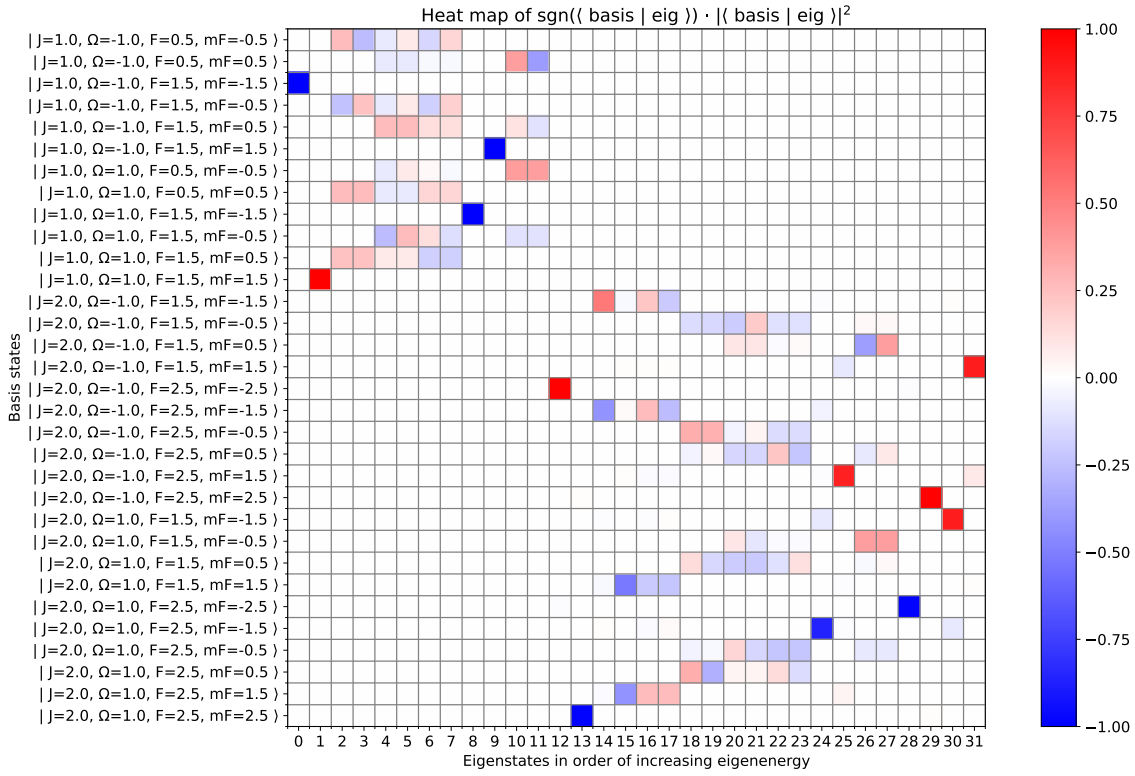

Figure 4.6: **Heat map of the coefficients of the eigenstates expanded out in our chosen basis set.** This heat map is obtained by diagonalizing the 32-level Hamiltonian (see Appendix C.3.1) of the $X\,^3\Delta_1(v=0, J=1, 2)$ manifold in our chosen basis set. The Hamiltonian is diagonalized at our usual experiment parameters $\mathcal{E}_{\text{rot}} = 60$ V/cm, $f_{\text{rot}} = 147.5$ kHz, and $\mathcal{B}_{\text{rot}} = 800$ μG corresponding to an $f \approx 50$ Hz. For an eigenstate expanded of the form $|\cdot\rangle = \sum_i c_i|i\rangle$, where $|i\rangle$ is the i^{th} basis state, the heat map shows $\operatorname{sgn} c_i|c_i|^2$ (information of the complex phase is lost in this representation; the sgn operator has a "branch cut" along the negative real axis). The eigenstates are ordered from least to most energetic.

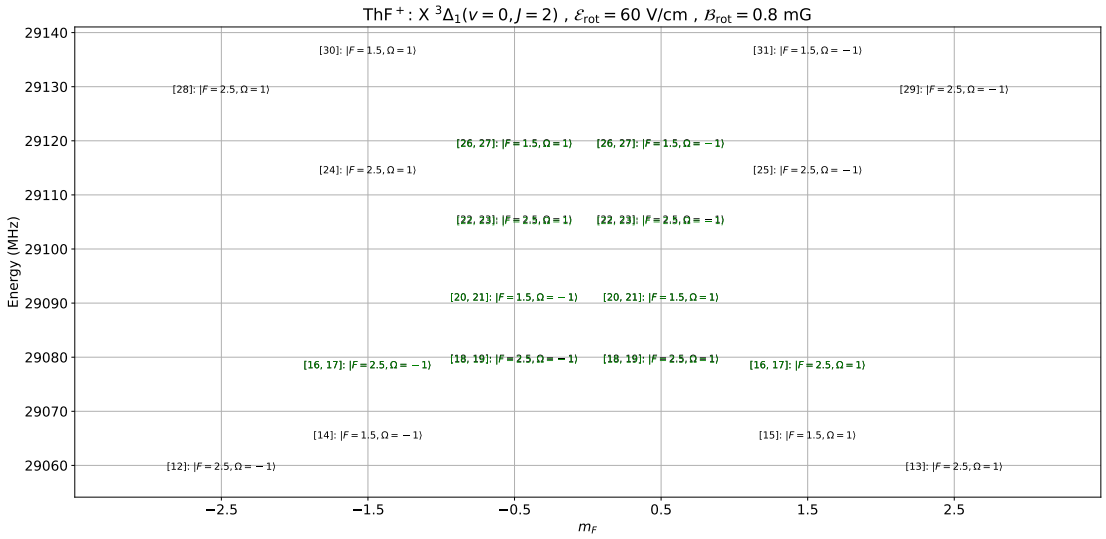

(a) $J = 2$.

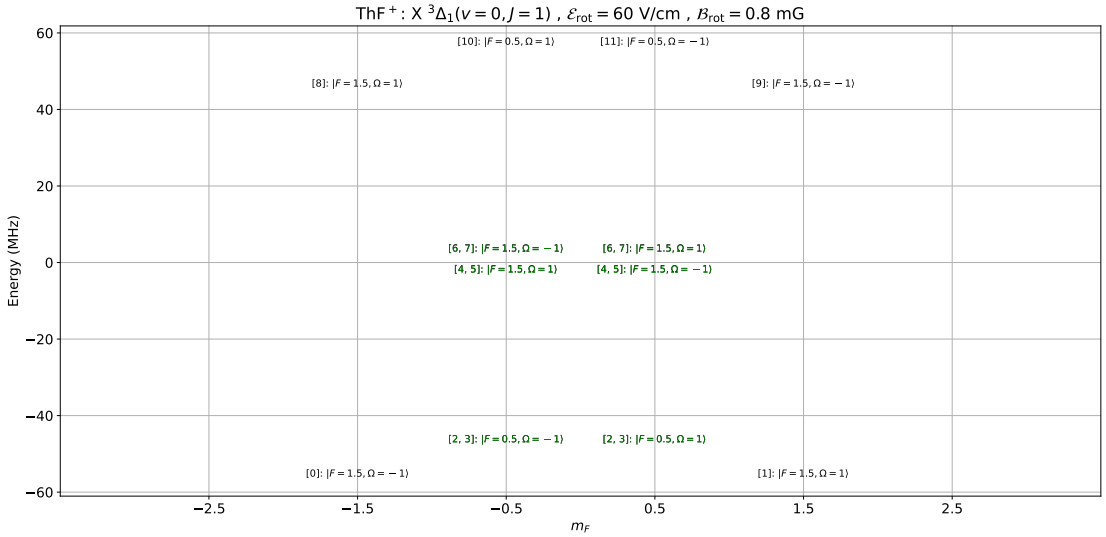

(b) $J = 1$.

Figure 4.7: **Energy level diagram of the 32-level system in $X\,^3\Delta_1(v = 0, J = 1, 2)$ expressed in our chosen the basis set.** Drawn to scale (c.f. Figure 4.2). The presence of an electric field, F is no longer a good quantum number except for the most stretched Zeeman states, but we still label our states with F to track how the states shift from zero electric field. Each line corresponds to a basis state. The indices prefixed to each basis state corresponds to the eigenstate that aligns most with that basis state (numbers on the horizontal axis of Figure 4.6). For example, [0] is predominantly $|J = 1, F = 3/2, m_F = -3/2, \Omega = -1\rangle$, as one can check with Figure 4.6. Basis states with multiple indices indicate an equal superposition state. For example, $[4, 5]$ means that states [4] and [5] are equal superpositions of $|J = 1, F = 3/2, m_F = -1/2, \Omega = 1\rangle$ and $|J = 1, F = 3/2, m_F = 1/2, \Omega = -1\rangle$.

4.1.3 Ramsey spectroscopy within the $J = 1$ eEDM-sensitive state; Magnetic g-factor

The last spectroscopic constant that we determine is the magnetic g-factor for $X\,^3\Delta_1$. We use a rotating electric field to polarize our molecular ions without ejecting them from our ion trap. The rotation micromotion traced out by the ions couples to the applied quadrupole magnetic field gradient to give an averaged net non-zero magnetic field along the instantaneous quantization axis in the frame of the ions, thus resulting in Zeeman shifts of the molecular states. Details of the underlying mechanism can be found in Section 4.11 of Ref. [25].

The rotation frequency is fast compared to trap secular frequencies, but slow compared to typical energy differences between quantum states within the molecular ions. As the ions follow the rotation of the field adiabatically, there is a non-inertial-frame term in the Hamiltonian in the frame of the rotating ions. This non-inertial-frame term introduces rotational coupling between states of $\Delta m_F = \pm 1$, and couples the $m_F = \pm 3/2$ states through a third order process. Restricting ourselves to the Hilbert space involving only the $m_F = \pm 3/2$ states, the good eigenstates of the system are $|m_F = +3/2\rangle \pm |m_F = -3/2\rangle$ at zero external magnetic field, and approach $|m_F = \pm 3/2\rangle$ asymptotically as the external magnetic field strength increases (see part (c) of Figure 1.4). Thus, as the strength of the applied magnetic field is swept, the energy difference between the $m_F = \pm 3/2$ states traces out a hyperbola like that shown in Figure 4.8, where the vertical offset is due to the avoided crossing introduced by the rotational coupling.

Following the procedure reported in Ref. [56], we map out the the energy differences between the $m_F = \pm 3/2$ states for both the upper and lower doublets by performing Ramsey spectroscopy on $X\,^3\Delta_1$, which is prepared with sequence up to panel (d) in Figure 4.1. We repeat the experiment at various applied magnetic field strengths. The data and fits are shown in Figure 4.8.

Since we operate at $d_{\mathrm{mf}}\mathcal{E} \sim A_{||}$, the lower doublet is energetically closer to more $m_F = \pm 1/2$ states than the upper doublet. Thus, the lower doublet has a stronger rotational coupling than the upper doublet, resulting in a much larger avoided crossing seen in the plot for the lower doublet than the upper doublet in Figure 4.8.

By measuring the frequencies at long Ramsey times for each doublet individually, we can also measure

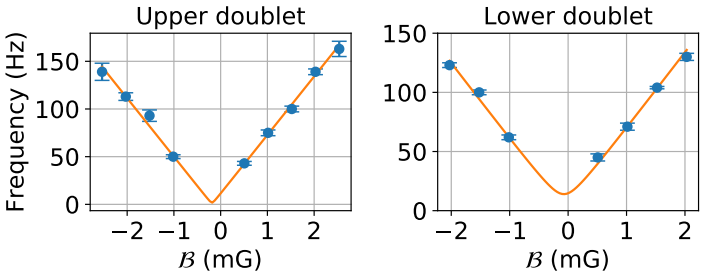

Figure 4.8: **Energy differences between the $m_F = \pm 3/2$ states; measurement of the magnetic g-factors.** The fits are performed with our model which takes into account the avoided crossing introduced by going into the rotating frame of the molecules. The energy difference at the avoided crossing is fixed by our *ab initio* calculations through diagonalizing the 12-level Hamiltonian (see Appendix C.3.1). The only fit parameters are the asymptotic gradients (corresponding to $3g_{F=3/2}\mu_B/h$) and the horizontal offset due to ambient fields. The error bars are 1σ error estimates extracted from a non-linear fit to each Ramsey fringe.

the difference in the g-factor between the two doublets. The ratio $\delta g/g$ is measured to be $-0.00255(6)$ (see Figure 4.9a) at $\mathcal{E}_{\text{rot}} = 60$ V/cm. Diagonalizing the 32-level Hamiltonian[1] involving the $X\,^3\Delta_1(v = 0, J = 1, 2)$ manifold gives a theoretical value of about -0.00223. The 15% discrepancy may come from coupling between the $X\,^3\Delta_1$ and the $^3\Delta_2$ states that is not accounted for in the 32-level Hamiltonian; we saw a similar correction in HfF^+.

[1] Although we are looking at the g-factors of the $J = 1$ manifold, coupling with the $J = 2$ states through the Stark Hamiltonian modifies the g-factor significantly, so we need to use the 32-level Hamiltonian instead of the 12-level one.

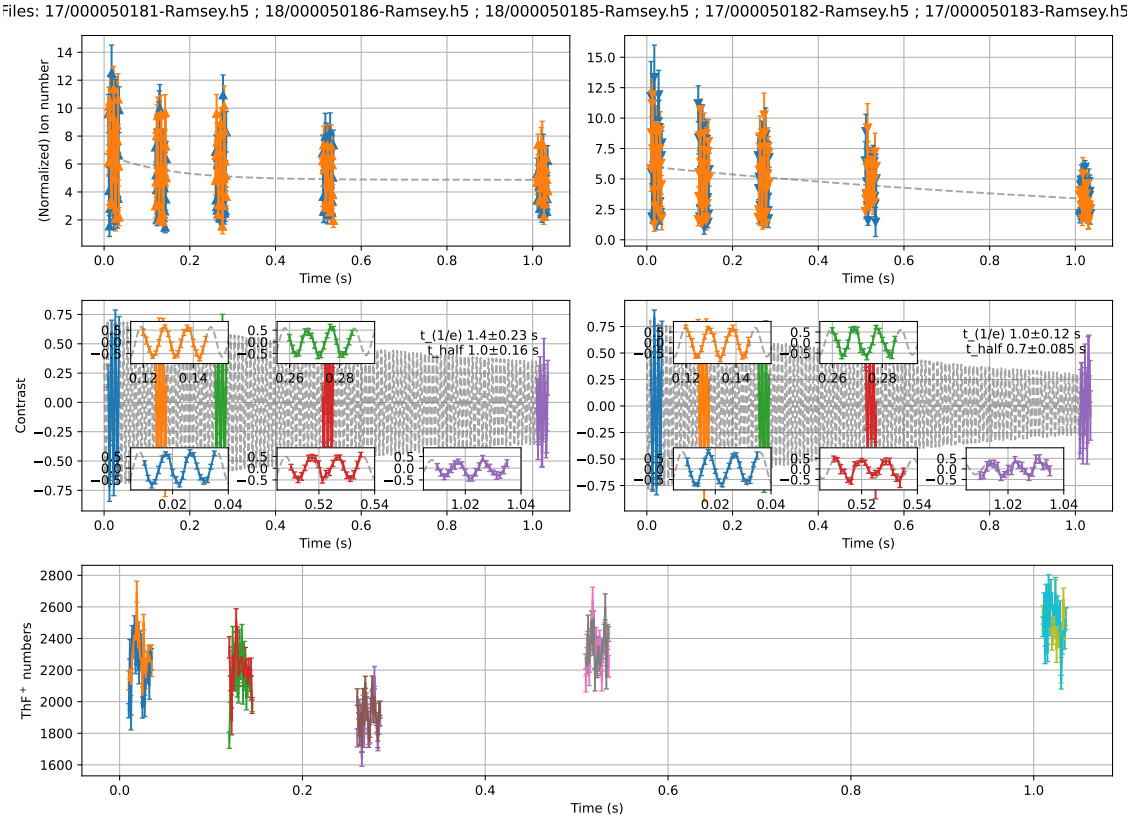

(a) Ramsey fringes for the lower (left) and upper doublets (right). The top row indicates the dissociated Th^+ numbers from the $m_F = 3/2$ (blue) and $m_F = -3/2$ (yellow) states, while the middle row is the contrast obtained through the difference between the two chops. The left column corresponds to the lower doublet, while the right column corresponds to the upper. The last row is the total ThF^+ numbers, and it is used for normalization. An exponential decay is fit to the results in the top row, giving us some hints on T_1 decoherence. An exponentially decaying sine is fit to the results in the middle row, with insets showing the zoomed in view comparing the fit to the raw data. Through the fits, we obtain the Ramsey frequencies for the lower (f^{l}) and upper (f^{u}) doublets used in the plot in part (b) below.

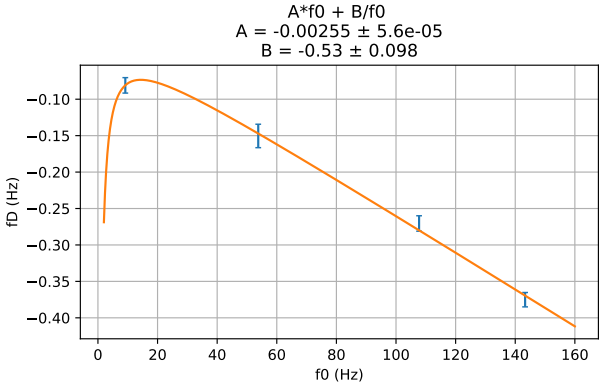

(b) Global fit to repeated instances of Figure 4.9a at various $f^0 := (f^{\mathrm{u}} + f^{\mathrm{l}})/2$. The vertical axis corresponds to $f^D := (f^{\mathrm{u}} - f^{\mathrm{l}})/2$. The quantities f^{u} and f^{l} are defined above in part (a). The fit is to the functional form $f^D = Af^0 + B/f^0$, where $A = \delta g/g$, and $B = \Delta\,\Delta^D$ (see Equations 8.24a and 8.24c). The fit value of $B = -0.5(1)$ is consistent with our model predicting a value of -0.45.

Figure 4.9: **Measuring $\delta g/g$ in ThF^+ at $\mathcal{E}_{\mathrm{rot}} = 60$ V/cm.** By performing the experiment at several Ramsey frequencies, we can perform a global fit to extract the difference in g-factor between the two doublets.

4.1.4 Summary of Results & Remarks

Table 4.1 shows the measured and calculated spectroscopic structural constants for $X\,^3\Delta_1$.

Parameters	Exp.	Theory	Previous work	Notes
$A_{\|\|}/2\pi$ (MHz)	$-20.1(1)$	-21.5	-	-
$\omega_{\rm ef}/2\pi$ (MHz)	5.29(5)	-	5.21(4) [43]	-
$d_{\rm mf}$ (D)	3.37(9)	3.46	4.03 [41], 3.46 [22]	-
$\|g_{F=3/2}\|$	0.0149(3)	See main text.	-	-
$\delta g_{F=3/2}/g_{F=3/2}$	-0.00255(6)	-	-	At $\mathcal{E}_{\rm rot} = 60$ V/cm.

Table 4.1: **Measured spectroscopic structural constants for $X\,^3\Delta_1$.** $A_{||}$, $\omega_{\rm ef}$, $d_{\rm mf}$, $g_{F=3/2}$, and $\delta g_{F=3/2}$ are the ^{19}F magnetic hyperfine coupling constant, Ω-doubling splitting constant, molecular frame electric dipole moment of ThF^+, the average value of the magnetic g-factors of the $F = 3/2$ hyperfine level in $X\,^3\Delta_1$ for the upper and lower doublets, and the difference in magnetic g-factors between the upper and lower doublets, respectively. Theoretical calculations by our collaborator Prof. Lan Cheng from Johns Hopkins University and previous work are also shown here for comparison. $A_{||}$ and $\omega_{\rm ef}$ have units of rad/s and for convenience we divide by 2π and present our results in millions of cycles per second.

Our spectroscopy is not sensitive to the sign of the magnetic g-factor shown in Table 4.1. Neglecting the rotational contribution to the g-factor, and converting $|g_{F=3/2}|$ into $G_{||}$, we get $-0.042(2)$ if $g_{F=3/2} > 0$ and 0.048(2) otherwise. The latter is not far away from the theoretical predictions of $G_{||} = 0.034$ [22] and 0.035 calculated by our collaborator Prof. Lan Cheng from Johns Hopkins University. We do not have a systematic estimate for the error in the theoretical value of $G_{||}$, therefore there remains some ambiguity in sign of the g-factor.

The spectroscopic constants measured in ThF^+ are similar to those in HfF^+ [56]. This means that we will be operating in a familiar experimental parameter space. Therefore, the eEDM experimental complexity will not increase with the planned molecule upgrade from HfF^+ to ThF^+.

4.2 Blackbody Radiation Excitation and T_1 Relaxation Time

4.2.1 Background

$X\,^3\Delta_1$ has been shown to be the ground electronic state of ThF^+ [43]. Hence the coherence time of $X\,^3\Delta_1$ is not subject to spontaneous decay. However, stray photons, e.g. blackbody radiation, can excite ThF^+ from $X\,^3\Delta_1$, and they subsequently either decay into other long-lived states where they no longer contribute to the measurement statistics, or back into $X\,^3\Delta_1$ with corresponding delayed decay in coherent spectroscopy contrast.

The transition rate between two states $1 \to 2$ for incoherent excitation is given by:[2]

$$\Gamma(f, T, \mu_{12}) = \frac{|\mu_{12}|^2}{6\epsilon_0 \hbar^2} \rho(f, T), \tag{4.1}$$

where μ_{12} is the transition dipole moment, and $\rho(f, T)$ is the spectral energy density from Planck's law:[3]

$$\rho(f, T) = \frac{8\pi h f^3}{c^3} \frac{1}{e^{\frac{hf}{k_B T}} - 1}, \tag{4.2}$$

where the first term is the density of states, while the second term is the mean photon number. We can calculate the $1/e$ lifetime by taking the inverse of the transition rate:

$$\tau(f, T, \mu_{12}) = 1/\Gamma(f, T, \mu_{12}).$$

A simple relation exists between frequency and wavenumbers ($\tilde{\nu}$):

$$f[\text{Hz}] = 100 \cdot c[\text{m/s}] \cdot \tilde{\nu}[\text{cm}^{-1}].$$

All that remains is to determine μ_{12}. There are three types of possible pathways for blackbody radiation excitation from $X\,^3\Delta_1(v = 0, J = 1)$:

Electronic transitions. Electronic transitions are typically on the order of 1000 cm^{-1}. This sits on the tail of the exponentially decaying mean photon number at 300 K. Hence, we are not concerned with electronic transitions.[4]

[2] See, for instance, Equation 9.47 of Ref. [57] or Equation 2 of Ref. [58].
[3] See, for instance, Equation 5.113 of Ref. [57] or Equation 1 of Ref. [58].
[4] The only exception is transition to the $a\,^1\Sigma^+$ state at just 314 cm^{-1} above the ground state. However, the transition is highly forbidden by selection rules, so the excitation rate to $a\,^1\Sigma^+$ is also highly suppressed.

Rotational transitions. Rotational transitions sit on the other side of the spectrum, where the transition frequencies are so small (~ 30 GHz) that the density of states ($\sim f^3$) is so small that the transition rates are also highly suppressed.

Vibrational transitions. These transition frequencies are at the anti-Goldilocks range where they are neither so large as to sit on the exponentially decaying tail of the mean photon number, nor so small as to have negligible density of states. The excitation to $v = 1$ accounts for the main source of blackbody radiation excitation from $X\,^3\Delta_1(v = 0)$. The expression for μ_{12} for vibration excitation is:[5]

$$\mu_{v,v+1} = \sqrt{\frac{v+1}{2}}\sqrt{\frac{\hbar}{2\pi m\omega_e \cdot 100c}}\frac{\mathrm{d}d_{\mathrm{mf}}}{\mathrm{d}R}, \tag{4.3}$$

where $\omega_e = 656.96(1)$ cm^{-1} from our previous spectroscopy work [43], m is the reduced mass of ThF^+, and $\frac{\mathrm{d}d_{\mathrm{mf}}}{\mathrm{d}R}$ is something that we will determine in this section.

An energy level diagram of the lowest few vibronic states in ThF^+ is shown in Figure 4.10.

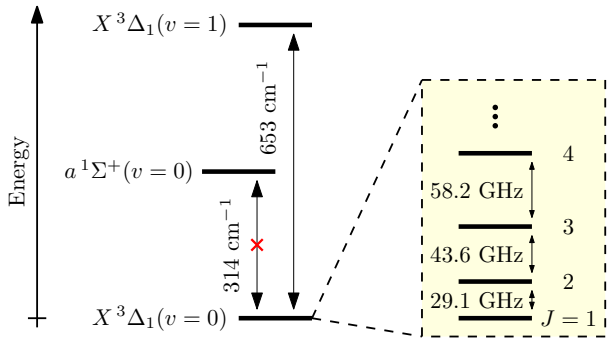

Figure 4.10: **Energy level diagram of the lowest few vibronic states in ThF^+.** The transition between $X\,^3\Delta_1$ and $a\,^1\Sigma^+$ is forbidden by selection rules. A zoomed-in view of the rotational states within the ground vibronic state is shown in the dashed box. 1 cm$^{-1} \approx 30$ GHz.

The blackbody radiation excitation rate from $X\,^3\Delta_1(v = 0)$ through $X\,^3\Delta_1(v = 1)$ is related to the spontaneous decay lifetime of the $v = 1$ states. This relation comes through the transition dipole moment between the $v = 0$ and $v = 1$ states. One should also note that the spontaneous decay rate (Einstein's A

[5] See, for instance, Equation 7 in Ref. [58].

coefficient) is: [6]

$$A = \frac{16\pi^3 f^3 |\mu_{12}|^2}{3\epsilon_0 hc^3}.$$

Using the above, we get the relationship between Γ (blackbody radiation excitation rate) and A (spontaneous decay rate) to be:

$$\Gamma = \frac{A}{e^{\frac{hf}{k_B T}} - 1}.$$

Hence, a measurement of the lifetime of the $v = 1$ state will allow us to predict the blackbody radiation excitation rate from $X\,^3\Delta_1$.

4.2.2 Measuring the $v = 1$ spontaneous decay lifetime

To measure the spontaneous decay lifetime of the $v = 1$ state, we first prepare all our ions in the ground vibronic state $X\,^3\Delta_1(v = 0)$ selectively with REMPI, and optically excite all our ions to the $\Omega = 0^-$ excited state, allowing for the ions to decay back into the $X\,^3\Delta_1(v > 0)$ states, as illustrated in Figure 4.11(a). We note that the branching ratio from the $\Omega = 0^-$ state to the $X\,^3\Delta_1$ manifold is very close

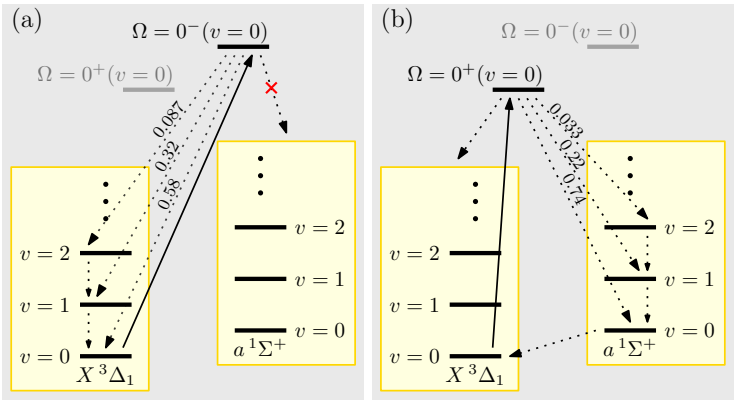

Figure 4.11: **State preparation for measurement of excited state lifetime.** (a) For measurement of $X\,^3\Delta_1(v = 1)$ state lifetime. (b) For measurement of $a\,^1\Sigma^+(v = 0)$ state lifetime. Solid line indicates laser used for optical pumping. Dotted lines indicate spontaneous emission. Numbers attached to dotted lines indicate Franck-Condon factors determined from our previous spectroscopy work [43].

to unity. Off-diagonal Franck-Condon factors allow the $v \geq 1$ manifolds to be populated through optical pumping. The whole optical pumping process takes about 100 ms. We then allow the ions to decay from the excited vibrational states to lower ones, and read out the population in each vibrational state with

[6] See, for instance, Equation 9.56 from Ref. [57]

resonance-enhanced–multi-photon dissociation [46, 55] much like how we have described in Section 4.1.1. We dissociate through the R(1) line for both the $v = 0$ and $v = 1$ manifolds. Our result is shown in Figure 4.12.

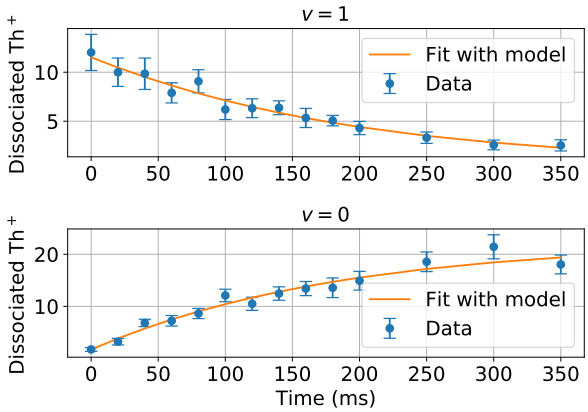

Figure 4.12: **Vibrational population decay from $v = 1$ to $v = 0$ of the ground electronic state in ThF^+.** All the population was pumped from the ground vibrational manifold into the excited vibrational manifold through the $\Omega = 0^-$ state [43]. Population in each vibrational manifold is read out with photodissociation. The observed vibrational decay lifetime agrees with our model, which is used to predict the blackbody radiation excitation lifetime from $X\,^3\Delta_1$. The total dissociated Th^+ numbers do not appear to be conserved in these two plots because the dissociation efficiencies for these two vibrational manifolds are not the same.

To extract the spontaneous decay lifetime of the $v = 1$ state from Figure 4.12, we employ the following model:

(1) We allow for non-zero initial population in the $v = 1$ and $v = 2$ states. The $v = 1$ and $v = 2$ states are populated by decay from the $\Omega = 0^-(v' = 0)$ state, and the Franck-Condon factors are such that we may approximate the initial populations of $v \geq 3$ as zero.

(2) The decay rates from each vibrational manifold are governed by their respective Einstein's A coefficients. We also assume that only $\Delta v = \pm 1$ transitions are allowed.

(3) Fit parameters include (i) absolute scaling to account for different detection efficiencies for the $v = 0$ and $v = 1$ manifolds; (ii) number of background ions; (iii) ratio of initial populations in the $v = 1$ and $v = 2$ manifolds; and (iv) $\mathrm{d}(d_{\mathrm{mf}})/\mathrm{d}r$, with this being held the same across the fits for $v = 0$ and $v = 1$.

Note that we can group (i) the effect of imperfect optical pumping from the $v = 0$ manifold, which results in an initial non-zero population in the $v = 0$ manifold, and (ii) background ions detected for the $v = 0$ manifold together into a single $v = 0$ "background ion" fit parameter in the fitting model. With the above model, we obtain $\mathrm{d}(d_{\mathrm{mf}})/\mathrm{d}r = 7(2)$ D/Å, in good agreement with Prof. Lan Cheng's calculations. This value corresponds to spontaneous decay lifetimes of 0.16(11) s and 0.08(6) s for $v = 1 \to v = 0$ and $v = 2 \to v = 1$, respectively.

Using the value of the molecular dipole, we predict the effective lifetime (T_1 relaxation time) of $X\,^3\Delta_1(v = 0, J = 1)$ to be about 3 s at room temperature (300 K), which is limited by blackbody radiation excitation from $X\,^3\Delta_1$ to the first excited vibronic state $X\,^3\Delta_1(v = 1)$.

4.2.3 Suppression of blackbody radiation excitation

We can suppress blackbody radiation excitation from $X\,^3\Delta_1(v = 0)$ by introducing cryogenics to lower the temperature of the setup. The effective lifetime of $X\,^3\Delta_1(v = 0)$ increases drastically with a decrease in temperature (Table 4.2), and we anticipate establishing a blackbody environment at 180 K, which will be a workable balance between technical convenience and sufficiently long interrogation times.

	77 K	120 K	150 K	180 K	200 K	300 K
To $X\,^3\Delta_1(v = 1)$	32000	400	84	29	17	3.5
To $a\,^1\Sigma^+$	2200	270	130	80	64	33
Combined	2100	160	51	21	13	3.2

Table 4.2: **Prediction of blackbody radiation excitation lifetime (in seconds) out of the $v = 0$ vibrational level in $X\,^3\Delta_1$, in a radiative environment of the indicated temperature.**

We calculate blackbody radiation excitation across rotational levels to occur at a time scale of 10^3 seconds and above, even at 300 K. Since we plan to measure the eEDM with an interrogation time of about 20 s, which is only about 10 times longer than our current experiment using HfF^+, the effects of rotational blackbody radiation excitation are small and shall be neglected for the rest of the discussion.

Usual selection rules forbid transition between $X\,^3\Delta_1$ and $a\,^1\Sigma^+$, but our molecular ion falls under Hund's case (c), so these states contain slight admixtures of states of other character. Hence, a transition between $X\,^3\Delta_1$ and $a\,^1\Sigma^+$ is not entirely forbidden. By using an $\Omega = 0^+$ state [43] that couples both to

$X\,^3\Delta_1$ and $a\,^1\Sigma^+$ for optical pumping, we populate the $a\,^1\Sigma^+(v=0)$ manifold through a process similar to the experiment for measuring the $X\,^3\Delta_1(v=1)$ spontaneous decay lifetime [refer to Figure 4.11(b)]. We observe the spontaneous decay lifetime from $a\,^1\Sigma^+(v=0)$ back to $X\,^3\Delta_1(v=0)$ to be about 6 s, which is about 40 times longer than from $X\,^3\Delta_1(v=1)$. We calculate blackbody radiation excitation from $X\,^3\Delta_1$ to $a\,^1\Sigma^+$ to be in excess of 30 seconds (Table 4.2).

The net effect of blackbody radiation excitations to $a\,^1\Sigma^+$ and $X\,^3\Delta_1(v=1)$ at 180 K gives an expected lifetime of $X\,^3\Delta_1$ to be about 20 s.

We tested the effects of the cryogenic suppression of blackbody radiation excitation in our new setup (see Figure 7.9) by comparing the rate of population loss from the $X\,^3\Delta_1(v=0, J=1)$ manifold at 170 K and 300 K. The results are summarized in Figure 4.13.

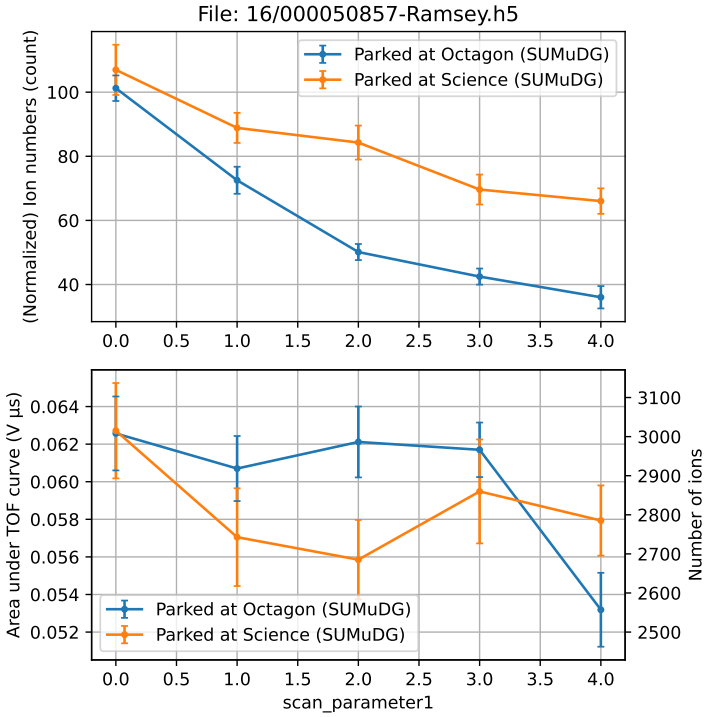

Figure 4.13: **Effect of suppressing blackbody radiation excitations at room temperature.** The top plot shows the detected ion population in the $X\,^3\Delta_1(v=0, J=1)$ manifold vs time held in the trap. The blue (yellow) points correspond to holding the ions at 300 K (170 K). The bottom plot shows the total ThF^+ ions detected, and serves as shot-to-shot normalization of the counted Th^+ ions. The experiment sequence is as follows.

(1) We create ions in the $X\,^3\Delta_1(v=0, J=1, F=3/2, m_F=-3/2)$ manifold with state preparation steps up to (c) in Figure 4.1.

(2) We move our ions into the cryogenic part of the trap, with an ambient temperature of 170 K. At that location, the ions can see about 0.5% of the full 4π steradians of the 300 K environment. See Figure 7.9 for more details of this new setup. The ions are translated into the cold region in 200 ms.

(3) For the yellow points, we hold the ions here for a variable amount of time (horizontal axis in the plot, unit in seconds).

(4) We then move our ions back out into the warm in 200 ms.

(5) For the blue points, we hold the ions here for the same amount of time that the yellow points are held in the cold.

(6) We then dissociate ions in the $J=1$ rotational manifold.

The results show that we lose ions slower from the $X\,^3\Delta_1(v=0, J=1)$ manifold when they are held in the 170 K environment than in the 300 K environment.

4.3 Experiment sequence

Now that we understand all that we need to of the quantum states of ThF^+, we can now design an experiment sequence for performing an eEDM experiment.

4.3.1 State preparation and detection

4.3.1.1 Lasers and microwaves

Figure 4.14 summarizes the lasers (and recommended wavelengths) used for state preparation and detection. We first prepare our ions in the ground vibronic manifold using REMPI (Chapter 2) through the [32.85] intermediate state. We address the bound-to-bound transition with Lion (LiopTec LiopStar-N, linewidth < 0.04 cm^{-1} before doubling, 180 μJ of UV pulse energy at trap) that is pumped with a 532 nm pump beam from Horse (Spectra-Physics INDI) which also acts as the second photon (1.1 mJ of 532 nm pulse energy at trap). We then usher our ions within the ground electronic manifold using our cw lasers and microwaves. Here are detailed descriptions of the cw lasers and microwaves used (each of the lasers/microwaves is prefixed with a code name in parenthesis; to be elaborated in Section 4.3.1.2):

(S) Sheep P(2) (Precilaser, 76 mW at trap, 2σ diameter of 10 mm, retroreflected). Sheep is a P(2) transition connecting the $X\,^3\Delta_1(v=0, J=2)$ to the $\Omega = 0^-\,[14.59]\,(v=0, J=1)$ state (part (b) of Figure 4.1). Upon exciting the ions in the $X\,^3\Delta_1(v=0, J=2)$ manifold to the $\Omega = 0^-\,[14.59]\,(v=0, J=1)$ manifold, they can decay back into the $X\,^3\Delta_1(v, J=1,2)$ manifolds, with Sheep turned on, all the ions will ultimately end up in the $X\,^3\Delta_1(v=0, J=1)$ dark manifold. Transitions between $X\,^3\Delta_1$ and $\Omega = 0^-\,[14.59]$ turn out to have unity branching ratio, so we only need to close the vibrational decay channels. Relevant Franck-Condon factors are shown in Figure 4.16a.

(U) 43 GHz microwave. We use the 43 GHz[7] microwave to couple the $X\,^3\Delta_1(v=0, J=2)$ and $X\,^3\Delta_1(v=0, J=3)$ states together so that we can also pump the $X\,^3\Delta_1(v=0, J=3)$ states into the $X\,^3\Delta_1(v=0, J=1)$ manifold.

[7] The author notes that we are treating microwaves differently from the optical wavelengths. At the point of this writing, the author is not aware if microwaves have feelings, but if they are proven to have emotions in the not so distant future, the author wishes to apologize in advance for not considering the feelings of microwaves. Deep down the author's heart, "43 GHz" is affectionally called "Lamb".

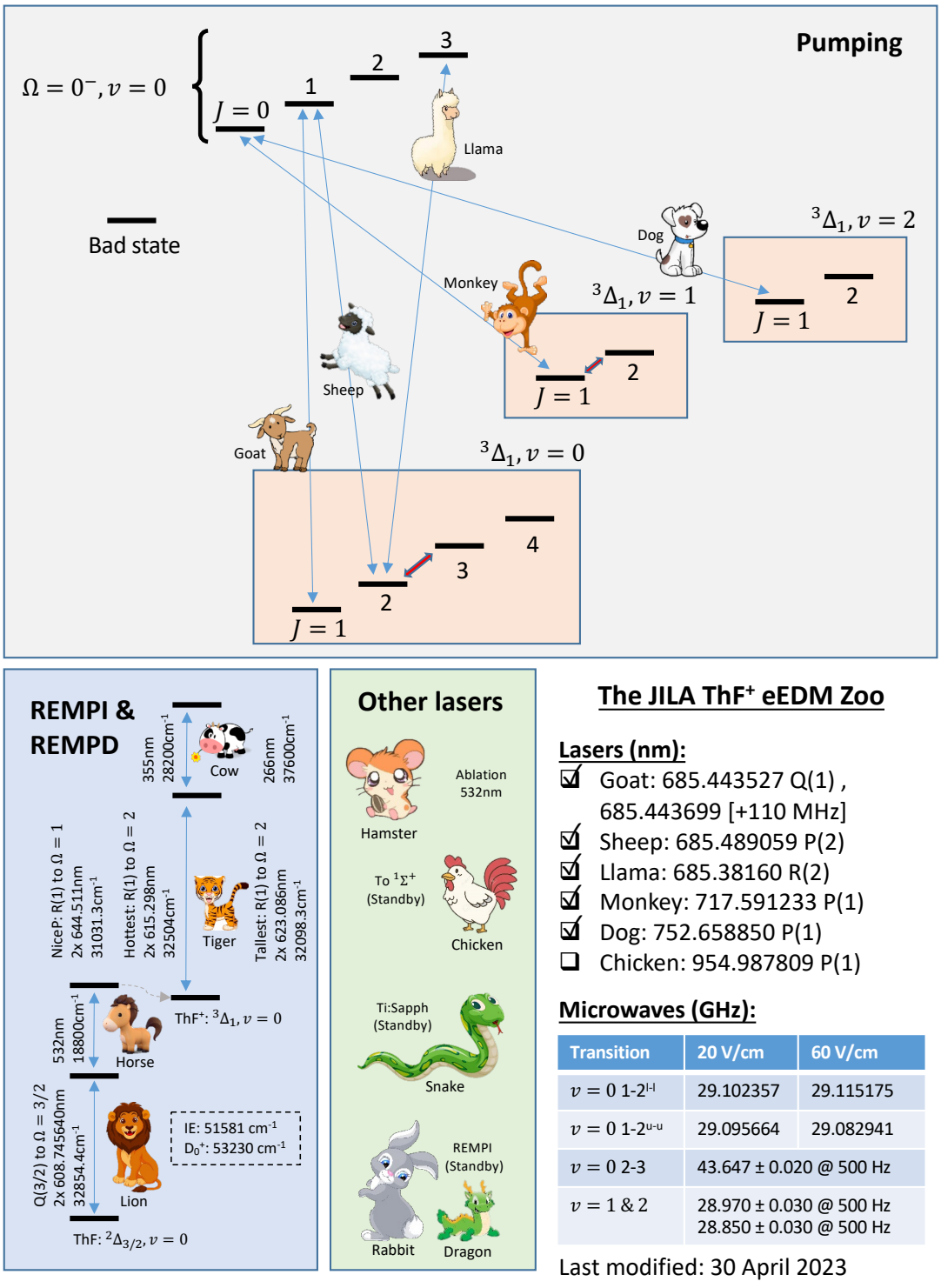

Figure 4.14: **Summary of the lasers (and recommended wavelengths in vacuum) used for state preparation and detection.** We have decided to name our lasers after animals. Lasers with functions related to each other are named after animals related to the corresponding animal of the first laser with that function named.

(M) Monkey P(1) (Home-built ECDL, 15 mW at trap, 2σ diameter of 14 mm, retroreflected). Monkey is a vibrational repump connecting the $X\,^3\Delta_1(v=1, J=1)$ manifold to $\Omega = 0^-$ [14.59] ($v = 0, J = 0$).

(D) Dog P(1) (Toptica DL-Pro, 31 mW at trap, 2σ diameter of 7.4 mm). Like Monkey, Dog is a vibrational repump, but connecting the $X\,^3\Delta_1(v=2, J=1)$ manifold.

(u) $v = 1, 2$, $J = 1 \leftrightarrow 2$ microwave. We chirp a 29 GHz microwave across a range of about 60 MHz to couple the $J = 2$ to the $J = 1$ in both the $v = 1$ and $v = 2$ vibrational manifolds of $X\,^3\Delta_1$ so that they can also be repumped with Monkey and Dog. We are able to address the $J = 1 \leftrightarrow 2$ transitions in the $v = 1, 2$ manifolds but not the $v = 0$ because of vibrational dependence of the rotation constant (Equation 2.5b). Figure 4.15 plots the transitions for the $v = 0, 1, 2$ manifolds. The transition with the lowest frequency that couples to a doublet in the $v = 0$ manifold corresponds to a transition between the $(v = 0, J = 1, F = 3/2, m_F = \pm 3/2, \Omega = \mp 1)$ to the $(v = 0, J = 2, F = 5/2, m_F = \pm 5/2, \Omega = \pm 1)$. This transition seems to be forbidden from $\Delta\Omega = 0, \pm 1$ selection rule, but is weakly allowed because of a slight admixture of the $(v = 0, J = 2, F = 5/2, m_F = \pm 5/2, \Omega = \mp 1)$ states through Ω-doubling, i.e. the molecules in the $J = 2$ manifold are not fully polarized yet at $\mathcal{E}_{\text{rot}} = 60$ V/cm. This transition happens at the frequency 29.013247 GHz (third blue blob to the right of the 29.0 GHz tick mark in Figure 4.15) at $\mathcal{E}_{\text{rot}} = 60$ V/cm. For the frequency chirp to couple the $J = 1$ and $J = 2$ states in $v = 1, 2$, we ensured that the chirped frequency stays below this frequency.

(G or G*) Goat Q(1) (Precilaser, 0.48 mW with 0.5% duty cycle at trap, 2σ diameter of 9 mm). Goat is a circularly polarized light that is strobed at f_{rot} at 0.5% duty cycle by using the $(-1)^{\text{st}}$ order diffracted beam of a gated AOM at 110 MHz. Goat moves the population within $X\,^3\Delta_1(v=0, J=1)$ to the stretched Zeeman states $X\,^3\Delta_1(v = 0, J = 1, F = 3/2, m_F = 3/2)$ (part (c) of Figure 4.1 during state preparation). Goat also acts as our depletion laser to remove ions from one of the stretched m_F states before we perform REMPD for our state detection. Goat is non-cycling enough that we still manage to deplete most of the ions in the unwanted stretched m_F states for our state

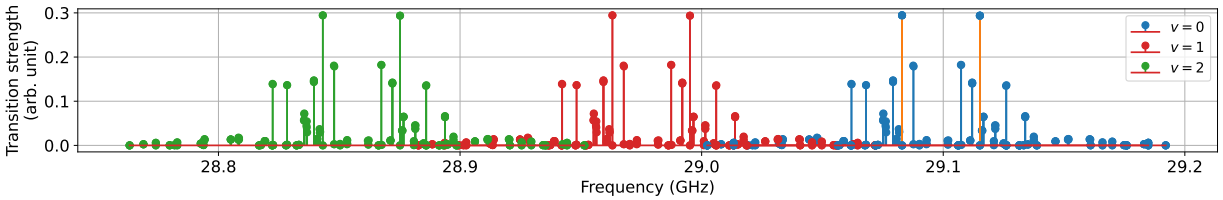

Figure 4.15: **Overlapping transitions of the $J = 1$ to $J = 2$ transition in the $X\,^3\Delta_1(v = 0, 1, 2)$ manifolds.** The transition frequencies are obtained by solving the 32-level Hamiltonian of the $X\,^3\Delta_1(v = 0, J = 1, 2)$ manifold, and looking for E1-allowed transitions between the eigenstates. We then scale the frequencies by B_v/B_0 to obtain the transition frequencies for the $v = 1, 2$ manifolds. The transition strengths are determined from the Clebsch-Gordan coefficients. The two lines highlighted in yellow are the stretched-to-streched transitions (L) and (U) mentioned in Section 4.1.2 at $\mathcal{E}_{\text{rot}} = 60$ V/cm. Note that the strong transitions (corresponding to the (L) and (U) transitions of the $v = 0, 1, 2$ manifolds) happen to stay clear of transitions belonging to the other vibration manifolds. This will not be true if we use $\mathcal{E}_{\text{rot}}$ much larger than 60 V/cm.

detection sequence; about 8% of the ions in the unwanted stretched m_F states end up in the wanted stretched m_F states (see Section 4.3.1.3). In the ideal situation, we may want Goat to sit on the P(1) transition for state preparation for higher cycling efficiency (no chance of falling down to the $X\,^3\Delta_1(v = 0, J = 2)$ manifold), and use another laser (maybe Chicken) on the Q(1) transition to the $\Omega = 0^+$ [10.47] electronic state that also couples to the $a\,^1\Sigma^+$ state for cleaner and faster depletion. A 0.5% duty cycle was chosen for Goat for two reasons. First, the strobe was required so that when Goat is strobed on, $\mathcal{E}_{\text{rot}}$ is quite precisely parallel or anti-parallel with the Goat laser beam to enforce a good circular polarization on Goat. Second, our Doppler shift from rotation micromotion at about 4 GHz could become large enough to redshift Goat to a Q(2) transition (about 1 GHz away from the Q(1) transition) for longer duty cycle; this Doppler shift would not be a problem if we change Goat from Q(1) to P(1) instead.

(L) Llama R(2) (Home-built ECDL + TA, 23 mW at trap, 2σ diameter of 9.7 mm). During our experiment, ions get bumped to higher rotational states through ion-ion collisions, or get excited to higher rotational states through blackbody radiation that takes ions out of the $X\,^3\Delta_1(v = 0)$ into the $X\,^3\Delta_1(v = 1)$, whereupon they can decay back to the $X\,^3\Delta_1(v = 0)$ manifold. Llama is turned on during our state detection sequence to shelf ions from the $X\,^3\Delta_1(v = 0, J = 2)$ so that our power broadened REMPD lasers parked on the $J = 1$ dissociation line do not accidentally dissociate $J = 2$

ions.

For completeness, I shall also briefly mention the history/status of the other lasers and microwave mentioned in Figure 4.14:

Hamster (Continuum Minilite, 3 mJ per pulse focused down to a diameter of 150 μm). Laser used for ablation of the thorium metal. Hamster replaced Mouse (Litron Nano-S-130) after the latter decided to retire.

Chicken (Home-built ECDL), not currently in use. We used this laser during the early ThF spectroscopy days to populate the $a\,^1\Sigma^+$ through the $\Omega = 0^+$ [10.47] state for diagnostics after creating our ions in the ground vibronic state.

Snake (Coherent MBR-110). A Ti:Sapph laser used in the spectroscopy work in Ref [43]. Snake can perform the same function as Chicken, and with even higher frequency tunability!

Rabbit (Sirah Matisse), not currently in use. A cw ring dye laser that we used to seed Dragon with. The output is then doubled into UV for a very narrow linewidth laser pulse to address individual Q lines for the first photon in our REMPI protocol. Mainly used for a proof of principle work. The ring dye laser (and the pulsed dye amplifier downstream) is much more complicated to maintain than a normal pulsed dye laser, and we do not need to resolve the Q lines for REPMI (we could just pump the whole Q branch), so we swapped Rabbit+Dragon for Lion.

Dragon (Radiant Dye Lasers Narrowamp), not currently in use. A pulsed dye amplifier. Seeded by Rabbit. Used for the first photon for the REMPI process. Currently decommissioned and enjoying its rightful vacation.

(^ or v) $v = 0$, $J = 1 \leftrightarrow 2$ microwave. We use this to deplete one of the two doublets in the $(v = 0, J = 1)$ manifold for diagnostics, e.g. to characterize the state-selectivity of our two-state detection anisotropy measure. We checked that the intensity of the microwaves is low enough that we do not accidentally deplete the other doublet from power broadening; we also ensured that the frequencies used do not

happen to drive other transitions through accidental degeneracy. When operating in a two-state detection mode, we do not use this microwave frequency.

4.3.1.2 Code names

On a day to day basis, we run our experiments with various combinations of lasers and microwaves that are turned on. It will be very cumbersome to label an experiment with names like "($J = 2$ rotational cooling) + ($J = 2 \leftrightarrow 3$ microwave) + ($v = 1$ vibrational repump) + ($v = 2$ vibrational repump) + ($v = 1, 2$ microwaves coupling $J = 1 \leftrightarrow 2$) + (m_F strobe pumping)". Naming our lasers and microwaves after animals allows us to shorten the above into "Sheep + 43 GHz + Monkey + ($v = 1, 2$, $J = 1 \leftrightarrow 2$) + Dog + Goat". This is still too long for our liking. We go one step further and abbreviate them with their one-character code names introduced with each laser/microwave in Section 4.3.1.1, so the above will look like "SUMuDG". Short and sweet. Cute and concise. The order of the code names does not matter, for instance "SUMuDG" means the same thing as "SMDGUu".

Most of the abbreviated code names are just the first letter of the name of the laser (e.g. "S" for Sheep).[8] Goat has two code names: "G" and "G*". The former refers to Goat with σ^+ polarization, and the latter refers to σ^-. The $v = 0$ $J = 1 \leftrightarrow 2$ microwave also has two code names: "^" and "v", referring to the microwave frequencies for depleting the upper and lower doublets, respectively.

Using this convention presents two additional advantages. First, having this convention also allows us to turn lasers and microwaves on or off very easily when we run our experiments simply by including or excluding the code names from our experiment user interface (see Section 9.3.4.2). Second, these abbreviated code names appear on all the plots of our automatically processed data, allowing for easy forensics on which lasers/microwaves were turned on during the experiment just by looking at the abbreviated code names.[9]

In some of the figures that follow, one may see code names in the legends for the plots. The author has also taken the extra effort to annotate the legends with descriptions for readers who are uninitiated with the code names for clarity.

[8] The Latin alphabet only has $2 \times 26 = 52$ letters. The author is trying to advocate for expanding the set of usable characters to include Chinese, Japanese, and Korean characters. The possibilities are (practically) endless!

[9] The full names are too long and clutter the plots.

4.3.1.3 Optical pumping model

Our state preparation stage is usually 300 ms long, and our state detection stage is about 40 ms long. The choices for these timings are informed by our optical pumping model, and are fine-tuned by scanning how long it takes for the lasers and microwaves to do their job, and are limited by the laser intensities that we currently operate at.

The optical pumping model involves solving differential equations of the form:

$$\frac{\mathrm{d}}{\mathrm{d}t}n_i(t) = \left(\sum_j \Gamma_{j\to i} n_j(t)\right) - \left(\sum_j \Gamma_{i\to j}\right) n_i(t), \tag{4.4}$$

where $\Gamma_{i\to j}$ are rates at which population move from the i state to the j state. We assume that (i) the lifetime of the $\Omega = 0^-$ [14.59] excited state is short as compared to the laser/microwave excitation rates, and (ii) the branching ratio to $X\,^3\Delta_1$ from $\Omega = 0^-$ [14.59] is unity. Hence, the i and j states are states from the $X\,^3\Delta_1$ electronic manifold. We also make use of the fact that rotational transitions are slow compared to the typical rates that we are looking at, so we do not include rates connecting different rotational states within the same vibronic manifold.

The first term on the R.H.S. of Equation 4.4 corresponds to population going into the i state, while the second term corresponds to population going out of the i state. One can then easily vectorize the equation, assume that the evolution is time independent (i.e. Γ rates are not functions of time), and solve it as a simple linear algebra differential equation:

$$\frac{\mathrm{d}}{\mathrm{d}t}\mathbf{n}(t) = \mathbf{\Gamma}\,\mathbf{n}(t) \implies \mathbf{n}(t) = e^{\mathbf{\Gamma}t}\mathbf{n}(0), \tag{4.5}$$

where $\mathbf{n}(t)$ is a vector with the population of all the states that we are interested in, and $\mathbf{\Gamma}$ is a matrix with dimensions $\dim(\mathbf{n}) \times \dim(\mathbf{n})$ governing all the rate constants, and it includes (i) laser pumping rates, (ii) microwave pumping rates, (iii) blackbody radiation excitation rates, and (iv) spontaneous decay rates. It does not include rotational heating through ion-ion collisions, and it assumes that the $\Omega = 0^-$ [14.59] state is short-lived as compared to the fastest pumping rates. Expansions to this model for time dependent $\mathbf{\Gamma}(t)$ or to include the two aforementioned effects are straightforward.

The optical pumping model takes in as input (i) the measured depletion rates of individual lasers from relevant states, and (ii) the calculated Franck-Condon and Hönl-London factors (see Figure 4.16). We

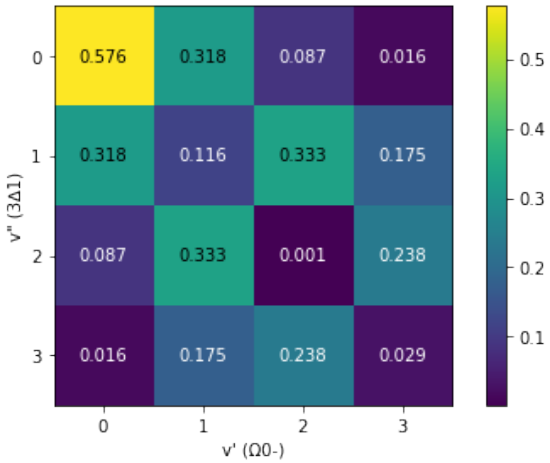

(a) Franck-Condon factors for transitions between $X\,^3\Delta_1$ and $\Omega = 0^-$[14.59].

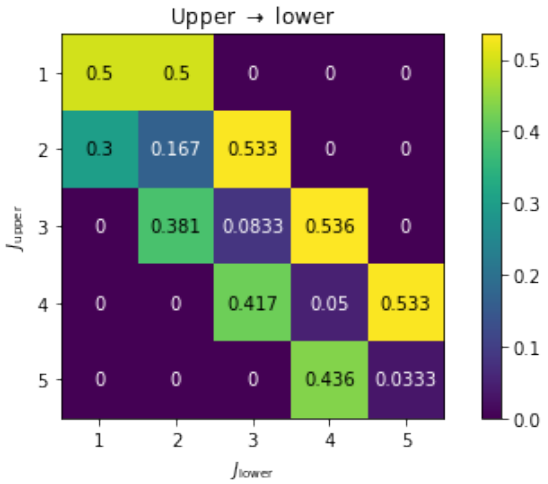

(b) Hönl-London factors for $\Omega = 0^-$[14.59] $\rightarrow X\,^3\Delta_1$.

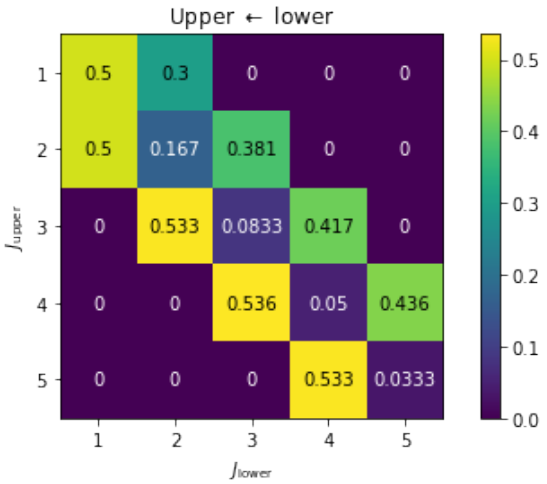

(c) Hönl-London factors for $\Omega = 0^-$[14.59] $\leftarrow X\,^3\Delta_1$.

Figure 4.16: **Relevant Franck-Condon and Hönl-London factors for transitions between $X\,^3\Delta_1$ and $\Omega = 0^-$ [14.59].** Franck-Condon factors are calculated from the measured spectroscopic constants (B_e, ω_e) using equations from Ref [59]. Hönl-London factors are calculated with equations from Ref [60], being careful with the state multiplicities. Here is an example of how to get the element in $\mathbf{\Gamma}$ that represents the rate at which population moves from $(v = 0, J = 2)$ to $(v = 0, J = 1)$ from the effect of Sheep P(2). For convenience, we call the rate at which Sheep moves population out of $(v = 0, J = 2)$ to the $\Omega = 0^-$ state to be A_{Sheep}. The rate at which population falls back to $(v = 0, J = 2)$ is $A_{\text{Sheep}}\text{FC}_{0'0''}\text{HL}_{1'2''}$, where the single- (double-) primed numbers indicate the upper (lower) state. Hence the net rate at which population is moving out of $(v = 0, J = 2)$ is $A_{\text{Sheep}}(1-\text{FC}_{0'0''}\text{HL}_{1'2''}) =: A_{\text{Sheep,meas.}}$, which is the rate that we measured with our setup. The rate at which Sheep moves population into $(v = 0, J = 1)$ is the product of the rate at which population is moving out of $(v = 0, J = 2)$ and the probability that it falls down to $(v = 0, J = 1)$. This is given by $A_{\text{Sheep,meas.}}\text{FC}_{0'0''}\text{HL}_{1'1''} = A_{\text{Sheep,meas.}} \times 0.576 \times 0.5$. The relevant Hönl-London factors are the ones associated with decay (part (b)), but the factors for excitation are also included for convenience to compare rates across Sheep P(2), Monkey P(1), and Goat Q(1).

neglect the Zeeman m_F sublevels in all our states in the optical pumping model except for the $(v = 0, J = 1)$ rotational state, which is split into the "D" and "B" states. The "D" ("B") state represents the states that are dark (bright) to the circularly polarized Goat Q(1) laser. For instance, a σ^+-polarized Goat Q(1) laser can only address the $m_F = \{-3/2, -1/2, 1/2\}$ states but not that $m_F = 3/2$ states. The former forms the "B" state, and the latter forms the "D" state. One can tell from Figure 4.7 that there are actually two (ten) states in the "D" ("B") state. Spontaneous decay into the $(v = 0, J = 1)$ manifold are split into a 1:5 ratio between the "D":"B" states. Of note, we also neglect the effect of polarization of all lasers except for Goat Q(1).[10]

We verified the model by comparing its predictions to experiments, and we saw very good agreement. Here we present an example of matching predictions from the model with results from experiment.

After our Ramsey sequence, we map the phase difference acquired during the Ramsey evolution into population difference in the two $m_F = \pm 3/2$ states. Since our state detection protocol using REMPD does not discern between the two states, we have to deplete one of the m_F states before we dissociate to read out population in the other state. We use circularly polarized Goat Q(1) to perform this depletion. It is important to understand what Goat does to the ion population. Ideally we want Goat to deplete all the population in one of the m_F states and leave the other m_F states untouched. Figure 4.17 looks at the effect of Goat Q(1) on moving population within our molecule. The time dependence shown in the figure only cares about the pumping rates of the lasers, which can be changed by changing the beam intensity and mode overlap of the laser beam and the ion cloud.

Without the effect of spontaneous decay and BBR excitation (or equivalently if Goat's pumping rate is much faster than the rates of spontaneous decay and BBR excitation), we see that we end up pumping 8% of "B" (states bright to Goat) into "D" (states dark to Goat). This means that in using Goat Q(1) to deplete the unwanted m_F state at the end of our Ramsey sequence, we end up with 8% pollution in our signal. At this point in time, this is still within acceptable range, but if one wishes to improve upon it, one would use Chicken or Snake for depletion instead of Goat.

With the effect of spontaneous decay and BBR excitation, one can imagine that if we turn Goat

[10] The rotation of the rotating electric field mixes the polarization of the lasers that are not strobed.

on past some amount of time, we do not win in terms of contrast, i.e. we will end up with unwanted ion migration into the dark m_F states through vibrational decay. In fact, Figure 4.18 shows the total population in the $(v = 0, J = 1)$ manifold (= "D" + "B") as a function of time at which Goat is turned on, and we can see that past a certain pumping time, we start to see growth in the ion numbers in "D" (+"B") through vibrational decay. This means that with our current laser intensities and mode overlap, we do not win by having our depletion Goat Q(1) on for more than 50 ms, i.e. there is no point in having a state detection stage longer than 50 ms. In fact, we are parking ourselves at 40 ms.

Figure 4.19 shows a comparison of model prediction and experiment result. We expect a population growth in "D" (corresponding to chop "Prep. + det. (same pol.)" in the figure) after a certain time, and we indeed see it in the experiment. The optical pumping model is not perfect because it makes several simplifications (e.g. state lifetime of the $\Omega = 0^-$ [14.59] is infinitely short compared to typical pumping rates; treats the rotational manifolds as one state without sub-structure, except for $(v = 0, J = 1)$ with the "D" and "B" sub-structure), and it certainly does not include all the effects seen by our ions (e.g. "D"-"B" mixing effects through m_F changing collision; ion-ion collisions causing rotational heating), but it is good enough for us to design our state preparation and detection scheme.

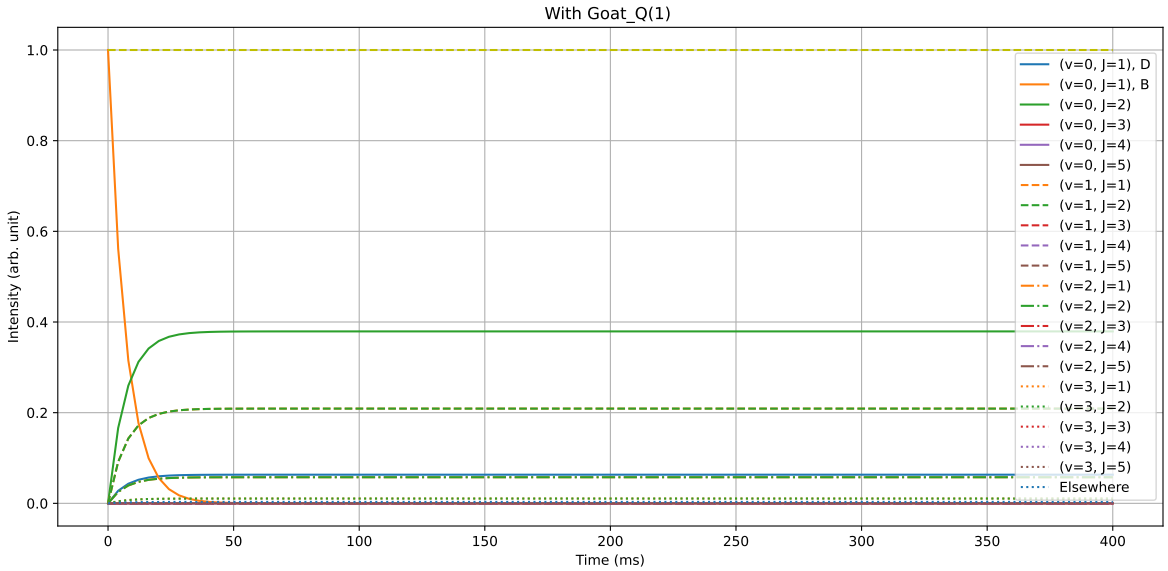

(a) The effect of having only Goat Q(1) on.

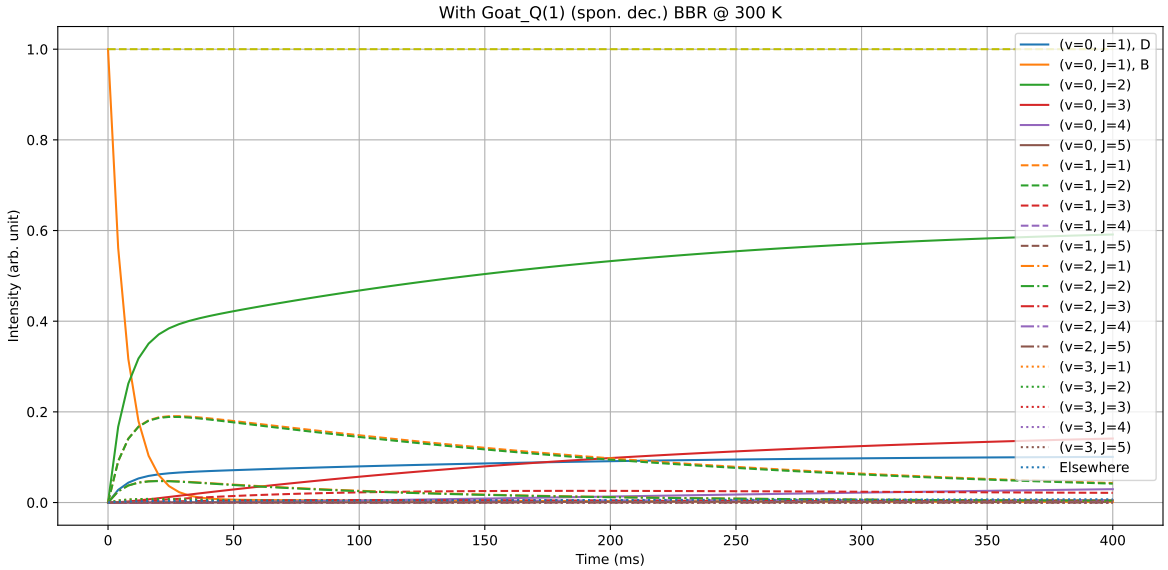

(b) Spontaneous decay and BBR excitation are turned on.

Figure 4.17: **From the optical pumping model: distilling out the effects of spontaneous decay and BBR excitation from the effect of Goat Q(1).** Here we consider all states with $v \leq 3$ and $J \leq 5$. The $(v = 0, J = 1)$ manifold is split into "D" and "B" representing the states that are Dark and Bright to the circularly polarized Goat Q(1) laser, respectively. We start with population all in the "B" state, and we turn Goat Q(1) on. Note that the early time behavior is the same with and without the effects of spontaneous decay and BBR excitation because the pumping rate of Goat is much faster than the rates of decay from ions shelved in the higher vibrational states by Goat and the BBR excitation rate out of the $v = 0$ manifold. The effects of spontaneous decay become apparent at later times when ions shelved in higher vibrational manifolds start to decay down, and if they fall back into the "B" state, they in turn can be addressed by Goat again. More discussion in the main text.

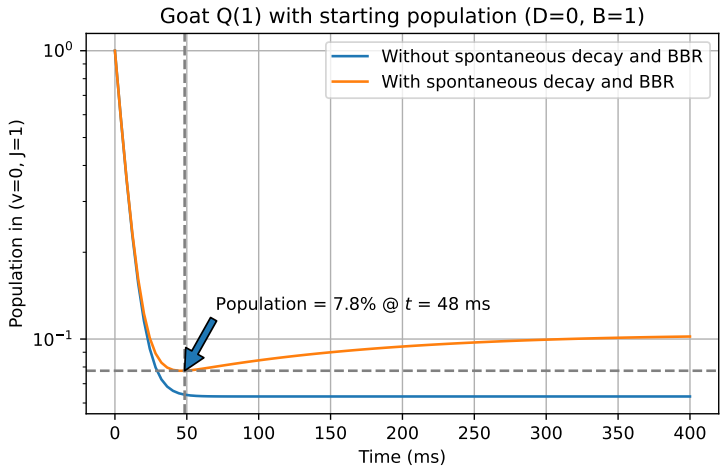

Figure 4.18: **From the optical pumping model: population in the $(v = 0, J = 1)$ state, which is a sum of population in "D" and "B", plotted as a function of time at which Goat is turned on.** Without the effect of spontaneous decay and BBR excitation, the population in the $(v = 0, J = 1)$ manifold saturates at 6%, but with the aforementioned effects, we reach a lowest population fraction of about 8% at around 50 ms of Goat on time. Thereafter we see significant unwanted population growth.

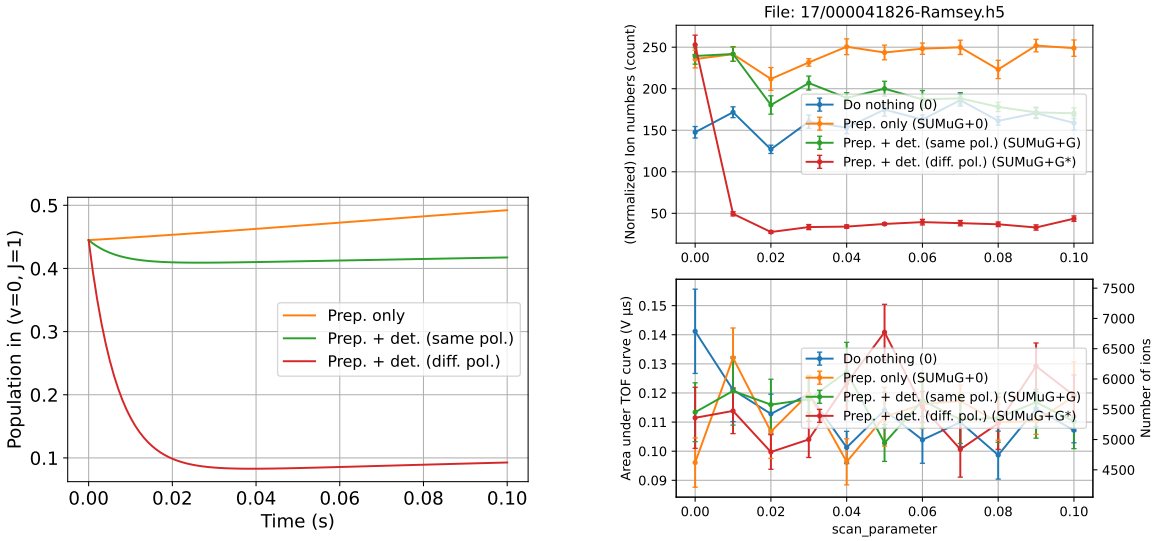

(a) Predictions from the optical pumping model.

(b) Checking predictions with experiment.

Figure 4.19: **Comparing predictions from the optical pumping model with experiment.** The top plot on the right corresponds to the number of dissociated Th^+ detected, while the bottom plot is a check on the total ThF^+ numbers in the trap; the lines in the bottom plot should look flat. We see that the population in "B" (corresponding to the chop "Prep. + det. (diff. pol.)", red line) decays at early time and increases slightly after about 20 ms, both in the simulation on the left plot and in the experiment on the top right plot. The population in "D" (corresponding to the chop "Prep. + det. (same pol.)", green line) decays with time in the experiment, but not in the simulation. We believe this is because the model does not include the effect of "D"-"B" mixing through mechanisms like m_F-changing collisions. We can model this mixing by including an *ad hoc* decay rate of about 3 s^{-1} to make the two plots agree more.

4.3.1.4 Current scheme and possible future upgrades

With our current scheme using 300 ms of state preparation (with Goat Q(1), Sheep P(2), 43 GHz microwave, Monkey P(1), Dog P(1), and the $v = 1, 2$ microwaves), we expect about 55% of all our ions to be in the $X\,^3\Delta_1(v = 0, J = 1, F = 3/2, m_F = 3/2)$ states and another 2% in the $X\,^3\Delta_1(v = 0, J = 1, F = 3/2, m_F \neq 3/2)$ states after state preparation. 25% of our ions are hiding in the $X\,^3\Delta_1(v = 0, J = 4)$, with another 10% in the $X\,^3\Delta_1(v = 1, J > 1)$, and the rest (8%) spread out across the higher vibrational states. We could leave our state preparation lasers and microwaves turned on for longer, but leaving them on for much longer than 100 ms starts to give diminishing returns. Figure 4.20 shows two plots for visualizing the diminishing returns after 100 ms.

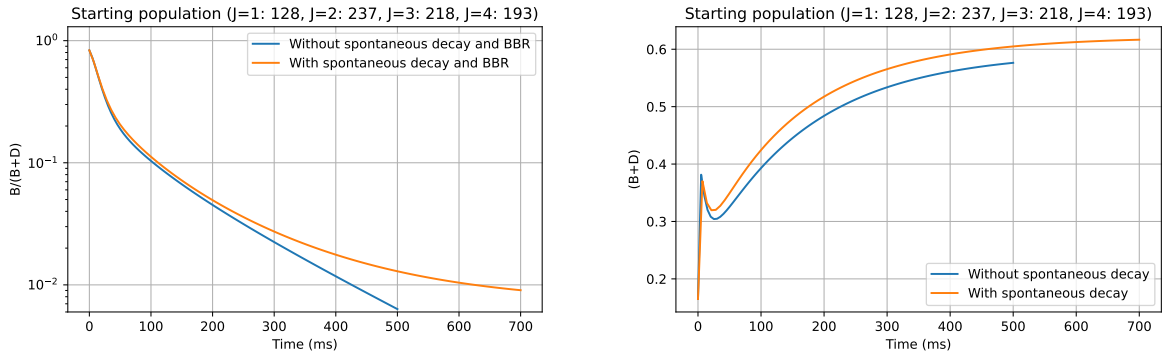

(a) "Impurity" of the $J = 1$ manifold.

(b) Fraction of ions in the $J = 1$ manifold.

Figure 4.20: **Plots of "impurity" and population migration in and out of the $J = 1$ manifold as a function of state preparation time.** "Impurity" is defined as the fraction of the population within the $J = 1$ manifold in the "B" state; we want "impurity" to be as close to zero by the end of our state preparation sequence. The initial population numbers (shown on the title of each plot) used for the simulation come from counting dissociated Th^+ ions by scanning the R branch of the first photon in the REMPD transition used, and taking into account the Hönl-London factors. (a) With our current pumping rates (limited by the current laser and microwave intensities), we expect to go below an "impurity" of 10% at 100 ms. Beyond 100 ms, BBR excitation kicks in to excite population in the "D" state into the higher vibrational states, so the lasers have to fight harder to get the ions back. (b) The sharp rise in the population in $J = 1$ (="B"+"D") at the start comes from Sheep and the 43 GHz microwave moving population from the $J = 2\&3$ into $J = 1$. The decrease after that comes from Goat moving population into the $m_F = 3/2$ states through the $\Omega = 0^-$ [14.59] state; this is an inefficient process because only about 6% end up in the $m_F = 3/2$ states after the first pass.

We can make several upgrades to our system to make the state preparation sequence more efficient. Firstly, we can recover the population in $X\,^3\Delta_1(v = 0, J = 4)$ by including a repump through microwaves connecting the $J = 3$ and $J = 4$. This will give us an additional 25% ions. Secondly, we can recover the

population in $X\,^3\Delta_1(v=1, J>1)$ by using stronger microwaves coupling the $X\,^3\Delta_1(v=1, J=1)$ and $X\,^3\Delta_1(v=1, J=2)$, and also microwaves coupling to higher rotational states. Lastly, we can also make Goat's m_F pumping a more efficient process by switching Goat from Q(1) to P(1); using P(1) would also alleviate the problem of Doppler shifting Q(1) into Q(2) because the P lines are much more separated than the Q lines. A quick study on the pumping rates of the lasers indicate that we are still not in the saturation regime yet, so we can still win more with more laser power (which will allow us to expand the beam more for the same/higher intensity with a better overlap with the entire ion cloud). We did not do a full study on the saturation curve for the microwaves because it turns out that the setup made it much harder to turn the knob on microwave power, but it seems like we are still in the linear regime so there is still more to be gained with higher microwave power.

For state detection, we turn the lasers (Goat Q(1) and Llama R(2) only) on for 40 ms. We have already discussed limitations in the state detection scheme in the previous section. Goat Q(1) and Llama R(2) couple to the $\Omega = 0^-$ [14.59] excited state, with unity branching ratio back to $X\,^3\Delta_1$. Fortunately Goat Q(1) only brings 6% of our population back into the dark state, i.e. Goat is $\sim 94\%$ efficient in depletion. Llama R(2) does not move population into the dark state through the R(2) transition, but in principle ions could take the pathway $(v=0, J=2) \xrightarrow{\text{R(2)}} (v=2, J=3) \xrightarrow{\text{spon. decay}} (v=1, J=2) \xrightarrow{\text{spon. decay}} (v=0, J=1)$ to go back to the dark state. To make this process less cycling, we can change their wavelength to address the $\Omega = 0^+$ [10.47] excited state instead with a less than unity branching ratio back into the $X\,^3\Delta_1$ manifold, shelving ions in the $a\,^1\Sigma^+$ manifold.

4.3.2 Ramsey sequence

Upon preparing the ions in the $X\,^3\Delta_1(v=0, J=1, F=3/2, m_F=3/2)$ states, we wish to perform a Ramsey experiment by performing a $\pi/2$ pulse to prepare a superposition of the $m_F = 3/2$ and $m_F = -3/2$ states (see part (c) of Figure 1.4). The previous eEDM experiments with HfF^+ use a $\pi/2$ pulse sequence as follows:

(1) Ramp $\mathcal{E}_{\text{rot}}$ down from 58 V/cm to 7 V/cm in 16 µs;

(2) Hold for 1 ms;

(3) Ramp $\mathcal{E}_{\text{rot}}$ back up to 58 V/cm in 16 µs.

Since $\mathcal{B}_{\text{rot}} \propto \mathcal{E}_{\text{rot}}$ and the rotational coupling[11] (Δ) between the $m_F = \pm 3/2$ states increases with decreasing $\mathcal{E}_{\text{rot}}$ to about $\Delta \sim 500$ Hz in HfF^+ with an $f_{\text{rot}} = 375$ kHz, the above $\pi/2$ sequence effects a "simultaneous $\pi/2$ pulse" for both the upper and lower doublets; the "simultaneous" is in quotes because the upper and lower doublets actually have a differential Δ of about 50 Hz at 7 V/cm, but it is small enough compared to 500 Hz so that while they are actually $\pi/2 \pm \epsilon$ pulses, the ϵ is small. Figure 4.21a shows a plot of the Δs in HfF^+.

We borrowed wisdom from the HfF^+ experiment and tried to perform the same $\pi/2$ pulse on ThF^+, but we have not been very successful. We notice that we lose a lot of ions from our desired quantum states after each $\pi/2$ pulse. It turns out that the spectroscopic constants of ThF^+ are sufficiently different from HfF^+ to make the HfF^+ protocol hard to implement in ThF^+. However, the seemingly unfriendly spectroscopic constants of ThF^+ also opened a window of opportunity to realize a true simultaneous $\pi/2$ pulse in ThF^+, which we shall see in the next few sections.

[11] See Figure 1.4 for an illustrated explanation of the rotational coupling in the context of the eEDM-sensitive states. See Figure 4.21 for the plot of Δ vs $\mathcal{E}_{\text{rot}}$. See Section C.3.1 for the Hamiltonian that we diagonalize to extract Δ.

4.3.2.1 Working principle behind the old protocol

The energy splitting between the $m_F = \pm 3/2$ states goes as[12] (also see Figure 1.4):

$$f^{\mathrm{u,l}} = \sqrt{\left[\Delta^{\mathrm{u,l}}(\mathcal{E}_{\mathrm{rot}}, f_{\mathrm{rot}})\right]^2 + \left[f_0(\mathcal{E}_{\mathrm{rot}}, f_{\mathrm{rot}})\right]^2}, \tag{4.6}$$

where $\{\mathrm{u}, \mathrm{l}\}$ correspond to the upper and lower doublets, respectively, and it is made explicit that Δ and $f_0(\mathcal{E}_{\mathrm{rot}}, f_{\mathrm{rot}}) = 3g\mu_{\mathrm{B}}\mathcal{B}_{\mathrm{rot}}(\mathcal{E}_{\mathrm{rot}}, f_{\mathrm{rot}})$ both depend on $\mathcal{E}_{\mathrm{rot}}$ and f_{rot}. The dependence of $\mathcal{B}_{\mathrm{rot}}$ on those variables are $\mathcal{B}_{\mathrm{rot}} = B_{\mathrm{axgrad}} \cdot \frac{e\mathcal{E}_{\mathrm{rot}}}{m(2\pi f_{\mathrm{rot}})^2}$, while those of Δ are more complicated, but it suffices to say that Δ increases very quickly with decreasing $\mathcal{E}_{\mathrm{rot}}$ and increasing f_{rot}. Representing the $m_F = \pm 3/2$ states as the poles on a Bloch sphere, the Bloch vectors on the sphere precess about a precession vector pointing in the $(\Delta, 0, f_0)$ direction with frequency f as given in Equation 4.6. For perfect Rabi flopping, we want the Bloch vectors to precess around $(1, 0, 0)$. We can realize this in our system by ramping down $\mathcal{E}_{\mathrm{rot}}$ to reduce f_0 and increase Δ so that $f_0 \ll \Delta$ for our $\pi/2$ pulse. Except during the $\pi/2$ pulses, $\mathcal{E}_{\mathrm{rot}}$ is large enough that $f_0 \gg \Delta$ so that the Bloch vectors precess around the poles. This is the working principle behind the $\pi/2$ pulses in the first two generations of the JILA eEDM experiment using HfF^+.

The above picture is painted as a two-level system, but there are many more energy levels in our molecule. It turns out that the width of the hyperfine crossing "resonance" in ThF^+ is so much broader than HfF^+ (see Figure 4.21b) that we can get population leakage from our two-level system into other states when we sweep across the hyperfine crossing, e.g. unstretched Zeeman states through rotational coupling of neighboring m_F states and, worse still, into the other doublet through Ω-doubling coupling. Furthermore, the two doublets have such different Δs that it is not possible for us to perform a "simultaneous $\pi/2$ pulse" for both doublets in ThF^+ ($\Delta^{\mathrm{u}} \approx 100$ Hz and $\Delta^{\mathrm{l}} \approx 300$ Hz at 7 V/cm with $f_{\mathrm{rot}} = 147.5$ kHz). We could perform a $\pi/2$ pulse for the upper doublet and a $3\pi/2$ pulse for the lower doublet simultaneously, but this still does not solve the problem of population leakage when we cross the hyperfine crossing. Instead, we implement a true simultaneous $\pi/2$ pulse protocol by always staying on the same side of the hyperfine crossing and parking ourselves at a special $\mathcal{E}_{\mathrm{rot}}$ during the $\pi/2$ pulse.

[12] The difference in g-factor for the upper and lower doublets are small for our discussion here, and are intentionally left out.

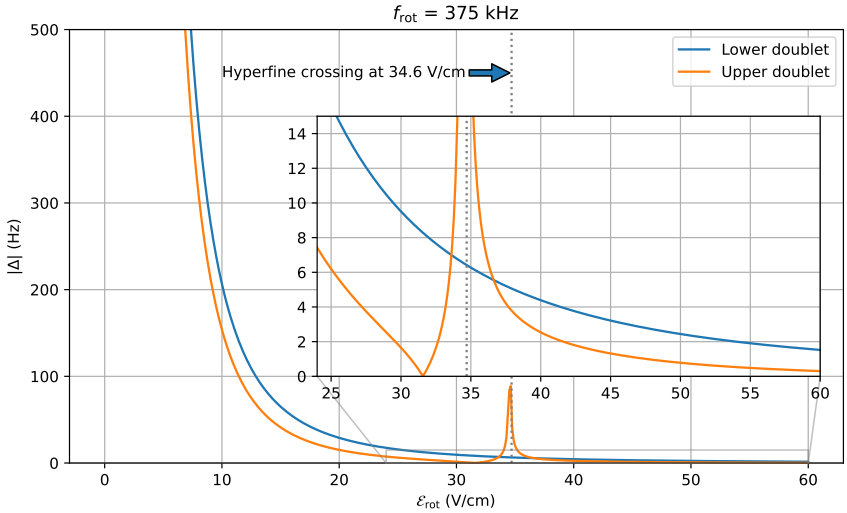

(a) HfF^+ with experiment parameters used in the second generation eEDM measurement.

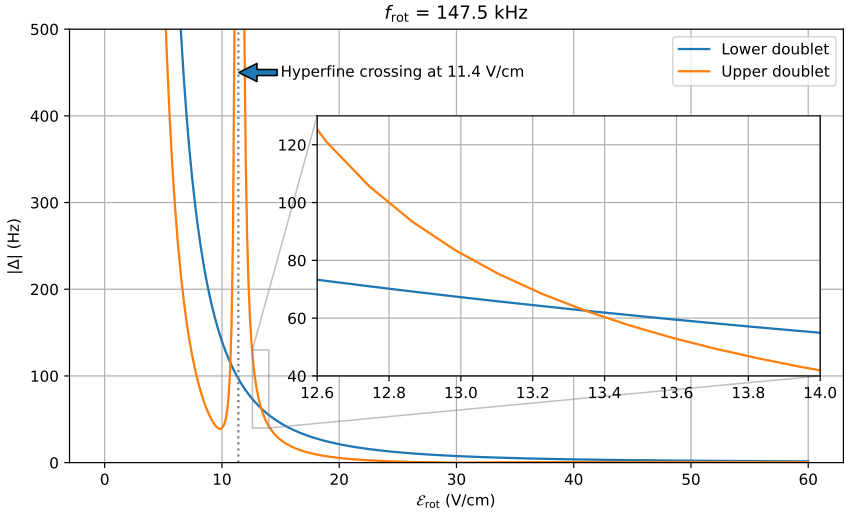

(b) ThF^+ with current experiment parameters.

Figure 4.21: **Plot of $|\Delta|$.** The plots are obtained by diagonalizing the 12-level Hamiltonian of the $X\,^3\Delta_1(v = 0, J = 1)$ manifold in the molecular frame (with zero magnetic field, and at various electric field $\mathcal{E}_{\text{rot}}$), and extracting the energy difference within the doublet for each of the upper and lower doublets. The Hamiltonian that we diagonalized is shown in Section C.2. After diagonalizing the Hamiltonian, we obtain eigenenergies like those shown in Figure 5.4. Δ^{u} would correspond to the energy difference between the states labeled [8] and [9] after the hyperfine crossing (or [6] and [7] before the hyperfine crossing). Δ^1 corresponds to the energy difference between the states labeled [0] and [1]. The part where Δ blows up corresponds to the hyperfine crossing, where the upper doublet crosses over the lower unstretched Zeeman states of the $F = 1/2$ manifold. Note that the hyperfine crossing occurs at a much higher $\mathcal{E}_{\text{rot}}$ in HfF^+ than in ThF^+ because of the much larger hyperfine coupling constant in the former (3 times). The differential Δ between the doublets is much larger in ThF^+ than in HfF^+ because of the much larger Ω-doubling constant in the former (7 times). Hard to see from this diagram is an interesting $\mathcal{E}_{\text{rot}} \approx 30$ V/cm for ThF^+ where $\Delta^{\text{u}} = 0$ Hz.

4.3.2.2 New protocol with the special $\mathcal{E}_{\text{rot}}$

It turns out that the values of Δs for both doublets cross at a special $\mathcal{E}_{\text{rot}}$ of about 13.35 V/cm in ThF^+ with $f_{\text{rot}} = 147.5$ kHz (see Figure 4.21b). It also turns out that 13.35 V/cm brings a few other benefits:

(1) It is sufficiently large for the molecules to retain their polarized orientations ($d_{\text{mf}}\mathcal{E}_{\text{rot}} \approx 23$ MHz $\gg$ $\omega_{\text{ef}} = 5.3$ MHz).

(2) It is sufficiently small as compared to 60 V/cm. We intend to have an $f_0 = 50$ Hz when we nominally operate at 60 V/cm, and since a magnetic field quadrupole-typed Zeeman induced f_0 scales linearly with $\mathcal{E}_{\text{rot}}$, f_0 will be reduced to about 10 Hz at 13.35 V/cm. This is small compared to $\Delta^{\text{u}}(\mathcal{E}_{\text{rot}} = 13.35 \text{ V/cm}) = \Delta^{\text{l}}(\mathcal{E}_{\text{rot}} = 13.35 \text{ V/cm}) \approx 65$ Hz, allowing us to perform Rabi flopping that goes almost from pole to pole on the Bloch sphere, retaining good contrast.

Hence, without needing to go through the hyperfine crossing, and with a $\pi/2$ pulse that is truly simultaneous for both the upper and lower doublets, the $\pi/2$ pulse protocol for ThF^+ is:

(1) Ramp $\mathcal{E}_{\text{rot}}$ down from 60 V/cm to 13.35 V/cm in 1.2 ms;

(2) Hold for 4.1 ms;

(3) Ramp $\mathcal{E}_{\text{rot}}$ back up to 60 V/cm in 1.2 ms.

We note that while we ramp $\mathcal{E}_{\text{rot}}$ down to 13.35 V/cm, Δ^{l} is always higher than Δ^{u}, and one might naïvely think that there would be an additional phase accumulated by the lower doublet than the upper doublet after the procedure. We propose two reasons not to worry. Firstly, it turns out that the ramp is fast enough that the extra phase accumulation is much less than 1% of a radian. Secondly, We could always compensate for the difference by parking at an $\mathcal{E}_{\text{rot}}$ that is slightly smaller than 13.35 V/cm. Regardless, the value for the special $\mathcal{E}_{\text{rot}}$ is something that can be scanned experimentally. In fact, as we shall see in Figure 4.23, we scanned for the special $\mathcal{E}_{\text{rot}}$, and found it to be about 13.7 V/cm. We believe the discrepancy with 13.35 V/cm comes from a combination of COMSOL simulation precision (to convert applied voltage on the

electrodes to electric field strength along the trap axis) and imperfections in the experiment setup. This discrepancy is also consistent with our estimated error of d_{mf} (see Table 4.1).

It is also interesting to note that the value of the special $\mathcal{E}_{\mathrm{rot}}$ varies very slowly with f_{rot} within our usual operating range between 147.5 kHz and 400 kHz. Figure 4.22 shows a plot of the special $\mathcal{E}_{\mathrm{rot}}$ vs f_{rot}.

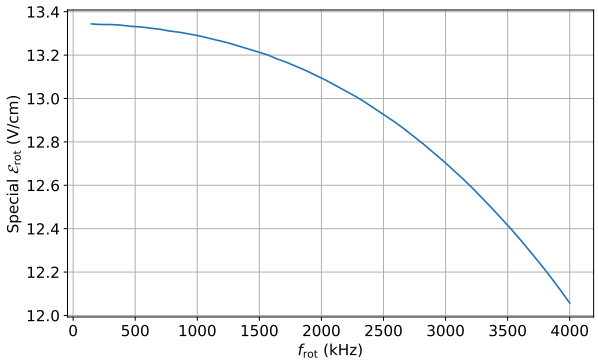

Figure 4.22: **Plot of the special $\mathcal{E}_{\mathrm{rot}}$ vs f_{rot}.** As f_{rot} increases, $\Delta^{\mathrm{u,l}}$ increase as $\sim f_{\mathrm{rot}}^3$. Hence the value of the special $\mathcal{E}_{\mathrm{rot}}$ changes very little, until f_{rot} is starting to be comparable to the hyperfine splitting ($\approx$ 15 MHz).

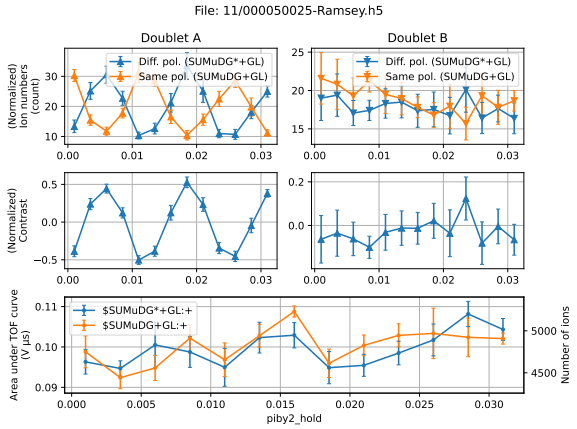

(a) $\mathcal{E}_{\text{rot}} = 12.6$ V/cm.

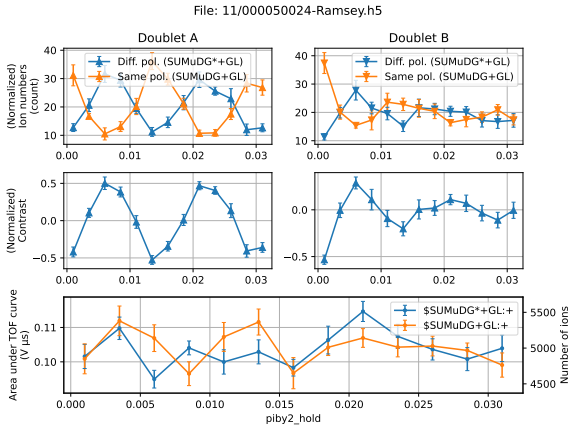

(b) $\mathcal{E}_{\text{rot}} = 13.35$ V/cm.

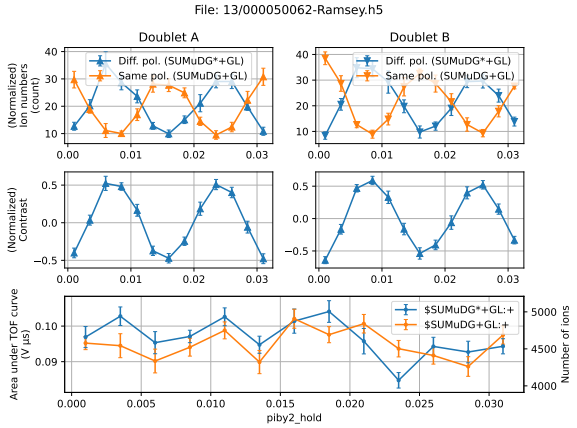

(c) $\mathcal{E}_{\text{rot}} = 13.7$ V/cm.

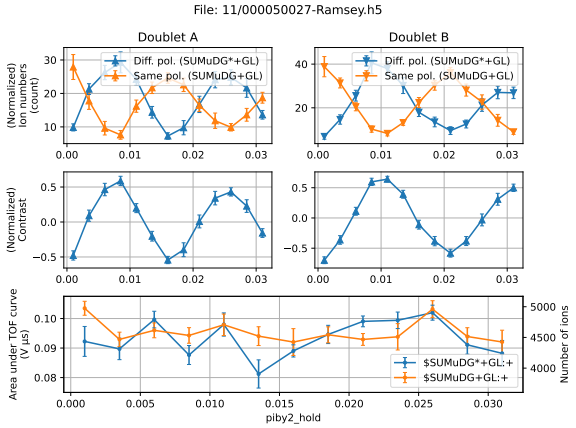

(d) $\mathcal{E}_{\text{rot}} = 14.0$ V/cm.

Figure 4.23: **Rabi flopping of both doublets at various $\mathcal{E}_{\text{rot}}$.** The top row in each subfigure corresponds to the measured Th^+ ion numbers. The second row corresponds to the contrast, which is the difference of the measured numbers of the two chops, divided by the sum. The last row corresponds to the total ThF^+ numbers detected, for normalization. The numbers in each doublet are extracted by using angular resolved photofragments as demonstrated in Figures 3.8 and 3.9. In this set of runs, Doublet A (B) corresponds to the ions in the lower (upper) doublet. From our model, and assuming that $\mathcal{E}_{\text{rot}}$ in the trap is what we believe it is, we expect both doublets to have the same Rabi frequency at $\mathcal{E}_{\text{rot}} = 13.35$ V/cm (see Figure 4.21b). However, (b) shows that the upper doublet is decohering very quickly, and is at a slightly higher frequency than the lower doublet. This is probably because $\mathcal{E}_{\text{rot}}$ is slightly closer to the hyperfine crossing than the special $\mathcal{E}_{\text{rot}}$ point, causing us to loss ions from the upper doublet into the unstretched Zeeman states at the hyperfine crossing. Going to a lower $\mathcal{E}_{\text{rot}} = 12.6$ V/cm gives a higher lower doublet Rabi frequency (as expected, see Figure 4.21b), and a totally decohered Rabi flopping for the upper doublet as it gets even closer to the hyperfine crossing. Going to a higher $\mathcal{E}_{\text{rot}} = 14.0$ V/cm makes the Rabi frequency for both doublets go down as expected. The sweet spot happens to be around $\mathcal{E}_{\text{rot}} = 13.7$ V/cm.

4.3.3 Summary

The experiment sequence in the baby Bucket Brigade (see Figure 7.9) is summarized in Figure 4.24.

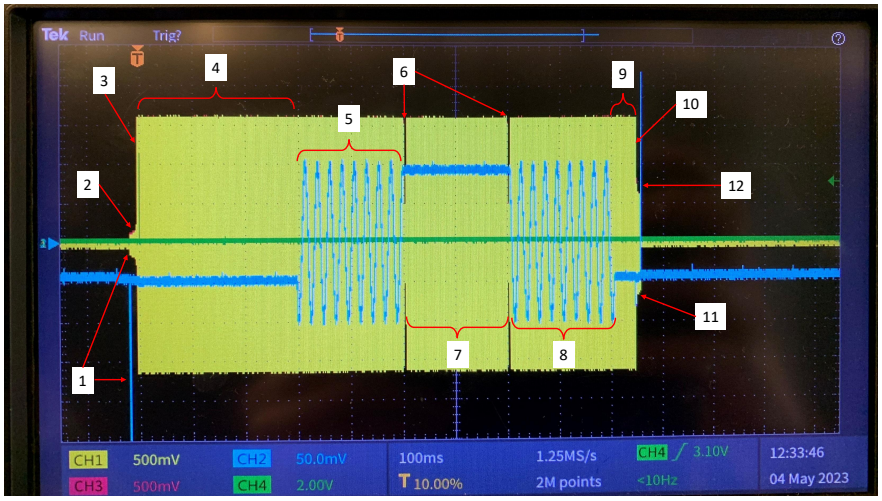

Figure 4.24: **Summary of experiment sequence.** The channels 1 (yellow) and 2 (cyan) correspond to pickup voltages on Rod 8 (radial electrode) and the Southeast Quadrant Ring ("end cap") (see Figure 7.9). (0, not shown on the scope trace) We pulse the nozzle and fire the ablation laser to create neutral ThF entrained in supersonic expansion beam of neon buffer gas at room temperature (ultimate flow speed of about 800 m/s). The steps are detailed in the main text. Also compare with Figure 7.9.

(1) We turn on the radial trap, fire the REMPI lasers to ionize the neutral ThF into the ThF^+ $X\,^3\Delta_1(v = 0)$ manifold, and apply a stopping voltage to stop the ions into a trap with secular frequencies of about 2 kHz in all directions.

(2) We move the ions to the center of the trap, while turning the radial trapping frequency up to about 4 kHz from 2 kHz.

(3) We ramp up $\mathcal{E}_{\text{rot}}$ from zero to 60 V/cm.

(4) State preparation for 300 ms, where we send in all the state preparation lasers and microwaves to prepare the ions in the $X\,^3\Delta_1(v = 0, J = 1, F = 3/2, m_F = 3/2)$ states.

(5) We translate our ions into the Science region by modulating the potentials on the Rings (see Figure 7.9).

(6) We apply our $\pi/2$ pulse to prepare our ions in a superposition of the $X\,^3\Delta_1(v = 0, J = 1, F = 3/2, m_F = 3/2)$ and $X\,^3\Delta_1(v = 0, J = 1, F = 3/2, m_F = -3/2)$ states by ramping down our $\mathcal{E}_{\text{rot}}$ to 13.7 V/cm with the protocol mentioned in Section 4.3.2.2.

(7) Ramsey free evolution time, followed by another $\pi/2$ pulse labelled by (6) to map the phase difference between the states into a population difference.

(8) We translate our ions out from the Science region back into the Octagon (see Figure 7.9).

(9) State detection at 40 ms, where we send in the lasers (and microwaves) to transfer population from either the $m_F = 3/2$ of $m_F = -3/2$ states to states outside the $J = 1$ manifold.

(10) We ramp $\mathcal{E}_{\text{rot}}$ down to 20 V/cm to retain the polarization of our molecule, but to ensure that $\mathcal{E}_{\text{rot}}$ is small enough that the ions to do not miss the ion detector because of their huge transverse rotation micromotion speeds.

(11) We ramp the radial trapping frequency back to about 2 kHz, and move the ions to overlap with the REMPD lasers.

(12) We fire our REMPD lasers and kick our ions out of the trap towards our ion detector.

Chapter 5

Interlude

5.1 Revisiting wisdom lost in time

Before we get too excited with our newfound tools using ThF^+, it serves to revisit some JILA eEDM wisdom that have been either (i) lost in time, or (ii) taken for granted. We shall see if the wisdom (mostly built upon HfF^+) still holds for ThF^+. This section does not aim to shed any new insight on top of the ancient wisdom, and mainly serves as a quantum repeater or a buffer op-amp for wisdom from previous generations to remind the younger students in the group why we chose to use ThF^+ the way it is being used now. As an exercise, we shall also explore the feasibility of a new proposal on how to measure the eEDM with ThF^+ from the Hutzler group [29].

5.1.1 Wisdom up till now

The whole state preparation and detection scheme in ThF^+ has been built around performing the eEDM experiment on the ${}^3\Delta_1(v=0, J=1, F=3/2, m_F=\pm 3/2)$ states. We shall now revisit the wisdom behind the choice for each of the quantum numbers.

5.1.1.1 Using the ${}^3\Delta_1$ state

The ${}^3\Delta_1$ electronic state is wonderful for an eEDM measurement for a few reasons. Summarizing the points in Ref. [25], we have:

Ω-doubling. The ${}^3\Delta_1$ electronic state has an Ω doublet structure with a very relatively small energy gap between the parity doublets. This allows the molecule to be polarized very easily with very modest

electric fields as compared to atoms. A high degree of polarization allows the ensemble of molecules in our ion cloud to sing in unison like in a choir, instead of cancelling each other's effects like in a canteen. We borrowed this idea liberally from Prof. David DeMille's PbO experiment [61].

$|\Omega| = 1$: small g factor. With an $|\Omega| = 1$ structure and a $|\Lambda| = 2$ in a $^3\Delta_1$ state, the projections of the spin and angular momentum of the electron onto the internuclear axis are anti-parallel, i.e. $\mathbf{L}\cdot\hat{n} =: \Lambda = \pm 2$ when $\mathbf{S}\cdot\hat{n} =: \Sigma = \mp 1$. Given that the g-factor for the spin of the electron is quite nearly two times that of its orbital angular momentum, the net g-factor of the $^3\Delta_1$ state can be highly reduced. The reduced g-factor makes us less susceptible to drifts in external magnetic fields, reducing systematic effects in our system.

Co-magnetometry. Having two doublets (from the Ω doublet structure) with very similar sensitivities to external fields, but sensitivities of opposite sign to the physics that we are probing allows us to perform co-magnetometry to have excellent rejection of many systematic effects.

5.1.1.2 Using the $(v = 0, J = 1)$ state

Within the $^3\Delta_1$ electronic state, we use the $v = 0$ vibrational manifold because it is the ground vibronic state, where the state lifetime is not limited to any form of spontaneous decay to lower energy levels. Within the $v = 0$ vibrational manifold, we use the $J = 1$ rotational manifold because this is the manifold which has the lowest multiplicities, making quantum control much easier.

Furthermore, much in the spirit of Figure 3.2, since we are in the $^3\Delta_1$ electronic state with $|\Omega| = 1$, we want to be in the $J = |\Omega| = 1$ rotational manifold for the electron spin to be most aligned with the internuclear axis to have the best sensitivity to the eEDM.

5.1.1.3 Using the stretched Zeeman state ($m_F = \pm 3/2$)

Within the $^3\Delta_1(v = 0, J = 1)$ rovibronic manifold, we choose to use the stretched Zeeman states because the eEDM is sensitive to the electron spin. The electron spin is fully aligned with the projection of the net angular momentum onto the internuclear axis in the stretched Zeeman states ($|F = 3/2, m_F =$

$\pm 3/2\rangle = |F = 3/2; m_J = \pm 1(\Sigma = \mp 1, \Lambda = \pm 2), m_I = \pm 1/2\rangle)$, whereas the unstretched Zeeman states come with a superposition of electron spin projections onto the internuclear axis (e.g. $|F = 3/2, m_F = 1/2\rangle = \frac{1}{\sqrt{3}}|F = 3/2; m_J = 1, m_I = -1/2\rangle + \sqrt{\frac{2}{3}}|F = 3/2; m_J = 0, m_I = 1/2\rangle)$. Therefore, using the stretched Zeeman states gives us the best sensitivity to the eEDM.

5.1.2 Other exotic ways

In light of proposals to perform eEDM measurements in unconventional ways (but still using diatomic molecules) [28, 29, 34], one wonders if we could win by breaking ourselves free from tradition.[1] In fact, Ref. [29] proposes to perform an eEDM measurement in ThF^+ by using a first-order electric field-insensitive transition at a magic[2] electric field strength. The physics behind this protocol is that as we increase the electric field strength, we go from the "quadratic Stark regime" where F is a relatively good quantum number to the linear Stark regime where F is no longer a good quantum number, but m_F still is. This results in non-trivial shifts in energy levels within the molecule, which can result in transition energies between states to have a zero first-order gradient w.r.t. the field strength. This is much like the magic trapping wavelength concept for trapping neutral atoms [62] or magic magnetic fields for first-order field-insensitive qubit transitions [63].

The proposal from Ref. [29] involves a transition between a $(J = 1, m_F = 1/2)$ and a $(J = 2, m_F = 1/2)$ state at an electric field strength of 18.6 V/cm. Figure 5.1 shows a plot of transition frequencies as a function of applied electric field. We shall attempt to analyze the proposal from Ref. [29], and see how it can or cannot apply to our experiment.

[1] Also known as peer pressure from people who are no longer around.

[2] Although not yet officially defined in textbooks, the author notes that "magic" is now a technical term in AMO physics with a specific meaning: (*adj.*) used in AMO physics to refer to a specific value of an experiment parameter that allows the system to be insensitive to changes in that experiment parameter; e.g. "magic wavelength" [62].

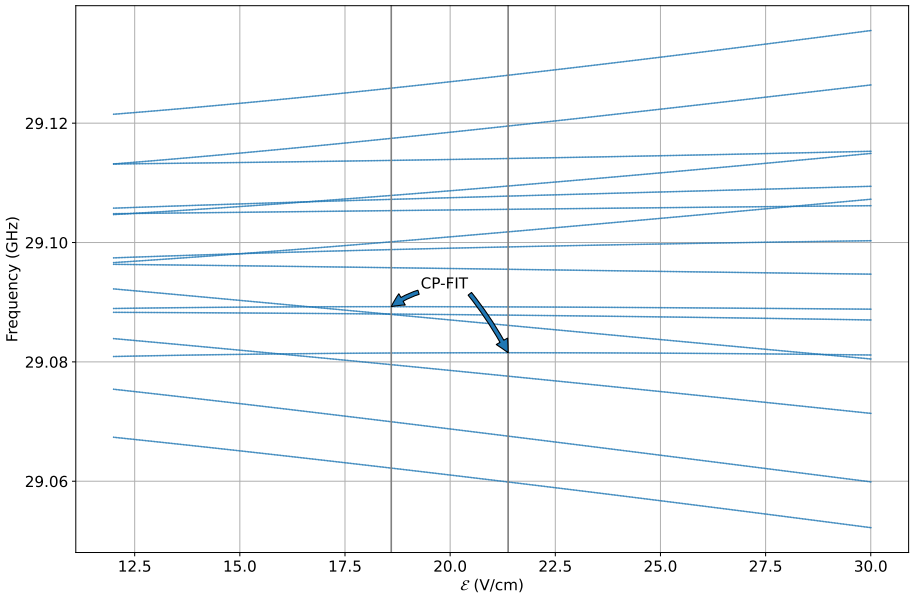

(a) All transitions.

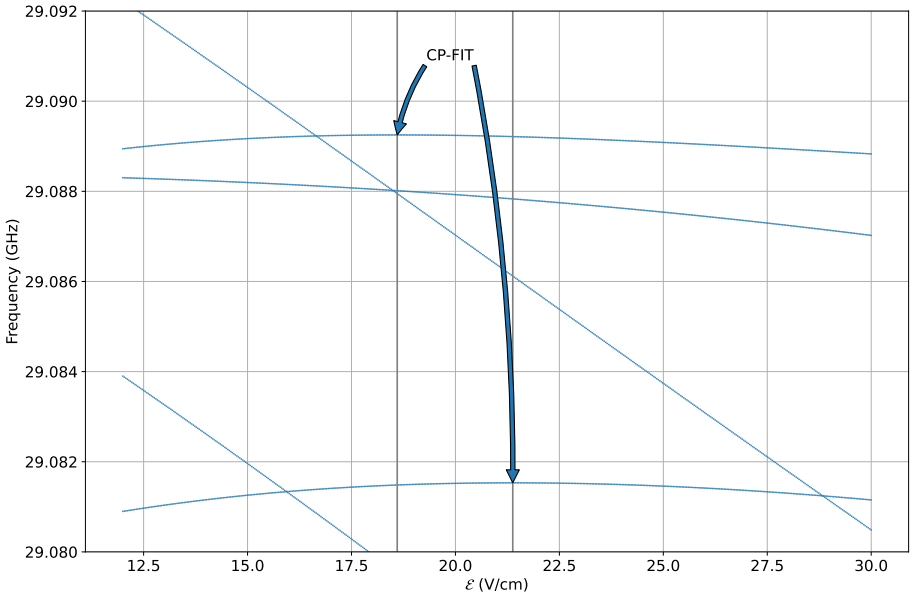

(b) Zoomed in for better view of the curvature.

Figure 5.1: **Transition frequencies of all transitions connecting the** $(J = 1, m_F = \pm 1/2)$ **states to the** $(J = 2, m_F = \pm 1/2)$ **states.** CP-FIT stands for CPV-sensitive field-insensitive transitions, as defined in Ref. [29]. These plots are obtained in a similar way as Figure 4.5, but only showing the $m_F = \pm 1/2$ transitions, and plotting the lines with the same intensities instead of being weighted by transition strength. The CP-FIT are transitions that are insensitive to the applied electric field to first order, and they show up as transition energies with zero gradients on the plots. The rotating frequency f_{rot} is set to zero in these plots. The vertical lines indicate 18.6 V/cm and 21.3 V/cm, where the CP-FITs are. The lines for the CP-FITs look flat on this scale (2 MHz per small division in the zoomed in plot), but if there is a 1% deviation in $\mathcal{E}$, it would correspond to a 200 Hz deviation on the CP-FIT frequencies.

5.1.2.1 Co-magnetometry

In our eEDM experiment, there are four states involved (see Figure 5.2). We tend to measure the

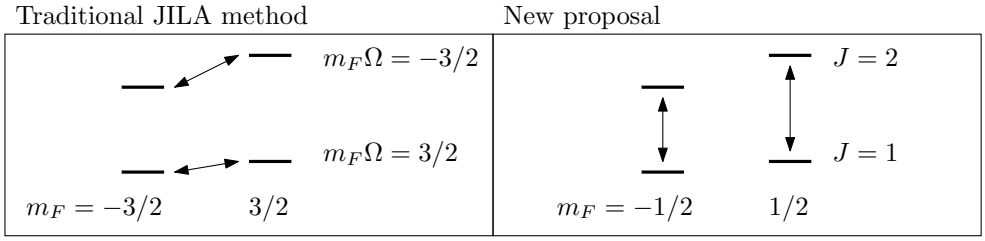

Figure 5.2: **The four states used in a typical eEDM experiment with co-magnetometry.** In our traditional JILA method, we measure the frequencies of the upper and lower Stark doublets. Ramsey spectroscopy is performed "horizontally" across the doublets. The energy difference of the upper (lower) Stark doublet is $E_{\text{Zeeman}} + E_{\text{EDM}}$ ($E_{\text{Zeeman}} - E_{\text{EDM}}$). Taking the difference in energies between the doublets reveals E_{EDM}. In the new proposal from Ref. [29], Ramsey spectroscopy will be performed "vertically" across the rotational states. The energy difference of the $m_F = 1/2$ ($m_F = -1/2$) pair is $E_{\text{mol. rot.}} E_{\text{Stark}} + E_{\text{EDM}}$ ($E_{\text{mol. rot.}} E_{\text{Stark}} - E_{\text{EDM}}$). Taking the difference in energies between the two m_F pairs reveals E_{EDM}.

frequency within each Stark doublet, and perform co-magnetometry across the Stark doublets. The new proposal changes it to measuring the frequency within each m_F manifold, and performing checks on systematics by comparing the frequencies measured for the different m_F. This is a paradigm shift, but it certainly sounds like we could do this with our current setup.

5.1.2.2 Ramsey frequency

Our Ramsey frequencies have been on the order of $f \sim 100$ Hz. In the third generation experiment, we are also aiming for 50 Hz. In contrast, the new proposal is looking at a Ramsey frequency of about 29 GHz. This is huge. To perform a Ramsey experiment on this transition, and aiming for a precision on the order of 1 mHz, we would need to have a stable microwave source down to a part in 3×10^{13}. This sounds challenging, but not entirely impossible.

5.1.2.3 State preparation

Our current state preparation protocol involves (i) creating our ions in the ground vibronic state of ThF^+, (ii) using lasers and microwaves to move our ion population to $X\,^3\Delta_1(v = 0, J = 1, F = 3/2, m_F =$

3/2), and (iii) performing a $\pi/2$ pulse by ramping $\mathcal{E}_{\text{rot}}$ down to prepare a superposition of the $m_F = 3/2$ and $m_F = -3/2$ states for Ramsey spectroscopy.

The new proposal involves preparing ions in the $m_F = 1/2$ states. In our setup, this would probably mean that we will need to prepare our ions in the $X\,^3\Delta_1(v = 0, J = 1, F = 3/2, m_F = 3/2)$ states first like what we have been doing, and then performing a coherent transfer to the $X\,^3\Delta_1(v = 0, J = 1, F = 3/2, m_F = 1/2)$ state, probably through stimulated Raman adiabatic passage (STIRAP). One would need to find a good intermediate state to use for STIRAP, or some form of adiabatic rapid passage scheme that would allow for such a population transfer. Unfortunately, our current setup (and our future Bucket Brigade setup, see Section 5.3) only allows lasers and microwaves to come in along the plane of the rotating polarizing electric field. This means that our lasers and microwaves can only be $\sigma^{\pm}$ or x polarized, not π. This would certainly limit schemes available to us, for example, a naïve two-photon process to move population from $m_F = 3/2$ to $m_F = 1/2$ would involve a σ^- and a π photon, but this cannot be done with our current setup.

Furthermore, the new proposal does not take into account that we need to work in a rotating frame to polarize our molecular ions with a rotating electric field without ejecting them out of the trap. There will be strong rotational coupling between the $m_F = \pm 1/2$ states on the order of a few 100 kHz. We can apply a magnetic field to offset the states through Zeeman shifts. This requires an axial magnetic field gradient of about 100 G/cm (about 30000 times of what we are applying now). This is getting tricky.

The new proposal also requires a different type of $\pi/2$ pulse. We would probably need to address the $(J = 1, m_F = 1/2) \rightarrow (J = 2, m_F = 1/2)$ transition directly with π-polarized microwaves. These microwaves will have to come in along the trap axis (perpendicular to the plane of the rotating polarizing electric field $\mathcal{E}_{\text{rot}}$, and they either have to be pulsed, or they can be circularly polarized, but we would need an f_{rot} of 29 GHz[3] . This sounds hard.

An alternative to the π-polarized microwaves is to use a two-photon Raman process, using photons of opposite helicities[4] . We would need to do some spectroscopy to make this happen.

[3] This would introduce additional complications because f_{rot} is now much larger than typical energy scales within the $J = 1$ manifold.

[4] We could use two photons with π-polarization, but as mentioned earlier on, our current setup (and the Bucket Brigade) does not allow us to address our ions with π-polarized lasers or microwaves.

5.1.2.4 What about the $m_F = \pm 3/2$ manifold?

Ref [29] calculated the case for $m_F = 1/2$, but what about $m_F = 3/2$? It would save us one step in the state preparation of moving our ions coherently into the $m_F = 1/2$ state, and it would also relieve us of the rotational coupling problem between $m_F = \pm 1/2$ states. It turns out that such a CP-FIT for the $m_F = \pm 3/2$ manifold does not exist for ThF^+ because of the relative sizes of the hyperfine splitting constant and the Ω doubling coupling constant.

The proposed scheme relies on the fact that the Stark shifts move in the direction determined by the sign of $m_F\Omega$, and that the hyperfine splitting is large compared to the Ω-doublet splitting. In this regime (hyperfine splitting more than Ω-doublet splitting, the lower Ω doublet of the more energetic hyperfine manifold will be Stark shifted down in energy, while the upper Ω doublet of the less energetic hyperfine manifold will be Stark shifted up, and if they have the same m_F, they will try to repel each other through an avoided crossing, resulting in non-trivial energy shifts (see Figure 5.3).

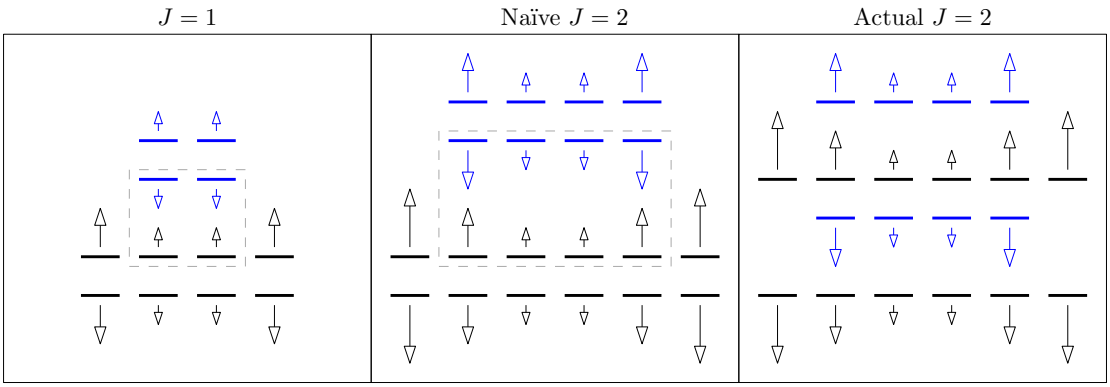

Figure 5.3: **States bumping into each other through Stark shifts.** The horizontal lines indicate Zeeman levels. Energy levels colored blue belong to one hyperfine manifold, and those colored black belong to another. The arrows indicate the Stark shifts ($E_{\text{Stark}} \sim m_F\Omega$) when an electric field is applied. In the $J = 1$ manifold, the $m_F = \pm 1/2$ states from one hyperfine manifold will come close to those from the other manifold, and there will be a strong interaction between the states, resulting in non-trivial energy shifts for these states. The same is the case for the naïve $J = 2$ manifold. It is called "naïve" because we naïvely assume that the energy levels are ordered like the $J = 1$ manifold, i.e. the hyperfine splitting is large compared to the Ω-doubling constant. This is true for HfF^+, but it is not true for ThF^+. For ThF^+, the hyperfine splitting is comparable to the Ω-doubling splitting in $J = 2$, resulting in an energy ordering of the states as shown in the right panel. In this ordering of states, Stark shifts do not cause states to bump into each other, giving rise to more trivial energy shifts of the states. A combination of the physics behind the left and the right panels allow for first-order field-insensitive transitions between the $J = 1$ and $J = 2$ in the $m_F = \pm 1/2$ states but not the $m_F = \pm 3/2$ states in ThF^+.

In ThF^+, the states in the $J = 1$ manifold are arranged such that the Ω-doubling is still a finer structure than the hyperfine splitting, but Ω-doubling and hyperfine splitting are of the same sizes for the states in the $J = 2$. There are no states to repel the $m_F = 3/2$ states in the $J = 1$ because there is only one pair of $m_F = 3/2$ states. There are two pairs of $m_F = 3/2$ states in the $J = 2$ (each pair corresponding to the $F = 3/2, 5/2$ hyperfine manifolds), but they do not repel each other head on through Stark shifts.

In contrast, the $m_F = 1/2$ scheme works for ThF^+ because the $m_F = 1/2$ states in the $J = 1$ bump into each other through Stark shifts. In general, it seems like for the scheme proposed in Ref. [29], we would require the hyperfine splitting to be large compared to the parity doublet splitting (e.g. Ω- or Λ-doubling for diatomic molecules, Coriolis interactions for polyatomic molecules).

5.1.2.5 Sensitivity to the eEDM

At 18.6 V/cm, the molecule is neither fully polarized in the $J = 1$ nor the $J = 2$ manifold. Hence the eigenstates will not be expected to have $|\langle\Omega\rangle| = 1$, but it would be some number less than that. In fact, the states involved for the 18.6 V/cm CP-FIT are:

$$\sqrt{0.67}\left|J=1,\Omega=1,F=\frac{1}{2},m_F=\frac{1}{2}\right\rangle - \sqrt{0.23}\left|1,1,\frac{3}{2},\frac{1}{2}\right\rangle + \sqrt{0.1}\left|1,-1,\frac{3}{2},\frac{1}{2}\right\rangle$$

$$\Updownarrow$$

$$\sqrt{0.61}\left|2,1,\frac{3}{2},\frac{1}{2}\right\rangle + \sqrt{0.01}\left|2,1,\frac{5}{2},\frac{1}{2}\right\rangle - \sqrt{0.31}\left|2,-1,\frac{3}{2},\frac{1}{2}\right\rangle + \sqrt{0.07}\left|2,-1,\frac{5}{2},\frac{1}{2}\right\rangle.$$

This means that the transition is between a state of $\langle\Omega\rangle = 0.8$ and $\langle\Omega\rangle = 0.24$, in contrast to the traditional JILA method that probes the transition between a state of $\langle\Omega\rangle = 1$ and $\langle\Omega\rangle = -1$. Therefore, our statistical sensitivity to the eEDM will be reduced to 28% if we wish to use the CP-FIT to give us first-order field-insensitive transitions.

Alas, it is not immediately clear if there is a sure win with the new proposal, given the various complications that come with it. It also seems like it would require a lot of work to realize this new proposal given where we currently are at. We can now go back humbled to performing an eEDM experiment with ThF^+ the JILA style.

5.2 Feasibility of using ThF^+ in an eEDM measurement

Things look promising for using ThF^+ in an eEDM experiment. We know how to create ions (Chapter 2). We learnt how to perform quantum control, and we have also have a good protocol for performing a Ramsey experiment (Chapter 4). We know how to perform state readout (Chapter 3). Now we can ask the question of whether we actually win by using ThF^+.

Since the first two generations of the JILA EDM experiment showed that HfF^+ is a good molecule to use, we shall discuss the feasibility of using ThF^+ by comparing it to HfF^+. Table 5.1 shows a simple comparison of the spectroscopic constants and other relevant parameters of ThF^+ and HfF^+.

Parameters	ThF^+	HfF^+
Mass (u)	251	199
$A_{\|\|}$ (MHz)	$-2\pi \times 20.1$	$-2\pi \times 62.2$
ω_{ef} (MHz)	$2\pi \times 5.29$	$2\pi \times 0.740$
d_{mf} (MHz/(V/cm))	$2\pi \times 1.70$	$2\pi \times 1.80$
$\|g_F\|$	0.0149	0.003
$\mathcal{E}_{\mathrm{eff}}$ (GV/cm)	35 [22, 41]	23 [24, 25]

Table 5.1: **Comparison of parameters of ThF^+ and HfF^+.** Uncertainties are not included in this table for brevity.

From Table 5.1, we can draw a few inferences:

(1) The combination of the smaller hyperfine splitting constant ($A_{||}$) and bigger Ω-doubling constant (ω_{ef}) in ThF^+ than HfF^+ has a few consequences (refer to Figure 5.4):

   (a) Since the Ω-doubling splitting constant is bigger in ThF^+, we expect $\Delta^{\mathrm{u/l}}$ to be bigger in ThF^+ than HfF^+ at similar strengths of $\mathcal{E}_{\mathrm{rot}}$.

   (b) The hyperfine states cross each other at a much smaller $\mathcal{E}_{\mathrm{rot}}$ in ThF^+ (11.4 V/cm) than HfF^+ (34.6 V/cm).

(2) Since the masses and molecular electric dipole moment are similar across the two species, we expect to be applying electric field strengths to ThF^+ that are similar to those used in the first two generations of the experiment. Hence, we do not expect significant changes to the technology surrounding the circuitry involved in generating electric fields.

(3) ThF^+ is much more susceptible to magnetic field noise than HfF^+ because of the much larger g-factor. This could mean that we may need some sort of magnetic shielding in the third generation experiment, e.g. the use of μ-metal.

(4) The effective electric field ($\mathcal{E}_{\text{eff}}$) in ThF^+ is only about 1.5 times that of HfF^+. Given conservative experimental parameters shown in Table 5.2, we see that swapping out HfF^+ for ThF^+ in the setup of the Gen. II experiment does not let us win in terms of the eEDM sensitivity.

Parameters	ThF^+	HfF^+ (Gen. II)
τ (s)	20	2
N_{single}	$50^\dagger$	500
$f_{\text{rep.}}$ (Hz)	0.05	0.5
$T_{\text{tot.}}$ (hours)	100	100
δd_e (e cm)	4.4×10^{-30}	6.7×10^{-30}

Table 5.2: **Naïve expected statistical sensitivity for ThF^+.** The value of δd_e for ThF^+ is extrapolated from that of HfF^+ using Equation 1.1. The actual sensitivity achieved in the Gen. II experiment [35, 36] is slightly better than the numbers shown here, but the numbers chosen here are easier numbers for easy comparison. †We have demonstrated having 5 dissociated Th^+ ions on the side of our Ramsey fringe (see, for instance, Figure 4.9a). This corresponds to a dissociation efficiency of only 2%, as compared to at least 20% in the Gen. II experiment. The dissociation efficiency is currently limited by the choice of the intermediate state in our REMPD scheme (see Section 3.4.2). We remain optimistic that a more suitable choice of the intermediate state for the REMPD scheme can bring our dissociation efficiency of ThF^+ to be on par with HfF^+ in Gen. II.

At this point, it may seem that ThF^+ is not that much more advantageous than HfF^+ in terms of eEDM statistical sensitivity despite the much longer coherence time in ThF^+. In fact, the long coherence times limits the repetition rate of the experiment, since the experiment can only be repeated once every 20 s. To get around this, we can multiplex the experiment such that the repetition rate is not limited by the coherence time that we are trying to probe. With this, we shall introduce the *Bucket Brigade*.

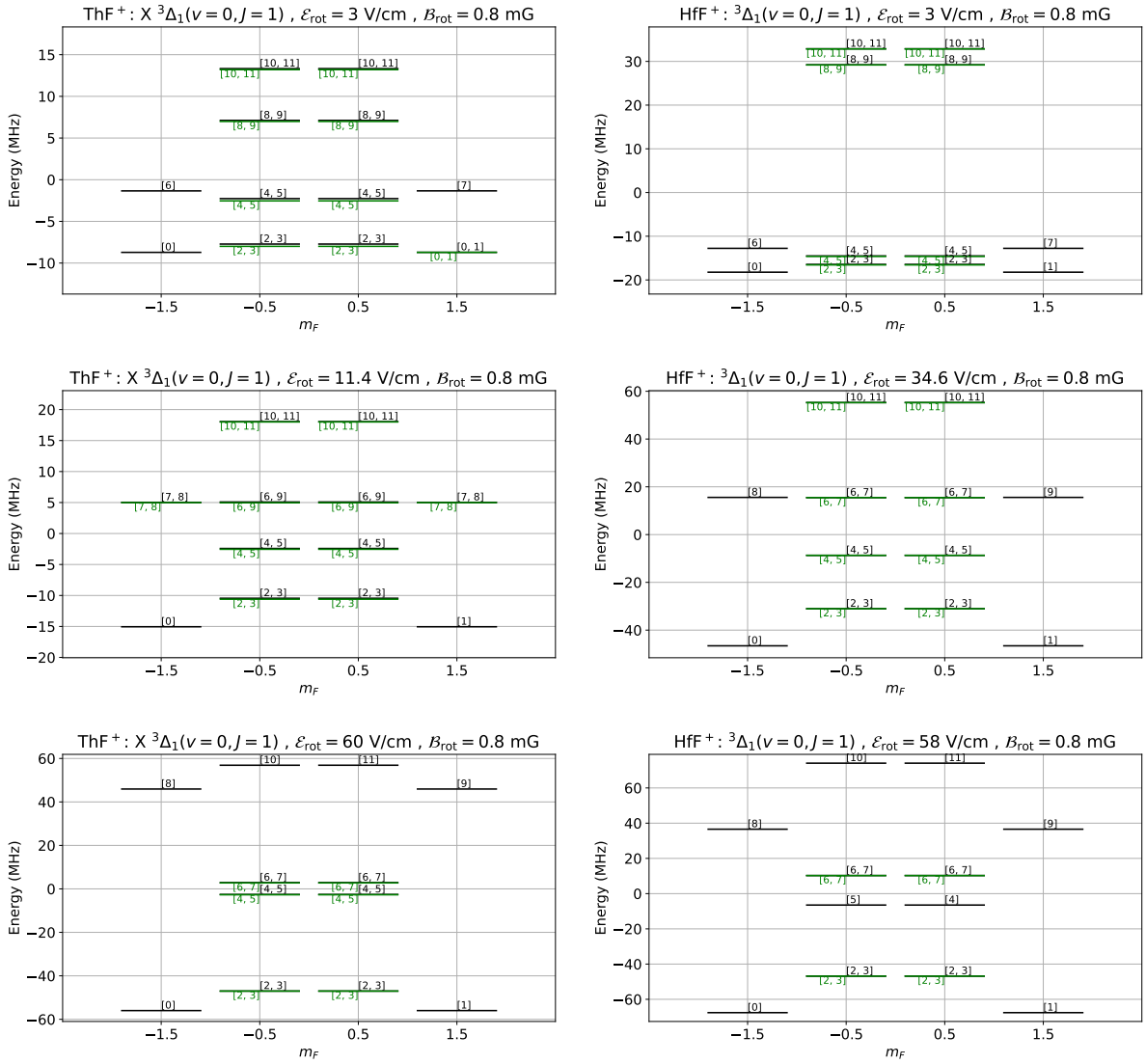

Figure 5.4: **Comparisons of energy levels between ThF$^+$ and HfF$^+$.** The left (right) column corresponds to plots for ThF$^+$ (HfF$^+$). The first row consists of plots of the energy levels in the $X\,^3\Delta_1(v = 0, J = 1)$ manifold at low $\mathcal{E}_{\rm rot}$ to show the differences in the energy structure across both species. Like in Figure 4.7, the basis states are labelled by their most dominant eigenstate in ascending order of eigenenergies. For the unstretched Zeeman states, rotational coupling breaks the degeneracy between the $m_F = 1/2$ and $m_F = -1/2$ states, and the energy levels are indicated by the black and green lines for the two superposition states. The second row shows the energy levels at hyperfine crossing. The third row shows the energy levels at at the nominal electric field strength where we perform our Ramsey evolution. The states are labeled with numbers from the least to the most energetic.

5.3 Bucket Brigade

The main idea behind the Bucket Brigade is multiplexing. The Bucket Brigade is a first-in-first-out conveyor belt of ion traps, each containing its own ion cloud. The conveyor belt is continuously loaded from the left, all the traps move together from left to right, and the ion clouds are removed from the Bucket Brigade on the right. A schematic diagram of the Bucket Brigade is shown in Figure 5.5.

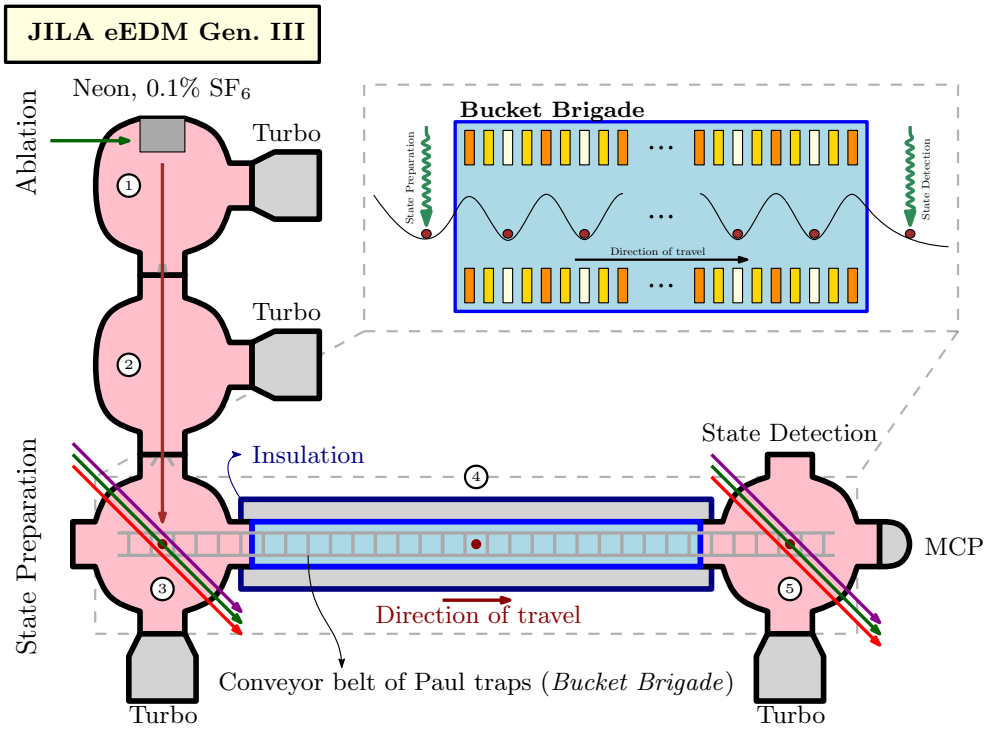

Figure 5.5: **Schematic diagram of the Bucket Brigade.** Our molecules go through five main vacuum chambers for an eEDM measurement. (1) We create a plume of neutral ThF by ablating a piece of metallic thorium, and reacting it with SF_6. The neutral plume of ThF is entrained in a supersonic expansion beam of neon. (2) The molecular beam goes through a differential pumping chamber. (3) The neutral ThF molecules are ionized with REMPI lasers and loaded into the first bucket in the Bucket Brigade. We would then perform state preparation and the first $\pi/2$ pulse of the Ramsey sequence on the ThF^+ ions. (4) Once the state preparation is completed, the ions will be ushered along the Bucket Brigade into the cryogenic area, where the ions perform Ramsey free evolution in a field-free region. While this is happening, steps (1-3) are cycled uninterrupted, i.e. new batches of ions are being prepared in the first bucket and ushered into the Bucket Brigade. (5) Once the ions exit the cryogenic area, we perform our state detection on the ions. The inset on the top right shows how the ushering is done: time-varying potentials will be applied to the ring electrodes (colors indicate magnitude of the potentials applied) to provide trapping forces along the axial direction (potential wells) that move from left to right. Not shown in the inset are the rods that run axially to provide radial confinement through RF-potentials. In the first two generations of the JILA eEDM experiment, steps (3-5) happen at the same place, i.e. that of step (3). Note that the Ramsey evolution happens concurrently for all the buckets, but they do not all begin and end at the same time.

With the multiplexing capabilities of the Bucket Brigade at a conservative repetition rate of about 2 Hz (limited by our state preparation sequence), the value of the eEDM sensitivity in Table 5.2 is then updated to that of Table 5.3.

Parameters	ThF^+	HfF^+ (Gen. II)
$\mathcal{E}_{\text{eff}}$ (GV/cm)	35 [22, 41]	23 [24, 25]
τ (s)	20	2
N_{single}	50	500
$f_{\text{rep.}}$ (Hz)	2	0.5
$T_{\text{tot.}}$ (hours)	100	100
δd_e (e cm)	7.0×10^{-31}	6.7×10^{-30}

Table 5.3: **Expected statistical sensitivity for ThF^+ in the Bucket Brigade.** The value for δd_e is extrapolated from that of HfF^+ using Equation 1.1.

At a repetition rate of 2 Hz and interrogation time of 20 s, the total number of buckets required to run the multiplexed experiment concurrently is 2 Hz $\times$ 20 s = 40. For a nominal bucket length of 8 cm (with hindsight from Chapter 7), this means a total length for the Bucket Brigade at slightly more than 3 m, which is still a reasonably sized table top experiment.

The value shown in Table 5.3 promises an order of magnitude improvement over Gen. II. As Prof. Holger Müller often says, and I paraphrase, "sometimes when you measure something an order of magnitude further, you can make an important discovery." This order of magnitude improvement that the Bucket Brigade and ThF^+ promises us is precious. The next few chapters will be dedicated to the design of the Bucket Brigade. To understand what levels of field homogeneity are involved in the design, we first begin by studying the ion cloud dynamics to understand (i) the ion cloud sizes, and (ii) collision rates that could lead to heating, decoherence from ion-ion collisions, or even suppressing decoherence due to spatial field inhomogeneity.

Chapter 6

Ion Cloud & Decoherence

6.1 Introduction

We introduced the Bucket Brigade, a multiplexed ion trap, in the previous chapter. The Bucket Brigade allows us to perform multiple experiments concurrently to take full advantage of the long coherence time of ThF^+. However, our critics are not convinced. They ask, "this setup is huge, how are you going to control the fields within such a huge volume?" This chapter is our reply to them, "you are rightfully concerned, and so are we, but allow us to show you some equations and plots to convince you that the Bucket Brigade is not as crazy as it sounds."

Many of our critics come from the quantum information sector. They need to ensure that their qubits, each with a highly localized position, do not decohere with each other. Such decoherence could come from spatial inhomogeneity of fields, such that each qubit precesses at a slightly different frequency. People employ tricks like spin echo [64] or dynamic decoupling [65] to deal with the aforementioned decoherence mechanism. However, there are also temporal variations of fields that could come from inadequate control of the generators of the field, or imperfect shielding of fields from time-varying ambient sources. It is not immediately obvious how one would deal with such temporal sources of decoherence. Our fellow ion trappers in the quantum information sector are working with ion traps on a chip, and they find themselves working very hard to make the fields well behaved in a microscopic volume. They are rightfully concerned that we intend to perform precision metrology with ions sampling fields in a volume with a size of two small adults.

To tackle the concerns, we need to understand fast how our ions decohere w.r.t. each other in an

environment with inhomogeneous fields. This will allow us to place limits on design constraints of the Bucket Brigade. Hence, we need to understand a few things: (i) what is a typical spatial extent of our ion cloud, (ii) how does the decoherence manifest in an ensemble of ions, (iii) what role does ion-ion collisions play in the context of decoherence, and (iv) what other relevant mechanisms could affect us in the greater context of an eEDM experiment using molecular ions? We shall start with simplified models, and tackle these questions with increasing order of complexity in our models with each proceeding section.

Despite the high level of detail and complexity of the content in this chapter, we will not be arriving at grand conclusions pointing us to definite directions for the design of the Bucket Brigade. Instead, we will be confirming many small pieces of intuition. The work in this chapter was mainly done at the start of the pandemic, which incidentally coincided with the transition from spectroscopy to Bucket Brigade design. Notwithstanding the lack of a grand conclusion, we still include work done on ion cloud dynamics and its consequence to decoherence here in this thesis, in a hope that future generations of students and post-docs can build on this work to push our understanding/control of decoherence in our ion cloud even further. This chapter proceeds as follows.

We first investigate what an ion cloud at dynamic equilibrium looks like when we put it in a trap, and also allow for there to be ion-ion Coulomb repulsion. We shall look at the mean field effects of ion-ion repulsion, and when they turn on to understand the regime that we will be in with our typical trap parameters (Section 6.2.1). We then proceed to simulate the dynamics of an ion cloud to understand the spatial extent of our ion cloud at dynamic equilibrium (Section 6.2.2).

At this point, we switch gears a little to look at how decoherence is introduced into our ensemble of ions. We first formally introduce the naïve decoherence rate, which is the decoherence rate in our ensemble of ions that is naïvely based only on the spatial inhomogeneity of our fields (Section 6.3.1). We then introduce a possible mechanism built into our trap that could suppress the naïve decoherence (collisional narrowing in Section 6.3.2). Subsequently we combine the two effects together to come up with a model for the net decoherence rate (Section 6.3.2).

We then proceed to combine experiment results (Section 6.4.1) with the aforementioned tools (Section 6.4.2) to help us build confidence in our model. Subsequently, we attempt to arrive at a closed analytic form

for the ion-ion collision rate (Section 6.5.1) and relate it to the collisional narrowing rate (Sections 6.5.2 and 6.5.3). We then briefly discuss heating of ion clouds in Paul traps (Section 6.5.4) before discussing all the above results in the context of the Bucket Brigade.

Finally, we close off this chapter with a brief discussion of other possible mechanisms of decoherence not included in the above model (Section 6.6.1), and a quick disclaimer on how understanding decoherence mechanisms in the experiment is highly non-trivial (Section 6.6.3).

6.2 Ion cloud dynamics

We use a Paul trap to confine our ions. Axial confinement is provided by DC voltages on end caps, while radial confinement is provided by RF voltages on radial electrodes. Our ions exhibit harmonic secular motion in the trap from the harmonic axial trapping potential, and the harmonic radial ponderomotive trapping potential. In addition, our ions also exhibit fast RF micromotion driven by the RF potential that increases in amplitude with radial distance from the trap axis. We shall simplify the analysis of our ion dynamics by averaging over the fast RF micromotion of the ions in our Paul trap, and model the trap as a 3D harmonic trap with angular trap frequencies $\{\omega_x, \omega_y, \omega_z\}$. The two equations that govern the size of the ion cloud at thermal equilibrium across all three spatial axes are given by Gauss's law and the Boltzmann distribution:

$$\nabla^2 \Phi_0(\mathbf{r}) = -\frac{e}{\varepsilon_0} n(\mathbf{r}), \tag{6.1a}$$

$$n(\mathbf{r}) = \frac{N}{V} \exp\left[-\beta\left(e\Phi_0(\mathbf{r}) + \frac{1}{2}m(\omega_x^2 x^2 + \omega_y^2 y^2 + \omega_z^2 z^2)\right)\right], \tag{6.1b}$$

where $V = \iiint \exp\left[-\beta\left(e\Phi_0(\mathbf{r}) + \frac{1}{2}m(\omega_x^2 x^2 + \omega_y^2 y^2 + \omega_z^2 z^2)\right)\right] \mathrm{d}V$ is a normalization constant. The quantity $n(\mathbf{r})$ is the ion number density of the cloud. The kinetic energies of the ions are taken care of by the $\beta := 1/(k_\mathrm{B} T)$ term.

It turns out that solving the above equations for arbitrary N, ω_x, ω_y, and ω_z is not easy. It also turns out that simulating the motion of all the ions in the trap can be computationally expensive. In the following sections, we shall employ the following strategy. First, we shall study Equations 6.1 with a spherical ion cloud to simplify the equations through the symmetry of the problem (Section 6.2.1). This will give us some intuitive understanding of the effects of mean field (i.e. when ion-ion repulsion becomes significant) and when it comes into play. We will then dive into simulations of ion motion in the ion cloud with scaled parameters to make it computationally less expensive, but nonetheless still giving us the physics that we want (Section 6.2.2).

6.2.1 Studying mean field effects with spherical ion clouds

6.2.1.1 Method

For a trap with spherical symmetry, Equations 6.1 reduce to a non-linear second order ODE:

$$\partial_r r^2 \partial_r \Phi_0(r) = -\frac{e r^2}{\varepsilon_0} \exp\left[-\beta\left(e\Phi_0(r) + \frac{1}{2}m\omega^2 r^2\right)\right],$$

which can be solved numerically with the shooting method (a method to solve a boundary value problem by reducing it into an initial value problem). We massage the second order ODE into a first order ODE of the following form[1] :

$$\partial_r \begin{pmatrix} \Psi_0 \\ \Phi_0 \end{pmatrix} = \begin{pmatrix} -\frac{e r^2}{\varepsilon_0} \exp\left[-\beta\left(e\Phi_0 + \frac{1}{2}m\omega^2 r^2\right)\right] \\ \Psi_0 / r^2 \end{pmatrix},$$

where $\Psi_0 = r^2 \partial_r \Phi_0(r)$ is a variable defined for convenience. The shooting method involves solving the ODE by starting with initial values on the R.H.S. (i.e. values of $p_0 := \beta e \Phi_0$ when $r = 0$) and "shooting" the ODE to non-zero r. We impose $\partial_r \Phi_0(r = 0) = 0$, which is equivalent to saying that we are coarse graining individual ions away in the ion density.

Of note, depending on the choice of the initial condition p_0, the solution could correspond to very different total ion numbers N. As the total number of ions N increases, mean field effects start to play a huge role, where the inter-ion Coulomb repulsion suppresses the increase in the ion number density at the center of the ion cloud. Hence, the total ion number of a solution can be very sensitive to the initial conditions given to the numerical solver, as can be seen from Figure 6.1. To solve for $\Phi_0(r)$ for a specific N, one would guess a p_0, solve for $\Phi_0(r)$, deduce N, make a better guess for p_0, and repeat until N is close enough to the desired value.

6.2.1.2 Results

From Figure 6.2, we can see that the mean field is strong enough to modify the harmonic potential near the center to give a "flat-top" ion density sliced profile in ion clouds.

Figure 6.3 show the sizes of the ion clouds at various trap frequencies, from which we can draw a few conclusions:

[1] 1D numerical solvers typically work with the form $y'(x) = f(y, x)$.

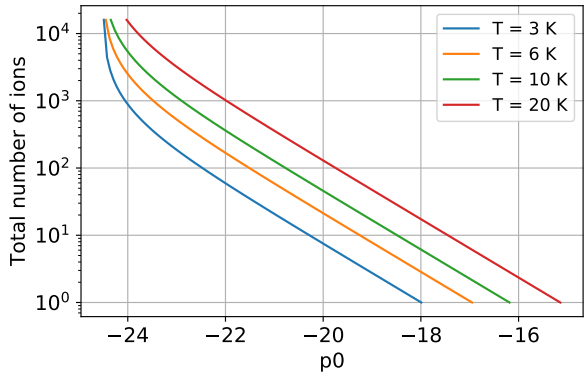

Figure 6.1: **Dependence of total ion number N on initial value $p_0 = \beta e\Phi_0$ used in the shooting method.** The plot shows that N is very sensitive to p_0 at high N in the strong mean field regime (low T). The plots showed here are for ThF^+ in a spherical trap of 1.6 kHz trap frequency.

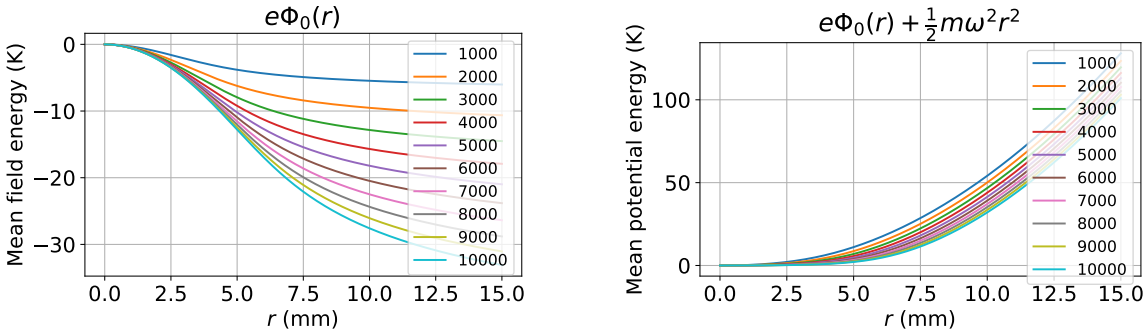

Figure 6.2: **Mean field energy $e\Phi_0(r)$ and mean potential energy as calculated, converted to kelvins.** We used $\omega = 2\pi \times 1$ kHz. The legend indicates total ion numbers. Note the for the plot on the right, having high ion numbers makes the potential energy curve flat at small r, before reverting back to a quadratic curve at larger r.

(1) The stronger the mean field effects, the more the ion density profile deviates from a Gaussian.

(2) The effect of ion-ion interaction decreases with increasing trap frequencies.

(3) The ion number density at $r = 0$ approaches a maximum density asymptotically as we ramp up mean field effects.

The maximum ion number density for a given trap can be evaluated at zero temperature, by demanding

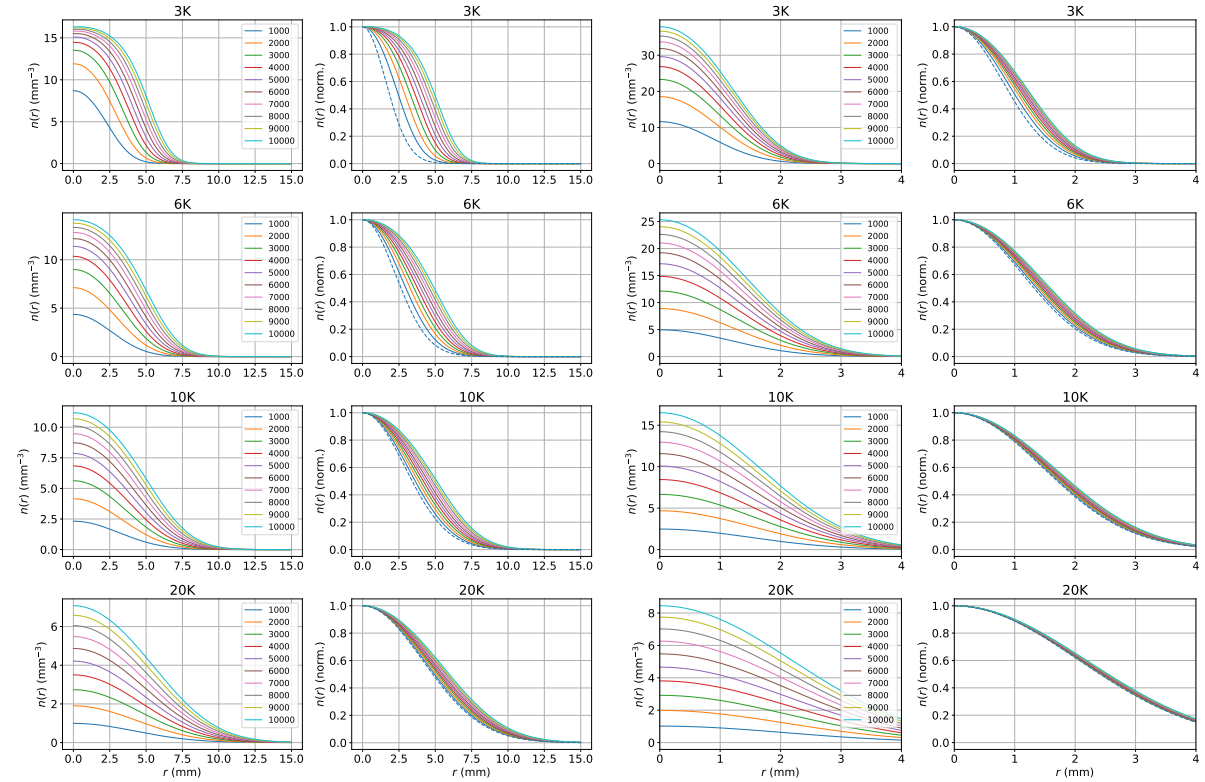

(a) Trap frequency of $\omega = 2\pi \times 1$ kHz

(b) Trap frequency of $\omega = 2\pi \times 2$ kHz

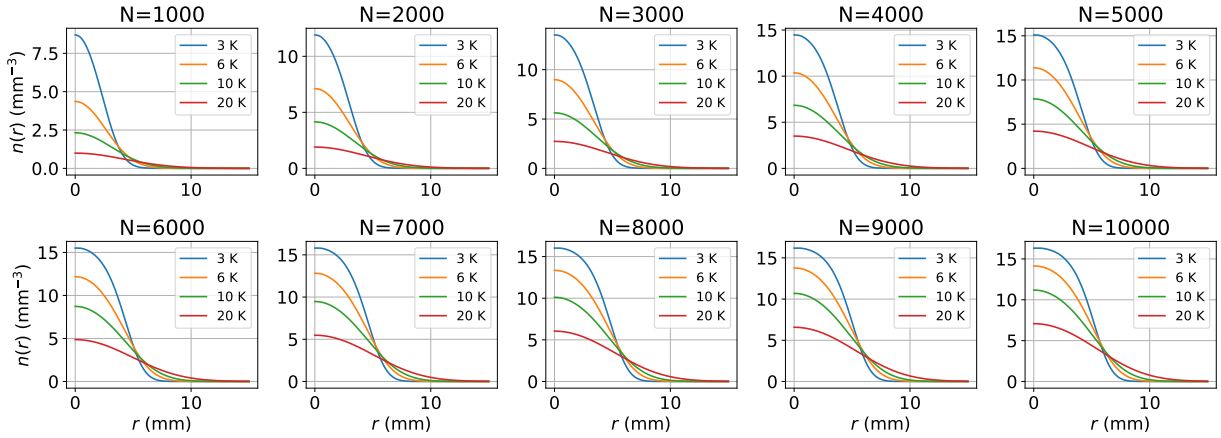

(c) Same data as trap frequency of $\omega = 2\pi \times 1$ kHz, rearranged to show thermal effects.

Figure 6.3: **Ion number radial density vs Total ion number.** The odd columns in (a) and (b) are the actual values for the ion number radial density $n(r)$, and the even columns are normalized to $n(r = 0) = 1$ to tease out the effects of the ion-ion interactions. The last two rows are just a rearrangement of the 1 kHz plots to show thermal evolution.

that the inter-ion Coulomb repulsion forces balance the trapping force:

$$\begin{aligned}
\mathbf{F}_{\text{Coulomb}} + \mathbf{F}_{\text{trap}} = 0 \implies \nabla \cdot [\mathbf{F}_{\text{Coulomb}}(\mathbf{r}) + \mathbf{F}_{\text{trap}}(\mathbf{r})] = 0 \\
-e\nabla^2\Phi(\mathbf{r}) = \nabla^2 \left[\frac{1}{2} m(\omega_x^2 x^2 + \omega_y^2 y^2 + \omega_z^2 z^2)\right] \\
e\rho_{\max}(\mathbf{r})/\epsilon_0 = m(\omega_x^2 + \omega_y^2 + \omega_z^2) \\
n_{\max}(\mathbf{r}) = \frac{m\epsilon_0}{e^2}(\omega_x^2 + \omega_y^2 + \omega_z^2). \qquad (6.2)
\end{aligned}$$

The above expression evaluates to 17 mm^{-3} (68 mm^{-3}) for a trap frequency of 1 kHz (2 kHz). We can see from Figure 6.3 that the number density at $r = 0$ approaches 17 mm^{-3} asymptotically as the total ion number increases for the {3 K, 1 kHz trap frequency} case.

Figure 6.4 shows how the ion number density at the center of the ion cloud varies with temperature for a fixed total ion number. Note that the number density at the center of the trap changes as a weak function of temperature at low temperatures.

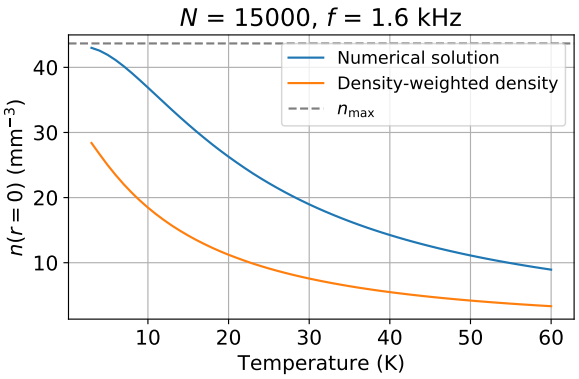

Figure 6.4: **Number density at ion cloud center vs temperature.** Variation of $n(r = 0)$ with T for N = 15000 at f = 1.6 kHz. The expression for the maximum total ion number permissible by an ion trap $n_{\max}$ is given in Equation 6.2. Jumping ahead to Section 6.5.1, a plot of the density-weighted density is shown here for comparison. Unlike the density at the center of the ion trap, the density-weighted density is a much stronger function of temperature at low temperatures.

6.2.1.3 Summary

To summarize, we simplified the geometry of the ion cloud to cast the governing equations into a form that we can solve numerically. With this numerical method, we explored mean field effects coming from ion-ion repulsion by varying the total ion number and temperature of the ion cloud. We saw that mean field effects manifest at low ion cloud temperatures and high ion numbers. We also saw that as mean field effects becoming more and more dominant, two things happen: (i) the net trapping potential curve becomes flatter at the center of the ion cloud, and (ii) the ion number density at the center of the ion cloud saturates to a value that depends on the trapping frequencies.

The results in this sections are not surprising. This simple exercise with a spherical ion cloud serves as a warm up to build some intuition. We are now ready to study the dynamics of the more general case of an aspherical ion cloud.

6.2.2 Simulating ion dynamics with aspherical ion clouds

6.2.2.1 Statement of problem

We can combine the Equations 6.1 to obtain defining PDE for a non-spherical cloud. The PDE can be written in two equivalent forms, expressed either as an equation for electric potential $\Phi_0(\mathbf{r})$ or ion number density $n(\mathbf{r})$:

$$\nabla^2\Phi_0(\mathbf{r}) = -\frac{e}{\varepsilon_0}\frac{N}{V}\exp\left[-\beta\left(e\Phi_0(\mathbf{r}) + \frac{1}{2}m(\omega_x^2x^2 + \omega_y^2y^2 + \omega_z^2z^2)\right)\right], \tag{6.3a}$$

$$\nabla^2\left[\log n(\mathbf{r})\right] + m\beta\left(\omega_x^2 + \omega_y^2 + \omega_z^2\right) = 4\pi\kappa\beta\cdot n(\mathbf{r}), \tag{6.3b}$$

where $\kappa := \frac{e^2}{4\pi\varepsilon_0}$. Note that N seems to be missing from Equation 6.3b, but it is hidden in the normalization criterion: $\int n(\mathbf{r})\,\mathrm{d}\mathbf{r} = N$. The above equations are hard to solve in either form with simple methods because the equations are:

(1) Non-linear partial differential equations (PDEs). The usual trick to tackle PDEs would be to use separation of variables (i.e. $\Phi_0(\mathbf{r}), n(\mathbf{r}) = X(x)Y(y)Z(z)$, but the $\Phi_0(\mathbf{r})$ term in the exponent for the first equation, and the $\log n(\mathbf{r})$ term in the second equation make the equation non-linear and void this trick.

(2) Not in the small variable expansion regime. Both $\Phi_0(\mathbf{r})$ and $n(\mathbf{r})$ are not small and cannot be expanded out with a series expansion to linearize the PDEs to solve it with the usual iterative tricks.

As a reminder, we wish to study the ion dynamics and use the results to estimate (i) the ion cloud sizes, (ii) collision rates between ions, and (iii) the resulting effects on decoherence. To this end, we should simulate the motion of ions in a trap, and come up with a model based on the simulation results to explain the dynamics of the ion cloud. We can then compare the model predictions with the ions in the Gen. II setup.[2] However, the typical ion number in the Gen. II setup is $N = 15000$, which is expensive to simulate because the number of ion-ion interaction terms scales as N^2; it took about 75 mins to simulate the dynamics of $N = 1000$ ions for 50 ms evolution time with trapping frequencies ~ 1 kHz, so simulating 15000 ions is simply not practical. Hence, we need to do some scaling of parameters to mimic the effect of having large ion numbers with only a small number of ions.

[2] At the time of this work, the only fully functioning ion trap in the JILA eEDM group is the Gen. II setup.

6.2.2.2 Scaling of parameters for realistic computation time

We want to study the ion cloud dynamics in the context of decoherence through, say, ion-ion collision. As alluded to in the previous section, we need to do some scaling of parameters. Firstly, we wish to maintain the ion density distribution, so that we can use the results to evaluate the effects of field inhomogeneity within the spatial extent of the ion cloud in the trap. Secondly, we want to keep the same the collision rate as the unscaled case so that we can study collision-induced decoherence effects. Therefore, we need to combine the equations governing the two pieces of physics, and scale them in a consistent way to keep the physics that we want to study invariant.

The equation governing collision rate is:

$$\Gamma_{\text{col.}}(T) \sim n(T) \cdot \frac{[\kappa\beta(T)]^2}{\sqrt{m\beta(T)}} \ln\left[\frac{1}{n(T)\,[\kappa\beta(T)]^3}\right], \tag{6.4}$$

We also made explicit that $\beta(T)$ is a function of temperature T. The above form for collision rate is informed by work in Section 6.5.1. In the above, $\kappa := \frac{e^2}{4\pi\varepsilon_0}$ is a measure of the Coulomb interaction strength. We see that $m\beta$ and $\kappa\beta$ have been grouped together suggestively to show that there are only two free parameters available for us to tweak.

We wish to reduce the number of ions in the simulation, but we want to keep the ion cloud size the same. We can scale $n \to n/\lambda$ and boost the Coulomb interaction strength up with $\kappa\beta \to \lambda \cdot \kappa\beta$ to keep the R.H.S. of Equation 6.3b invariant. The newly introduced λ term on the L.H.S. drops out under the laplacian. This scaling is equivalent to using λ times less ions for the simulation, but with $\sqrt{\lambda}$ times the original charge on each ion. However the aforementioned transformation will change Equation 6.4. One possible workaround would be to promote $m\beta$ into a field, but it is not obvious that a solution for such a field exists that can keep both the above equations invariant. Therefore, we employ a slightly modified battle strategy as follows:

(1) Simulate the effect of N singly charged ions with N/λ ions to reduce cost of computation. Each ion comes with a scaled up charge $\sqrt{\lambda}\,e$ to mimic the ion cloud size of the former (Section 6.2.2.3);

(2) Determine the field inhomogeneity sampled by the ions with the cloud sizes obtained (Section 6.3.1);

(3) Verify that there is good agreement between the simulated ion dynamics of the N/λ ions with the

scaled version of Equation 6.4 (Sections 6.5.1 and 6.5.2);

(4) Scale the collision model back down to that of N singly charged ions through Equation 6.4 and compare the predictions with experiment results from the Gen. II setup (Sections 6.4.1, 6.5.1, and 6.5.2).

(5) If the collision model works both in the unscaled version (matched with experiment data) and scaled version (matched with simulations), use it for the design of the Bucket Brigade (Section 6.5.5).

6.2.2.3 Simulation package & sample of simulation results

We used the *LAMMPS* simulation package from Sandia National Laboratory [66] to simulate the dynamics of 1000 ions. The cut-off range for pair-wise Coulomb interaction is set to 10 cm, which is larger than any anticipated size of clouds, to simulate the full effects of mean field. A sample of the simulation results is shown in Figure 6.5.

The final temperature of the ion cloud can be extracted from a Maxwell-Boltzmann distribution fit to the kinetic energies of the ions. Deviation from a Maxwell-Boltzmann distribution hints to us that the ion cloud may not have reached thermal equilibrium, and the dynamics will need to be simulated for longer.

In most of the discussions that follow, we will be looking at the simulation results of $N = 1000$ ions with charge $\sqrt{15}e$ in a trap with frequencies $\{2.0, 2.3, 1.5\}$ kHz and cloud temperature 4.3 K. This simulation mimics the ion cloud size of $N = 15000$ ions, so we can use the results to infer the amount of sampled spatial field inhomogeneity as a typical ion cloud in the Gen. II experiment (the Gen. II trap typically has about 15000 ions[3]).

Before we dive into the results of the simulations, we shall now take a look at how spatial Ramsey frequency inhomogeneity can affect decoherence of the fringes to understand what we need to look out for in the simulations.

[3] When this joint project started, the Gen. II trap had about 15000 ions, but we managed to push it up to an impressive 40000 ions as the experiment went on.

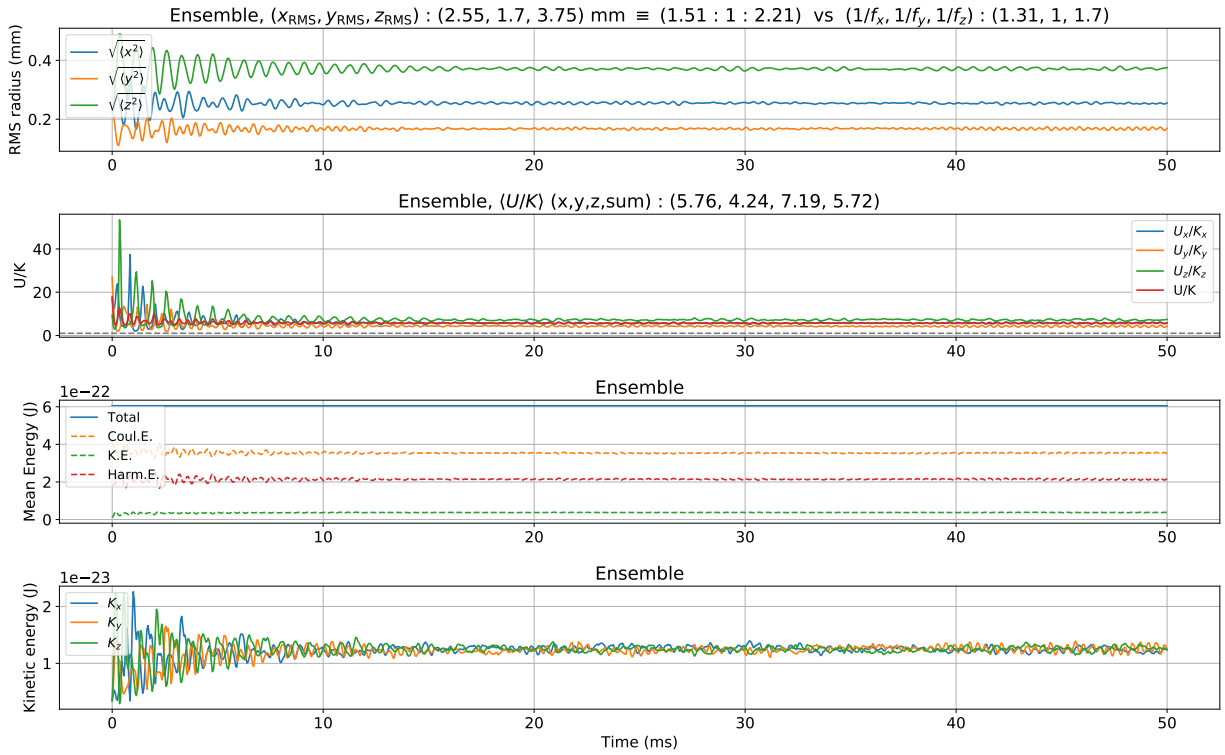

Figure 6.5: **Sample of results from a *LAMMPS* simulation.** This is a simulation of $N = 1000$ ions, each with charge $\sqrt{15}e$ to simulate the effects of 15000 ions in a harmonic trap with trap frequencies $\{1.3, 1.7, 1.0\}$ kHz, with a starting temperature of 0.5 K. A few points to note:

(1) The initial ringing of the RMS sizes in the top most plot shows breathing of the ion cloud as the ions were not initialized with positions and velocities that match the steady state solution. Ion cloud breathing damped out by 20 ms in this simulation instance. The final aspect ratio of the ion cloud at $\{1.51 : 1 : 2.21\}$ is bigger than what we would expect if there were no mean field effects, i.e. aspect ratio given by only the trap frequencies at $\{1.31 : 1 : 1.7\}$.

(2) The second row plots the ratio of the potential energy U and the kinetic energy K. The components of the energies are defined as such: $U_i := \frac{1}{2}m\omega_i^2 x_i^2$ and $K_i := \frac{1}{2}mv_i^2$, where m, ω_i, x_i, and v_i are the ion mass, angular trap frequency along the i-axis, position along the i-axis, and velocity along the i-axis, respectively. For a harmonic trap, virial theorem says that $U/K = 1$ (grey dashed line), but the ratios we have are clearly greater than 1, indicating that significant mean field effects are making our ion cloud bigger than what its temperature allows for.

(3) The third plot is a sanity check to show that total energy is conserved, and this shows that the size of the time step chosen is appropriate. The pair-wise Coulomb energy is much higher than the ions' kinetic and trap potential energies, which shows, once again, that mean field effects are not negligible.

(4) The last plot showed that the ion cloud is in thermal equilibrium across all three spatial dimensions, because all the kinetic energies along the three spatial axes converge together. Depending on the simulation parameters chosen, e.g. small number of ions or high ion cloud temperature, the ion cloud may not reach thermal equilibrium even after 50 ms of evolution time, so the simulation has to be extended until thermal equilibrium is reached as inferred from the convergence of kinetic energies along the three spatial axes.

In all the simulations, we allowed for the ion cloud to settle down before extracting (i) the sizes of the cloud, (ii) the ion number density profiles, and (iii) ion trajectories.

6.3 Decoherence from spatial inhomogeneity

In the previous sections, we introduced the tools that we will use to simulate the ion dynamics. We shall now switch gears a little to introduce the other set of tools required to understand decoherence in our ion cloud: a model for decoherence. We shall begin this section with a theoretical treatment of decoherence of Ramsey fringes of ions in an ion trap. We will add more realism with each proceeding section. We will finish off by comparing experiment results with our simulation model mentioned in the previous sections.

6.3.1 Frequency dependent decoherence rate (naïve decoherence rate), $\gamma_{\text{lin}}\overline{f}$

Suppose the ions evolve with Ramsey frequencies that do not depend on time, but fall under a normalized distribution $\mathbb{P}(\omega)$. The spread in frequencies could come from the spatial inhomogeneity of, say, the magnetic fields that each ion samples at its location. In the simplest scenario, this could happen if our ions are very cold, and well localized, but we allow the ion cloud to have some spatial extent, like in a string of ions [67], or in a Coulomb crystal [68]. Our setup does not allow us to probe each individual ions for their Ramsey phases; we are only able to read out the ensemble-averaged Ramsey phases. The resulting ensemble-averaged Ramsey fringe is given by:

$$\int \cos(\omega t)\,\mathbb{P}(\omega)\,\mathrm{d}\omega = \mathrm{Re}\left\{\int e^{i\omega t}\,\mathbb{P}(\omega)\,\mathrm{d}\omega\right\} = \mathrm{Re}\left\{\mathcal{F}\left[\mathbb{P}(\omega)\right]\right\}, \tag{6.5}$$

where $\mathcal{F}$ indicates Fourier transform.

We can represent the complex function $\mathcal{F}\left[\mathbb{P}(\omega)\right](t)$ as an Argand vector rotating on the Argand plane (complex plane) with time. Its projection onto the real axis at various times represents the ensemble-averaged Ramsey phase at the corresponding time. The envelope of the ensemble-averaged Ramsey fringe is given by the amplitude of the Argand vector:

$$\left|\int e^{i\omega t}\,\mathbb{P}(\omega)\,\mathbf{d}\omega\right| = \left|\mathcal{F}\left[\mathbb{P}(\omega)\right](t)\right|. \tag{6.6}$$

As an example, for a Gaussian frequency distribution where $\mathbb{P}(\omega) = \frac{1}{\sqrt{2\pi}\sigma_\omega} e^{-\frac{1}{2}\left(\frac{\omega-\omega_0}{\sigma_\omega}\right)^2}$, the expressions

in Equations 6.5 and 6.6 evaluate to

$$\mathrm{Re}\left\{\mathcal{F}\left[\mathbb{P}(\omega)\right]\right\} = e^{-\frac{1}{2}(\sigma_\omega t)^2}\cos\omega_0 t, \tag{6.7a}$$

$$\left|\mathcal{F}\left[\mathbb{P}(\omega)\right]\right| = e^{-\frac{1}{2}(\sigma_\omega t)^2}, \tag{6.7b}$$

where ω_0 is the mean angular frequency and σ_ω is the standard deviation of the angular frequency distribution. Figure 6.6 shows a plot of the above two equations.

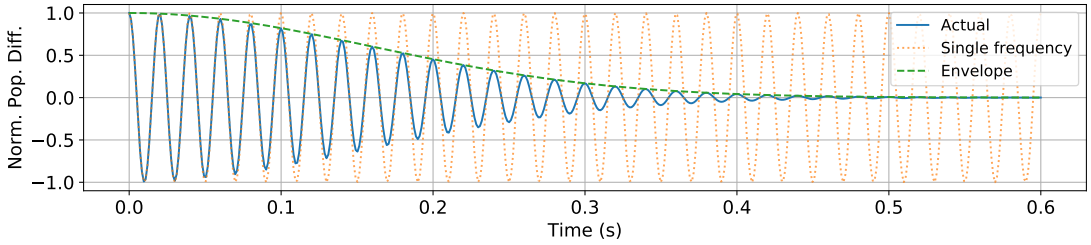

Figure 6.6: **Decoherence of an ensemble-averaged Ramsey fringe for a Gaussian frequency distribution.** The blue solid line and the green dashed lines are plots of Equations 6.7a and 6.7b, respectively, for $\omega_0 = 2\pi \times 50$ Hz and $\sigma_\omega = 2\pi \times 1$ Hz. The beige dotted line shows what the fringe would look like if $\sigma_\omega = 0$, i.e. no decoherence.

For any arbitrary $\mathbb{P}(\omega)$, its Fourier transform will be a function of $\sigma_\omega t$. Often times the spread in Ramsey frequencies seen by the ions comes from spatial field inhomogeneity in the trap, e.g. imperfect current-carrying coils that give inhomogeneous magnetic fields gradients for Zeeman splitting, or imperfect electrodes that give inhomogeneous electric fields that define the quantization axis. Such field inhomogeneity gives rise to a spread in Ramsey frequencies that depends on the mean frequency. Hence, we express σ_ω in a more illuminating form:

$$\sigma_\omega = 2\pi\sigma_f = 2\pi\overline{f}\sigma_{f/\overline{f}},$$

where $\overline{f}$ is the mean Ramsey frequency of the ensemble, and $\sigma_{f/\overline{f}}$ is the spread of the fractional frequency distribution $\mathbb{P}(f/\overline{f})$ with a mean at $f/\overline{f} = 1$.

We define a half-time $t_{1/2}$ that is the time at which the decoherence envelope drops to half, i.e.

$\mathcal{F}\left[\mathbb{P}(\omega)\right](\sigma_\omega t_{1/2}) = 1/2$, such that:

$$\begin{aligned}
\mathcal{F}\left[\mathbb{P}(\omega)\right]^{-1}(1/2) &= 2\pi\overline{f}\sigma_{f/\overline{f}}\, t_{1/2} \\
1/t_{1/2} &= \frac{2\pi\sigma_{f/\overline{f}}}{\mathcal{F}\left[\mathbb{P}(\omega)\right]^{-1}(1/2)}\,\overline{f} \\
&= \gamma_{\text{lin}}\,\overline{f}, \qquad (6.8)
\end{aligned}$$

where γ_{lin} captures all the details of the spatial field inhomogeneity. For decoherence effects due to spatial field inhomogeneity, we expect the rate of decoherence to be proportional to the mean Ramsey frequency. Note that the above only captures decoherence from spatial field inhomogeneity from fields generated by coils and electrodes. Equation 6.8 does not capture decoherence effects due to spatial field inhomogeneity of stray fields from, say, magnetic patches of the optical table around the setup. Decoherence from such sources are grouped under a background decoherence rate to be introduced in Section 6.3.3.

We note that $\gamma_{\text{lin}}\overline{f}$ is the naïve decoherence rate, which would be the actual decoherence rate (assuming spatial field inhomogeneity to be the only source of decoherence) if the ions are held in place, i.e. stationary. If this were the only decoherence related mechanism in our trap, we would expect the Ramsey phases of our ions to spread out ballistically, i.e. $\sim t$, because the spread of the phase goes as $\sigma_\phi = 2\pi\overline{f}\sigma_{f/\overline{f}}\, t \propto t$. However, we shall see in the next section that there can be a suppression of the ballistic expansion of σ_ϕ in our ion trap.

6.3.2 Suppressed decoherence from collisional narrowing, $\Gamma_{\text{c.n.}}$

Our thermal ions move around the trap, and they collide with each other to send each other into different trajectories around the trap. Associated with this is a rate at which the ions "reset" their trajectories, resulting in a corresponding "reset" of their Ramsey frequencies to another random frequency in $\mathbb{P}(\omega)$. Correspondingly, the spread in the ensemble of Ramsey phases is sub-ballistic, and is more of a classical random walk.

Using the ion simulation tools from Section 6.2.2 in combination with known field inhomogeneity in the Gen. II trap, we see from the simulation results that the spread of the Ramsey phases of ions in the ion cloud ensemble evolves diffusively, i.e. $\sigma_\phi \sim \sqrt{t}$. This result is shown in Figure 6.7.

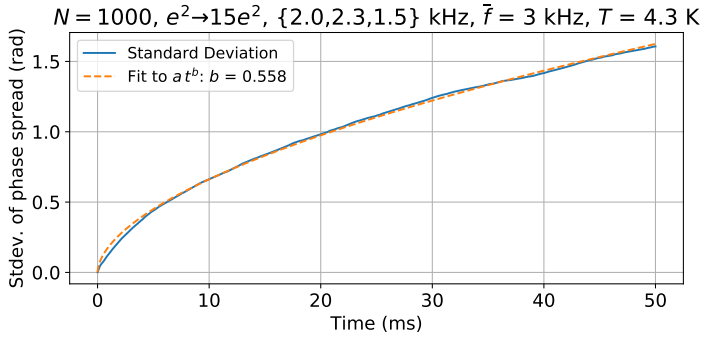

Figure 6.7: **Simulated result of the spread of Ramsey phases in an ensemble of ions.** The ion cloud has $N = 1000$ ions, each with a charge of $\sqrt{15}e$. The trap has frequencies {2.0, 2.3, 1.5} kHz, The ion cloud temperature is $T = 4.3$ K. The ions have a mean Ramsey frequency of 3 kHz. We introduced a realistic spatial dependence of the local Ramsey frequency based on known field inhomogeneity in the Gen. II trap. For book keeping, the Ramsey frequency is dominated by Berry's phase (instead of the usual Zeeman offset). The Berry's phase is an axial electric field effect. The electric field inhomogeneity is derived from a COMSOL model of the fields generated by the electrodes within the trap. The fit parameter $b = 0.558(9)$ is much closer to 0.5 (diffusive) than to 1 (ballistic) and show that the phases indeed spread out diffusively.

To quantify the suppressed decoherence, we introduce the following model. The total phase accumulated by any ion is given by:

$$\phi(t) = \int_0^t \omega(t')\,\mathrm{d}t' =: \overline{\omega}(t)\,t,$$

where we define the net Ramsey (angular) frequency $\overline{\omega}(t)$ given by the expression above. If we demand that the spread in $\phi(t)$ goes as $\sim \sqrt{t}$, then the spread in $\overline{\omega(t)}$ must go as $\sim 1/\sqrt{t}$. We shall guess it to be of the form:

$$\sigma_{\overline{\omega}}(t) := \frac{\sigma_\omega}{\sqrt{1 + 2\Gamma_{\text{c.n.}} t}}, \tag{6.9}$$

where $\Gamma_{\text{c.n.}}$ is a fitting parameter that we introduce for "collisional narrowing" (narrowing of decoherence because of momentum-changing ion-ion collisions), and σ_ω is the naïve spread in frequencies without collisional narrowing. $\Gamma_{\text{c.n.}}$ has units of inverse-time in this ansatz, and it is related to the ion-ion collision rate in the trap.[4]

At this point, it is important to address what kind of decoherence can be suppressed by ion-ion collisions. The ions are sloshing around within the ion trap. There are a few key points:

[4] Ions have collision cross section area of infinity because of the $1/r^2$ scaling of the field strengths, but here we only refer to collisions that change the ions' trajectories significantly.

(1) In the absence of ion-ion collision, each ion has a well defined total energy along each principal axes of the ion trap.

(2) The ion spends equal amounts of time on either side of the center of the trap along each of the principal axes of the ion trap.

(3) Any spatial inhomogeneity of the fields can be expanded out about the trap center as a sum of even and odd functions; see Figure 6.8.

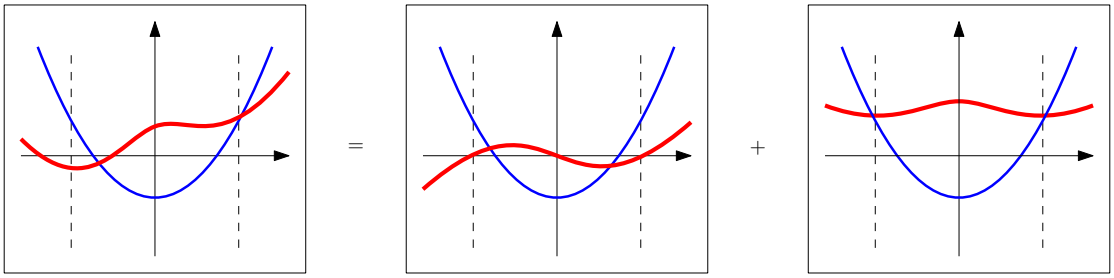

Figure 6.8: **Decomposing spatial inhomogeneity into odd and even functions about trap center.** The horizontal axis indicates position in the ion trap along a principal axis. The red line indicates the local Ramsey frequency sampled by the ions at that location. The red line on the left is decomposed into a sum of odd and even functions about the trap center. The blue line shows the harmonic potential of the ion trap. The dashed vertical line indicates the extrema of the sloshing motion of an ion of a given total energy. The effect of the odd component averages out to zero in one slosh cycle. The effect of the even component does not average out to zero, and the net value depends on the total energy of the ion.

(4) Spatial inhomogeneity of the fields that goes as an odd function about the trap center is averaged out by the ion as it sloshes around the ion trap. This is true regardless of the total energy of the ion.

(5) Spatial inhomogeneity of the fields that goes as an even function about the trap center is not averaged out by the ion as it sloshes around the ion trap. The net accumulated effect as seen by the ion also depends on its total energy along the relevant axes.

(6) In the absence of ion-ion collisions, then, ions with higher total energies along a particular axis will sample net frequencies that will be different from those with lower total energies.

(7) In the presence of ion-ion collisions, there can be energy and momentum exchange between the ions, sending the ions into a different trajectory with each collision, allowing the ions to sample the entire

spatial extent of the ion cloud "ergodically". This reduces the net spread of net frequencies seen by the ensemble of ions.

In the next section, we shall attempt to put γ_{lin} and $\Gamma_{\text{c.n.}}$ together to come up with a model to describe the net decoherence rate in our ion cloud.

6.3.3 Net decoherence rate, $\Gamma_{1/2}$

Here we attempt to derive an expression for the net decoherence rate as a result of the spatial field inhomogeneity ($\gamma_{\text{lin}}\overline{f}$) and suppression of the effects of such spatial inhomogeneity from ion-ion collisions ($\Gamma_{\text{c.n.}}$). Some of the parts may seem *ad hoc*, but we shall see in Section 6.4.1 that this model describes what we see in the Gen. II trap very well.

Suppose we have a Gaussian distribution[5] of frequencies, we can combine Equations 6.7b and 6.9 to show that the contrast of the ensemble-averaged of Ramsey fringe has the form:

$$C_{\text{G}}(t) = \exp\left[-\frac{1}{2}\frac{(\sigma\, t)^2}{1+2\Gamma_{\text{c.n.}}t}\right].$$

Here we make a few observations:

(1) At short times, $t \ll 1/(2\Gamma_{\text{c.n.}})$, the function behaves like a Gaussian, hence we expect it to start off with zero gradient, instead of an exponential decay.

(2) At long times, $t \gg 1/(2\Gamma_{\text{c.n.}})$, the function behaves like an exponentially decaying function.

(3) The time it takes to get to half contrast is:

$$t_{1/2} = \frac{\Gamma_{\text{c.n.}} + \sqrt{\Gamma_{\text{c.n.}}^2 + \sigma^2/(2\log 2)}}{\sigma^2/(2\log 2)}$$

Together with Equation 6.8, we get:

$$t_{1/2} = \frac{\Gamma_{\text{c.n.}} + \sqrt{\Gamma_{\text{c.n.}}^2 + (\gamma_{\text{lin}}\overline{f})^2}}{(\gamma_{\text{lin}}\overline{f})^2}.$$

[5] Invoking the central limit theorem on the field inhomogeneity sampled by our ions, barring any exotic forms of spatial inhomogeneity that break this limit.

From the above, we can define the net decoherence rate[6] as the inverse of $t_{1/2}$, which gives:

$$\Gamma_{1/2} := \frac{1}{t_{1/2}} = \frac{(\gamma_{\text{lin}}\overline{f})^2}{\Gamma_{\text{c.n.}} + \sqrt{\Gamma_{\text{c.n.}}^2 + (\gamma_{\text{lin}}\overline{f})^2}} + \Gamma_{\text{bg}}, \tag{6.10a}$$

where we added a background decoherence rate Γ_{bg} by hand to account for decoherence that come from other sources of spatial inhomogeneity such as those discussed in Section 6.6.1. In the limit of $\overline{f} \gg \Gamma_{\text{c.n.}}/\gamma_{\text{lin}}$, which is equivalent to saying that collisional narrowing is weak compared to the naïve decoherence, the above evaluates to:

$$\Gamma_{1/2} \approx \left[\frac{1}{\gamma_{\text{lin}}\overline{f}} + \frac{\Gamma_{\text{c.n.}}}{(\gamma_{\text{lin}}\overline{f})^2}\right]^{-1} + \Gamma_{\text{bg}}. \tag{6.10b}$$

Although the above expressions are evaluated for ions with Gaussian frequency distributions, we shall use see in the following section that the above form fits to our data surprisingly well.

6.4 Collisional narrowing in the ion trap

Now that we have a model for various rates that go into decoherence, we would like to test it against experiments and simulations. The naïve decoherence and background decoherence rates are easy to understand, these are just decoherence rates that either depend or do not depend on the Ramsey frequency. The collisional narrowing mechanism is a little unexpected, so we shall first check for its existence with experiments (Section 6.4.1) and simulations (Section 6.4.2).

6.4.1 Collisional narrowing in experiments

We worked with the Gen. II team[7] to measure the effects of spatial field inhomogeneity and collisional narrowing. The Gen. II trap is optimized to have very good spatial magnetic field homogeneity for their eEDM measurement. However, the axial electric fields are not optimized for spatial homogeneity, which means that there will be a spatially inhomogeneous Berry's phase (Chapter 8.3). The net frequency is a sum of very spatially homogeneous Zeeman frequency and very spatially inhomogenous Berry's frequency. Figure 6.9 shows the Berry's frequency part of the results of the experiment. We performed the following for the experiment:

[6] Rates are usually defined by the inverse of the time required to get to $1/e$ instead of $1/2$, but we are defining it this way for easy comparison with data from Gen. II.

[7] Many thanks to Dr. Yuval Shagam and Tanya Roussy for the experiment data.

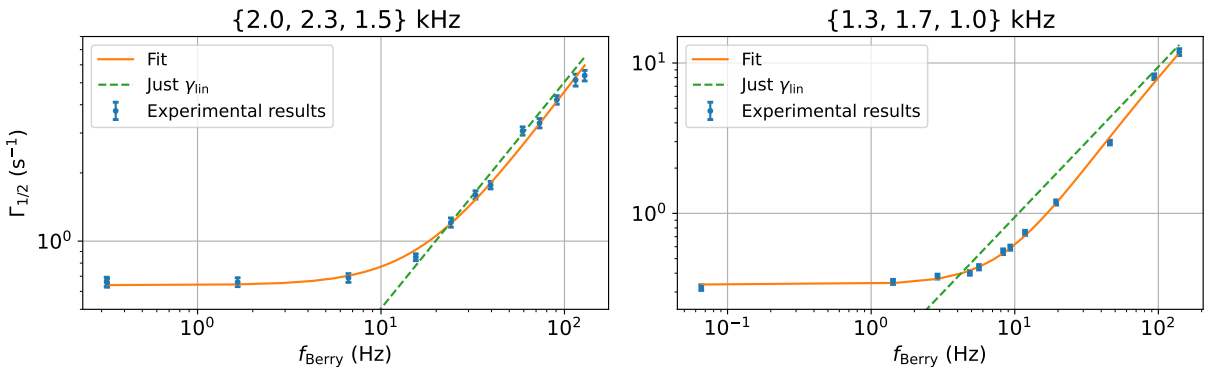

Figure 6.9: **Decoherence rates, $\Gamma_{1/2} = 1/t_{1/2}$, seen in the Gen. II setup through spatial inhomogeneity of Berry's phase.** The experiments were performed with two trap configurations (trap frequencies annotated on top of the plots). The fits are of the form in Equation 6.10b. The fit parameters for the tight trap (left plot) are $\gamma_{\text{lin}} = 0.050(5)$ $(\text{s} \cdot \text{Hz})^{-1}$, $\Gamma_{\text{c.n.}} = 1.4(5)$ s^{-1}, and $\Gamma_{\text{bg}} = 0.64(2)$ s^{-1}; while that for the loose trap (right plot) are $\gamma_{\text{lin}} = 0.094(6)$ $(\text{s} \cdot \text{Hz})^{-1}$, $\Gamma_{\text{c.n.}} = 2.2(5)$ s^{-1}, and $\Gamma_{\text{bg}} = 0.34(1)$ s^{-1}. Here is a qualitative understanding of how each of the fit parameters affect the shape of the fit: Γ_{bg} determines where the decoherence rate saturates at low frequency; γ_{lin} determines the horizontal displacement of the slope at high frequency away from the vertical axis; $\Gamma_{\text{c.n.}}$ determines sharpness of the ankle. Also shown on the plots are the green dashed lines, which are just plots of $\gamma_{\text{lin}} f_{\text{Berry}}$. Regions where the yellow fit line lies below the green dashed lines are regions where collisional narrowing is working.

(1) Introduce Berry's phase into the Ramsey fringes of ions in the Gen. II setup (method similar to that in Chapter 8.3).

(2) Extract the ensemble-averaged Ramsey fringes at various values of Berry's frequency.

(3) Determine the half-time $t_{1/2}$ and hence the decoherence rate $\Gamma_{1/2} = 1/t_{1/2}$.

The fit uncertainties on $\Gamma_{\text{c.n.}}$ are small, indicating that $\Gamma_{\text{c.n.}}$ is required in the fitting form of Equation 6.10b to make a good fit. One can also intentionally vary $\Gamma_{\text{c.n.}}$ or set it to zero, and see that the curve does not make a good fit with the data regardless of the choice for the other two fit parameters.

6.4.2 Collisional narrowing in simulations

We can also see the effects of collisional narrowing in simulations. Here we show the results of simulations of $N = 1000$ ions with charge $\sqrt{15}e$ in a trap with frequencies $\{2.0, 2.3, 1.5\}$ kHz and cloud temperature 4.3 K at various Berry's frequency (Figure 6.10). In the simulations, we model the spatial dependence of frequency due to the spatial inhomogeneity of electric fields in the Gen. II setup with the

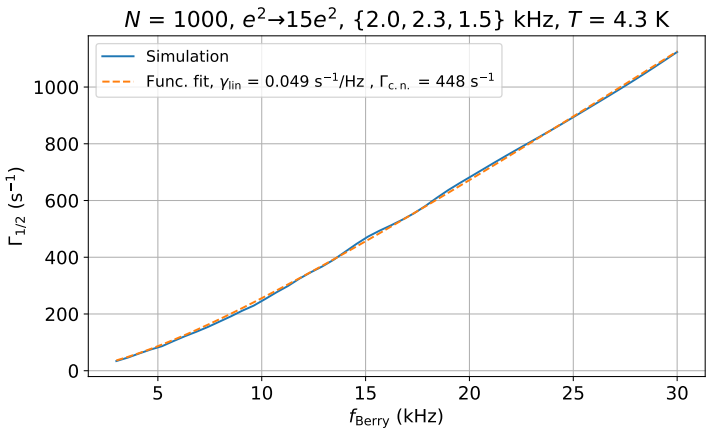

Figure 6.10: **Collisional narrowing seen in a simulation.** The simulation uses $N = 1000$ ions with charge $\sqrt{15}e$ in a trap with frequencies $\{2.0, 2.3, 1.5\}$ kHz and cloud temperature 4.3 K. We did not simulate the effects of background decoherence, so $\Gamma_{\text{bg}} = 0$ in the above fit. The rest of the fit parameters are $\gamma_{\text{lin}} = 0.0490(4)\ (\text{s} \cdot \text{Hz})^{-1}$ and $\Gamma_{\text{c.n.}} = 450(10)\ \text{s}^{-1}$.

following expansion in powers of the cylindrical coordinates:

$$f \approx \sum_{i,j} a_{i,j} z^i \rho^j,$$

where z and ρ are the axial and radial coordinates. We only keep expansion terms up to sixth order in position coordinates:

$a_{i,j}$	ρ^0	ρ^2	ρ^4	ρ^6
z^0	1.4636(2)	−0.08360(7)	$1.75(1)\times10^{-3}$	$-2.27(4)\times10^{-5}$
z^2	0.1714(1)	−0.01551(1)	$5.112(6)\times10^{-4}$	-
z^4	$4.62(3)\times10^{-3}$	$-4.32(1)\times10^{-4}$	-	-
z^6	$2.1(2)\times10^{-5}$	-	-	-

Table 6.1: **Coefficients of inhomogeneity expansion of f in the Gen. II setup.** Coordinates ρ and z are expressed in centimeters. Uncertainties are the standard deviations of the fits of the parameters over a 3 cm × 3 cm × 3 cm region centered at the trap center.

6.4.3 Summary

Through Equation 6.10b, we have a model for decoherence in our ion cloud. Our model splits the decoherence rate into a component that is fringe frequency dependent ($\gamma_{\text{lin}}\overline{f}$) and one that is frequency independent (Γ_{bg}). We also introduced a decoherence suppressing mechanism ($\Gamma_{\text{c.n.}}$) for the frequency dependent component. Using all the simulation tools that we have developed in the previous sections and also the Gen. II setup, we saw a good agreement between our model and results from experiment and simulations.

Our model has implications for the design of the Bucket Brigade. Our model is saying that we can get away with a little bit of imperfection in the field homogeneity, because collisional narrowing will make our ions decohere less than what we would naïvely expect from the overlap of the spatial extent of the ion cloud and the spatial inhomogeneity of the fields.

As scientists, we are entitled to be greedy (at the expense of working even harder). In the next section, we shall try to understand the collisional narrowing rate even more, and see if we can make it work even harder for us.

6.5 Collision rate

In the previous sections, we saw good agreement between our model through Equation 6.10b, and results from experiment and simulations. Our model relies heavily on the fact that ion-ion collisions can change the ions' trajectories and "reset" their Ramsey frequencies, resulting in a diffusive spread in Ramsey phases instead of a ballistic one. This rate of collisional narrowing has to be related to the rate of trajectory-changing ion-ion collisions. In the following sections, we shall try to understand the relationship between the rates of collisional narrowing and ion-ion collisions more rigorously.

6.5.1 Collision rate ansatz

Since the Coulomb force has infinite collision cross sectional area, it takes some art to define whether a collision has happened between two ions. We start this section off with a simple derivation of the generic form of collision rates involved between ions in an ion cloud to motivate an expression for the collision rate. We shall borrow wisdom from the plasma physics literature. Figure 6.11 shows a schematic diagram of the approach of two ions.

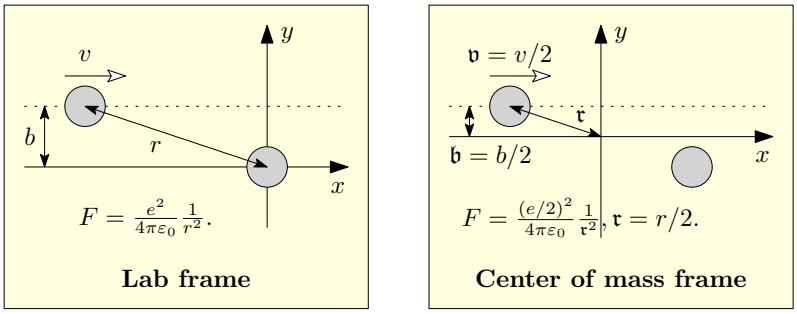

Figure 6.11: **Schematic of a collision between two singly positively charged ions.** In the lab frame, one ion starts off at rest, while the other comes in with an impact parameter b and an incoming speed v. The stationary "background ion" will receive a recoil from the incoming "test ion", which will make the scattering cross section harder to analyze. One neat trick is to switch over to the center of mass frame, and introduce an infinitely heavy "effective ion" at the origin of the center of mass., with an effective charge of $e/4$ with the incoming ion still having a charge e. The center of mass frame is moving to the right at speed $v/2$.

Working in the center of mass frame of the collision, we can use the results from Rutherford scattering (light incoming ion and heavy stationary ion) of relating the deflection angle Θ to the incoming speed $\mathfrak{v}$ and

impact parameter $\mathfrak{b}$:

$$\tan\frac{\Theta}{2}=\frac{Z_1Z_2e^2}{4\pi\varepsilon_0 m\mathfrak{v}^2\mathfrak{b}}=\frac{2e^2}{4\pi\varepsilon_0 mv^2b}=\frac{2\kappa}{mv^2b}\quad,\quad \kappa:=\frac{e^2}{4\pi\varepsilon_0}.$$

In the center of mass frame, the velocity of the incoming ion far away after the collision would be:

$$(v_x,v_y)=(\mathfrak{v},0)\to(\mathfrak{v}\cos\Theta,\mathfrak{v}\sin\Theta)=\frac{v}{2}\left(\frac{(mv^2b)^2-4\kappa^2}{(mv^2b)^2+4\kappa^2},\frac{4\kappa mv^2b}{(mv^2b)^2+4\kappa^2}\right).$$

Back in the lab frame, the change in the longitudinal velocity $\Delta v_{||}$ and transverse velocity $\Delta v_\perp$ are then given by:

$$\Delta v_{||}=-\frac{4(\kappa\beta)^2}{4(\kappa\beta)^2+(3b)^2}\cdot v,$$
$$\Delta v_\perp=\frac{6\kappa\beta b}{4(\kappa\beta)^2+(3b)^2}\cdot v,$$

where we used the equipartition theorem $\frac{1}{2}mv^2=\frac{3}{2}k_{\mathrm{B}}T=\frac{3}{2\beta}$. From the above, we can obtain the (kinetic) energy transfer coefficient, i.e. the fractional change in energy per collision:

$$\frac{\Delta\mathrm{KE}}{\mathrm{KE}}=-\frac{4(\kappa\beta)^2}{4(\kappa\beta)^2+(3b)^2}. \tag{6.11}$$

Now that we know how much the kinetic energy of an ion changes per collision, we need to know the rate of collision. The number of ions that each ion zips past per unit time is given by[8] :

$$n\cdot\frac{\int \mathrm{d}V}{\Delta t}=nv\int \mathrm{d}A=2\pi nv\int \mathrm{d}b\, b. \tag{6.12}$$

Putting Equations 6.11 and 6.12 together, the (fractional) rate of decay of (kinetic) energy is given by:

$$\Gamma_{\mathrm{KE}}=2\pi nv\int_0^{\lambda_{\mathrm{c.o.}}}\mathrm{d}b\, b\cdot\frac{4(\kappa\beta)^2}{4(\kappa\beta)^2+(3b)^2}=\frac{4\pi\sqrt{3}}{9}\cdot n\cdot\frac{(\kappa\beta)^2}{\sqrt{m\beta}}\log\left[\frac{9\lambda_{\mathrm{c.o.}}^2+4(\kappa\beta)^2}{4(\kappa\beta)^2}\right], \tag{6.13}$$

where $\lambda_{\mathrm{c.o.}}$ is the cut off length for the integration limit; the logarithmic term blows up if we do not use a finite cut off. In the two-component plasma literature, the cut off length used is the Debye screen length ($\lambda_D=\sqrt{\frac{\varepsilon_0 k_{\mathrm{B}}T}{ne^2}}=\frac{1}{\sqrt{4\pi n\kappa\beta}}$). The Debye screening length is the distance between two ions such that the Coulomb repulsion between these ions are screened by the other component in the plasma of opposite charge. The net result is that the ions do not accelerate away from each other as much as they would have without the second component.

[8] This is an operator, because b is different for collisions with different ions.

We have something similar in our ion trap. In addition to Coulomb repulsion between ions, our ions also feel a confining force from the trap. This means that beyond a certain ion-ion separation (for instance, when the ions are on opposite sides of the trap), their Coulomb repulsion no longer results in acceleration away from each other. It is as though the trap "screens" the Coulomb repulsion between ions beyond a certain ion-ion separation distance. This happens at a cut off length where the trapping force balances the Coulomb repulsion:

$$m\omega^2\lambda_{\text{c.o.}} = \frac{\kappa}{\lambda_{\text{c.o.}}^2}.$$

For a thermal cloud, we know that:

$$\frac{1}{2}m\omega^2\lambda_{\text{therm.}}^2 = \frac{1}{2\beta},$$

where $\lambda_{\text{therm.}}$ is the 1σ radius of the thermal cloud. We also know that the $\lambda_{\text{therm.}}$ is related to the ion number density (n) through:

$$n\lambda_{\text{therm.}}^3 \sim N,$$

where N is the total ion number. Combining the above three relations, we have

$$\lambda_{\text{c.o.}}^2 \sim \left(\kappa\beta n^{-2/3}\right)^{2/3}.$$

Substituting the above into Equation 6.13 gives

$$\Gamma_{\text{KE}} \sim A \cdot n \cdot \frac{(\kappa\beta)^2}{\sqrt{m\beta}} \log\left[\frac{B}{n\cdot(\kappa\beta)^3}\right], \tag{6.14}$$

where A and B are constants. A simple dimensional analysis check gives $[\beta] = [1/(\text{N}\cdot\text{m})]$, $[\kappa] = \left[\text{N}\cdot\text{m}^2\right]$, $[n] = \left[1/(\text{m}^3)\right]$, so that $[\kappa\beta] = [\text{m}]$, and $[m\beta] = \left[1/(\text{m}\cdot\text{s}^{-1})^2\right]$.

The above form, together with many others in plasma literature [69, 70] and studies of ion cloud dynamics [71] suggest the following ansatz for the ion-ion collision rate (this is such an important ansatz that I shall name it the "AB ansatz"):

$$\Gamma_{\text{col.}}(T) = A \cdot \tilde{n}(T) \cdot \frac{[\kappa\beta(T)]^2}{\sqrt{m\beta(T)}} \cdot \log\left[\frac{B}{\tilde{n}(T)[\kappa\beta(T)]^3}\right], \tag{6.15}$$

where A and B are dimensionless parameters to be fit, and $\tilde{n} = \frac{1}{N}\int n(\mathbf{r})\cdot n(\mathbf{r})\,\mathrm{d}V$ is the density-weighted density of the ion cloud. The density-weighted density depends on temperature through the temperature-dependence of the ion number density. Deriving Equation 6.15 from first principles will give different values

on A and B depending on the assumptions used. As an experimental physicist, I shall simulate the dynamics of our ion cloud, perform a fit to A and B, verify the results with the experiments done on the Gen. II setup, and challenge interested theorists out there to derive the analytical form for A and B.

6.5.2 More collision-related rates

The next question is: what quantity should we compare Equation 6.15 to in our ion dynamics simulation? Ultimately, we wish to find an expression for $\Gamma_{\text{c.n.}}$, which is the rate at which the ions reset their perceived Ramsey frequencies. In the context of our trapped ion experiment, frequency resets correspond to position resets, which corresponds to trajectory resets. By monitoring the rate at which the ion changes its trajectory, we would be able to relate that to $\Gamma_{\text{c.n.}}$. A good quantity, then, is to measure the decay rate of the self correlation of the kinetic energy of the ions along, say, the x-direction, because this is the rate at which the ions forget about their trajectories along the x-direction, i.e. changed their trajectories. We define the self correlation function of the kinetic energy in the x-direction to be:

$$g^{(1)}_{\text{KE}_x}(\tau) := \frac{\overline{[\text{KE}_{x,i}(t) - \overline{\text{KE}_x(t)}] \cdot [\text{KE}_{x,i}(t+\tau) - \overline{\text{KE}_x(t+\tau)}]}}{\overline{\text{KE}_x(t)}^2} \quad , \quad \text{KE}_x := \frac{1}{2}mv_x^2, \tag{6.16}$$

where the overline represents averaging over all ions and all time. We fit the above expression to an exponential decaying function:

$$g^{(1)}_{\text{KE}_x}(\tau) = a \exp\left(-\Gamma_{\text{KE}_x}\tau\right),$$

where we extract the decay rate Γ_{KE_x}, and a is just a normalization constant. Figure 6.12 shows the fits to the self correlation function of the kinetic energy in the x-direction for the simulation involving $N = 1000$ ions with charge $\sqrt{15}e$ in a trap with frequencies $\{2.0, 2.3, 1.5\}$ kHz and cloud temperature 4.3 K.

We repeat the above process with simulations of the same ion cloud at various ion cloud temperatures. We then fit all the simulation results to the form in Equation 6.15 to obtain the fit parameters:

$$A = 0.41(1), \tag{6.17a}$$

$$B = 19(5). \tag{6.17b}$$

The fit is shown in Figure 6.13. For completeness, the density-weighted density used in the fits shown in

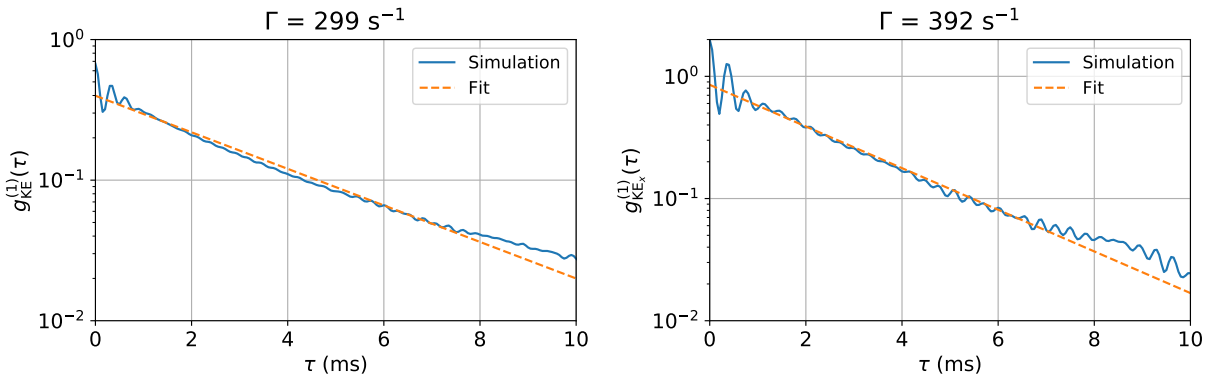

Figure 6.12: **Fits to the self correlation function of the kinetic energies.** Right: the self correlation function of the kinetic energy in the x-direction as given by Equation 6.16. Left: the same thing as the right plot, but evaluated for the total kinetic energy.

Figure 6.13 is shown in Figure 6.14.

We now have a few collision-related rates, and this was a long section, so here is a summary:

Collisional narrowing, $\Gamma_{\text{c.n.}}$. This is the rate at which the naïve decoherence is suppressed. We wish to get an expression for this as a function of ion number density and temperature of the ion cloud. This can be extracted by fitting Equation 6.10b to our ensemble-averaged Ramsey phases.

Decay rate of self correlation function of kinetic energy in x-direction, Γ_{KE_x}. This is the rate at which the ions forget about their trajectories along the x-direction, corresponding to the rate at which they change their trajectories.

Collision rate with the AB ansatz, $\Gamma_{\text{col.}}$. This is given by Equation 6.15. The fit parameters A and B are obtained by fitting Γ_{KE_x} to a series of simulations (using scaled parameters to save on computational resources), and performing a global fit using Equation 6.15 to the obtained values of Γ_{KE_x}.

The three collision-related rates above are extracted through different means, and what remains now is to see if they are equivalent measures of each other. We shall extract these three rates from various instances of simulations, and perform a comparison across them.

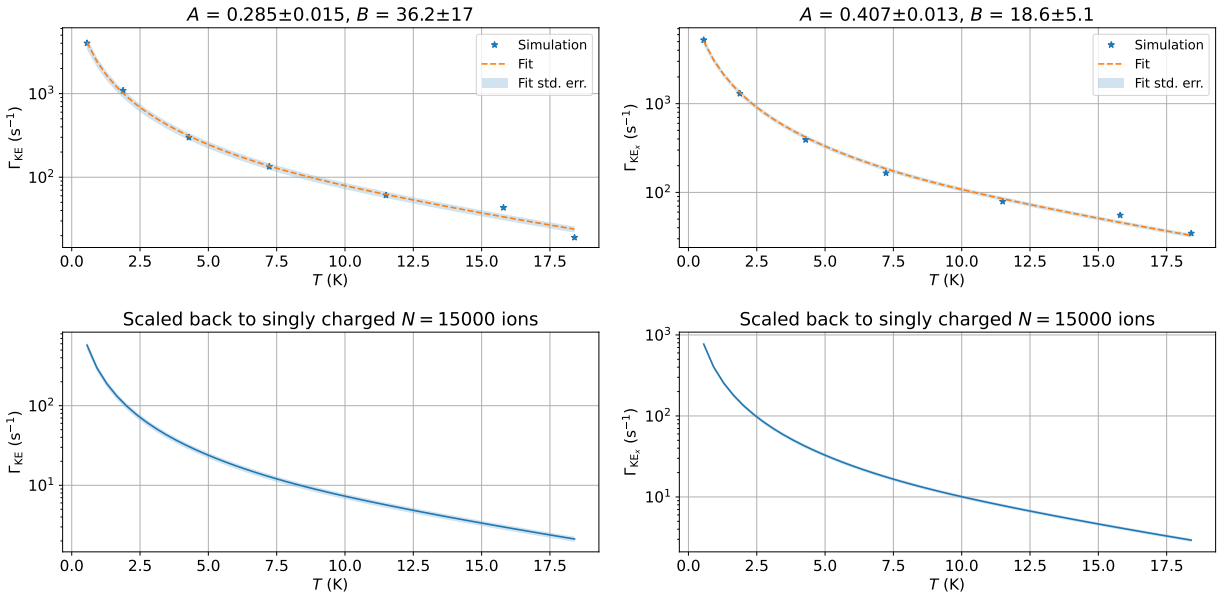

Figure 6.13: **Fit of Equation 6.15 to the decay rate of Equation 6.16 for the total kinetic energy (top left) and the kinetic energy in the x-direction (top right).** We simulated an ion cloud of $N = 1000$ ions with charge $\sqrt{15}e$ in a trap with frequencies $\{2.0, 2.3, 1.5\}$ kHz at various temperatures. The shaded region indicates the region spanned by the standard error of the fit parameters. The bottom plots are predictions of the decay rates of $N = 15000$ singly charged ions using the A and B parameters from the fit. There are a few points to note regarding the fit and scaling:

(1) The expression for κ used in the fits are $\frac{(Ze)^2}{4\pi\varepsilon_0} = \frac{15e^2}{4\pi\varepsilon_0}$. When scaling back to singly charged ions, κ should go back to its original definition of $\frac{e^2}{4\pi\varepsilon_0}$.

(2) The parameters A and B are dimensionless numbers independent of the ion cloud parameters $\tilde{n}$, m, and β, hence the values obtained for A and B from this fit should apply to all ion clouds of similar aspect ratio regardless of their cloud parameters.

(3) All information on the trap frequencies are already embedded in $\tilde{n}$, so as long as $\tilde{n}$ is correctly evaluated, A and B should be good parameters to use regardless of trap frequencies.

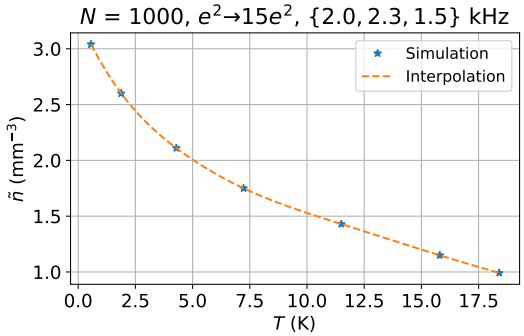

Figure 6.14: **Density-weighted density for an ion cloud.** The ion cloud has $N = 1000$ ions with charge $\sqrt{15}e$ in a trap with frequencies $\{2.0, 2.3, 1.5\}$ at various temperatures.

6.5.3 Comparison of various collision-related rates

Table 6.2 compares the predictions of Equations 6.15 and 6.17 against simulations of ion clouds with various cloud parameters. Since these are simulations of just $N = 1000$ ions, the collision rates are low, so they take a long time to reach thermal equilibrium. Simulating just one case took about half a day of work.

Case	RMS sizes (mm)	Γ_{KE_x} (s^{-1})	$\Gamma_{\mathrm{col.}}$ (s^{-1})	$\Gamma_{\mathrm{c.n.}}$ (s^{-1})	γ_{lin} $(\mathrm{s{\cdot}Hz})^{-1}$
Loose A	(1.3, 0.94, 1.8)	60	50	43	0.016
Tight A	(0.96, 0.87, 1.3)	40	55	82	0.011
Tight B	(1.2, 1.0, 1.7)	21	10	10	0.016

Table 6.2: **Comparison of simulation results of different ion cloud parameters against prediction from Equations 6.15 and 6.17.** The "loose" and "tight" cases corresponds to trap frequencies of {1.3, 1.7, 1.0} kHz and {2.0, 2.3, 1.5} kHz, respectively. The "A" cases correspond to a cloud temperature of about 2 K, while the "B" case correspond to a cloud temperature of about 5 K. All the above cases are simulations of $N = 1000$ singly charged ions. Γ_{KE_x} is obtained from a fit to Equation 6.16. $\Gamma_{\mathrm{col.}}$ is obtained from the prediction of Equations 6.15 and 6.17. $\Gamma_{\mathrm{c.n.}}$ and γ_{lin} are obtained from fitting the corresponding versions of Figure 6.10.

Note that all three rates Γ_{KE_x}, $\Gamma_{\mathrm{col.}}$, and $\Gamma_{\mathrm{c.n.}}$ agree with each other very well to within a factor of two. This is very settling, and not surprising. The former two should agree with each other since $\Gamma_{\mathrm{col.}}$ was obtained through Equations 6.15 and 6.17, the latter of which was obtained through a fit to Γ_{KE_x} in Figure 6.13. Their stark agreement further shows that Equation 6.15 has captured all the physics related to the ion cloud parameters. The first and the last rates should also agree because of the discussion above that led to Equation 6.16. At last, we now have a way to connect measurable quantities from simulations (Γ_{KE_x}) to a prediction model in closed analytical form ($\Gamma_{\mathrm{col.}}$) to the real physical effect that we care about ($\Gamma_{\mathrm{c.n.}}$).

Towards the end of this study, the Gen. II experiment had more important things to do (e.g. measure the eEDM) so we did not pursue this further with experiments. It is unfortunate that we could not do a clean 1-to-1 comparison of our model with experiments. Nevertheless, we are still equipped a self-consistent model that we can use in the design of the Bucket Brigade.

Before we move on to talk about the design of the Bucket Brigade, there remains one loose end. We see how the temperature of the ion cloud goes into Equation 6.15, but it has been known for a long time that ion clouds in Paul traps heat up [71–76]. The next section is devoted to understand the heating of ion

clouds in Paul traps.

6.5.4 Heating of ion clouds in Paul traps

When ion clouds heat up, they expand and can feel more of the spatial field inhomogeneity in the trap, leading to faster decoherence for the ensemble of Ramsey fringes. The short explanation for heating in Paul traps is that ion-ion collisions in Paul traps interrupt the RF micromotion of the ions, and redistribute some micromotion energy into the secular motion degree of freedom. The ions then launch into new Mathieu trajectories after the collision. Since micromotion is a driven motion, Paul traps can do work on the ions through ion-ion collisions and heat the ion cloud up. We shall attempt to model heating of ion cloud in our Paul trap. Borrowing wisdom from Chen *et al.* [71] the heating rate is given as:

$$\dot{T} = \Gamma_{\text{col.}} \bar{\epsilon} (T + \eta T_{\text{ex}}), \tag{6.18}$$

where

- $\Gamma_{\text{col.}}$ is the ion-ion collision rate;
- $\bar{\epsilon} \approx \frac{2}{3}\left(1 + q_0^{2.24}\right)$, for $q_0 \leq 0.4$, is the average fractional increase in the energy of an ion per collision;
- q_0 is the Mathieu q_0 parameter (refer to Appendix A);
- $\eta \approx 3/5$, for small q_0, from equipartition theorem with 5 partitions in total: 3 in secular motion and 2 in RF micromotion;
- T_{ex} is the temperature of the excess micromotion [77], which we take to be zero in our ion cloud (no DC field displacing ions from RF null; no excess micromotion).

A big caveat in using Equation 6.18 is that it was obtained from experiments performed on ion crystals. This is a region where the ions are cold enough that they condense into a crystalline structure. We operate at much higher ion cloud temperatures, so our ions are closer to being a "gas" than a crystalline "solid". Nevertheless, we shall use Equation 6.18 and see how far we can go. Figure 6.15 compares the prediction of Equation 6.18 with temperature measurements taken in the Gen. II setup, and shows a decent agreement between model and experiments.

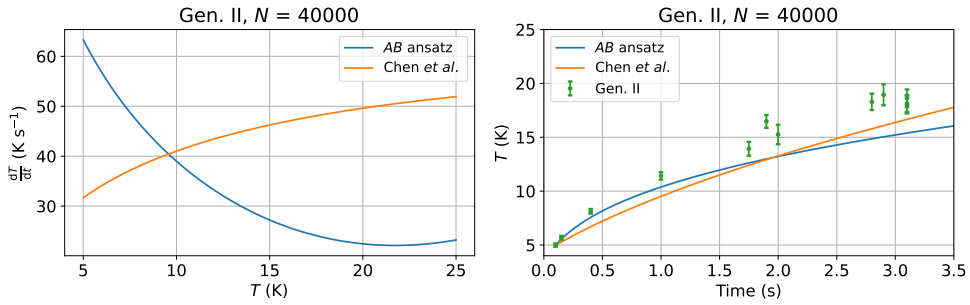

Figure 6.15: **Ion cloud heating rates predicted by Equation 6.18 and comparison to experiment.** The yellow plots use the original equation in Chen *et al.* [71] with the Chandrasekhar-Spitzer collision rate, while the blue plots correspond to using $\Gamma_{\text{col.}}$ (given by Equations 6.15 and 6.17) for the collision rate. Chen *et al.* used a slightly unconventional definition of $\rho_{\max}$ in their paper that is a factor of 4 smaller than the usual definition of the maximum ion number density in a Paul trap. The yellow plots here are without the correction. Comparison with temperature measurements from the Gen. II experiment shows good support for using Equation 6.15 for $\Gamma_{\text{col.}}$ in Equation 6.18. The total ion number in the experiment is about $N = 40000$. The temperature measurements are performed with Doppler broadening measurements with a laser shining along one axis of the ion cloud.

One way to reduce the heating rate would be to reduce $\bar{\epsilon}$ in Equation 6.18. This can be done by reducing the Mathieu q_0 parameter subjected to the same secular frequencies. We can show with Equation A.4 that

$$q_0 = \frac{2}{\Omega}\sqrt{2\omega_i^2 + \omega_z^2} \quad , \quad i \in \{x, y\} \tag{6.19}$$

where Ω is the trap RF angular frequency, and ω are the secular trap angular frequencies. This means that we can keep the secular frequencies the same, but have a smaller q_0 by increasing Ω. Unfortunately, substituting Equation 6.19 into the expression for $\bar{\epsilon}$ shows that we do not win with increasing Ω as quickly as we would like (Figure 6.16); it looks like we are stuck with the heating rate in our trap.

Now that we have all the ingredients required (from the discussion at the end of Section 6.2.2.2), we can proceed to use the model for decoherence on the design of the Bucket Brigade.

6.5.5 Relevance to the Bucket Brigade and ThF^+

The current plan for an eEDM experiment with ThF^+ in the Bucket Brigade involves about 1500 ions per bucket. We assume that we can recreate the same conditions as the Gen. II experiment and load 1500 ions into the Bucket Brigade at 5 K. Simulation results show that such an ion cloud has only weak mean

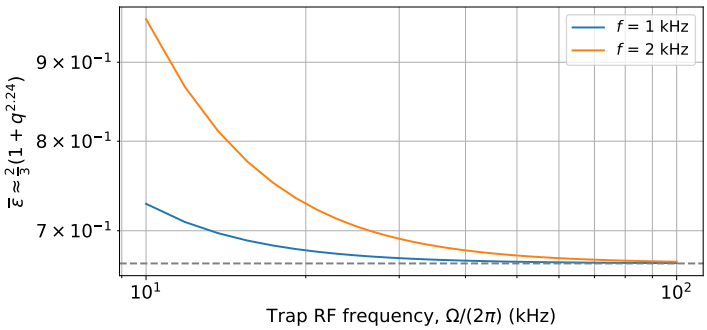

Figure 6.16: **Plot of $\bar{\epsilon} \approx \frac{2}{3}\left(1+q_0^{2.24}\right)$ against Trap RF frequencies.** We plan to operate at $\Omega = 2\pi \times 50$ kHz. The plot shows that it does not help us much by going to higher RF frequencies. The grey dashed line shows the lower bound of $\bar{\epsilon} = 2/3$.

field effects, and can be modelled as an ion cloud with a 3D Gaussian number density distribution:

$$n_{\text{thermal}}(x,y,z) = \frac{N}{(2\pi)^{3/2}\sigma_x\sigma_y\sigma_z}\exp\left[-\frac{1}{2}\left(\frac{x^2}{\sigma_x^2}+\frac{y^2}{\sigma_y^2}+\frac{z^2}{\sigma_z^2}\right)\right], \tag{6.20}$$

where N is the total ion number, and σ_i, $i \in \{x,y,z\}$ are the widths of the cloud, which are related to the temperature of the cloud through:

$$\frac{1}{2}k_BT = \frac{1}{2}m\omega_i^2\sigma_i^2 \quad \Longrightarrow \quad \sigma_i = \frac{1}{2\pi f_i\sqrt{m\beta}} = 3\text{ mm}\times\frac{2\text{ kHz}}{f_i}\times\sqrt{\frac{T}{50\text{ K}}}. \tag{6.21}$$

Using Equations 6.20 and 6.21, we can show that the density-weighted density for such a thermal cloud is given by:

$$\tilde{n}_{\text{thermal}} = N\, f_x f_y f_z\, (\pi m\beta)^{3/2}. \tag{6.22}$$

Using Equation 6.22 in 6.18, we obtain the plots shown in Figure 6.17.

Now that we know how the ion cloud sizes change with time with the initial ion cloud and trap parameters that we plan to use in the Bucket Brigade, we can use this information in Equation 6.15 to estimate the rate of collision, and hence collisional narrowing, of our ions in the trap. The results are shown in Figure 6.18.

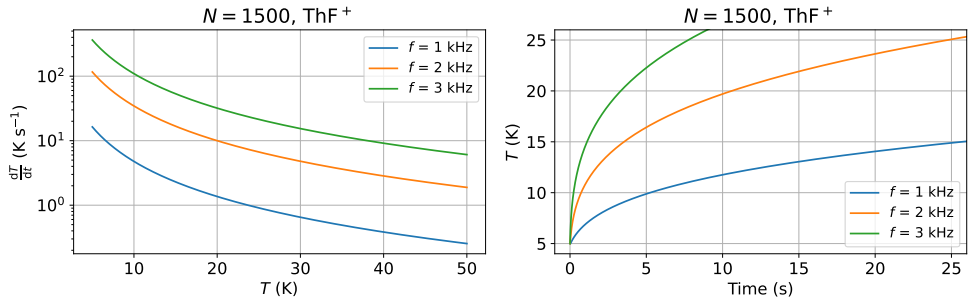

Figure 6.17: **Ion cloud heating rates predicted by Equation 6.18 for ThF^+ in the Bucket Brigade at various secular trap frequencies.** For simplicity, the plots assume spherical clouds, i.e. $f_x = f_y = f_z = f$.

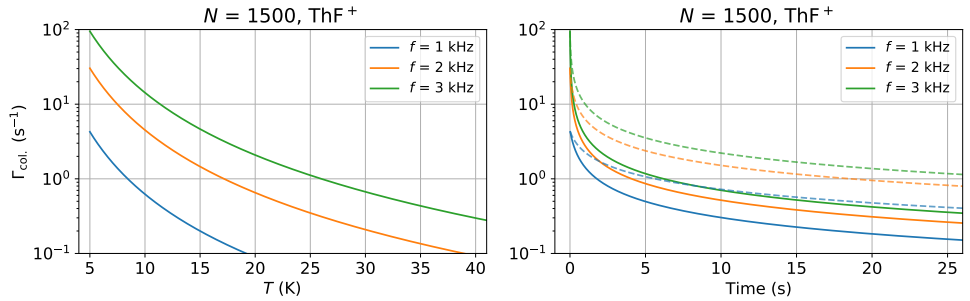

Figure 6.18: $\Gamma_{\text{col.}}$ **predicted by Equation 6.15.** The plot on the left is a direct application of Equation 6.22 on 6.15, while the plot on the right (solid lines) accounts for the time-dependence of the temperature of the ion cloud given in Figure 6.17. The dashed lines are the "time-averaged" $\Gamma_{\text{col.}}$ given by $\overline{\Gamma_{\text{col.}}}(t) := \frac{1}{t}\int_0^t \Gamma_{\text{col.}}(t')\,\mathrm{d}t'$ to give a rough sense of the effective collision rate.

6.6 Further discussion

We now have decent confidence in our decoherence model, having checked our model predictions with simulations and experiment results on several fronts. We are already applying our model in preliminary investigations of decoherence in the Bucket Brigade.

We understand how our ion cloud dynamics can suppress some form of decoherence through ion-ion collisions. Ironically, ion-ion collisions can also turn out to be a source of decoherence through Berry's phase [25]. Before we move on to discuss the design of the Bucket Brigade, it serves to cover some other points

related to decoherence.

6.6.1 Collisions that could change m_F

In the above sections, we assumed that our molecules remain in the $m_F = \pm 3/2$ subspace, even with collisions. This is not strictly true. Handwavingly, when two ions come together, there is a characteristic time scale of the collision given by the ratio of the characteristic collision distance and the characteristic speed of the collision. The physics is as follows.

(1) The molecular ions are polarized by an electric field. The quantization axis is also determined by the direction of the electric field.

(2) When another ion approaches, the net electric field direction as seen by the first ion will be modified by the electric field of the second ion.

(3) If the approach is adiabatic compared to typical energy scales in the molecule, then the molecule can track its quantum state adiabatically throughout the approach. After the ions separate, the first ion will still stay in its initial quantum state.

(4) However if the approach is not adiabatic compared to typical energy scales in the molecule, then the quantum state of the first ion will be projected diabatically onto the new polarization axis during the approach. After the ions separate, the first ion will then be left in a state that can be very different from its initial one.

(5) Here comes the handwaving part. Suppose the incoming ion has comparable velocity components in the transverse and longitudinal directions w.r.t. the approach, such that far away from the first ion, we have $\frac{1}{2}k_BT = \frac{1}{2}m(v_\perp^2 + v_{||}^2)$ with $v_\perp \sim v_{||}$. At closest approach, all the longitudinal kinetic energy is converted into Coulomb repulsion potential energy $\frac{1}{2}mv_{||}^2 = \frac{e^2}{4\pi\epsilon_0 r_{\min}}$. We can define a transit time to be the time it takes for the incoming ion to move by $2r_{\min}$ in the transverse direction, i.e. $r_{\min}$ in

the transverse direction on both sides of the closest longitudinal approach:

$$t_{\text{trans.}} \sim \frac{2r_{\min}}{v_\perp} \quad , \quad \frac{1}{2}mv_\perp^2 \sim \frac{1}{2}\times\frac{1}{2}k_{\text{B}}T \quad , \quad \frac{e^2}{4\pi\epsilon_0 r_{\min}} \sim \frac{1}{2}mv_\perp^2$$
$$= \frac{2\sqrt{2}}{\pi}\frac{e^2\sqrt{m}}{\epsilon_0}\frac{1}{(k_{\text{B}}T)^{3/2}}$$
$$\approx 3\times 10^{-5}\cdot T^{-3/2},$$

where T is the ion cloud temperature in kelvins, and $t_{\text{char.}}$ in seconds.

In our experiment, our molecules are in the $m_F = \pm 3/2$ subspace. The energy scale of interest is the Stark splitting between the $m_F = \pm 3/2$ states and the $m_F = \pm 1/2$ states. From Figure 5.4, this energy scale in ThF^+ (HfF^+) is 10 MHz at $\mathcal{E}_{\text{rot}} = 60$ V/cm (20 MHz at $\mathcal{E}_{\text{rot}} = 58$ V/cm). Demanding $1/t_{\text{trans.}}$ to be smaller than the aforementioned energy scales, we demand the ion cloud temperature to be less than 50 K for ThF^+ (80 K for HfF^+). These are not crazy high temperatures. For ion clouds with temperatures higher than this, there is a significant chance that ion-ion collisions could drive our molecules out of the eEDM-sensitive subspace, leading to T_1 type losses. The ions could also come back to the $m_F = \pm 3/2$ subspace after a few collisions, mimicking a T_2 loss signal.

6.6.2 Spatial sampling by an ion in an anharmonic trap

In all the above analysis, we assumed that our ion motions are highly non-ergodic in the absence of ion-ion collisions, where the ion only samples a very limited volume of the ion cloud. We had to invoke ion-ion collision to throw the ions into different trajectories, whereupon we introduce collisional narrowing, a mechanism that reduces the spread of the mean Ramsey frequencies of the ion ensemble. However, ion motion in an anharmonic trap can sample more of the ion cloud than a harmonic one. We compare the trajectories of an ion in two traps in Figure 6.19.

With an anharmonic trap, the ion naturally "resets" its trajectory and samples a larger space within the ion cloud. This would give rise to a decoherence narrowing effect similar to that of collisional narrowing. The total energy of the ion is still unchanged throughout the secular motion, though.

In our ion trap, sources of anharmonicities could come from (i) mean field effects from the ions, (ii) small size of the trap as compared to the size of our ion cloud, such that ions at the edge of the ion cloud

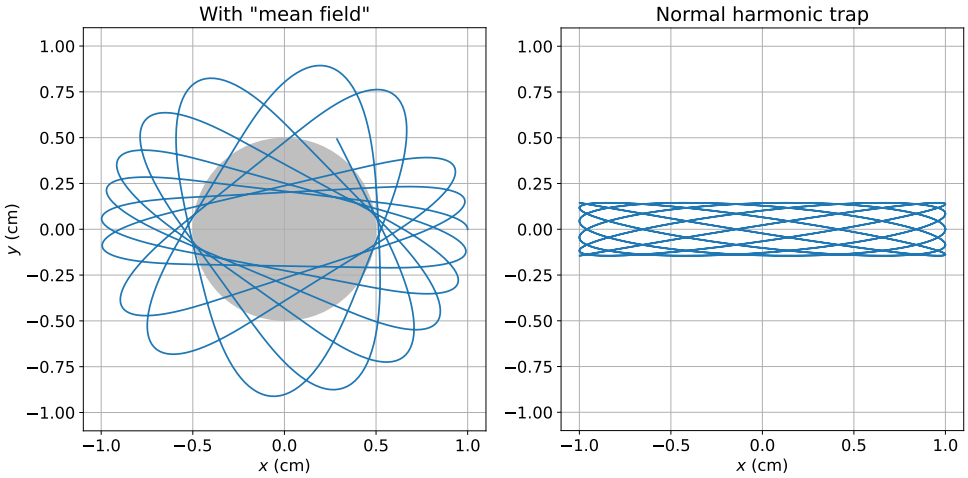

Figure 6.19: **Simulated trajectories of an ion in two different traps.** The ion has the same initial conditions in both the left and right plots: $\mathbf{v}(t=0) = 10\,\hat{y}$ m/s, and $\mathbf{r}(t=0) = 1\,\hat{x}$ cm.

Right: the confining field has the form $\mathcal{E}_i = -\frac{m\omega_i^2}{e} r_i$, where $\omega_i = 2\pi \times 1$ kHz and $2\pi \times 1.1$ kHz for the x and y directions, respectively. The area traced out by the Lissajous figure is rather small; the ion only samples a very limited volume of the entire space.

Left: the confining field has the form $\mathcal{E}_i(r > R_0) = \frac{m\omega_i^2}{e}\left(-r_i + \frac{R_0^3}{r^3} \cdot r_i\right)$, where $R_0 = 5$ mm, and $\boldsymbol{\mathcal{E}}(r \leq R_0) = \mathbf{0}$. This is a very simplified model of the field seen by a hot ion in a very cold ion cloud such that mean field effects dominate (like those shown in Figure 6.2). The region where mean field effects null out fields is indicated by the grey circle $r \leq R_0$. The ion samples more of the volume of the entire space, and its direction of motion also "precesses" around.

can sample the deviation of the trapping potentials from a true quadrupole, and (iii) other imperfections within our trap.

6.6.3 Difficulty in measuring ion cloud properties in the experiment

To match experiment results to the model we developed in this chapter, we would like to be able to measure a few properties of the ion cloud: (i) temperature of the ion cloud along all three principal axes[9] , and (ii) ion cloud density. However, the tools at our disposal are rather limited:

Thermal Doppler broadening of laser transition. In the Gen. II experiment, a laser beam with a linewidth narrower than the thermal Doppler width goes down the axial direction of the trap to serve as a depletion laser for the doublets. We can infer the temperature of the ion cloud by mea-

[9] In addition to serving as an input parameter into our model, measuring in all three axes tells us if the ion cloud is in thermal equilibrium in all three dimensions.

suring the width of the transition. However, we can only do this for the axial direction. We could have a laser going in from the radial direction, but RF and rotation micromotion also broadens the transition.

Velocity map imaging of ions on ion detector. With our long time-of-flight in the prototypical Bucket Brigade (Section 7.9), we can perform velocity map imaging of ions, where the ion positions on our ion detector corresponds to their velocity right before ejection from the trap. However, stray charges along the flight path contribute to lensing effects that only give us velocity mapping along one transverse axis (y) and not the other (x). Spatial variation of field strengths of the voltages seen by the ions during the ejection also contribute to axial focusing effects. Furthermore, there could also be ion-ion repulsion during the flight after the trap is turned off. All these effects complicate the interpretation of our measurements on the actual temperature and ion number density of our ion cloud.

We need to sharpen our detection tools to push our understanding of our ion cloud up a notch. This would involve serious planning and significant changes to the current design of the setup. While we work on this at the back of our minds, let us proceed to look at the electrode design of the Bucket Brigade.

Chapter 7

Design of the Bucket Brigade

7.1 Introduction

The Bucket Brigade is the second of the two main upgrades from Gen. II to III. In contrast to the Paul traps that we have been using in the Gens. I, II, and ThF/ThF$^+$ spectroscopy setup, the Bucket Brigade (i) is much larger in scale, (ii) has the capability to translate ions across meter-scale distances along the trap axis, and (iii) allows for near-continuous multiplexed operation. Furthermore, all the above has to be done in an environment that is highly controlled and devoid of noise for precision measurements that aim to surpass our current Gen. II record. We are requiring a lot out of the Bucket Brigade.

Translating ions within a multi-sectioned trap is not new. Multiplexing operations on ions at different parts of the multi-sectioned trap is also not new. These were already envisioned in the quantum CCD architecture [78] two decades ago. Midway through the pandemic, the first trapped ion quantum CCD computer architecture was also demonstrated [79]. Not long after, news also came from the industry side (Quantinuum) with their version of the quantum CCD ion chip design [80]. Needless to say, we are neither the first nor the only ones working on a multiplexed ion trap based on the quantum CCD architecture. But, ours is the biggest.[1]

We do not aim to design the perfect Bucket Brigade from the get go. We do not claim to have foresight at such a level. We understand the weight of this big undertaking. We also take seriously all the helpful comments from our critics. We shall take the design one step at a time. We will start to scratch the surface

[1] One can argue that large scale experiments with storage rings count as multiplexed ion traps. However, the author wishes to point out that ion confinement in storage rings is implemented rather differently (not of quantum CCD-type) from all the aforementioned traps, so storage rings should be treated as a separate class.

of the design with this chapter.

This chapter is structured as follows. First we will look at performing axial confinement and ion translation with Rings (Section 7.2). Next, we will look at radial confinement and introducing the rotating electric field with Rods (Section 7.3). We then introduce the baby Bucket Brigade, a prototype of the Bucket Brigade (Section 7.4). Thereafter we have an overview of the electrode drivers to see how we control voltages on all our electrodes (Section 7.5). Finally, we introduce a new tool in our JILA eEDM kit, parametric excitation of ions (Section 7.6).

7.2 Rings: Axial confinement & Translation of ions

Axial confinement in linear Paul traps are typically introduced with end caps: electrodes on both ends of the trap in the axial direction. These end caps are placed at a positive DC voltage w.r.t. the DC ground on the radial electrodes to confine positively charged ions. On ion chips based on the quantum CCD architecture, the "end caps" are displaced away from the trap axis, but the potentials added onto them still allows for axial confinement of the ions. There are also many more such "end caps", each at a different potential. These potentials can be spatially modulated to create the various ion trap wells required of a multiplexed ion trap.

We employ a similar strategy. We shall have Rings to serve as our "end caps". To understand our design constraints, we will first study the fields in our cylindrically symmetric setup. We start with static axial confinement first. We begin with the case where the Rings are "continuous" in the axial direction (Section 7.2.1) to understand how the axial trap secular frequency depends on the basic design parameters. We will then work with the more realistic Rings that are discretized (Section 7.2.2) to see how discretizing the Rings change the analysis. Subsequently, we explain how we translate ions by modulating the potentials on the discretized Rings (Section 7.2.3). Finally, we end off with a brief discussion on the shielding effects of the radial electrodes on the fields generated by the Rings (Section 7.2.4). Without spoiling too much, Figure 7.1 shows a CAD drawing of the Bucket Brigade for a quick visualization of the critical components involved and definitions of some of the coordinates to be used in this section.

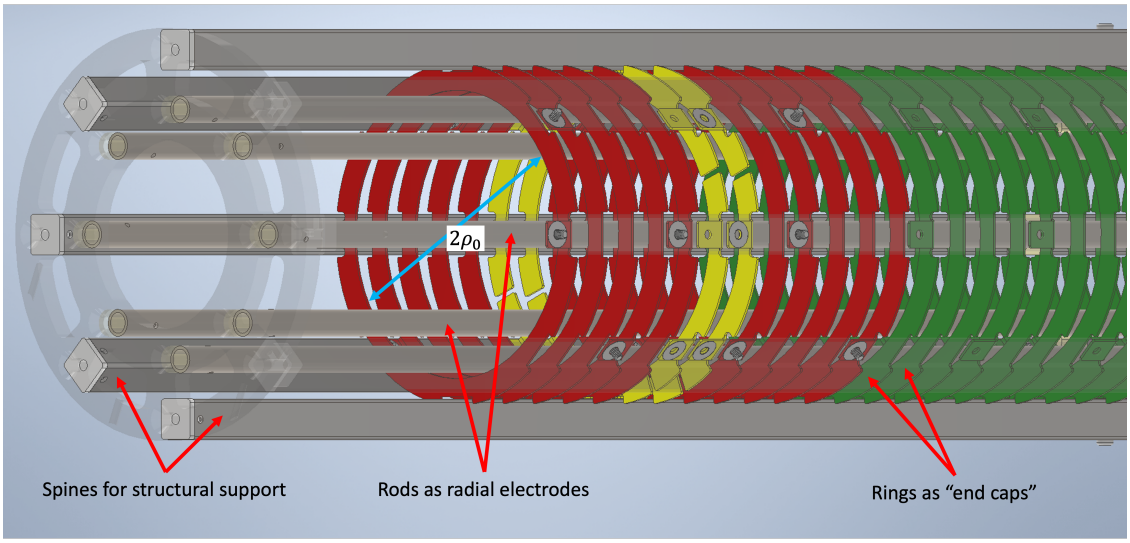

Figure 7.1: **Spoiler: perspective view of a CAD drawing of the Bucket Brigade to visualize the relevant relationship between various electrodes.** The inner diameter of the Rings is $2\rho_0$. Some of the structural support is hidden for a better view of the Rings. The radial distance from the trap axis is defined to be ρ, and the axial coordinate towards the right along the trap axis is z. The Rings colored red are the Special Rings; yellow Rings are the Quadrant Rings; green rings are the Translation Rings; all to be discussed in more detail in Section 7.4.

7.2.1 "Continuous rings"

7.2.1.1 Analytic solution

We begin with a simple model, where we solve for the potential inside the volume of a long cylindrical electrode, where we impose an arbitrary boundary condition on the inner surface of the long cylinder. This is equivalent to the limit of having infinitely many Rings that are infinitely thin and infinitely close to each other. The potential applied on the electrode holds the form:

$$V(\rho_0, z) = V_0 \sin kz. \tag{7.1}$$

Using separation of variables on Laplace's equation in cylindrical coordinates gives:

$$\left(\partial_\rho^2 + \frac{1}{\rho}\partial_\rho + \frac{1}{\rho^2}\partial_\phi^2 + \partial_z^2\right) P(\rho)\Phi(\phi)Z(z) = 0. \tag{7.2}$$

Now we need to solve the above with the boundary condition given by Equation 7.1.

Cylindrical symmetry dictates that $\Phi(\phi) = 1$. Assuming that the trap is infinitely long, the sinusoidal modulation of potential at the boundary implies that $Z(z) = \sin kz$, where $k = \frac{2\pi}{\lambda}$, with λ the periodicity of

the potential modulation in the axial direction. The solution now looks like:

$$V(\rho, z) = P(\rho) \sin kz.$$

Now the partial differential equation for $P(\rho)$ is:

$$\left(\partial_\rho^2 + \frac{1}{\rho}\partial_\rho\right) P = k^2 P.$$

The solutions to the above are the modified Bessel functions.[2] Further demanding that the potential at $\rho \to 0$ to be finite, the solution then holds the form:

$$V(\rho, z) = \alpha J_0(ik\rho) \sin kz,$$

where α is a constant of proportionality, and $J_0(x)$ is the zeroth order Bessel function of the first kind. Matching the above to the boundary condition at the electrode with Equation 7.1 gives:

$$V(\rho, z) = V_0 \frac{J_0(ik\rho)}{J_0(ik\rho_0)} \sin kz. \tag{7.3}$$

To aid us in the later sections, we note a few approximate forms of the Bessel function in the two extreme limits:

$$J_0(ik\rho) = \begin{cases} 1 + \frac{(k\rho)^2}{4} + \frac{(k\rho)^4}{64} + \mathcal{O}(\rho^6) & k\rho \ll 1, \\ \frac{e^{k\rho}}{\sqrt{2\pi k\rho}} \left[1 + \mathcal{O}\left(\frac{1}{k\rho}\right)\right] & k\rho \gg 1. \end{cases} \tag{7.4}$$

The small $k\rho$ expression will be useful in evaluating the potential in the vicinity of the ion cloud, while the large $k\rho$ expression will be useful in simplifying the expression for the potential on the boundary.

It is useful to note that voltage waveforms on the Rings with larger k (smaller λ) will decay much faster in amplitude as we approach $\rho \to 0$. Figure 7.2 shows a quick comparison of the waveforms with various k and the relevant coordinate parameters.

7.2.1.2 Dependence of axial frequency on design parameters

We intend to work with an ion cloud that is small compared to the periodicity of the spatial modulation of the axial potential, i.e. $\Delta z \ll \lambda = \frac{2\pi}{k}$ (see Figure 7.2). Expanding the potential along the axis in z about

[2] The interested reader can refer to Jackson's Classical Electrodynamics 3rd edition, equations 3.100 and 3.101.

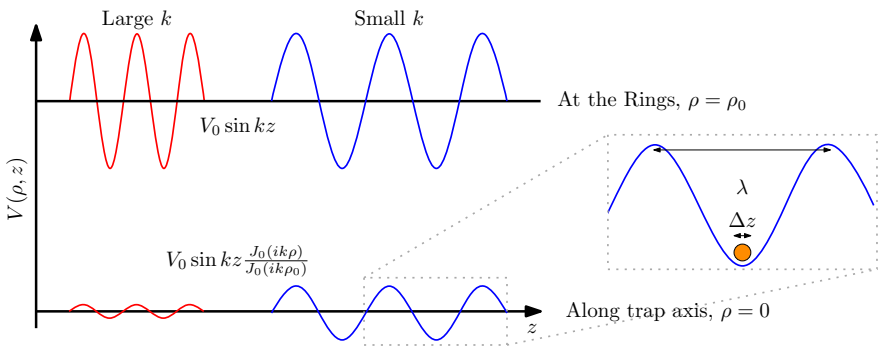

Figure 7.2: **Schematic comparison of waveform amplitude decay from the Rings with various k.** Red (blue) wiggles show potential waveforms with large (small) k. The upper trace shows $V(z)$ as applied onto the "continuous rings" electrode, and the lower trace shows how this potential would look like along the trap axis, $\rho = 0$. The orange disk indicates the size of our ion cloud, which is small compared to $\lambda = 2\pi/k \gg \Delta z$. Within the vicinity of the ion cloud center, the potential can be approximated as harmonic.

a potential minimum gives:

$$V(\rho, z) \approx \text{constant} + V_0 \frac{J_0(ik\rho)}{J_0(ik\rho_0)} \frac{(k \cdot \Delta z)^2}{2}.$$

Plugging the above into the equation of motion:

$$m\, \partial_t^2(\Delta z) = -e\, \partial_{\Delta z} V = -eV_0 k^2 \frac{J_0(ik\rho)}{J_0(ik\rho_0)} \cdot \Delta z,$$

implies that the oscillation frequency at $\rho = 0$ is:

$$\omega = \sqrt{\frac{eV_0 k^2}{m} \frac{1}{J_0(ik\rho_0)}} = \sqrt{V_0} \sqrt{\frac{4\pi^2 e}{m\lambda^2} \frac{1}{J_0(ik\rho_0)}} \sim \sqrt{V_0} \cdot \sqrt{\frac{e}{m}} \cdot \left(\frac{\rho_0}{\lambda^5}\right)^{1/4} \cdot e^{-\frac{\pi\rho_0}{\lambda}}, \tag{7.5}$$

where in the last step, we expanded the Bessel's function out ($k\rho_0 \gg 1$) for a more intuitive feel of how the overall expression scales with the relevant parameters. Using the exact expression, we show values of axial frequencies for some combination of the design parameters in Table 7.1.

If we wish to operate in a experiment parameter space familiar to us in the Gens. I and II experiment, we want to aim for between 1 and 10 kHz. Fortunately, the numbers show that we can get these frequencies with very modest voltages applied if we pick the right geometry design parameters.

7.2.1.3 Peak-to-peak voltage along trap axis

One important aspect of the Bucket Brigade is that ions need to stay within their bucket. We do not want ions to spill over to the neighboring bucket. We want to know the "axial energy" of an ion at which it

$\rho_0 \setminus \lambda$	2 cm	4 cm	6 cm	8 cm	10 cm	12 cm
1 cm	13200	11800	9080	7190	5910	4990
2 cm	3320	6620	6620	5910	5170	4540
3 cm	767	3370	4410	4510	4270	3940
4 cm	172	1660	2830	3310	3400	3310
5 cm	37.8	802	1780	2380	2650	2720
6 cm	8.22	383	1110	1690	2030	2210
7 cm	1.78	182	682	1190	1550	1770
8 cm	0.382	85.8	419	830	1170	1420
9 cm	0.0818	40.3	256	578	884	1120
10 cm	0.0175	18.9	156	401	664	890

Table 7.1: **Axial frequencies at various geometries.** The numbers shown here are $\frac{\omega}{2\pi\sqrt{V_0}}$ in units of Hz. For example, for an electrode modulation peak-to-peak voltage at $V_{\text{pp}} = 2V_0 = 2$ V, distance to electrode from trap axis $\rho_0 = 7$ cm, modulating wavelength $\lambda = 8$ cm, the axial angular frequency is $2\pi \times \sqrt{1} \times 1190 = 2\pi \times 1.19$ kHz. Mass is assumed to be that of ThF^+.

spills over classically from one potential well to the next. We have, in the convenient unit of kelvins:

$$T_{\text{max}} = \frac{1}{k_B} \frac{eV_{\text{pp}}}{J_0(ik\rho_0)}.$$

The maximum energy of the ions that can be trapped within this potential well for typical values of ρ_0 and λ is shown in Table 7.2.

Even though we want to work with design parameters such that our ions of a certain temperature do not spill over to the neighboring buckets, the ions will be sampling the anharmonic part of the axial trap well before they start spilling over. We do not want the ions to sample anharmonic parts of the trap for fear of systematic effects on our eEDM measurement (Section 7.2.2.2). The numbers above serve only as a hard limit (instead of the recommended values), beyond which we have no hope of using the Bucket Brigade for a multiplexed ion trap experiment.

If the ions in the Bucket Brigade have similar thermal energies as compared to the Gens. I and II experiments, we expect ion cloud temperatures between a few kelvins to a few hundred kelvins. Fortunately, the numbers show that our ions will not be spilling over to neighboring buckets with very modest voltages applied if we pick the right geometry design parameters.

$\rho_0 \setminus \lambda$	2 cm	4 cm	6 cm	8 cm	10 cm	12 cm
1 cm	4230	13500	17900	20000	21100	21700
2 cm	266	4230	9520	13500	16200	17900
3 cm	14.2	1100	4230	7860	11000	13500
4 cm	0.711	266	1740	4230	6980	9520
5 cm	0.0344	62.2	689	2190	4230	6440
6 cm	0.00163	14.2	266	1100	2500	4230
7 cm	0.0000763	3.19	101	544	1450	2730
8 cm	3.53×10^{-6}	0.711	38.1	266	831	1740
9 cm	1.62×10^{-7}	0.157	14.2	129	472	1100
10 cm	7.37×10^{-9}	0.0344	5.26	62.2	266	689

Table 7.2: **Potential barrier of the wells along the trap axis.** The numbers are expressed in temperature for an electrode peak-to-peak voltage of $V_{\text{pp}} = 2$ V. For example, if the distance to the electrode from trap axis is $\rho_0 = 7$ cm, and the modulating wavelength is $\lambda = 8$ cm, the ions start spilling over classically once their "axial energy" exceeds 544 K.

7.2.2 Discrete rings

Having infinitely many Rings would allow us to set voltages on all those Rings such that the ions along the trap axis will see a perfectly sinusoidal modulation of the potential along the axial direction. If we desire, we could even change the sinusoidal potential to something that looks more like a piece-wise series of harmonic traps, allowing the ions to feel a much bigger volume of trap harmonicity.

However, both the former and the latter have problems. The problem with the former is that we cannot control an arbitrarily large number of Rings in the experiment, it is simply impractical. We have to settle for a finite number of Rings, countable with about ten pairs of hands. This means that our "boundary condition"[3] will no longer be a single sinusoid with only one periodicity; it will be a sum of the various harmonics. This may complicate the analysis.

The problem with the latter is that Laplace's equation in cylindrical coordinates attenuates higher harmonics of spatial variations very quickly, as we will see in this section. To realize arbitrary modulation, like the piece-wise stitched harmonic traps, we will have to apply very high potentials on the Rings to fight against the attenuation. It looks like we have to settle for a simple sinusoidal modulation. However, it turns out that we can use this to our advantage to tackle the problem of the previous paragraph.

[3] The boundary conditions are strictly only introduced by the surfaces of the discrete Rings, and not the space between Rings. Nevertheless, if we look at the potential at $\rho < \rho_0$, the spatial modulation of the potential along the axial direction can be decomposed into the various harmonics of the fundamental periodicity.

7.2.2.1 Suppression of the higher harmonics

If we have an arbitrary cylindrically symmetric potential at $\rho = \rho_0$, we can decompose it into the various harmonics:

$$V(k, z, \rho_0) = V_0 + \sum_{n=1} \left(V_n^{(\mathrm{s})} \sin nkz + V_n^{(\mathrm{c})} \cos nkz \right).$$

Equations 7.3 and 7.4 then say that the potential at $\rho \ll \{\rho_0, \lambda\}$ is given by:

$$V(k, z, \rho) \approx V_0 + \sum_{n=1} \left(V_n^{(\mathrm{s})} \sin nkz + V_n^{(\mathrm{c})} \cos nkz \right) \cdot \left[1 + \frac{(nk\rho)^2}{4} + \frac{(nk\rho)^4}{64} \right] / \frac{e^{nk\rho_0}}{\sqrt{2\pi nk\rho_0}}. \tag{7.6}$$

We see that the attenuation factor increases exponentially with the order of harmonicity n. Hence, the waveform of the potential along the trap axis is predominantly that of the first harmonic unless we amplify the higher harmonics components at the source. The attenuation factors for various $\lambda = 2\pi/k$ are shown in Table 7.3.

$\lambda \setminus n$	1	2	3	4	5	6	7
8 cm	60.8	1.54×10^4	4.52×10^6	1.41×10^9	–	–	–
16 cm	4.67	60.8	937	1.54×10^4	2.61×10^5	4.52×10^6	7.95×10^7
50 cm	1.23	2.11	4.25	9.28	21.1	49.1	116

Table 7.3: **Attenuation factors of various harmonics.** The values shown are $J_0(ink\rho_0)$. They are evaluated at $\rho_0 = 7.5$ cm. The dashes are numbers that are too big and meaningless to include. For a reasonable bucket length of about $\lambda = 8$ cm, we see that any higher harmonics will be so quickly suppressed that the trapping potential along the trap axis is essentially a pure sinusoid.

A consequence of the above is that we do not need to have too many Rings per bucket. As alluded to earlier, having more Rings allows for more parameters for us to tweak to adjust the waveform of the potential, but since the attenuation of higher harmonics is so strong, we would have to apply unrealistic magnitudes for the higher harmonics to be able to take advantage of having more rings. Therefore, we have chosen to use a lucky[4] number of four Rings per bucket.

[4] Four is an unlucky number in Chinese numerology. It is homophonous with "death" in various Chinese languages like Cantonese, Teochew, and Mandarin. However, we shall associate the "death" with "uncertainties" in the Bucket Brigade design.

7.2.2.2 Anharmonicity

Lastly, we shall take a look at the harmonicity of the axial trapping potential. Since the potential takes the form of a sinusoid, expanding the potential about the potential minimum at $z_{\min}$ is:

$$V(k,z,\rho) \approx V_0 \left[-1 + \frac{[k(z-z_{\min})]^2}{2} - \frac{[k(z-z_{\min})]^4}{24}\right] \cdot \left[1 + \frac{(k\rho)^2}{4} + \frac{(k\rho)^4}{64}\right] \Big/ \frac{e^{k\rho_0}}{\sqrt{2\pi k\rho_0}}.$$

Evidently the first anharmonic term comes in as the fourth power of $z - z_{\min}$. Demanding the ratio of the fourth power term to the harmonic term to be less than 10% (1%) at 1 cm away gives $\lambda > 6$ cm (18 cm).

The anharmonicity does not hurt the trapping of the ions. However, it could hurt our precision metrology through systematic effects. Suppose in addition to a potential of the above form, we have an unwanted axial electric field from, say, imperfectly shimmed axial trapping voltages for the rings. The result of this additional axial electric field is that the minimum of the quadratic component of the trapping field will be displaced from that of the quartic component (see Figure 7.3 for a graphical explanation). For the ions

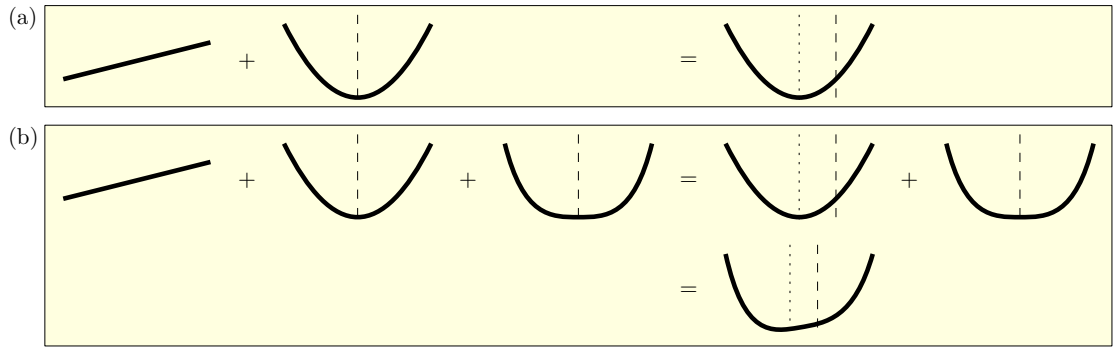

Figure 7.3: **Graphical representation of summing a linear potential to quadratic and quartic potentials.** (a) Adding a linear potential (uniform axial electric field) to a quadratic potential (harmonic axial trapping potential) results in a displaced quadratic potential. The dashed line indicates the the position of the original axis of symmetry, and the dotted line indicates mean position of ions sloshing around in the said potential. (b) Adding a displaced quadratic to a quartic potential (anharmonic part of the axial trap) results in a trap that is asymmetrical about the mean ion position (indicated by the dotted line).

to remain trapped axially, the time averaged axial electric field seen by the moving ions has to be zero, i.e. $\int_{z>0} \mathcal{E}_z \, \mathrm{d}t + \int_{z<0} \mathcal{E}_z \, \mathrm{d}t = 0$. However, since the potential is no longer symmetric, it has to spend more time on one side of the equilibrium position than the other, and we may end up with a non-zero time-averaged higher moment of the axial electric field $\int_{z>0} \mathcal{E}_z^3 \, \mathrm{d}t + \int_{z<0} \mathcal{E}_z^3 \, \mathrm{d}t \neq 0$. The result of having a non-zero time-averaged higher moment of $\mathcal{E}_z$ is that it can manifest as a systematic effect on our precision metrology (see Equation

8.15 and Section 8.3).

We shall leave this problem for another day; systematic effects are not of our immediate concern now. Future graduate students and post-docs may want to bookmark this section for when the time comes to study systematic effects (with ions) in the (prototypical) Bucket Brigade.

7.2.3 Translation of ions

Translating the ions is trivially simple, we modulate the potentials on the Rings in space and time:

$$V(z_n, t) = V_0 \sin(k z_n - 2\pi f_{\text{rep}} t)\,, \tag{7.7}$$

where z_n corresponds to the axial position of the n^{th} ring, and f_{rep} is the repetition rate of the Bucket Brigade experiment from Equation 1.1.

7.2.4 Shielding effect from Rods

In our analyses of the Rings, we have been neglecting the radial electrodes, the Rods. Our Rods will have RF voltages on them for the radial confinement of ions. They will also have the voltages for the rotating electric field that polarizes our molecular ions. We require the rotating electric field to be spatially homogeneous, so we have chosen to have the Rings to sit outside the Rods. This is so that the fields from the Rods at the center of the trap will experience a much less severe shielding effect from the Rings. Consequentially, the fields from the Rings will be shielded by the Rods.

To investigate the level of shielding, we shall first look at realistic dimensions of Rings and Rods. The Bucket Brigade should fit inside a vacuum chamber of 8″ outer diameter (0.120″ thick wall), so a reasonable dimension for the Rings will be 1 mm thick Rings with inner and outer diameters of 15 cm and 17 cm, leaving about 1.4 cm worth of space between the outer circumference of the rings and the inner wall of the vacuum chamber. There will be eight Rods at 1 cm in diameter, sitting at 6.5 cm away from the trap center. The geometry is summarized in Figure 7.4.

Using the above dimensions, we run simulations in COMSOL to look at the shielding effect of the Rods on the Rings. A comparison of the results with and without Rods are shown in Figure 7.5.

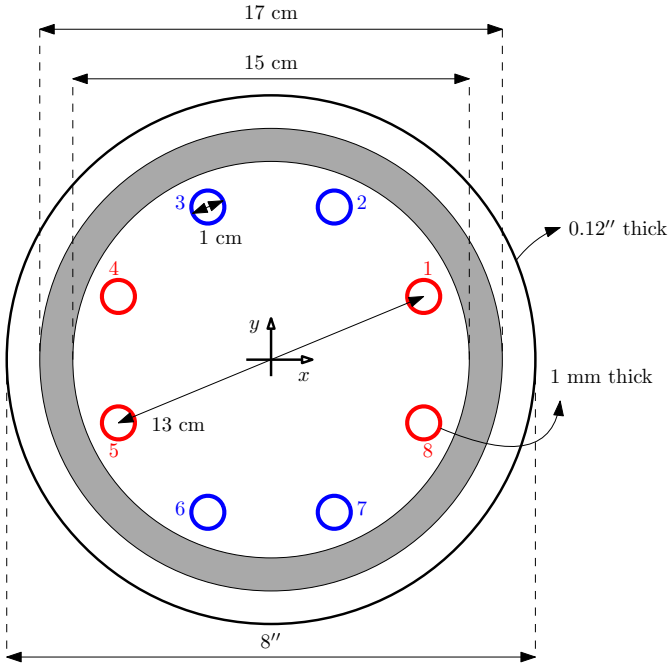

Figure 7.4: **Cross sectional view of the Bucket Brigade involving the Rods, Rings, and the vacuum chamber.** The rods are color coded to indicate the pairing of the rods for the RF-potentials. The rods are numbered here for future reference.

The simulation results from Figure 7.5 show that the Rods attenuate the potentials from the Rings by about a factor of two. To compensate for this attenuation, we only need to amplify the potentials that we wish to apply on the Rings by the same factor. Hence, for an axial trapping frequency of 1 kHz at $\lambda = 8$ cm, we just need $V_0 = 2$ V (refer to Table 7.1).

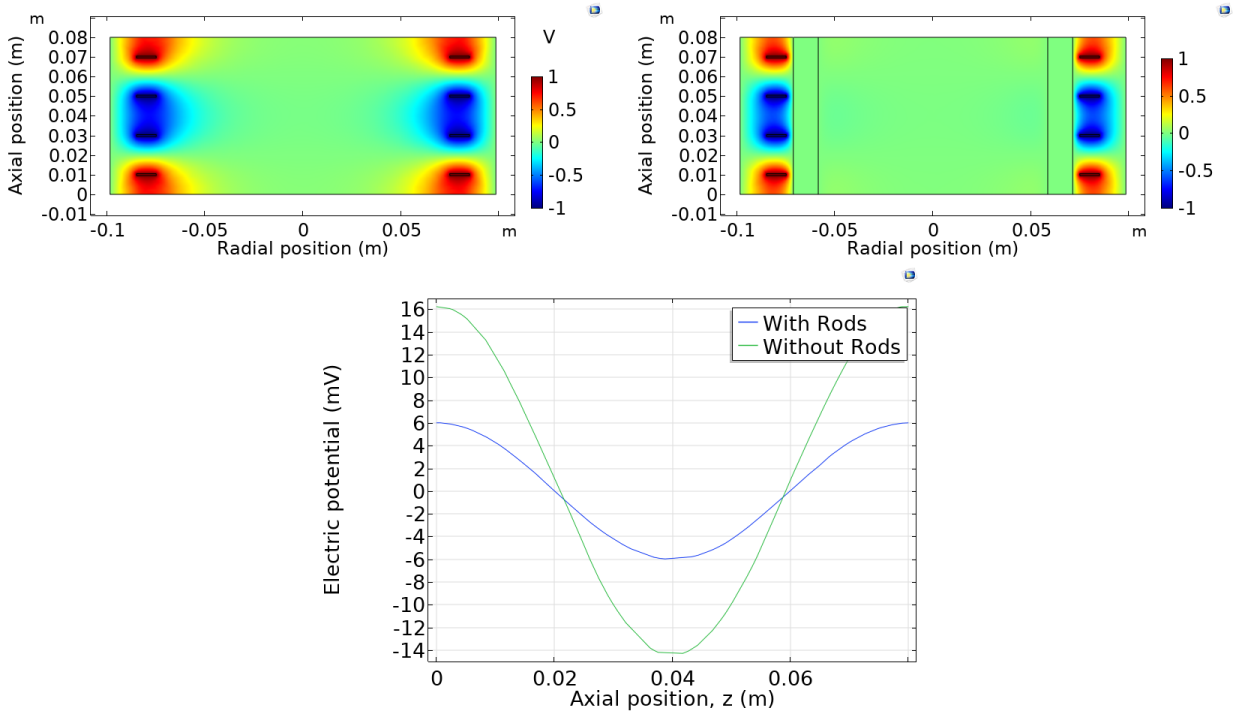

Figure 7.5: **Attenuation of potentials of Rings by Rods.** Top row: the left (right) column shows simulation results without (with) Rods; the vertical lines on the right plot represents the edges of the Rods. Potentials applied on the Rings are $V(z) = -\sqrt{2}\ \mathrm{V} \times \cos\left(\frac{2\pi}{8\ \mathrm{cm}} z\right)$, where $z \in \{-3, -1, 1, 3\}$ cm. We imposed periodic boundary conditions on the top and bottom faces of the simulated domain. The top row shows see-through color maps of electric potentials; the trap axis is the vertical direction. Bottom row: the profile of the electric potential along the trap axis. The amplitude for the case without Rods is about 16 mV, which agrees with the attenuation factor from Table 7.3. On the bottom-right plot, the amplitude is further attenuated by a factor of about 2.7 to about 6 mV.

7.3 Rods: Radial confinement & $\mathcal{E}_{\text{rot}}$

We will be using Rods to supply radial potentials. These potentials include the RF radial confinement, and the potentials to create a rotating electric field to polarize our molecular ions V_{rot}. The geometries of the Rods have already been alluded to earlier on in Figure 7.4. We will be analyzing the radial confinement properties of our trap with the established machinery of the Mathieu parameters (see Appendix A for more details). We shall now briefly investigate the RF trapping properties (Section 7.3.1) for us to understand what kind of RF voltages we need to apply for the radial secular frequencies we want. We then look at simulation results of the homogeneity of the rotating field at various sections along the Bucket Brigade (Section 7.3.2) to justify the dimensions chosen for the Bucket Brigade.

7.3.1 Radial confinement in a Paul trap

The physics behind confinement of ions with time-oscillating fields can be found in many literature (see, for example, Ref. [81]). The basic idea goes as follows:

(1) Maxwell's equations forbid us from having an electric potential minimum in free space, so we cannot trap ions (electric monopoles) with static electric fields only (one can however engineer static electric fields to trap electric dipoles, see, for example, Ref. [82]).

(2) We apply a time-oscillating quadrupolar field in the x-y plane, which has a field strength that is zero at all times along what we call the trap axis (the z-axis).

(3) The time-oscillating quadrupolar field moves the ion along with it. We call this motion the micromotion of the ion. Since the frequency of the oscillation of the field is typically in the RF range, we call the micromotion the RF micromotion.

(4) The phase of the motion of the ion is matched with the phase of the oscillation of the field in such a way that the ion sees a time-averaged net restoring force towards the trap axis. This is the ponderomotive force. An ion would feel a ponderomotive force in the presence of a time-oscillating

spatially inhomogeneous electric field. For a field that oscillates as:

$$\vec{\mathcal{E}}(\mathbf{r},t) = \vec{\mathcal{E}}(\mathbf{r})\cos\omega_{\mathrm{rf}}t,$$

the ponderomotive force that the ion of charge q and mass m feels is given by:

$$\mathbf{F} = -\frac{q^2}{4m\omega_{\mathrm{rf}}^2}\nabla\left|\vec{\mathcal{E}}(\mathbf{r})\right|^2. \tag{7.8}$$

(5) For a quadrupolar field, the expression for $\vec{\mathcal{E}}(\mathbf{r})$ is proportional to $\mathbf{x}-\mathbf{y}$. This means the ponderomotive force that an ion sees in a time-oscillating quadrupolar electric field is given by:

$$\mathbf{F}_{\mathrm{quad.}} \propto -\nabla(x^2+y^2),$$

which is just a harmonic trap in the x and y directions, i.e. the radial directions. The motion associated with the time-averaged restoring force is called the secular motion of the ion in the trap. The secular frequency is usually much lower than the RF frequency.

The summary above shows how an ion in a time-oscillating quadrupolar electric field can feel a restoring force back to the trap center. However, we did not mention how the amplitude of the secular motion of the ion could change with time. Depending on the trap parameters chosen (e.g. RF frequency, RF voltage amplitudes, and charge-mass ratio of the ion), the amplitude of the secular motion could increase with time like in a resonance. These trapping conditions are deemed unstable. The ponderomotive picture only holds if (i) the micromotion is small compared to the secular motion (hence the term "micro"motion), and (ii) the spatial variation in the fields are slow compared to the amplitude of the micromotion. We want to work in this parameter space. Fortunately, some machinery has already been built to allow us to analyze the parameter space, and, say, the stability of the trap more quantitatively, as we shall see below.

For a more quantitative approach, the potentials involved in Paul traps are usually parameterized in the form of Equations A.1 and A.2. The relevant variables are defined in Section A.2. Using these forms, we can calculate the Mathieu parameters, and use Equation A.4 to determine the secular frequencies. Hence the first step to understand our radial confinement is to extract the relevant parameters (equivalent radius of radial electrodes R_0 and equivalent axial distance of the end caps Z_0) from our Bucket Brigade with the

help of COMSOL. The relevant dimensions, definitions of our axes, and Rod numbering are shown in Figure 7.4. Applying positive (negative) RF voltage $V_{\mathrm{rf},0}$ to the red (blue) rods in Figure 7.4 and evaluating the electric potential along the x- and y-axes gives Figure 7.6.

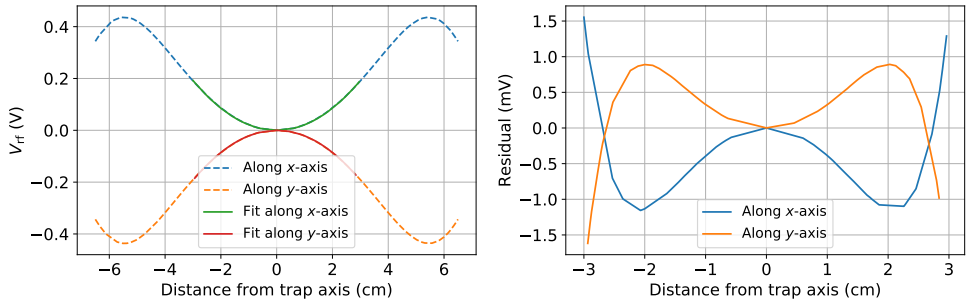

Figure 7.6: **RF electric potentials in the Bucket Brigade, evaluated along the x- and y-axes.** For the purpose of the plots, we used $V_{\mathrm{rf},0} = 1$ V. The fits are done within the region of $[-3, 3]$ cm. The residuals from the fit are shown in the plot on the right. The profiles look identical when the 1D slices are taken at the axial positions (i) between two Rings and also (ii) on the plane of the rings within this plotting region. This says that the Rings are not significantly modifying the fields from the Rods within the region shown in the plot.

From Figure 7.6, we find that $R_0 = 6.838$ cm, which is not that far away from the actual 6.5 cm radial distance of the rods from the trap axis. A similar analysis on the axial confining potential using the results of Section 7.2.4 gives $Z_0 = 25.5$ cm. Voltages required for secular frequencies of 1 kHz in all three directions, are $U_{\mathrm{ec},0} = 3.35$ V, and $V_{\mathrm{rf},0} = 20.8$ V. The resulting Mathieu stability plot is shown in Figure 7.7.[5]

So far, all the voltages required look reasonable. The final values that we settled on for the prototypical Bucket Brigade are shown in Appendix B.1. The values shown there are slightly different from those shown above because we scaled the transverse dimension down a little to make space for structural support.

7.3.2 Rotating electric field, $\mathcal{E}_{\mathrm{rot}}$

To produce a rotating electric field $\mathcal{E}_{\mathrm{rot}}$, the potentials we apply on the n^{th} rod (compare with Figure 7.4) is given by:

$$V_n = V_{\mathrm{rot}} \cos\left(\omega_{\mathrm{rot}} t + \frac{(2n-1)\pi}{8}\right),$$

[5] It is interesting to note that operating in the stability region does not guarantee stability in the presence of higher order multipole time-oscillating potentials in the trap [83]. Our trap certainly has higher order multipoles because our electrodes are not shaped like hyperboloids. It seems, though, that the instabilities in Alheit *et al.* [83] only come in at $q > 0.45$. We typically operate at $q \approx 0.14$, so this should not be a problem for us.

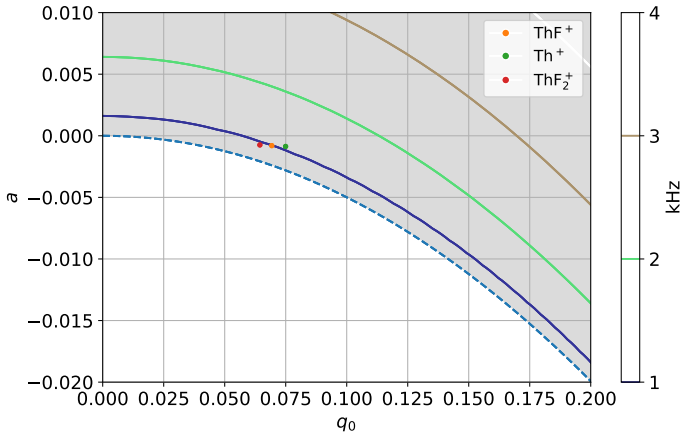

Figure 7.7: **Mathieu stability plot for the Bucket Brigade.** The colored dots represent the positions of the three species (ThF^+, Th^+, ThF_2^+) that we care about in our trap. The grey area bound by the dashed lines indicate stable trapping region. The solid colored lines indicate contours of radial trapping frequency for ThF^+. Please refer to Appendix A for more information regarding the Mathieu parameters a and q_0.

where ω_{rot} is the rotational angular frequency of the rotating electric field, and the phases are chosen such that $\mathcal{E}_{\text{rot}}$ points in the negative x direction at $t = 0$ and rotates clockwise with time. Using COMSOL to evaluate the fields resulting from potentials applied to the Rods gives results shown in Figure 7.8.

From the results in Figure 7.8, we see that the deviation crosses the 0.1% and 0.01% marks at 1.6 cm and 1.1 cm, respectively. We want all the ions in the ion cloud to see the same $\mathcal{E}_{\text{rot}}$, so we want the deviation to be as small as possible within the extent of the ion cloud. Expecting a typical ion cloud size of $4\sigma \sim 1$ cm, and requiring a 0.01% homogeneity level[6] , we cannot afford to shrink the dimensions of the Bucket Brigade down by much. One can say that we were lucky to have chosen to work with the current set of design parameters; any smaller and we would have to calculate everything again with a bigger dimension.

Ponderomotive potentials go as $|\vec{\mathcal{E}}|^2$ (see Equation 7.8), and the ponderomotive energy associated with $\mathcal{E}_{\text{rot}}$ is about 93500 K at the trap axis. For an ion cloud temperature of about 30 K, we see that the deviation of the ponderomotive potential exceeds that of the ion cloud temperature beyond 1.3 cm from the trap axis. We certainly do not wish to lose ions to the $\mathcal{E}_{\text{rot}}$ ponderomotive potential (but in fact we do, see Figure 7.20), so we would want to have small cold ion clouds given the current electrode configuration.

From COMSOL, we further see that for every 1 V of V_{rot}, we get 10.655 V/m of $\mathcal{E}_{\text{rot}}$. This means

[6] The 0.01% value comes from demanding the ions to decohere less than 10% of a cycle after 50 Hz × 20 s = 1000 cycles.

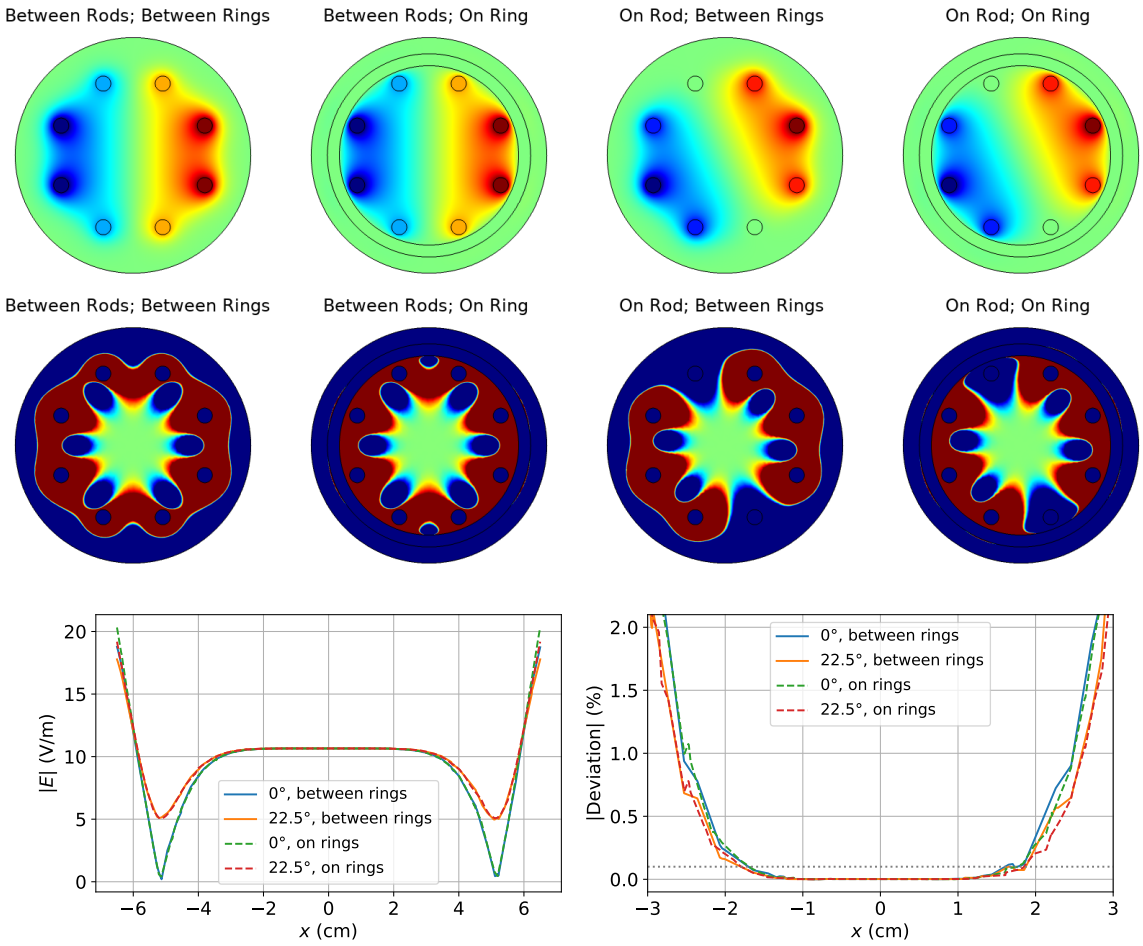

Figure 7.8: **Plots of $\mathcal{E}_{\text{rot}}$ spatial homogeneity.** Top row: color maps of electric potential, with planes chosen to be between the rings, or on the plane of the rings. Second row: plots of the magnitude of the resultant electric field; range of color map is chosen such that the colors saturate beyond 1% from the value at the center (10.655 V/m). Last row: 1D slice of the magnitude of the resultant electric field along the x-axis. For the first two rows, the odd columns correspond to $\mathcal{E}_{\text{rot}}$ pointing along the negative x-axis (0°), while the even columns correspond to $\mathcal{E}_{\text{rot}}$ making 22.5° with the negative x-axis. Color legends are also removed for clarity; warmer (cooler) colors indicate more positive (negative) values. The grey dotted line in the bottom right plot indicates 0.1%.

that for a nominal $\mathcal{E}_{\text{rot}} = 60$ V/cm, we need to apply $V_{\text{rot}} = 563$ V. This is still a reasonable voltage that we can deal with.

Once again, the final values that we settled on for the prototypical Bucket Brigade are shown in Appendix B.1. The values shown there are slightly different from those shown above because we scaled the transverse dimension down a little to make space for structural support.

7.3.3 Summary

With the current geometry, we saw that we can introduce the fields that we want, both radially and axially, with reasonable voltages. The field homogeneity requirements for the Rods and the harmonic axial region for the Rings are also at a comfortable level for the ion cloud size that we expect to work with. In principle, this could work. In practice, we have to find out. There could be many things that could affect the experiment in ways that are easier found out by the method of doing it, instead of trying to search through the whole parameter space exhaustively. There remains a lot to be said for building a prototype.

The next section will introduce a prototype of the Bucket Brigade. We will be using the prototype to test out our design ideas, and to have a feel of the construction and assembling tolerances.

7.4 The baby Bucket Brigade (b.B.B.)

Having a trap design that works in principle is a good start, but we still need to test this out experimentally. To do so, we have constructed a prototype of the Bucket Brigade with realistic diameter and operating voltages, but only 1/3 as long as what we anticipate for the full design. We affectionally call this prototype the *baby Bucket Brigade (b.B.B.)*. In addition to testing out the trap design on the b.B.B., we also aim to test out many other new ideas that we wish to implement in the Gen. III experiment (to be discussed in the later chapters).

7.4.1 Setup

A CAD drawing of the setup is shown in Figure 7.9, and critical components are elaborated on in the caption. The drawing is a bird's eye view from the top, but we made some minor changes in the final design. For example, the turbomolecular pump attached to the Six-way Cross was drawn to be lying on the horizontal plane, but it is now on the top flange of the Six-way Cross to make access to other flanges friendlier to the lab users. All the electrical feedthroughs for the electrodes inside the Cold Tube are mounted on various blanks on the unused ports of the Six-way Cross. Electrical feedthroughs for the microchannel plate and the Accelerating Rings are mounted on the zero length reducer that the microchannel plate assembly is mounted on. A picture of the setup is shown in Figure 7.10.

An 80 L/s turbomolecular pump (Varian V81) maintains the vacuum in the differential pumping chamber, while the Six-way Cross has a 500 L/s turbomolecular pump (Varian V551) and a 1000 L/s (for hydrogen) nonevaporable getter (SAES CapaciTorr Z1000). The source chamber also has a Varian V551 attached to it. The molecular pumps are backed up by scroll pumps (Agilent IDP-15). Typical vacuum pressures read by the ion gauges are 10^{-9} Torr in the differential pumping chamber and in the Six-way Cross.

The distance from the molecular beam source to the trap is about 21″. The length of the whole b.B.B. is about 1 m long. The distance between the Octagon to the microchannel plate assembly is about 70 cm. The microchannel plate assembly consists of two 4 cm diameter microchannel plates in the chevron

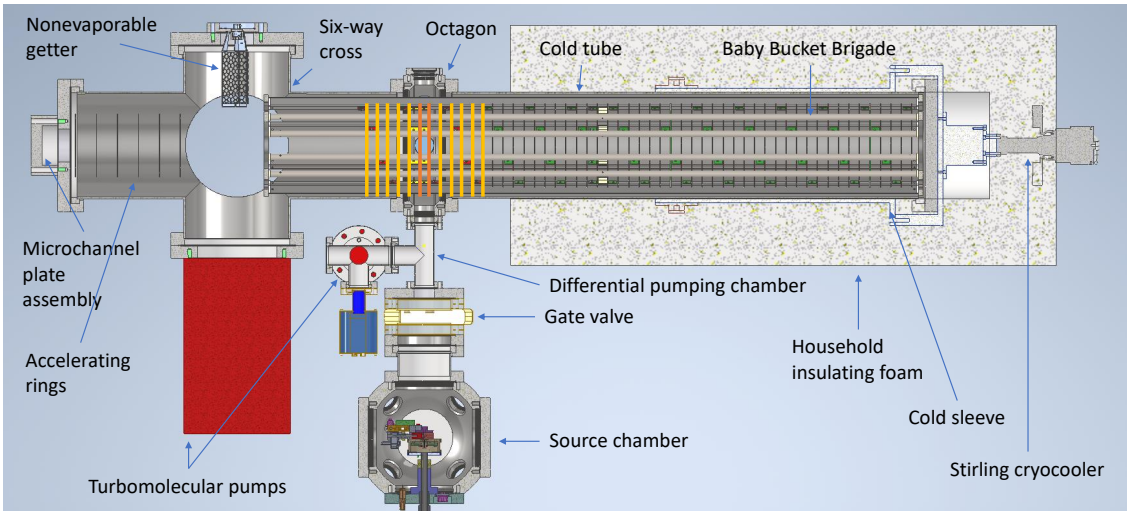

Figure 7.9: **CAD drawing of the b.B.B. setup.** A typical experimental sequence proceeds as follows (also compare with Figure 4.24):

(1) We ablate a piece of thorium metal in the source chamber to create a plume of thorium plasma that is reacted with sulfur hexafluoride to create neutral thorium monofluoride.

(2) The neutral molecules are entrained in a supersonic expansion buffer gas of neon at room temperature, which then passes through a gate valve and a differential pumping chamber (separated from the neighboring vacuum chambers with a 3 mm diameter copper skimmer on each side) before it reaches the Octagon. The first skimmer is charged to 30 V to reject charged particles.

(3) As the ions arrive at the center of the 10″ diameter Octagon, we fire REMPI lasers through the 2.75″ windows to ionize the neutral molecules state-selectively into the $X\,^3\Delta_1(v=0)$ vibronic manifold.

(4) More lasers go through other windows on the Octagon for state preparation into the eEDM-sensitive $X\,^3\Delta_1(v=0, J=1, F=3/2, m_F=\pm 3/2)$ states.

(5) The ions are then ushered down into the Cold Tube, where we perform our $\pi/2$ pulses to do Ramsey spectroscopy.

(6) At the end of the Ramsey sequence, the ions are ushered back into the Octagon where they are addressed with lasers for state detection (e.g. state clean up, state-selective REMPD).

(7) The ions are then ejected through the Six-way Cross towards the microchannel plate assembly for detection. The Accelerating Rings can be turned on to accelerate the ions even further, or to be used as some crude form of ion optics.

Rings with special functions are highlighted with thick colored lines: yellow indicates Special Rings, while orange indicate Quadrant Rings. See Figure 7.1 for a closer view on the Rings. More on these rings in Section 7.4.2.

configuration, followed by a phosphor screen. The potential difference across the front and back sides of the plates are kept at slightly less than -2 kV, with the front plate floated to -2.6 kV for a higher ion impact velocity. The phosphor screen is at 3 kV. We read out signals from the microchannel plates capacitively (see

Ref [39] and Noah Schlossberger's thesis), and we also use a camera to capture the phosphorescence from the phosphor screen.

Figure 7.11 shows the constructed b.B.B.. One can argue against using kapton tape close to the ions in an ion trap experiment (and this comes back to bite us again and again when we observe patch charge effects when we try to translate the ions along the b.B.B.), but that was the quickest solution to tidy the loose ends while keeping the electrodes insulated from one another. We find solace in the fact that the kapton tapes are only used on the side of the b.B.B. that sits in the warm region of the setup, while the part that sits inside the Cold Tube does not have the tapes.

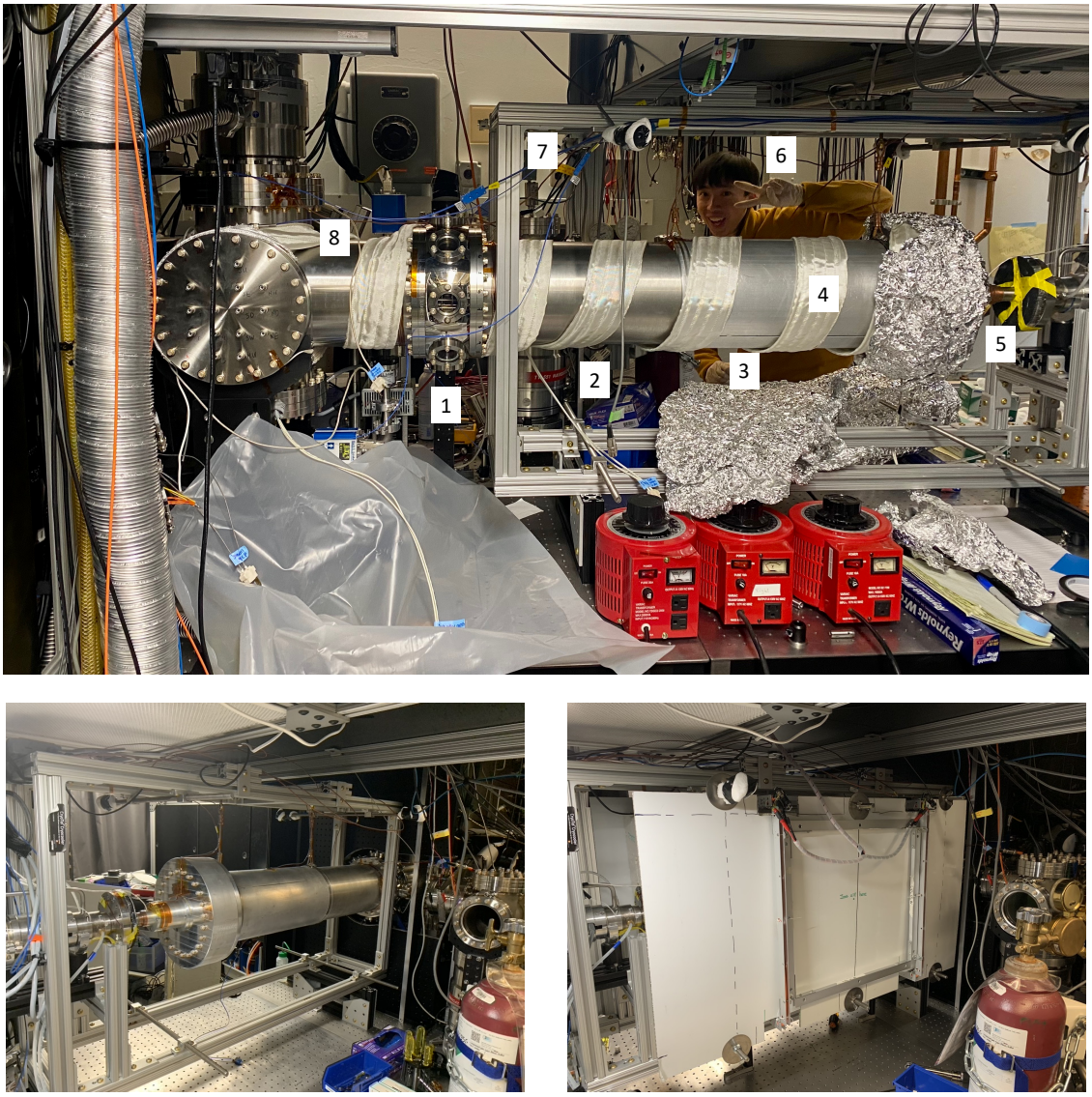

Figure 7.10: **Pictures of the b.B.B. setup.** Top row: (1) The Octagon. The 2.75″ windows mounted on the Octagon are the ones we use to send in laser beams. The windows on the vertical axis are uncoated, and are used for the higher energy pulsed lasers. The rest of the windows are AR coated for the cw lasers. (2) The Cold Tube. A 8″ diameter 316LN stainless steel tube that houses the b.B.B.. (3) The Cold Sleeve. An aluminum cold jacket the hugs the Cold Tube, conducting the cold from the cryocooler. Made in-house at JILA. (4) The "Science" location where the ions sit for BBR suppressed Ramsey evolution. The "Science" region is deep enough inside the cold to suppress BBR related T_1 type losses, and far enough from the magnetic cryocooler. (5) The cryocooler. (6) A graduate student for scale. (7) The Cradle. The Cold Tube is suspended from the Cradle for structural support. (8) The Six-way Cross. One can see the turbomolecular pump attached on to the top flange. Some of the electrical feedthroughs for the electrodes can also be seen on the blank facing the camera. The full b.B.B. is way more congested than the picture shown here. This picture was taken after we took out several components to bake the system. Not shown in this picture include (i) the vertical breadboard that sits between the Octagon and the Cradle for the optics into the Octagon, (ii) the household insulating foam and panels that hold the foam, and (iii) all the disconnected cables from the trap drivers. Bottom row: views of the b.B.B. setup from the other side. One can also see the back side of the (black) vertical breadboard in these pictures. The gas canister on the right contains the neon buffer gas, seeded with sulfur hexafluoride. The vacuum chamber on the right is part of the Source Chamber. Bottom left: without the foam. Bottom right: with the foam and panels that hold the foam.

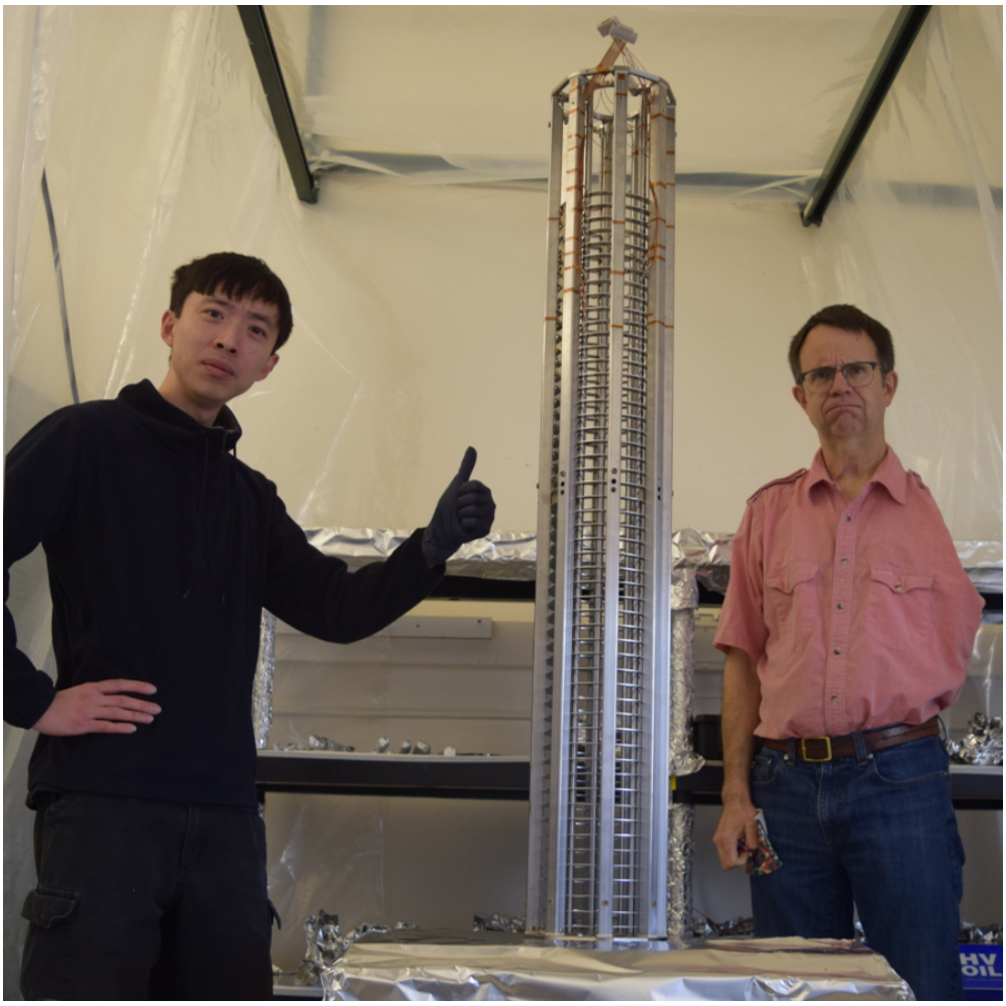

Figure 7.11: **Picture of the b.B.B., with yours truly and an approving-looking advisor for scale.** The outer most square rods are mechanical supports (affectionally called Spines). The Spine are terminated on both ends with "End Plates". The Spines have a square cross section with side lengths of 0.75″. Midway through the b.B.B., where screwholes on the Spines can be seen, there is a thicker Ring that also acts as a structural support. The horizontally orientated rings are the Rings, and the Rods are lined up along the Spines inside the Rings. Some kapton tape is used to keep the wiring tidy. Vacuum-compatible d-sub connectors can be seen at the top of the picture. These connectors allow for error-free connection of the wires with the electronic feedthroughs at the vacuum flange, because we only need to verify the connection once on the bench in a comfortable configuration, and just connect the d-sub connectors when we slide the b.B.B. into the confined space of the vacuum chamber on the busy optical tables. The whole assembly was assembled (by graduate students Sun Yool Park and Anzhou Wang, with the help of JILA instrument maker Calvin Schwadron) inside a makeshift clean room with a HEPA filter for good vacuum practice. The top end of the b.B.B. in this picture corresponds to the side facing the ion detector.

7.4.2 Trap loading & Ion kick out

We split two Rings right at the center of the Octagon into four quadrants each. The quadrants are oriented such that each Quadrant Ring (denoted as thick orange lines in Figure 7.9) has one quadrant in the up, down, away-from-Source-Chamber and towards-Source-Chamber directions. Using a voltage difference across the away-towards pair, we can apply a stop pulse to stop the newly created ions that are moving at 800 m/s. We can use a combination of voltage differences across the up-down pair and the overall voltage difference across the two Quadrant Rings to steer the ions during the stop pulse in the case of imperfect alignment of the electrodes w.r.t. molecular beam.

For the ion kick out, we apply a potential gradient along the axial direction with the Special Rings (denoted as thick yellow lines in Figure 7.9) and the Quadrant Rings. At the end of the kick out acceleration, the ions travel at about 4 km/s towards the ion detector.

The rest of the Rings only serve to translate the ions in and out of the Cold Tube, and are connected with every fourth neighbor to reduce the number of independently controlled electrodes. Hence, we have a total of 4×2 (Quadrant Rings) + 1×10 (Special Rings) + 1×4 (Translating Rings)[7] $= 22$ independently controlled Ring voltages.

7.4.3 Remarks on wisdom acquired

We started designing the b.B.B. at the start of the pandemic (circa April 2020). We cleared out some lab space and knocked down some walls to make space for the new setup a year later (circa April 2021). We celebrated the "effective end of the pandemic" by painting the walls of our new lab space in July 2021, and started populating the new lab space with equipment in August 2021. We saw our first ions in the b.B.B. in June 2022, one week after DAMOP. We have our first dissociation of ThF^+ in the b.B.B. in October 2022. Finally, we have our first Ramsey fringe in the b.B.B. in February 2023.

The b.B.B. design, construction, and fine tuning turned out to be a much bigger problem than anticipated. I shall briefly mention some wisdom that we acquired along the way to inform/inspire future generations of students and post-docs working on the design of the full Bucket Brigade.

[7] Although we have only four independently controlled voltages for the Translating Rings, we have 41 such Rings in total.

7.4.3.1 Tolerance

The position tolerance on the Rings are very forgiving because of Laplace's equation; any effect from unintentional displacements of the Rings with spatially sinusoidal modulated voltages applied to them will manifest as a higher spatial harmonic of the potential that is exponentially suppressed by the radial distance from the electrodes (see Section 7.2.2).

In comparison, the Rods have a much more stringent position tolerance. A simple COMSOL simulation suggests that at if we demand a 0.1% $\mathcal{E}_{\text{rot}}$ spatial homogeneity requirement along the trap center at the size of our ion cloud, we can only tolerate a 200 μm radial or 1 mm azimuthal displacement of the Rods.

7.4.3.2 Shielding effect of insulator spacers

The b.B.B. has a lot of macroscopically sized electrodes in close proximity. They need to be held together for structural integrity, but insulated from one another for independent voltage control. One would naïvely assume that using thin insulating spacers to, say, insulate Rods from the Spines would do little to fields seen by ions along the trap axis some centimeters away. However, fellow graduate student Anzhou Wang quickly found out through COMSOL simulations that the dielectric insulators modify the field lines sufficiently enough to change the field strength along the trap axis. We can compensate for this effect by introducing a metallic spacer along with the insulating spacer. The dimensions chosen for the insulating and metallic spacers were guided by COMSOL simulation.

7.4.3.3 Patch charges and baking

During the early days of moving ions up and down the b.B.B., we noticed that there was a bad patch around 30 cm into the Cold Tube (see Figure 7.12). We could not move ions past that location without ramping up the radial confinement of the trap. Initially we guessed that perhaps some of the electrodes at that region were not connected correctly, but it turned out in the end that a light bake of the Cold Tube at about 100 °C over the weekend solved the problem. We do not claim to understand what happened fully, but the story is that there were some patch charges in that region that got baked away.

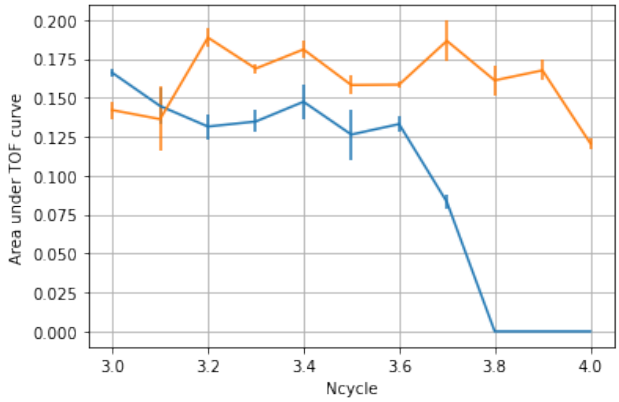

Figure 7.12: **Losing ions past 30 cm into the b.B.B..** Data from 7 September 2022, RID 20202. The blue trace corresponds to moving the ions into various locations of the b.B.B. (in units of Ncycles, where each Ncycle corresponds to translating the ions in by one bucket, or 8 cm) in 300 ms, holding them there for 10 ms, before moving them back out into the Octagon again in 300 ms. The vertical axis is the area under the time-of-flight curve, corresponding to the number of ions we retain after the operation. The yellow trace corresponds to holding the ions at the Octagon for the same amount of time as the blue trace to act as a control. Note that we lose ions completely by the time we move to Ncycle = 3.8, corresponding to 30 cm into the b.B.B.. This problem was fixed by baking the setup.

7.4.3.4 Long time of flight

With a distance of about 70 cm between the trap and the ion detector, and a kick-out velocity of about 4 km/s (20 eV of kinetic energy for Th^+), any stray fields during the 180 µs of time of flight could steer our ions in unexpected ways. For reasons not fully understood, we require a slight steering of the ions along the x direction (Eastward direction in the lab, towards the Source Chamber w.r.t. the setup) to let the ions hit the detector. We also see that the positions of the ions on our detector are mapped from positions (velocities) of the ions in the trap along the x (y, vertical) directions. The kick out angle that the steering makes w.r.t. the trap axis is about 1°, which could be explained by (i) slight misalignment of the b.B.B. w.r.t. the ion detector, or (ii) small patch charges on the side of the chamber (e.g. window on the Octagon on the other side of the molecular beam) that break azimuthal symmetry.

7.4.3.5 Recessed ion detector

Towards the end of the spectroscopy of ThF^+ before we started work on the b.B.B., we obtained a new microchannel plate assembly to replace the one that was broken. We wanted a bigger microchannel

plate (4 cm) than our broken one (2 cm), but to make the entire setup fit into a 4.5″ flange (limited by our setup back then), the assembly was about 1″ recessed from the end of the flange to make wiring easier (see Figure 7.13). This turned out to introduce a lot of focusing effects on our ion cloud. At the time of this

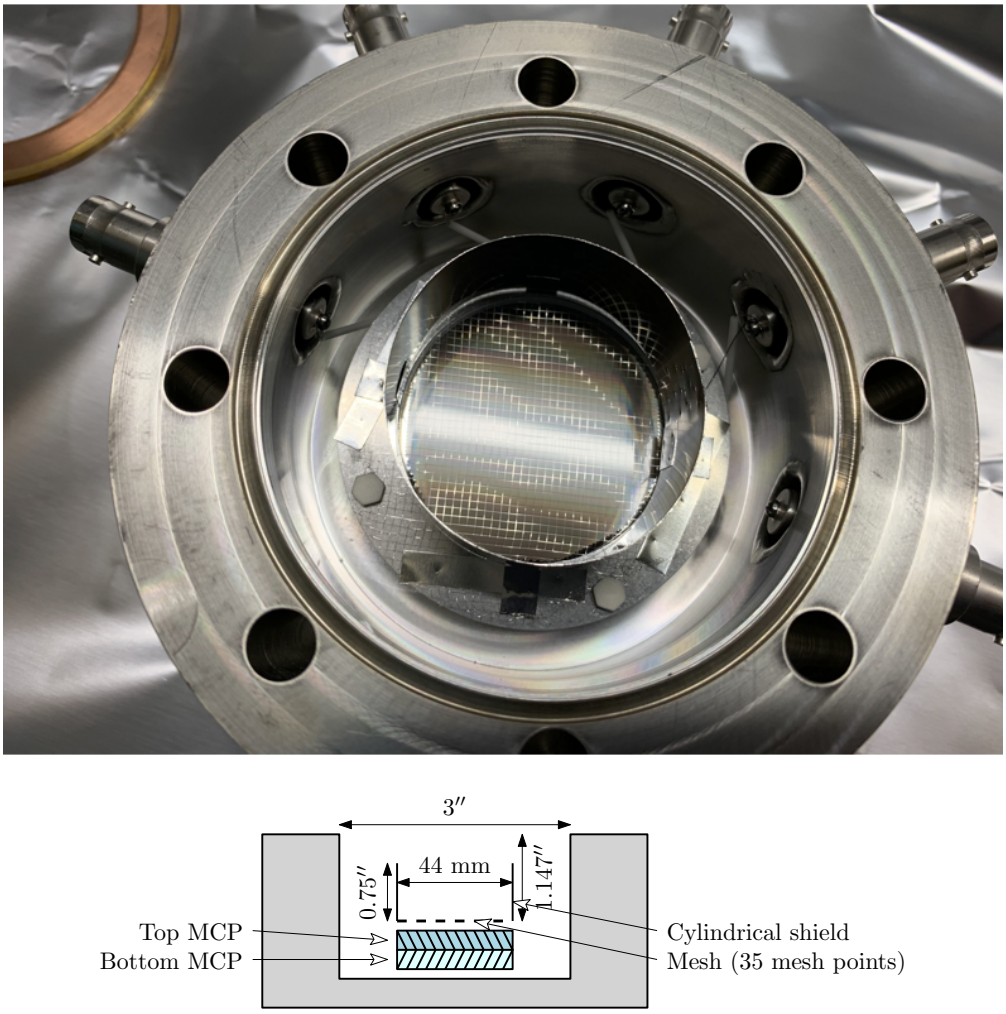

Figure 7.13: **Picture of the microchannel plate assembly.** The assembly (Beam Imaging Solutions BOS-40) is housed inside a 4.5″ flange, with the microchannel plates about 1″ below the surface of the flange to give access to electrical connections in this tight space. There is a mesh in front of the microchannel plate. A cylindrical shield that is electrically connected to the mesh shields the incoming ions from the fields from the electrical feedthroughs. Top: Going clockwise from the left most feedthrough, the electrical connections are made to (i) phosphor screen, (ii) back side of the back microchannel plate, (iii) where the two microchannel plates meet, (iv) front side of the front microchannel plate. The unused feedthrough is connected to the mesh (and grid) after taking this photograph. Bottom: a cross section view from the side with the relevant dimensions. MCP stands for microchannel plate.

writing, there is a plan to redesign the microchannel plate assembly to reduce the aforementioned effect.

7.5 Electronics design

Now that we have seen how the b.B.B. setup looks like, it is time to discuss how we drive the voltages on our electrodes. First we shall look at the Rods (Section 7.5.1), then the Rings (Section 7.5.2).

7.5.1 Rod driver

Studies on systematics on the Gen. II setup shed light on the importance of stomping on the higher harmonic of V_{rot} [36]. Furthermore, our Rods have substantial capacitance, and op-amps do not have infinite slew rates. Hence, we decide to design a tank circuit to drive the voltages on the Rods. As will be elaborated on in the following sections, this tank circuit involves a transformer with weak coupling between the primary and secondary coils. There will be four such tank circuits to drive four pairs of Rods. Each tank circuit drives a pair of Rods that are on opposite sides of the setup, e.g. Rods 1 and 5 in Figure 7.4 form a pair. A typical tank circuit will look like that shown in Figure 7.14.

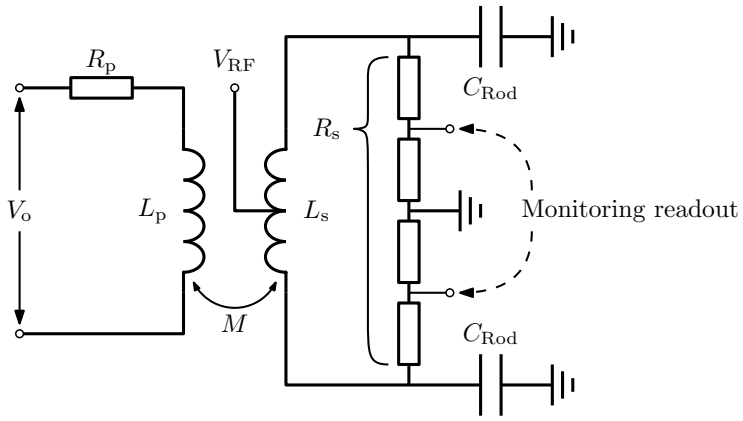

Figure 7.14: **Tank circuit used to drive voltages on the Rods.** Voltage V_{o} will be sent into the primary circuit with op-amps, with a current-limiting resistor R_{p}. The inductances of the primary and secondary coils are L_{p} and L_{s}, respectively. The inductors are coupled through a mutual inductance M. A common-mode RF voltage V_{RF} will be sent to the rods via a center-tap on the secondary inductor. A series of potential dividing resistors with total resistance R_{s} will be used to readout the voltage for monitoring purposes. The Rods are modelled as capacitors with capacitance C_{Rod}.

We will first begin with a foreword on some of the design considerations that we have learned from an early prototype. We then discuss transformers with perfect coupling to borrow intuition from textbook examples. This is followed by a discussion of transformers with imperfect coupling. Finally, we will briefly

discuss the final design.

7.5.1.1 Foreword on transformer design

Before we launch into detailed discussion of the transformer, we shall look at a piece of wisdom (or a shortcut) that we acquired from an early prototype of the transformer. We will also introduce a neat trick to help with analyzing circuit diagrams with transformers.

Air core We used a ferrite core to link the fluxes between the primary and secondary coils in an early prototype of the transformer. However, there are two problems with it. First, saturation effects in the ferrite core by the flux from the primary coil could result in distorted waveforms with higher harmonics on the secondary. The saturation effects do not have to be severe for this to be a problem for our systematic studies; a slightly saturated ferrite core could already give us measurable systematic effects that have got to do with second harmonics in $\mathcal{E}_{\text{rot}}$ (see Section 8.4). Second, the ferrite core heated up during operation, and it turned out that the permeability of the ferrite core has a substantial temperature dependence. This prompted a need for a non-trivial temperature control system. We decided to avoid the problem totally by using two concentric solenoids as our primary and secondary coils, with an air core coupling the two.

For a system like this, we have governing equations (in the Fourier domain):

$$V_{\text{p}} = j\omega L_{\text{p}} i_{\text{p}} + j\omega M i_{\text{s}} \tag{7.9a}$$

$$V_{\text{s}} = j\omega M i_{\text{p}} + j\omega L_{\text{s}} i_{\text{s}}, \tag{7.9b}$$

where $j = \sqrt{-1}$, M is the mutual inductance, V is the voltage across each inductor, ω is the angular frequency of the voltage signal, L is the inductance, i is the current going through the inductor, and the subscripts 'p' and 's' stand for the primary and secondary inductors, respectively.

T-model equivalent circuit Equations 7.9 can be massaged into a T-model equivalent circuit form, enabling easier analysis of the circuit:

$$V_{\text{p}} = j\omega(L_{\text{p}} - M) i_{\text{p}} + j\omega M(i_{\text{p}} + i_{\text{s}}) \tag{7.10a}$$

$$V_{\text{s}} = j\omega M(i_{\text{p}} + i_{\text{s}}) + j\omega(L_{\text{s}} - M) i_{\text{s}}. \tag{7.10b}$$

The equivalent circuit is shown in Figure 7.15.

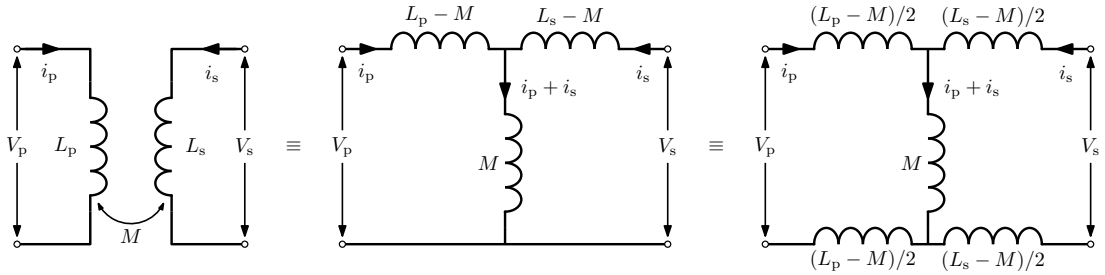

Figure 7.15: **T-model equivalent circuit.** A transformer (L.H.S.) can be modelled as a T-model equivalent circuit (R.H.S.).

7.5.1.2 Transformer with perfect coupling

The physics behind a transformer with perfect coupling, i.e., $M = \sqrt{L_p L_s}$, is well understood and is included in standard undergraduate courses on introduction to circuits. Defining the turns ratio $n = N_s/N_p$, we know that $V_s = nV_p$ from Faraday's law of induction, and $i_s = i_p/n$ from conservation of energy. In fact, we can show this with the T-model equivalent circuit. For a loaded transformer with load impedance Z_L, the total impedance seen by the source on the primary side is given by:

$$Z_{tot} = j\omega(L_p - M) + \frac{1}{\frac{1}{j\omega M} + \frac{1}{j\omega(L_s - M) + Z_L}} = \frac{\omega^2 M^2 - \omega^2 L_p L_s + jZ_L\omega L_p}{Z_L + j\omega L_s}. \tag{7.11}$$

The voltage across the load on the secondary side is related to that on the primary by (through Ohm's law):

$$\frac{V_s}{V_p} = \frac{Z_L}{j\omega(L_s - M) + Z_L} \frac{\frac{1}{\frac{1}{j\omega M} + \frac{1}{j\omega(L_s - M) + Z_L}}}{Z_{tot}} = \frac{MZ_L}{L_p Z_L + j\omega(L_p L_s - M^2)} \tag{7.12}$$

and we can see that Equation 7.12 reduces to $V_s/V_p \to \sqrt{L_s/L_p} = n$ in the case of perfect coupling, and where we use the relation[8] $L_s/L_p = n^2$.

Equation 7.11 deserves some special attention before we move on to talk about transformers with imperfect coupling. At perfect coupling, and in the limit where $|\omega L_s| \gg |Z_L|$, we see that the expression reduces to $Z_{tot} \to Z_L/n^2$, where we make use of $L_s/L_p = n^2$. We can interpret the limit of $|\omega L_s| \gg |Z_L|$ to be the case where the load does not change the voltage/current of the circuit on the secondary side too much. This means that for small loads on the secondary side, the circuit is equivalent to replacing the inductor on the primary side with a load with impedance Z_L/n^2, and ignoring the secondary side altogether. This may

[8] This assumes that the inductors of both coils have geometries similar to each other, or if the coils share a ferrite core, such that the only difference between the two only come from the winding numbers.

be useful for estimating requirements on current flowing in the primary circuit. Also as a sanity check, in the opposite limit $|\omega L_\mathrm{s}| \ll |Z_\mathrm{L}|$, where the secondary side is like an open circuit, we have $Z_\mathrm{tot} \to j\omega L_\mathrm{p}$, as expected.

7.5.1.3 Transformer with imperfect coupling

Going back to Equation 7.12, and introducing the general expression $M = K\sqrt{L_\mathrm{p} L_\mathrm{s}}$, where $K \in [0, 1]$ is the coupling constant, we have:

$$\frac{V_\mathrm{s}}{V_\mathrm{p}} = \sqrt{\frac{L_\mathrm{s}}{L_\mathrm{p}}} \frac{K Z_\mathrm{L}}{Z_\mathrm{L} + j\omega L_\mathrm{s}(1 - K^2)} \tag{7.13}$$

We see that the denominator on the right hand side can be made small, which would make V_s large compared to V_p, if the load is capacitive. Note that this can happen even if $|Z_\mathrm{L}|$ is not small. In other words, for a carefully designed circuit, we can "step up" the voltage across a capacitive load on the secondary side with imperfectly coupled primary and secondary coils. Furthermore, this "stepping up" is frequency dependent because of how ω goes into the denominator. This is essentially a tank circuit, which is just what we need to stomp on the second harmonic of V_rot that is plaguing the Gen. II systematics studies.

The optimum coupling that gives the maximum $|V_\mathrm{s}/V_\mathrm{p}|$ for a fixed ω occurs at:[9]

$$K = \sqrt{\frac{\sqrt{|Z_\mathrm{L}|^2 + \omega L_\mathrm{s}\left[\omega L_\mathrm{s} + 2\mathfrak{Im}(Z_\mathrm{L})\right]}}{\omega L_\mathrm{s}}} \approx 0.25, \tag{7.14}$$

where typical parameters in our setup are $L_\mathrm{s} = 10$ mH, $\omega = 2\pi \times 150$ kHz, $Z_\mathrm{L} = 1/\left(1/R_s + j\omega C\right)$, with $R_s = 500$ kΩ and $C = C_\mathrm{Rod}/2 = 120$ pF. Hence, we see that we need to design bad coupling into the transformer.

Designing imperfectness into a system is easy. We decide to have the following: a 400-turn secondary coil in the form of a solenoid with diameter 4.5″ and length about 14 cm using AWG 28 magnet wire, and a 400-turn primary coil in the form of a circular wire loop with average diameter 1.7″ using AWG 30 magnet wire. The primary coil sits within the secondary, and shares the same axis with the secondary. Estimates of the inductances of the coils are about 10 mH each, and the mutual inductance near 2.5 mH. Pictures of a prototype are shown in Figure 7.9.

[9] As we will see in Equation 7.15, the resonant frequency has a K dependence. The fact that there is an optimal K for that

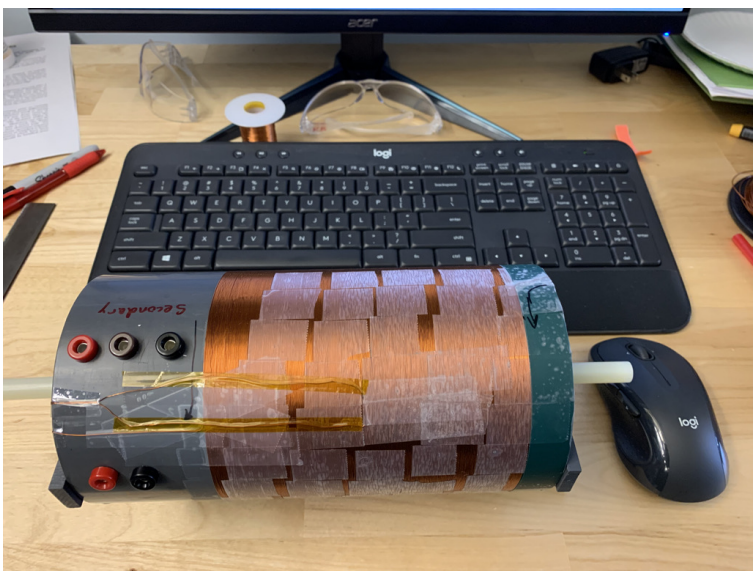

Figure 7.16: **Pictures of a prototype transformer.** Left: overview of the transformer, showing the secondary coil, with keyboard and mouse for scale. Right: view of the primary coil inside the secondary coil. The primary coil is mounted on a rod that can move along the axis of the transformer. This allows us to shim away the RF pickup on the primary coil from the center tap on the secondary. The primary coil has an inner diameter of 1.5″ and outer diameter of 1.9″. Measured primary, secondary, and mutual inductances are 10 mH, 9.9 mH, and 2.0 mH, respectively.

Tests of the prototype indicate very good agreement with our model, and a second harmonic suppression of at least 34 dB. Of note, we have a few design guidelines:

(1) There are two resonances: parallel and series. The parallel resonance happens at frequency $\omega_{\text{parallel}} = 1/\sqrt{L_s C}$, and it is where the impedance seen by the source at the primary side is the largest, i.e., smallest magnitude of driving current on the primary side. The series resonance happens at

$$\omega_{\text{series}} = \sqrt{\frac{1 - \frac{L_s}{2R_s^2 C}(1 - K^2)}{L_s C (1 - K^2)}}, \tag{7.15}$$

and it is where the ratio $|V_s/V_p|$ is the largest; we want to be operating here. This can be inferred from substituting $M = K\sqrt{L_p L_s}$ into Equation 7.11 to get:

$$Z_{\text{tot}} = j\omega L_p \frac{Z_L + j\omega L_s(1 - K^2)}{Z_L + j\omega L_s},$$

and recognizing that $Z_L = 1/(1/R_s + j\omega C)$; parallel (series) resonance occurs when the denominator (numerator) is minimum. Evidently, for fixed L_s and K, we can fine-tune the series resonant

gives a maximum $|V_s/V_p|$ comes from the resonance curve moving to higher frequencies with increasing K, and the optimal K is where the resonance peak overlaps with the desired ω.

frequency by adjusting C.

(2) At $R_s \gg \sqrt{L_s/C} \approx 9$ kΩ, we have $\omega_{series} \approx 1/\sqrt{L_s C(1-K^2)}$, so changing the value of R_s only changes the Q-factor[10] ($Q \sim \omega_{series} R_s C$), and not the series resonant frequency. Hence, we can fine-tune the Q-factor by adjusting R_s.

(3) All the design guidelines are based on analyses without the current-limiting resistor R_p, because the expressions are much cleaner this way. The presence of R_p moves the resonant frequencies a little, for instance, it moves the series resonance to a slightly lower frequency, and also reduces the Q-factor by a bit. $V_o = V_p + R_p i_p$ (see Figures 7.14 and 7.15) will also have to be higher than V_p to drive current through R_p. Since op-amps do not work with arbitrarily high voltage rails, and that they can only draw finite current, there are some design constraints for R_p.

(4) To drive all eight Rods, we have four transformers to drive four pairs of Rods. In the testing of the transformers, we discovered that there are capacitive couplings between neighboring Rods. This results in capacitive couplings between transformers on the order of ~ 7 pF. It is straightforward to expand the above analyses to include the effects of coupled transformers using the principle of superposition[11] . However, the expressions are so complicated looking that they do no shed more light than the expressions for uncoupled transformers above, so we do not show them here. The general features of how the resonance depends on various parameters remain largely the same. In the design of the final system, we iterate between analytical simulations using our model (cross-checked with LTspice) and testing the transformers in the actual setup.

[10] There is a correction factor on the order of unity at the parameters that we are using. The Q-factor is defined as (Circulated power)/(Dissipated power), i.e., $Q = \frac{V_s^2/[1/(\omega_{series}C)]}{V_s^2/R_s + i_p^2 R_p} = \omega_{series} R_s C \times \frac{L_p L_s R_s K^2 \omega_{series}^2}{L_p L_s R_s K^2 \omega_{series}^2 + R_p[R_s^2(1-L_s C\omega_{series}^2)^2 + \omega_s^2 L_s^2]} \approx \omega_{series} R_s C \times 0.4$. One can see that in the absence of the current limiting resistor R_p on the primary side, the correction factor goes to 1.

[11] Treating the voltage sources of "undriven" transformers as shorts.

7.5.1.4 Final design

It takes more than one person to construct and fine tune the transformers. Fellow graduate student Noah Schlossberger and undergraduate Antonio Vigil also played huge roles. Here, I will just broadly lay out the steps we took to get to the final product, and I would recommend interested readers to refer to Noah's thesis for the details.

We tested out the transformers individually and their performances matched very well with the model that we mentioned in the previous sections. However, as alluded on earlier, when the transformers are put together the transformers talk to each other through capacitive coupling, resulting in output waveforms with modified amplitudes and phases. As Noah details in his thesis, we overcome this problem by calibrating a "transfer matrix" that takes in desired output voltage amplitudes and phases on the Rods, and spit out recommended input voltage amplitudes and phases from the op-amps. This is done by measuring the difference voltage across each transformer though a precision monitor circuit box that sits right outside the vacuum flange with the electrical feedthroughs to the Rods. With this, we manage to shim the amplitudes down to less than 0.1% and the phases down to less than 0.5°.

The transformers certainly do not know when to start driving the Rods, so they are only one set of components in a bigger ecosystem of what constitutes the Rod driver. Figure 7.17 shows an overview of the whole Rod driver ecosystem.

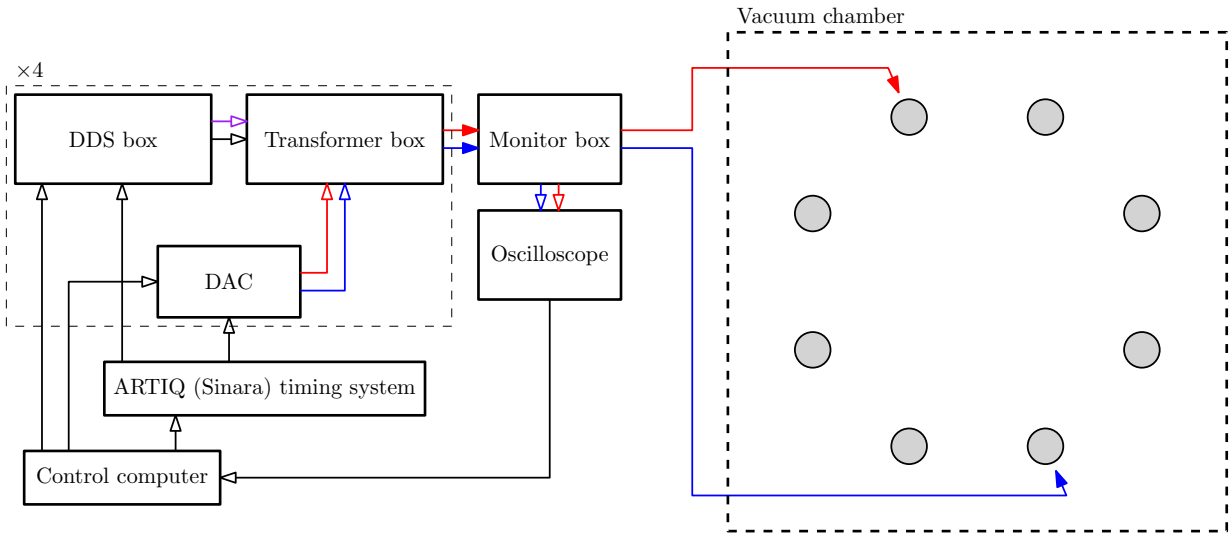

Figure 7.17: **Schematic of an overview of the Rod driver.** A control computer programs (i) the DDS box on the relevant (low voltage) waveforms to output for the RF frequencies (V_{RF}) and the rotating electric field (V_{rot}), (ii) the Sinara Zotino DAC for any DC shims we wish to apply to the Rods (V_{DC}), and (iii) the Sinara timing system (more details in Chapter 9) to synchronize the timing of the DDS and DAC. The output from the DDS and DAC go into the transformer box, where V_{RF} and V_{rot} are amplified with HV op-amps PA94. V_{RF} is summed onto V_{rot} on the secondary coil, whereupon V_{DC} is added on through resistors. The HV outputs are sent to the monitor box, where we have a voltage divider for us to readout the voltages safely at low voltages on an oscilloscope; these can then be fed back into the system through our control computer. The HV outputs then go from the monitor box to the Rods through the feedthroughs on the vacuum chamber. The flow of all communication signals and low voltages are indicated by unfilled arrows, and high voltages are indicated with filled arrows. The schematic is drawn for one Rod-pair for brevity, but there are four Rod-pairs for a total of eight Rods; we use four separate channels in the DDS and DAC boxes to feed into four sets of transformer boxes, one for each Rod-pair. The DDSes are of the same design used in the Gen. II JILA eEDM experiment. They are designed in-house by electronics shop staff Felix Vietmeyer, and put together with the help of electronics shop staff James Fung-A-Fat. The PA94 HV op-amps in the transformer box are cooled with processed chilled water.

7.5.2 Ring driver

As alluded to earlier on in Section 7.4.2, we use 22 independently controlled Ring voltages to (i) stop our ions into our trap, (ii) move our ions within the trap transversely to overlap with the laser beams, (iii) move our ions within the b.B.B. axially in and out of the cold region, and (iv) kick our ions towards our ion detector. All the voltage control is governed by our Ring driver. A schematic overview of our Ring driver is shown in Figure 7.18.

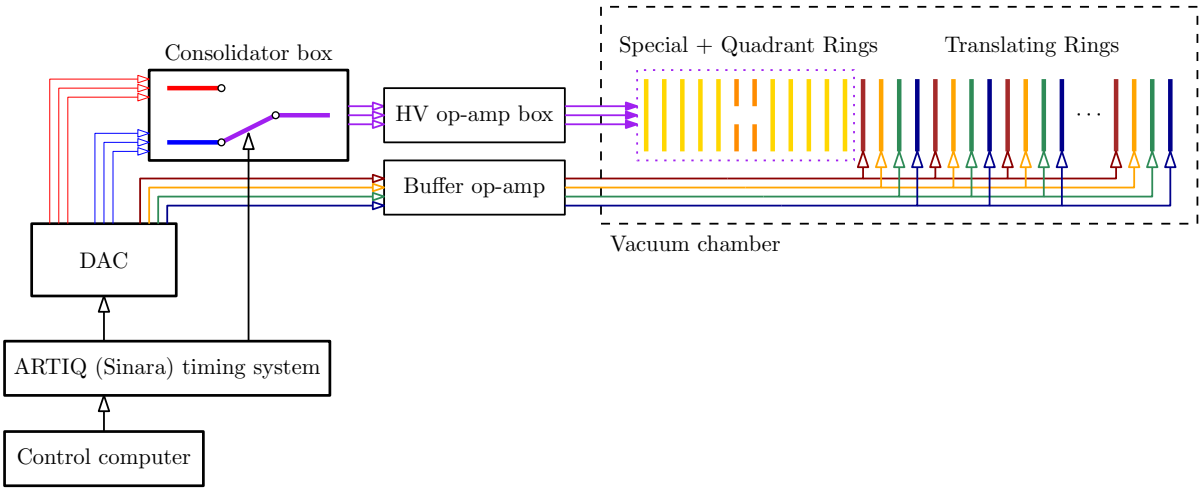

Figure 7.18: **Schematic of an overview of the Ring driver.** Control signal and low voltages are represented by unfilled arrows, while the high voltages are indicated by filled arrows. A control computer programs the FPGA based Sinara timing system, which then sets the voltages on the 64-channel DAC (Sinara Zotino). Two sets of voltages are sent to a "consolidator box" through SCSI cables. The "consolidator box" was designed in-house by electronics shop staff Terry Brown. It consolidates the voltages, sends them through buffer op-amps, and performs a simultaneous switch between the two sets of voltages. This allows for fast switching between two sets of voltages for, say, ion stopping voltages and trapping voltages; the DACs are not fast enough to do the switch on a ~ 10 ns time scale. The Sinara timing system controls the timing of the switch. The output from the "consolidator box" is amplified with PA94 HV op-amps before being sent to individual Special and Quadrant Rings (see Figure 7.9), each Ring having its own electrical feedthrough on the vacuum flange. A third set of voltages are sent from the DACs into a set of buffer op-amps, before going to the Translating Rings. In our current setup, the buffer op-amps live inside the "consolidator box". For the Translating Rings, there are only four electrical feedthroughs on the vacuum flange. We connect every fourth Translation Ring to the same electrical bus for a total of four distinct buses. In our current setup, we use the Spines as the buses, being careful to electrically insulate the Translating Rings from the Spines with the irrelevant voltages. The PA94 HV op-amps are cooled with processed chilled water.

7.6 Parametric excitation

Before we close off this chapter on the electric fields inside the b.B.B., let us look at a feature newly introduced into the JILA eEDM toolkit: parametric excitation of the ion motion inside our trap. This idea has been inspired by our fellow ion trappers, see for example Refs. [84, 85].

7.6.1 Motivation

Diagnosing the trap is a key part in ensuring success in our eEDM measurement. We have been able to diagnose our ion trap very well in the first two generations of the JILA eEDM experiment. Here is a quick summary of how we have been diagnosing our trap. We give our ions an intentional kick in the direction that we are interested in. This will make the ions slosh around the trap at the respective secular frequency. We then eject our ions out of the trap, and the position that they fall onto the ion detector will move around at the secular frequency of interest. We can then extract the frequencies of the trap by repeating this for all three principle axes of the trap.

However, the above protocol may not work in Gen. III. We may want to diagnose parts deep inside our b.B.B., where we do not have access to electrodes that can kick our ions onto the ion detector. Fortunately we have an extra channel on our DDS that we can feed onto our Rods, giving us access to parametric excitation at all locations of the b.B.B.. To diagnose any part of the b.B.B., we just need to (i) create ions in the Octagon like we always do, (ii) move the ions to that desired location, (iii) apply parametric excitation, (iv) move the remaining ions back to the Octagon, (v) eject them towards the ion detector like we always do, and (vi) repeat by scanning the frequency of the parametric excitation, and look for dips in the remaining ion numbers. We shall now see how parametric excitation works.

7.6.2 Mechanism

We introduce a time-varying quadrupole potential in the radial direction to trap our ions radially. The frequency of this quadrupole potential is at 50 kHz. As a result of the ponderomotive potential, the ions have a radial secular trap frequency of about 2 kHz. Suppose we add on top of the 50 kHz quadrupole potential a 4 kHz quadrupole potential (twice the secular frequency), we can excite the radial mode of

motion resonantly, and amplify the secular motion of the ions. For generality, let us suppose that the exciting quadrupole potential is at an angle θ w.r.t. the principle axes of the secular motion, the equation of motion is (limiting ourselves to the 2D x-y plane):

$$\begin{aligned}\frac{\mathbf{F}}{m} =& -\omega_x^2\mathbf{x} - \omega_y^2\mathbf{y} \\ &+ \alpha\cos\Omega t\left[(x\cos\theta + y\sin\theta)\hat{x} + (x\sin\theta - y\cos\theta)\hat{y}\right],\end{aligned} \tag{7.16}$$

where $\omega_{x,y}$ are the angular secular frequencies along the principle axes x and y, α is a measure of coupling strength of the excitation to the ions, and Ω is the exciting angular frequency. The first line is just a particle in a harmonic trap, and the second line is the additional quadrupole potential. We can rewrite the above as:

$$\begin{pmatrix}\ddot{x}(t)\\ \ddot{x}(t)\end{pmatrix} = \left[-\begin{pmatrix}\omega_x^2 & 0\\ 0 & \omega_y^2\end{pmatrix} + \alpha\cos\Omega t\begin{pmatrix}\cos\theta & \sin\theta\\ \sin\theta & -\cos\theta\end{pmatrix}\right]\begin{pmatrix}x(t)\\ y(t)\end{pmatrix}. \tag{7.17}$$

We can solve the above perturbatively for small α using the method of series expansion in powers of α (we are solving for $x(t)$ here, but the same applies for $y(t)$ by symmetry):

$$x(t) = x_{(0)}(t) + \alpha x_{(t)} + \mathcal{O}(\alpha^2), \tag{7.18}$$

where the subscript (n) indicates the n^{th} order term in the expansion series.

The zeroth order term is:

$$x_{(0)}(t) = X_0\cos\left(\omega_x t + \phi_x\right),$$

where X_0 and ϕ_x are the amplitude and initial phase. This is just the solution to the ion motion along the x direction in a harmonic trap.

The equation governing the first order term is:

$$\begin{aligned}\ddot{x}_{(1)}(t) &= -\omega_x^2 x_{(1)}(t) + \cos\Omega t\left[x_{(0)}(t)\cos\theta + y_{(0)}(t)\sin\theta\right] \\ &= -\omega_x^2 x_{(1)}(t) + \frac{1}{2}\Bigg\{X_0\cos\theta\big[\cos\left(\Delta_x t + \phi_x\right) + \cos\left(\Sigma_x t + \phi_x\right)\big] \\ &\qquad + Y_0\sin\theta\big[\cos\left(\Delta_y t + \phi_y\right) + \cos\left(\Sigma_y t + \phi_y\right)\big]\Bigg\},\end{aligned}$$

where $\Delta_i := \Omega - \omega_i$ and $\Sigma_i := \Omega + \omega_i$. The equation is just an oscillator with a forced motion, and the

inhomogeneous solution to the above is:

$$x_{(1),\text{inhomo.}}(t) = \frac{1}{2}\Bigg\{ X_0 \cos\theta \left[\frac{\cos\left(\Delta_x t + \phi_x\right)}{\Omega(\Omega - 2\omega_x)} + \frac{\cos\left(\Sigma_x t + \phi_x\right)}{\Omega(\Omega + 2\omega_x)} \right] + Y_0 \sin\theta \left[\frac{\cos\left(\Delta_y t + \phi_y\right)}{[\Omega - (\omega_x + \omega_y)][\Omega + (\omega_x - \omega_y)]} + \frac{\cos\left(\Sigma_y t + \phi_y\right)}{[\Omega + (\omega_x + \omega_y)][\Omega - (\omega_x - \omega_y)]} \right] \Bigg\}. \tag{7.19}$$

The homogeneous solution is grouped together with $x_{(0)}(t)$. Let us take a moment to analyze the above solution.

The first term in the square brackets with the X_0 term has a $\Omega - 2\omega_x$ term in the denominator. This means that our ions will have huge amplitudes in the x direction when $\Omega = 2\omega_x$, i.e. when the driving frequency is twice the trap secular frequency. This is the resonant excitation.

The first term in the square brackets with the Y_0 term has a $\Omega - (\omega_x + \omega_y)$ term in the denominator. This means that if Ω happens to be the sum of the two secular frequencies, our ions will also have motion with a huge amplitude. This is the crossover term.

The picture above assumes that our trap is harmonic to an infinite range. In practice, our trap starts to become anharmonic as we move a few centimeters away from the trap axis, and the ions will start to spill out of the trap because our trap depth is finite.

In summary, if we sweep the driving frequency Ω, we expect to see ion loss when Ω is either $2\omega_i$ or $\omega_x + \omega_y$. If the secular frequency is different in x than in y (as is usually the case), we expect to see three dips in ion numbers, two corresponding to the secular frequencies, and one corresponding to the crossover. Figure 7.19 shows an example of data from such a scan.

7.6.3 Further discussion

As alluded to earlier on in this section, parametric excitation was developed as a diagnostic tool for us to understand our trap at various locations inside the b.B.B. where we do not have access to electrodes that can kick our ions. An example of how we can use parametric excitation to diagnose our b.B.B. is shown in Figure 7.20.

The dosage (voltage on the Rods $\times$ time applied) can be adjusted to pick out certain details. For

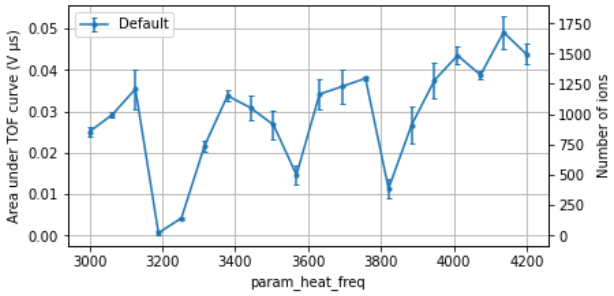

Figure 7.19: **Number of ions remaining in the trap after parametric excitation.** Data was taken at the Octagon on 25 October 2022, RID 25916. The horizontal axis is the excitation frequency $\Omega/(2\pi)$, and the vertical axis is the area under the curve from our ion detector, corresponding to number of ions detected. The ions are exposed to the parametric excitation for 50 ms, with a peak voltage of 150 mV on the Rods (compared to 25.6 V for the radial confinement). The dips at 3.2 kHz and 3.8 kHz correspond to the secular frequencies for the x and y directions. We confirmed this by kicking our ions intentionally (without the parametric excitation) in the x and y directions within the Octagon, and ejecting them onto our ion detector to observe their sloshing frequencies. The dip at 3.5 kHz is the crossover dip. We can employ either the kicked ion method or parametric excitation to learn about our trap at the Octagon, but we can only use parametric excitation at other locations inside the b.B.B..

example, one can choose to reduce the voltage if the parametric excitation is too saturated (dip is too broad and goes all the way down to zero), or to reduce the voltage but increase total excitation time to make the width of the dip narrower.

We now have a multiplexed ion trap, the b.B.B., and we have all the electronics and electrodes to perform the multiplexing. We are now in a good position to move on to the next chapter to investigate various methods of using the b.B.B. to offset our Ramsey frequency away from zero. We shall also see why we want to do this in the next chapter.

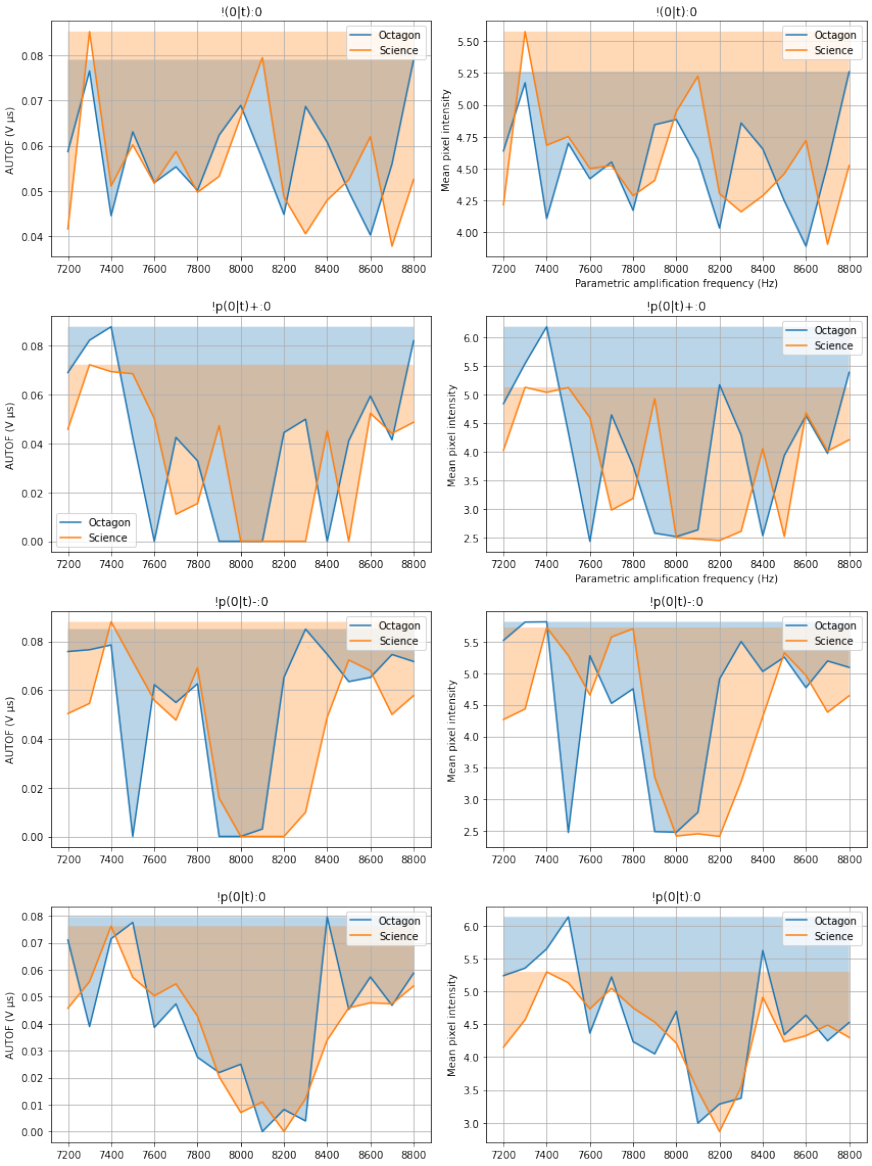

Figure 7.20: **Using parametric excitation to diagnose the trap.** Here we wanted to understand if turning on $\mathcal{E}_{\text{rot}}$ in the b.B.B. would introduce ponderomotive potentials that could change the trap secular frequencies. We wanted to understand this both at the Octagon (chop named "Octagon"), and in the Cold Tube where we intend to perform our long Ramsey interrogation (chop named "Science"). The first row corresponds to a background experiment where we do not turn $\mathcal{E}_{\text{rot}}$ and the parametric excitation on. The last row is a control experiment where turn on parametric excitation but not $\mathcal{E}_{\text{rot}}$. There is only one broad dip at around 8.2 kHz because we ramped our trap up to about 4 kHz. The second (third) row corresponds to having parametric excitation on, and $\mathcal{E}_{\text{rot}}$ rotating in the anti-clockwise (clockwise) direction as seen from the Cold Tube towards the ion detector. Note that the single broad dip from the last row has split into three different dips with $\mathcal{E}_{\text{rot}}$ turned on. This suggests that $\mathcal{E}_{\text{rot}}$ is doing something to our trap frequencies by modifying it through ponderomotive potentials. Also note that the second and third rows look different, implying that having $\mathcal{E}_{\text{rot}}$ rotating in one direction changes our trap differently than having $\mathcal{E}_{\text{rot}}$ rotating in the other direction. This set of data was taken during the early days (18 April 2023) of understanding our trap. The system is much more well behaved now; this plot is just to show a possible application of parametric excitation in our new setup.

Chapter 8

Generating f_0 in the Bucket Brigade

8.1 Introduction

To measure the eEDM, we need to measure the energy difference between the stretched Zeeman states of the "upper Stark doublet" and the "lower Stark doublet" (see Figure 1.4). We apply a deliberate frequency offset (f_0) to the states within the doublets and subtract away this known additional energy difference from the measured quantity to obtain the contribution from the eEDM. We do this for two reasons.

First, we expect the eEDM to be very small, we expect a very small energy difference, corresponding to a very small Ramsey frequency, which is hard to measure because of the $1/f$ noise (the power spectrum density of noise in our setup typically scales with frequency as $1/f$). Hence, we bias the energy difference between the stretched states deliberately to a non-zero value f_0.

Second, the polarization axis of our molecules rotates, so there is a non-inertial-frame coupling (Δ) in the molecules' rotating frame that couples the Zeeman states within the doublets (see Figure 1.4). We apply a frequency offset $f_0 \gg \Delta$ so that each Zeeman state within the doublets remains a good eigenstate.

In the first two generations of the JILA eEDM experiment, we introduce the frequency offset between the stretched Zeeman states within the doublets through Zeeman shifts with applied magnetic fields. This is certainly not the only way to introduce frequency offsets in our experiment. We will be investigating various plans of introducing frequency offsets in the Bucket Brigade in this chapter. Many of these plans were inspired by systematic effects that we saw in the first two generations of the JILA eEDM experiment; we intend to turn these bugs into features. The feasibility of each of these plans will be judged based on the

following criteria:

Criterion 8.1 (Spatial homogeneity across Bucket Brigade) The Ramsey frequency, f_0, seen by an ion packet should not change too much[1] across the whole Bucket Brigade from shot to shot.

Criterion 8.2 (Spatial homogeneity within ion cloud) Our ion cloud has a non-zero spatial extent (Equation 6.21). Whatever mechanism we use to generate f_0, we care about its spatial variation within a ± 1 cm radius region (looking out to 2σ radius to include 95% of all ions) around the cloud center. For an f_0 of 50 Hz and a free evolution time of 20 s, we have 1000 such Ramsey oscillations. For a spread in frequencies corresponding to 10% of an oscillation at the end of 20 s, we would need $< 0.01\%$ difference in f_0 as seen by (i) the ensemble of ions in each ion cloud, and (ii) different ion packets from shot to shot.

We did not get creative with names this time for the various plans. The following is a quick summary of the various plans for easy comparison.

Plan A Zeeman shift with an axial magnetic quadrupole, $\mathbf{B} = B_{\text{axgrad}}(x, y, -2z)$, and rotational micromotion; used in the first two generations of the JILA eEDM experiment.

Plan B Berry's phase; an adaptation of a systematic effect seen in the first two generations of the JILA eEDM experiment.

Plan C Zeeman shift with uniform ambient magnetic field and an oscillating uniform electric field that is going as a second harmonic of $\mathcal{E}_{\text{rot}}$; an adaptation of a systematic effect seen in the first two generations of the JILA eEDM experiment.

Plan D Zeeman shift with transverse magnetic quadrupole field, $\mathbf{B} = B_{\text{transgrad}}(\mathbf{x} - \mathbf{y})$, and an elliptical $\mathcal{E}_{\text{rot}}$.

Plan E Zeeman shift with rotating magnetic field introduced by currents flowing along the electrodes.

We will be focusing more effort in analyzing Plans A and B in the context of the Bucket Brigade, using them as classic examples of how we can introduce a frequency offset with the Zeeman shift and Berry's phase,

[1] f_0 can be allowed to change a little throughout the whole Bucket Brigade; if all the ion packets see the same variation as they go through the same stretch of Bucket Brigade, the variations in f_0 will not result in additional uncertainties in the measured Ramsey frequencies.

respectively. We will then introduce Plans C to E conceptually, which are ingenious ways of introducing Zeeman frequency offsets differently from Plan A.

8.2 Plan A: Co-moving axial magnetic quadrupole

8.2.1 Working principle

In the first two generations of the JILA eEDM experiment, we used a Zeeman effect to give us a frequency offset between the two stretched Zeeman states in a doublet. The physics behind this effect has been described in detail in the theses of previous members of the group who worked on the Gens. I and II experiments. A brief summary is as follows.

Current-carrying coils in the anti-Helmholtz configuration generate a magnetic field of the form $\mathbf{B} = B_{\text{axgrad}}(\mathbf{x} + \mathbf{y} - 2\mathbf{z})$ (see Figure 8.1). An electric field rotating in the x-y plane polarizes our ions in the

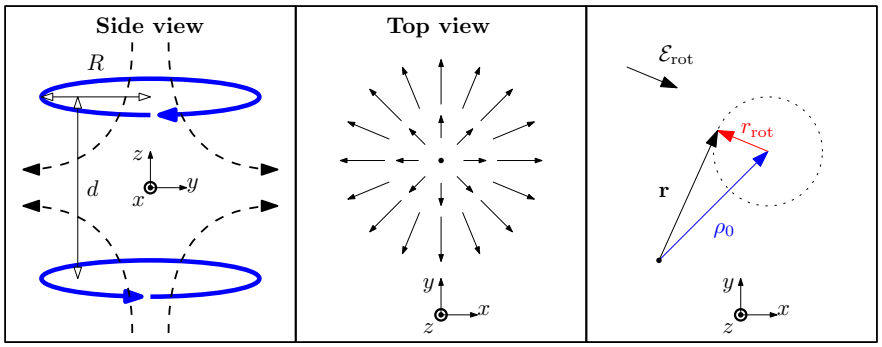

Figure 8.1: **Illustration of the coils and magnetic field configurations used to generate a Zeeman offset frequency.** In the side view, the blue arrows indicate the directions of the current flowing inside the two respective coils (for example, the current in the top coil is going clockwise looking from the top). The dashed lines indicate the fields generated by the coils. The spacing between the two coils is d, and the radius of each coil is R. For an anti-Helmholtz configuration, $d = \sqrt{3}R$. In the top view, the arrows indicate the radial magnetic field along the x-y plane. The length of each arrow represents the strength of the field at that position. In the right panel, $\mathbf{r}$ is the radial position vector of an ion from the trap center. This radial position vector can ve decomposed into a constant vector $\boldsymbol{\rho}_0$ and a rotating vector $\mathbf{r}_{\text{rot}}$. The rotating vector $\mathbf{r}_{\text{rot}}$ is anti-parallel with the direction of the rotating polarizing electric field $\mathcal{E}_{\text{rot}}$. As $\mathcal{E}_{\text{rot}}$ rotates in the x-y plane, $\mathbf{r}$ traces out a circle indicated by the dotted line. In the rotating frame of our molecules (defined by $\mathcal{E}_{\text{rot}}$), $\mathbf{r}_{\text{rot}}$ is non-rotating, and $\boldsymbol{\rho}_0$ rotates.

rotating frame, and induces a rotational micromotion with radius $r_{\text{rot}} = \frac{e\mathcal{E}_{\text{rot}}}{m\omega_{\text{rot}}^2}$. In the rotating frame of the ions performing rotational micromotion, they see a time-varying magnetic field of the form:

$$\mathbf{B}(t) = -B_{\text{axgrad}}\, r_{\text{rot}}\, \hat{n} + B_{\text{axgrad}}\, \rho_0\, (\cos\omega_{\text{rot}} t\, \hat{x} + \sin\omega_{\text{rot}} t\, \hat{y}),$$

where $\hat{n}$ indicates the polarization axis, and ρ_0 is the radial position of the ion within the trap.[2] The contribution of the time-varying part of the magnetic field averages out to zero in one cycle of the rotational micromotion. Only the first term contributes to the net Zeeman offset. Therefore, there is a net Zeeman offset between the stretched states of the form:

$$hf_0 = 3g\mu_B B_{\text{axgrad}}\, r_{\text{rot}} =: 3g\mu_B \mathcal{B}_{\text{rot}}. \tag{8.1}$$

We call this method of introducing a Zeeman frequency offset between the two Zeeman stretched states within each doublet: Plan A.

8.2.2 In the Bucket Brigade

As alluded to in Section 5.3, the Bucket Brigade consists of a conveyor belt of ion traps, where the radial confinement of ions is provided by Rods with RF-fields, and the axial confinement is provided by the Rings, acting as "end caps" of the usual Paul traps. The ions are moved down the Bucket Brigade by modulating the potentials on the Rings periodically with a fixed and well chosen phase difference between neighboring Rings. We now try to implement a naïve version of Plan A in the Bucket Brigade, where each bucket of ions has its own "anti-Helmholtz" coils translating along with it.[3] We do not intend to do this with anti-Helmholtz coils that move physically with the ions. Instead, we plan to have arrays of current carrying coils, with currents that are modulated periodically in time and space with a well chosen phase difference between neighboring coils.

There are many length related parameters in this analysis. Before we proceed further, we shall summarize the definitions of some variables here:

Distance along the translation direction/trap axis, z. We define the z axis to be the direction along which ions translate, with $z = 0$ at the center of the Bucket Brigade.

[2] The ion could be performing secular motion within the trap, so ρ_0 is actually a time-varying variable, but the time scale at which this is happening (1 kHz) is slow compared to the rotational micromotion (150 kHz), so ρ_0 can be treated to be time-independent by separation of time scales.

[3] Here we draw the distinction between anti-Helmholtz and "anti-Helmholtz" in quotes. The former refers to the classic anti-Helmholtz coil pair (e.g. left panel of Figure 8.1) with a fixed ratio between the coil separation distance (d) and coil radius (R) at $d = \sqrt{3}R$. This fixed ratio gives $\partial_z^k B_z(z = 0) = 0$ for $k \in \{0, 2, 3, 4\}$ for a pair of coils centered at $z = 0$ with their symmetry axis pointing along the z direction. The latter one in quotes refers to the combined geometry and current amplitude configuration of a set of coils that gives the condition $\partial_z^k B_z(z = 0) = 0$ for $k \in \{0, 2, 3, 4\}$.

Axial position of the n^{th} translating ion packet, $Z_n(t)$. For an ion packet that is translating at speed v_{trans}, then we have $Z_n(t) = v_{\text{trans}}t$. The n index is just a placeholder, but for concreteness, we cay that the first packet that we send in corresponds to $n = 1$.

Radius of the coils, R. We work with the simple case where all the coils have the same radius R.

Distance between the two coils in the classic anti-Helmholtz setup, d. In the classic anti-Helmholtz setup, there are only two coils. These coils have counter-propagating currents, and they are separated by the distance d (see Figure 8.1 for the configuration). In an anti-Helmholtz configuration, there is a special relation between the distance between the coils and the radius of the coils, $d = \sqrt{3}R$, where the axial gradients (and higher order) of the axial magnetic field is zero up to and including the fourth order except for the first order gradient, i.e. $\partial_z^k B_z(z) = 0$ for $k \in \{0, 2, 3, 4\}$. Symmetry of the setup makes all the even order derivatives zero. The $d = \sqrt{3}R$ condition allows for the coils centered around $z = 0$ to give a zero third order gradient of the axial field $\partial_z^3 B_z(z = 0) = 0$. This means that there is a substantial volume of region where there is a very homogeneous first order axial magnetic field gradient; $\mathbf{B} = B_{\text{axgrad}}(\mathbf{x}, \mathbf{y}, -2\mathbf{z})$ is a good approximation within a large volume.[4]

Distance between two coils in the Plan A setup, l. In contrast to the classic anti-Helmholtz setup, we will need an array of coils in the Bucket Brigade setup to generate field gradients throughout the whole Bucket Brigade. The coils will have separation distance of l from each other. Note that l and d are not related to each other, they describe entirely different systems.

Bucket length or distance between neighboring sets of coils in the coil array, Λ. As alluded to earlier on, we plan to have an array of current-carrying coils, each with a time-modulated current to effect an "anti-Helmholtz" magnetic field gradient that moves with the ion buckets. There will be four coils per bucket of ions. The separation between each set of four coils is $\Lambda = 4l$ (see Figure 8.2).

We also note that the spacing between two neighboring buckets of ions is the bucket length: $Z_n(t) - Z_{n+1}(t) = \Lambda$.

[4] $\partial_z B(z) = -2B_{\text{axgrad}}$

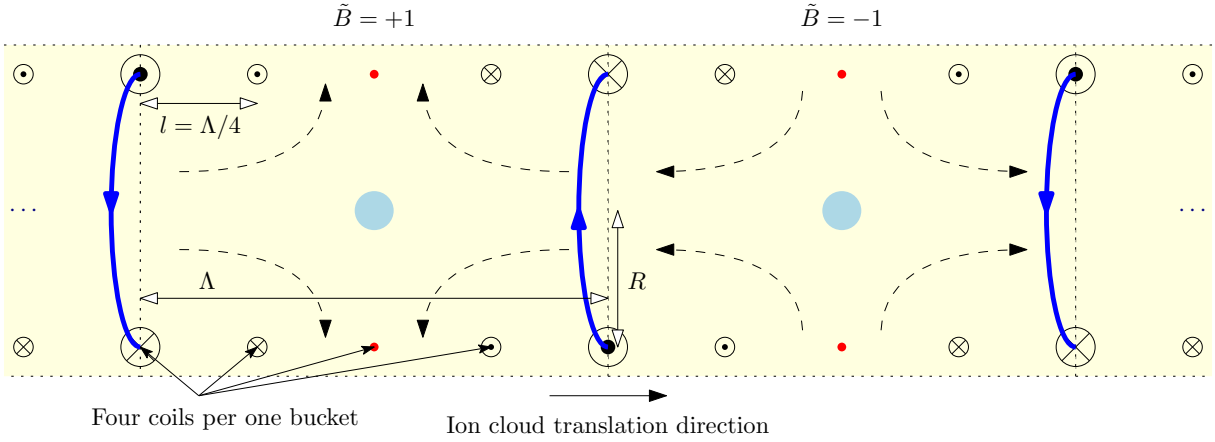

Figure 8.2: **Plan A: using current-carrying coils to introduce an axial magnetic field gradient.** This is a cross-section view of a section of the Bucket Brigade. The ions move from left to right. The light blue disks indicate the ion clouds in the Bucket Brigade. The dashed lines are visual aids to indicate the boundary of each bucket. The arrow head/tail symbols indicate the magnitudes and directions of the current in the coils; the red dots indicate presence of coils with no current flowing in this snapshot in time. The coils will sit outside the vacuum chamber, and are fixed in position. For better visualization, I have included additional blue arrows to indicate the direction of the current in some of the coils coming out of the page. The dashed arrows indicate the direction of the local magnetic fields generated by the current-carrying coils. There are four coils per bucket, with each set of coils separated by Λ. The radius of the coils is R. To introduce a non-zero B_{axgrad}, the currents in the coils have to flow in opposite directions on either side of the ions. This gives rise to the configuration where the sign of B_{axgrad} alternates with each bucket. $\tilde{B} = +1$ (-1) indicates the bucket with the radial magnetic field going outwards (inwards) radially.

One accidental feature of Plan A is that neighboring buckets have B_{axgrad} of opposite signs, as can be seen from Figure 8.2. This alternating sign of B_{axgrad} corresponds to switching the sign of the Zeeman offset (the $\tilde{B}$-switch). Being able to switch $\tilde{B}$ frequently (once every other ion packet) allows us to understand and suppress systematic effects associated with magnetic fields. This is not necessary for an eEDM experiment, but is certainly very desirable to have. Plan A provides a very elegant solution to fast $\tilde{B}$-switching.

We shall now go into the details. First, we will determine the modulation on the currents required to give us as homogeneous a B_{axgrad} as possible at the ion locations (Section 8.2.2.1). Second, we will determine how long each bucket needs to be so that B_{axgrad} is homogeneous enough throughout the spatial extent of a typical ion cloud (Section 8.2.2.2). Finally, we discuss a slight variation of Plan A, which we call Plan A$'$ (Section 8.2.2.3).

8.2.2.1 Determining constraints on currents in coils

For Plan A to work, we need a non-zero $\partial_z B_z$. We also want many of the higher order derivatives to be zero. Unlike the case of a single pair of anti-Helmholtz coils with a single ion trap (Section 8.2.1), we cannot do this by setting the ratio of the coil separation d and the coil radius R to be some magical number; this might work at a specific ion location w.r.t. the coil positions, but it will not work for the entire length of the Bucket Brigade where we will be translating the ions. We can mimic the anti-Helmholtz condition of having zero higher order derivatives to the third order[5] by modulating the currents in the coils in a specific way. To understand how we want to modulate the currents, we need to sum the contributions of the fields from all the coils, and impose some constraints on them.

We first see that the analytical solution to $B_z(x, 0, z)$ with a coil placed at $z = 0$ on the x-y plane and a current flowing counter-clockwise is (by Biot-Savart law, also see Figure 8.3):

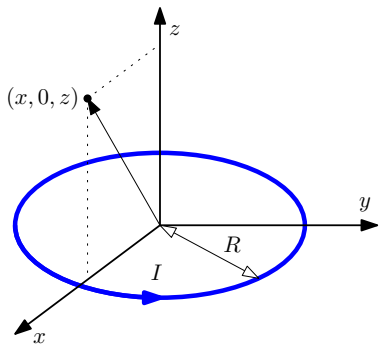

Figure 8.3: **Schematic of a coil with radius R in the x-y plane with current going clockwise.** We are interested in the axial magnetic field B_z at an arbitrary location (x', y', z'). By the symmetry of the setup, one can always rotate the coordinate system about the z axis such that the point of interest lies above the x axis such that the coordinates in the new system is $(x = \sqrt{x'^2 + y'^2}, 0, z = z')$. Hence, to evaluate the field at an arbitrary point, we just evaluate it for the case of $(x, 0, z)$, and perform the relevant rotation back to (x', y', z').

$$B_z(I, x, 0, z) = \frac{\mu_0 I R}{4\pi} \int_0^{2\pi} \mathrm{d}\phi \, \frac{R - x\cos\phi}{(R^2 + x^2 + z^2 - 2Rx\cos\phi)^{3/2}}$$

$$= \frac{\mu_0 I R}{4\pi} \big(R \cdot \mathbb{I}(\alpha, \beta) - x \cdot \mathbb{C}(\alpha, \beta)\big) \tag{8.2}$$

(8.3)

[5] We only include up to the third order because we plan to have only four coils per bucket. Each coil has a current flowing through it with a magnitude that we can use as a free tuning parameter. We want to keep $\partial_z B_z$ constant at the ion location during translation, and this uses up one free parameter, leaving us with only three more free parameters to tweak; one for each $k \in \{0, 2, 3\}$ in $\partial_z^k B_z$.

where

$$\mathbb{I}(\alpha,\beta) := 2\,\frac{\sqrt{\alpha-\beta}E\left(-\frac{2\beta}{\alpha-\beta}\right)+\sqrt{\alpha+\beta}E\left(\frac{2\beta}{\alpha+\beta}\right)}{\alpha^2-\beta^2} \tag{8.4a}$$

$$\begin{aligned}\mathbb{C}(\alpha,\beta) := -\frac{2}{\beta}\Bigg[&\frac{\alpha}{\alpha^2-\beta^2}\left(\sqrt{\alpha-\beta}\,E\left(-\frac{2\beta}{\alpha-\beta}\right)+\sqrt{\alpha+\beta}\,E\left(\frac{2\beta}{\alpha+\beta}\right)\right)\\ &-\frac{1}{\sqrt{\alpha^2-\beta^2}}\left(\sqrt{\alpha+\beta}\,K\left(-\frac{2\beta}{\alpha-\beta}\right)+\sqrt{\alpha-\beta}\,K\left(\frac{2\beta}{\alpha+\beta}\right)\right)\Bigg]\end{aligned} \tag{8.4b}$$

$$\alpha = R^2+x^2+z^2, \tag{8.4c}$$

$$\beta = -2Rx, \tag{8.4d}$$

where $E(x)$ and $K(x)$ are the elliptic E- and K-integrals. When $x \to 0$, the above expression reduces to $\frac{\mu_0 I R^2}{2(R^2+z^2)^{3/2}}$, as expected, where we use the limits:

$$\lim_{x\to 0} E(x) = \frac{\pi}{2}, \qquad \lim_{x\to 0} K(x) = \frac{\pi}{2}, \qquad \lim_{x\to 0}\frac{E(x)-K(x)}{x} = -\frac{\pi}{4}.$$

The Bucket Brigade consists of many such coils. These coils will be placed along the outside of the vacuum chamber, with spacing $l = \Lambda/4$ between neighboring coils, where Λ is the length of one bucket. The m^{th} coil (with current $I_m(t)$, where we conveniently define $m = 0$ to be the coil placed at the center of the Bucket Brigade) placed on the x-y plane at $z = m\Lambda/4$ (see Figure 8.2) will produce an axial magnetic field $B_z^{(m)}(I_m, x, 0, z)$ given by:

$$B_z^{(m)}(x,0,z,t) = B_z(I_m(t), x, 0, z - m\Lambda/4). \tag{8.5}$$

Using Equations 8.2 and 8.5, we sum the contributions from all the coils. We then solve for $I_m(t)$ by demanding that $B_z = \sum_m B_z^{(m)}$ fulfills the following constraints:

Constant B_{axgrad}. We want $\partial_z B_z(Z_n)$ to be a constant at the (moving) ion location for the entirety of the ion translation down the Bucket Brigade. This will give the ions a constant Zeeman frequency offset throughout the translation. Note that this constraint is set by a moving point instead of a stationary point.

Zero k^{th} order gradients of B_z. Given that we have four coils per bucket, and we have already imposed on ourselves one constraint from the above, we only have three more degrees of freedom. With these

three degrees of freedom, we demand that $\partial_z^k B_z(Z_n) = 0$ for $k \in \{0, 2, 3\}$. This will ensure that the ion ensemble does not decohere through spatial inhomogeneity of the fields during the translation. These three constraints must also be fulfilled at the (moving) ion location for the entirety of the ion translation.

With the above constraints, we solve for $I_m(t)$ at various times during the ion translation within the Bucket Brigade. We note that:

$$I_m(t) = I_{m+8}(t),$$

because the spatial periodicity happens every two buckets (see Figure 8.2), and there are four coils per bucket. We also note that:

$$I_m(t) = I_m(t + 2\Lambda/v_{\text{trans.}}),$$

from the temporal periodicity of the setup, where, once again, Λ is the length of a bucket, and $v_{\text{trans.}}$ is the constant speed at which the buckets are translating down the Bucket Brigade. From the above, we can also say that:

$$I_m(t) = I_{m'}\big(t - (m' - m) \cdot \Lambda/(4v_{\text{trans.}})\big). \tag{8.6}$$

Making use of the periodic conditions above, we solve for $I_m(t)$ with various Λ, and the results are shown in Figure 8.4.

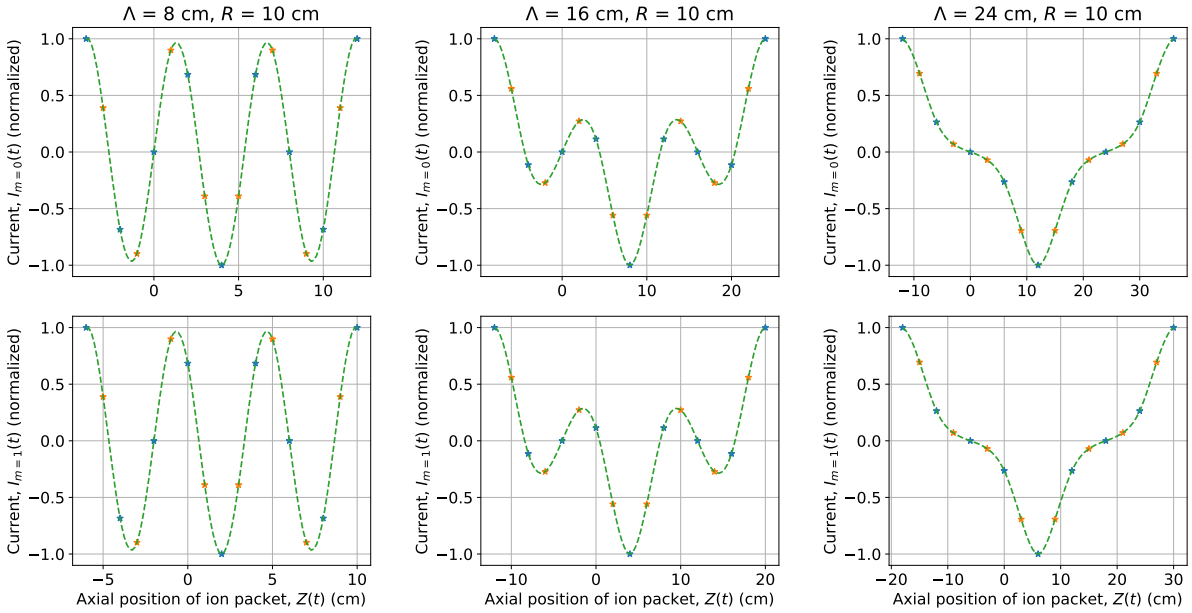

Figure 8.4: **Plan A: Temporal modulation of current in the m^{th} coil.** The plots show $I_m(t)$ plotted against $Z(t)$, where, once again, $Z(t)$ is the axial position of the ion packet. For example, when the ion packet is at the center of the Bucket Brigade, i.e. $Z = 0$, the current in the $m = 0^{\text{th}}$ coil ($I_{m=0}$) is the third blue point in the plots on the first row; I_1 corresponds to the fourth blue point, and so on. These modulations in $I_m(t)$ give a constant B_{axgrad} and $\partial_z^k B_z = 0$ for $k \in \{0, 2, 3\}$. The points indicate the values of t where we solve for $I_m(t)$, and the dashed lines are third order polynomial interpolation functions from the points. The blue (yellow) points correspond to instances where the ion packet is at a coil (between two coils). The points are solved for the case where the coil radius is $R = 10$ cm, with about 20 buckets on each side of the ion packet. To get $I_{m'}(t)$ for any arbitrary m', perform the relevant graph transformation on the plots with Equation 8.6. Note that the curves are not just simple sinusoids, in contrast to the sinusoidal voltages we send to Rings to translate the ions down the Bucket Brigade.

8.2.2.2 Spatial homogeneity

Using the values of currents in Figure 8.4, we can evaluate the spatial homogeneity of B_{axgrad} in the Bucket Brigade. Figure 8.5 shows the results for various bucket lengths Λ.

We can see from Figure 8.5 that we need a bucket length of at least 16 cm for the spatial variation of B_{axgrad} to be less than 0.01% (Criterion 8.2) within an ion cloud of radius 1 cm. This means that for a 40-bucket Bucket Brigade, the setup will be at least 40×16 cm $= 6.4$ m long. This is longer than the 3 m length that we are initially aiming for. If we limit ourselves to only 3 m, then we will lose half the number of buckets and take a 30% hit in statistical sensitivity.

It looks like Plan A can be a little tricky to implement as is. We cannot have short buckets if we want a region of spatial homogeneity large enough for our ion cloud. One thing to note is that we have limited ourselves to four coils per bucket in the above analysis. We could introduce more coils per bucket for more degrees of freedom to tweak the even higher order gradients of B_z to give us a greater region of homogeneity. However, at four coils per bucket in a 40-bucket Bucket Brigade, this is already 160 coils that we need to construct and control. Having more parts would introduce more sources of errors; we would only want to go down this road if necessary.

What if we give up on alternating $\tilde{B}$-switch with every bucket, and just have currents going through coils that do not change with time, but are allowed to vary according to the axial location of the coils? Could the fields can be more spatially homogeneous that way? We shall look at this in the next section.

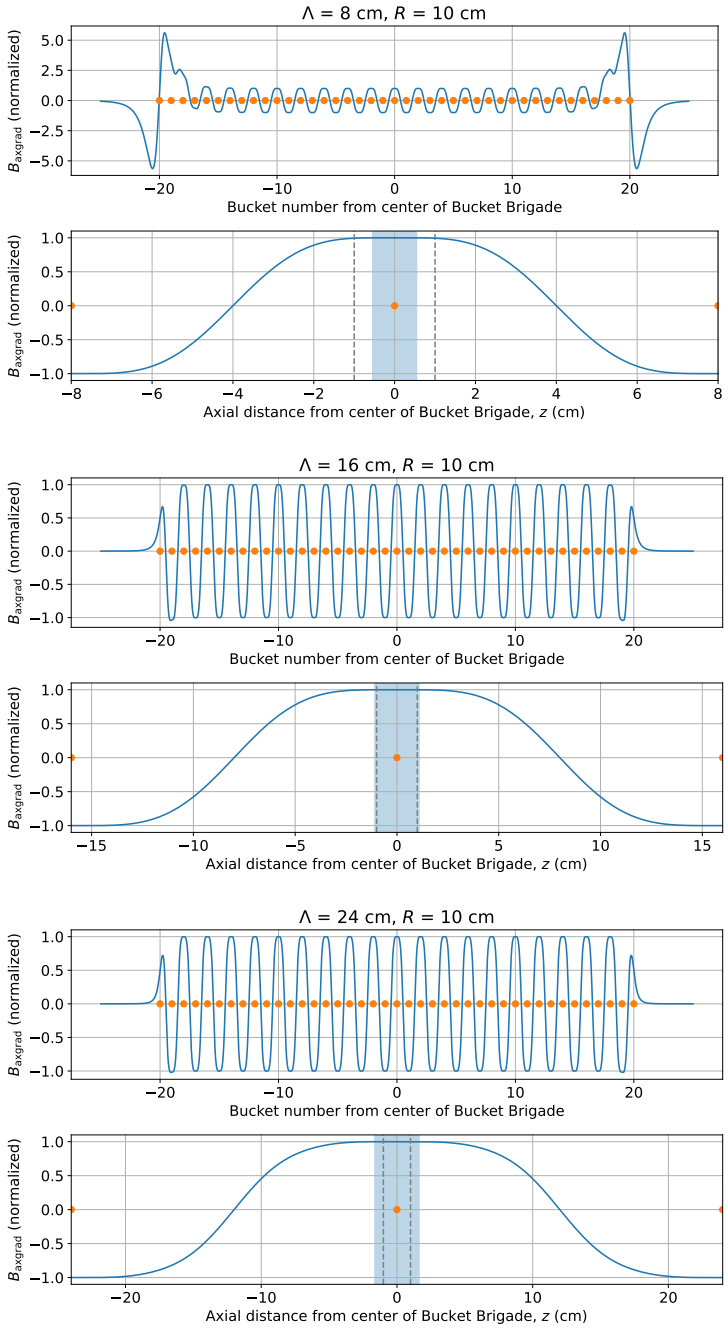

Figure 8.5: **Plan A: Plots of B_{axgrad} along the trap axis for various bucket length.** There is a coil at $z = 0$ (corresponding to the center of each plot) and there are coils going out to ± 20 buckets in either direction, with four coils per bucket, coil-coil spacing of $\Lambda/4$. The yellow circles indicate ion packets in the Bucket Brigade. The plots are normalized to the value of B_{axgrad} at the center of the Bucket Brigade. Every second plot is a zoomed in version of the first plot centered around the center of the Bucket Brigade. The blue shaded region indicates the region where B_{axgrad} is within 0.01% of the value at the center of the ion packet for this particular snapshot in time. The size of this region could change with the axial position of the ion cloud as it translates down the Bucket Brigade. Having only four coils per bucket only allows us to suppress higher order axial gradients in B_z up to the third order, and I did not investigate how the next non-zero higher order gradient varies with axial position of the ion cloud. The grey dashed lines indicate ± 1 cm from the center of the ion packet. From the plots, one can see that the field starts to settle down a few buckets into the Bucket Brigade, and it settles down much faster if each bucket is longer.

8.2.2.3 Plan A′: Stationary axial magnetic quadrupole

Suppose now we have coils right outside the vacuum chamber with radius $R = 10$ cm, and the current flowing through the m^{th} coil is $I_m = m \cdot i_0$, where i_0 is the difference in current between neighboring coils, and, once again, the $m = 0^{\text{th}}$ coil sits right at the center of the Bucket Brigade. The value of i_0 is directly proportional to the B_{axgrad} that we will get along the Bucket Brigade. Figure 8.6 shows the profile of B_{axgrad} along the trap axis of the Bucket Brigade for various inter-coil spacing l. Here we drop the constraint of having four coils per bucket.

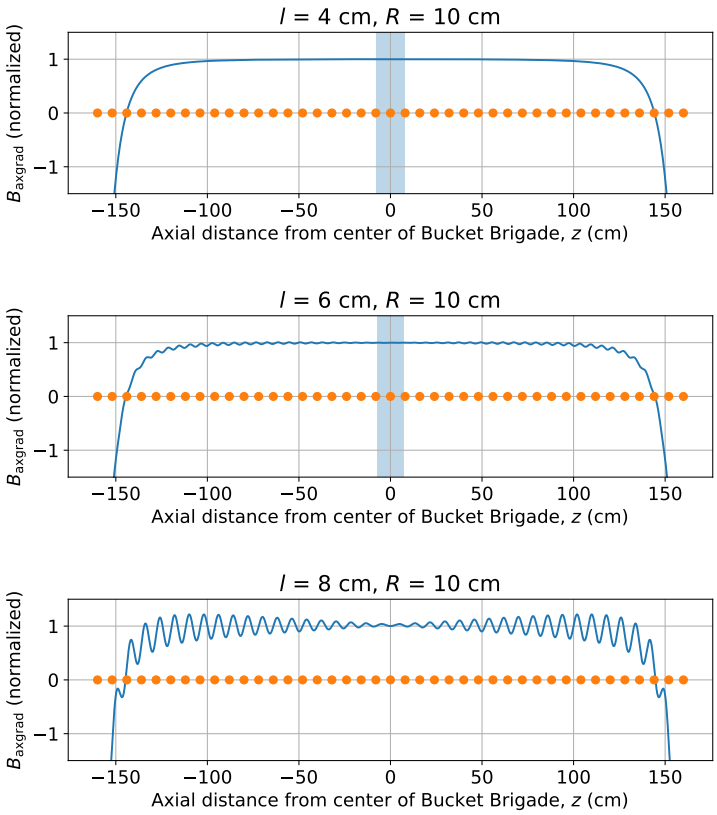

Figure 8.6: **Plan A′: Plots of B_{axgrad} along the trap axis for various bucket length.** There is a coil at $z = 0$ (corresponding to the center of each plot), and there are coils going out in both directions with spacing l, all the way until $z = \pm 160$ cm. The yellow circles indicate locations of the ion packets with bucket length $\Lambda = 8$ cm. The blue shaded region indicates where B_{axgrad} is within 0.01% of that at the center of the Bucket Brigade. When the inter-coil spacing is comparable to the coil radius R, there are noticeable fluctuations in B_{axgrad}.

One can tell from the plots in Figure 8.6 that the fields can be much more homogeneous. The edge

effects at the ends of the Bucket Brigade can be compensated for by use current magnitudes with non-linear dependence of the coils' axial positions. This would require some numerical modelling, but it is straightforward nonetheless.

In addition to being able to have homogeneous fields with short buckets, another advantage that Plan A′ has over Plan A is that the currents are do not vary in time in the former. This means easier control over the experiment; one can just send in DC currents instead of AC currents with special waveforms.

With Plan A′, switching the direction of the magnetic field will be a slow switch: we will have to clear the whole Bucket Brigade of ions, switch the direction of the currents, and load the whole Bucket Brigade again to perform the experiment with fields in the opposite direction. This is in contrast to Plan A, where the fields switch every bucket. Once again, this is not necessary for an eEDM experiment, but being able to switch the fields quickly allows for suppression of systematic effects in our precision measurement.

One consequence of using Plan A′ is that we will have large axial magnetic fields towards the ends of the Bucket Brigade. We need $B_{\text{axgrad}} = -\frac{1}{2}\partial_z B_z = 3$ mG/cm for an $f_0 = 50$ Hz. Suppose $B_z(z = 0) = 0$ G by the (anti-)symmetry of the current configuration, then at the end of the Bucket Brigade at about 1.5 m away, we have an axial field of $B_z(z = \pm 1.5 \text{ m}) = \mp 0.9$ G. It is not immediately clear what this axial magnetic field would do to our eEDM measurement. I shall leave this to the rest of the group to find out.

We have seen how we can implement Plan A (and its variant) that involves a Zeeman frequency offset from an axial quadrupole magnetic field in the Bucket Brigade. Before we move on to the other Plans, it serves to discuss (document (verb) in this thesis) one peculiar source of decoherence that could come from the combined effect of RF micromotion and axial quadrupole magnetic fields.

8.2.3 RF trapping field-induced decoherence

A form of decoherence within the ion cloud was brought up during one of our group meetings as part of a discussion on systematics in the Gen. II experiment. This form of decoherence has avoided our radar so far because its effects have not been seen directly in the Gen. I and II setups. Unlike the previous sections, where we were talking about decoherence effects due to spatial inhomogeneities in B_{axgrad}, the physics behind this new form of decoherence comes from the interplay between (a perfectly homogeneous)

B_{axgrad} and the RF trapping fields.

The physics behind Plan A involves the ions seeing an effective magnetic field in their rotating frame of the form (handwavingly; reproduced from Equation 8.1 for comparison with a latter equation):

$$\mathcal{B}_{\text{rot}} = B_{\text{axgrad}} r_{\text{rot}} = B_{\text{axgrad}} \frac{e\mathcal{E}_{\text{rot}}}{m\omega_{\text{rot}}^2}.$$

In other words, Plan A works because of how the rotating polarization axis moves in phase with the rotation micromotion, resulting in a net magnetic field as seen by ions in an axial quadrupole magnetic field.

In a spirit similar to the above, there is a small contribution to the net $\mathcal{B}$-field to the above with the form (handwavingly):

$$\mathcal{B}_{\text{rf}}(\mathbf{r}) = B_{\text{axgrad}} r_{\text{rf}}(\mathbf{r}) = B_{\text{axgrad}} \frac{e\mathcal{E}_{\text{rf}}(\mathbf{r})}{m\omega_{\text{rf}}^2},$$

where $\mathcal{E}_{\text{rf}}(\mathbf{r})$ is the RF electric field at location $\mathbf{r}$, ω_{rf} is the angular frequency of the RF field. Note that this is a position-dependent effect, because the RF field strength is a quadrupolar field.

The above handwaving expressions neglect the fact that the polarization axis is not rotating at a constant angular velocity. To be more precise, the net magnetic field as seen by the ions in their rotating frame has the form:

$$\mathcal{B}_{\text{rot}} = \overline{\mathbf{B}(\mathbf{r}) \cdot \hat{\mathcal{E}}(\mathbf{r})}, \tag{8.7a}$$

where the overline indicates time-averaged, and

$$\mathbf{B}(\mathbf{r}) = B_{\text{axgrad}}\,(x, y, -2z), \tag{8.7b}$$

$$\vec{\mathcal{E}}(\mathbf{r}) = \mathcal{E}_{\text{rot}}\,(\cos\omega_{\text{rot}}t, \sin\omega_{\text{rot}}t, 0) + \frac{2V_{\text{rf}}}{R_0^2}\cos\omega_{\text{rf}}t\,(x, -y, 0), \tag{8.7c}$$

where V_{rf} is the RF potential applied, and R_0 is a trap geometry parameter defined in Equation A.1.

Splitting up the ion motion into its various components based on time scales ($\omega_{\text{rot}} = 2\pi \times 150$ kHz $\gg$ $\omega_{\text{rf}} = 2\pi \times 50$ kHz), we have

$$\begin{aligned}
\mathcal{B}_{\text{rot}} &= B_{\text{axgrad}}\,\overline{\mathbf{r} \cdot \hat{\mathcal{E}}(\mathbf{r})} \\
&= B_{\text{axgrad}}\,\overline{(\mathbf{r}_0 + \mathbf{r}_{\text{rot}} + \mathbf{r}_{\text{rf}}) \cdot \hat{\mathcal{E}}(\mathbf{r})} \\
&= B_{\text{axgrad}}\,(0 + \overline{r}_{\text{rot}} + \overline{r}_{\text{rf}}),
\end{aligned} \tag{8.8}$$

where we see that the $\mathbf{r}_0$ term (instantaneous secular position) evaluates to zero through the symmetry of the fields in space and time, and the overlines on r_{rot} (rotation micromotion amplitude) and r_{rf} (RF micromotion amplitude) are just symbols to remind us that these are time-averaged values. Evaluating the time-averaged r's up to first order in $1/\mathcal{E}_{\text{rot}}$ gives (being very careful with the signs):

$$\overline{r}_{\text{rot}} = -\frac{e\mathcal{E}_{\text{rot}}}{m\omega_{\text{rot}}^2} + \frac{e}{m\omega_{\text{rot}}^2}\left(\frac{V_{\text{rf}}}{R_0^2}\right)^2 \frac{x^2+y^2}{2\mathcal{E}_{\text{rot}}} \tag{8.9a}$$

$$\overline{r}_{\text{rf}} = -\frac{e}{m\omega_{\text{rf}}^2}\left(\frac{V_{\text{rf}}}{R_0^2}\right)^2 \frac{x^2+y^2}{\mathcal{E}_{\text{rot}}}. \tag{8.9b}$$

Combining Equations 8.8, 8.9a, and 6.21, we evaluate[6] the expression at a 1σ ion cloud radius to get (substituting $x^2+y^2 \to \sigma^2$, and using the Mathieu parameters in Appendix A to convert V_{rf} into the angular secular frequencies):

$$\begin{aligned} f_0 &= 3g\mu_{\text{B}}|\mathcal{B}_{\text{rot}}| \\ &= \tilde{f}_0\left[1\big|_{\overline{\text{r}}_{\text{rot}}} - \frac{k_B T m\omega_{\text{rf}}^2}{(e\mathcal{E}_{\text{rot}})^2}\left(1+\frac{o^2}{2}\right)\Big|_{\overline{\text{r}}_{\text{rot}}} + \frac{1}{2}\frac{2k_B T m\omega_{\text{rot}}^2}{(e\mathcal{E}_{\text{rot}})^2}\left(1+\frac{o^2}{2}\right)\Big|_{\overline{\text{r}}_{\text{rf}}}\right], \end{aligned} \tag{8.10}$$

where $\tilde{f}_0 = 3g\mu_{\text{B}}|B_{\text{axgrad}}|\frac{e\mathcal{E}_{\text{rot}}}{m\omega_{\text{rot}}^2}$, $o := \omega_z/\omega_{\{x,y\}}$ is the oblateness of the ion cloud, and $\omega_{\{x,y,z\}}$ are the angular secular frequencies of the ions in the trap. Typical values at typical operating parameters in Gen. III[7] give fractional decoherence of 0.0048% and 0.043% for the $\overline{r}_{\text{rot}}$ and $\overline{r}_{\text{rf}}$ terms, respectively. Those for Gen. II[8] give 0.0016% and 0.088%. The surprising factor of 1/2 in the expression for $\overline{r}_{\text{rf}}$ comes from taking into account the fact that the RF micromotion amplitude changes sinusoidally as the ion performs its secular motion, so the average amplitude-squared is given by $\overline{\cos^2 \omega_{\text{sec}} t} = 1/2$.

Equation 8.10 also says that the oblateness of the ion cloud contributes to decoherence. The physics is easy to understand: a stronger confinement in the z direction necessitates a stronger V_{rm} to keep the ions confined radially, ultimately resulting in RF-induced decoherence. Moral of this paragraph: prolate good, oblate bad.

It is interesting why we are seeing decoherence much less than 0.088% in the Gen. II setup. One possible guess is collisional narrowing (the topic of Section 6.5.2). Our ansatz Equation 6.15 tells us that the

[6] The time averaging is done over a time domain $t \in [0, T]$ big enough that the rotation and RF micromotions come back to the same phase together, i.e., $T = 2\pi p/\omega_{\text{rot}} = 2\pi q/\omega_{\text{rf}}$ where p and q are very large integers.

[7] Gen. III: $T = 50$ K, $\omega_{\text{rf}} = 2\pi \times 50$ kHz, $\omega_{\text{rot}} = 2\pi \times 150$ kHz, $\mathcal{E}_{\text{rot}} = 60$ V/cm, $o \approx 1$.

[8] Gen. II: $T = 20$ K, $\omega_{\text{rf}} = 2\pi \times 50$ kHz, $\omega_{\text{rot}} = 2\pi \times 375$ kHz, $\mathcal{E}_{\text{rot}} = 58$ V/cm, $o \approx 1$.

rate of collisional narrowing decreases with increasing temperature and decreasing ion number density. We expect to have a hotter and less dense ion cloud in Gen. III than in Gen. II, so it may not be wise to pin our hopes of pulling the 0.2% decoherence down to 0.01% with collisional narrowing, especially when the effect is still not very well studied in the group at this point in time.

On the topic of Gen. II, Equation 8.10 also suggests that the mean frequency of the ion cloud shifts with temperature. As the temperature of the ion cloud increases, the modal radius of the ion cloud also increases, so the mean frequency of the ion cloud would increase. In fact, we saw that the ion cloud heats up with time in Section 6.5.4 and Figure 6.15. This is a possible systematic, and I shall leave detailed studies to my colleagues.

Plan A seems difficult: homogeneity requirements in B_{axgrad} demands either very long buckets or few buckets. Furthermore, we still get RF-field induced decoherence even if B_{axgrad} is perfectly homogeneous. But let us perform one last struggle: can we shim away/in gradients in B_{axgrad}? Doing so allows us to tweak some things:

Shim away the RF-induced decoherence. Since the decoherence effect discussed in this chapter behaves as though B_{axgrad} varies quadratically as we move away from the trap axis, we could try to shim this decoherence away by intentionally introducing a quadratic spatial variation of B_{axgrad}.

Shim away spatial inhomogeneity of B_{axgrad}. For decoherence through, say, axial variation of B_{axgrad}, it would be nice if we can use shimming coils as extra degrees of freedom to shim the spatial variation away. Subjected to constraints from Maxwell's equations.

A combination of the above. Maxwell's equations do not let us win for free. When we shim the curvature of B_{axgrad} away along one axis, we have to pay by introducing curvature in another axis. We would probably have to settle for a compromise between the two points mentioned above.

The next section will cover some basic ideas of what kinds of field gradient shimming are allowed by Maxwell.

8.2.4 Shimming away gradients in B_{axgrad}

Within our Bucket Brigade, we do not have sources of magnetic fields (ignoring the magnetic dipoles of our molecules). In a region absent of sources of magnetic fields, Maxwell's equations allow us to express the magnetic field as a gradient of a scalar potential field:

$$\mathbf{B}(\mathbf{r}) = -\nabla\Phi_B(\mathbf{r}),$$

where $\Phi_B(\mathbf{r})$ is the scalar magnetic potential. Together with $\nabla \cdot \mathbf{B}(\mathbf{r}) = 0$, we have:

$$\nabla^2\Phi_B(\mathbf{r}) = 0,$$

which, in turn, implies that $\Phi_B(\mathbf{r})$ can be expanded out in terms of spherical harmonics $Y_l^m(\Omega)$:

$$\Phi_B(\mathbf{r}) = \sum_{l=0,-l\leq m\leq l} \left(a_{l,m}r^l + \frac{b_{l,m}}{r^{l+1}}\right) Y_l^m(\Omega),$$

where Ω is a shorthand for the usual angular variables (θ, ϕ), l and m are the usual quantum numbers for total angular momentum and projection of the angular momentum onto the quantization axis, respectively, and a and b are constants to be determined through boundary conditions. We can simplify the above expression even further by noting that (i) the magnetic field is a field with real components, and (ii) the field does not blow up at $r = 0$. We define real spherical harmonics by:

$$Y_{l,m} = \begin{cases} \frac{i}{\sqrt{2}}\left(Y_l^m - (-1)^m Y_l^{-m}\right) & \text{if } m < 0, \\ Y_l^0 & \text{if } m = 0, \\ \frac{1}{\sqrt{2}}\left(Y_l^{-m} + (-1)^m Y_l^m\right) & \text{if } m > 0, \end{cases}$$

and write the scalar magnetic potential as:

$$\Phi_B(\mathbf{r}) = \sum_{l=0,-l\leq m\leq l} a_{l,m}r^l\, Y_{l,m}(\Omega). \tag{8.11}$$

We further label components of the magnetic field obtained from taking the gradient of the corresponding real spherical harmonic component of the scalar potential with the same quantum numbers, i.e.,

$$\mathbf{B}_{l,m}(\mathbf{r}) := -\nabla\left(r^l\, Y_{l,m}(\Omega)\right). \tag{8.12}$$

$$\mathbf{B}(\mathbf{r}) = \sum_{l=0,-l\leq m\leq l} a_{l,m}\mathbf{B}_{l,m}(\mathbf{r}). \tag{8.13}$$

There are many theses from our group that go in depth into the study of these spherical harmonics (for instance, check out Noah Schlossberger's upcoming thesis), and here I will just flash out some of the more important spherical harmonics:

$\mathbf{B}_{1,\{1,-1,0\}}$ Uniform field in the $\{x, y, z\}$ directions.

$\mathbf{B}_{2,0}$ Quadrupole field of the form $(x, y, -2z)$, i.e., term that gives a uniform $\partial_z B_z =: -2B_{\text{axgrad}}$.

$\mathbf{B}_{2,2}$ Quadrupole field of the form $(-x, y, 0)$.

$\mathbf{B}_{2,-2}$ Quadrupole field of the form $(y, x, 0)$; like $\mathbf{B}_{2,2}$, but rotated 45° along the z-axis.

$\mathbf{B}_{4,0}$ Term that gives a B_{axgrad} that varies with position as $x^2 + y^2 - 2z^2$.

$\mathbf{B}_{4,2}$ Term that gives a B_{axgrad} that varies with position as $x^2 - y^2$.

$\mathbf{B}_{4,-2}$ Term that gives a B_{axgrad} that varies with position as xy; like $\mathbf{B}_{4,2}$, but rotated 45° along the z-axis.

Note that any gradients in B_{axgrad} that are odd in $\{x, y, z\}$ will not result in an overall decoherence, because any positive (negative) phase accumulation on one side of the trap will be nulled out by the negative (positive) phase accumulation on the other side of the trap when the ion sloshes around the trap. Hence, the lowest order terms in the spatial variation of B_{axgrad} that contributes to decoherence are terms that go as $\{x, y, z\}^2$. Assuming that the secular trapping frequencies along the x, y, and z directions are incommensurate, or that trajectory-changing collisions happen frequently enough in the trap, terms like $\{xy, yz, zx\}$ also do not contribute to decoherence, so the only terms that contribute to decoherence are $\{x^2, y^2, z^2\}$. The $l = 4$ terms are the lowest order terms that give spatial variations of B_{axgrad} that vary as $\{x^2, y^2, z^2\}$, and the two $l = 4$ terms above are the only such terms at this order.

All the fields above can be engineered with a combination of coils, e.g., Helmholtz coils for $\mathbf{B}_{1,\{1,-1,0\}}$, anti-Helmholtz coils for $\mathbf{B}_{2,0}$, and it turns out that we can engineer a set of coils placed in strategic positions to create $\mathbf{B}_{4,0}$ and $\mathbf{B}_{4,2}$. The interested reader can find more details in Noah Schlossberger's upcoming thesis. The take home messages from evaluating these spherical harmonics and designing coil sets that generate these harmonics are:

(1) We can shim away any imperfections in B_{axgrad} with our $\mathbf{B}_{4,0}$ and $\mathbf{B}_{4,2}$ coils to reduce decoherence introduced by spatial inhomogeneity of B_{axgrad} that are even about the ion cloud center. This shimming effect only works for a local region, though; it will require much more design effort to design coil sets that shim away $\mathbf{B}_{4,0}$ and $\mathbf{B}_{4,2}$ along a line, say, down the entire Bucket Brigade.

(2) The $\mathbf{B}_{4,0}$ term gives a B_{axgrad} that varies with position as $x^2 + y^2 - 2z^2$. So for every two units of decoherence we shim away in the axial direction, we incur a cost of one unit of decoherence in the radial direction. This sounds like a win. We could make our ion cloud shaped like a pencil along the axial direction, and put all sources of decoherence into the radial modes with our $\mathbf{B}_{4,0}$ coils. We do not win forever with this method though. The suppression factor of decoherence through a combination of (i) making our ion cloud longer and (ii) dumping decoherence from our axial dimension to the radial dimension with our $\mathbf{B}_{4,0}$ coils as compared to a spherical ion cloud is given by (see Equation 8.10):

$$\text{Suppression factor} = \left(1 + \frac{o^2}{2}\right) \Big/ \left(1 + \frac{1^2}{2}\right) = \frac{2 + o^2}{3},$$

where, once again, $o = \omega_z/\omega_{\{x,y\}}$ is the oblateness of the ion cloud. Evidently, the best we can ever do is to suppress decoherence to 2/3 its original value, where $o \to 0$ is an ion cloud that is loose in the axial direction and tight in the radial.

8.2.5 Final remarks

Working with Plan A would allow us to continue to stay in a familiar place with regards to understanding our systematic effects. There is a new systematic effect when we translate ions down the Bucket Brigade, where the magnetic and electric fields conspire and vary in space such that it could mimic an eEDM signal, but this is beyond the scope of this thesis.

Plan A does not seem easy, but it certainly is not impossible. However, there is nothing limiting us from using other ways of introducing a frequency offset between the stretched states of the upper and lower doublets. In the next section, we shall look at how we can introduce a frequency offset with Berry's phase.

8.3 Plan B: Berry's phase

8.3.1 Working principle

The quantization axis of our ions is given by the direction of the rotating electric field, $\mathcal{E}_{\text{rot}}$. As $\mathcal{E}_{\text{rot}}$ rotates, the $\mathcal{E}_{\text{rot}}$ vector traces out a solid angle. The solid angle that $\mathcal{E}_{\text{rot}}$ traces out is directly related to the Berry's phase picked up by the quantum states [25]:

$$\phi_{\text{Berry}} = \Omega_{\text{s.a.}} m_F, \tag{8.14}$$

where $\Omega_{\text{s.a.}}$ is the solid angle, not to be confused with the quantum number Ω.

Defining α to be the instantaneous angle that $\mathcal{E}_{\text{rot}}$ makes with the horizontal plane, and expressing Equation 8.14 as the time-averaged energy difference between our stretched states ($m_F = \pm 3/2$), we get:

$$hf_0 = 3hf_{\text{rot}} \langle \sin \alpha \rangle, \tag{8.15}$$

where $\langle \cdot \rangle$ indicates time-averaging.

In the first two generations of the JILA eEDM experiment, we deliberately shim α to zero for all times and characterize this as one of our systematic effects. In the Bucket Brigade, however, this can serve as our Plan B for introducing a bias f_0 into our system.

At first glance, one may think that to get a non-zero $\langle \sin \alpha \rangle$, one needs to have a non-zero time-averaged electric field in the z-direction $\mathcal{E}_z$, which will move our ions out of the trap. However, it is possible to have a non-zero $\langle \sin \alpha \rangle$ AND a zero time-averaged electric field in the z-direction by modulating the amplitudes of $\mathcal{E}_{\text{rot}}$ and $\mathcal{E}_z$ as we shall see in the next section.

8.3.2 In the Bucket Brigade

In addition to providing axial confinement of the ions, the Rings in the Bucket Brigade can also provide a time-varying axial electric field $\mathcal{E}_z(t)$. An example of such a setup is shown in Figure 8.7.

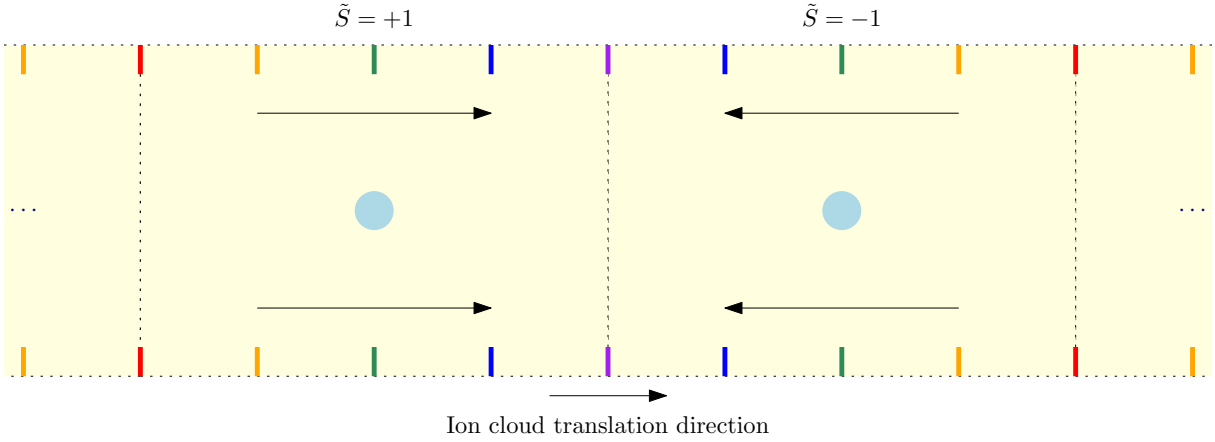

Figure 8.7: **Plan B: using the Rings to introduce a time-varying axial electric field.** This is a cross-section view of a section of the Bucket Brigade. The ions move from left to right. The blue disk indicates the ion clouds in the Bucket Brigade. The dashed lines are visual aids to indicate the boundary of each bucket. The thick lines indicate cross-sections of the Rings. The colors of the thick lines indicate the amplitudes of the voltages applied on the Rings: warmer (cooler) colors indicate more positive (negative) potentials. The straight arrows indicate the direction of the local $\mathcal{E}_z$ generated by the potentials on the Rings. The direction of the axial electric field flips with each neighboring bucket. $\tilde{S} = +\pm 1$ indicate buckets with the time-varying axial electric field pointing in directions that are π out of phase with each other.

Much like Plan A, Figure 8.2 also shows that Plan B allows for neighboring buckets to have $\mathcal{E}_z$ of opposite signs, which provides a very elegant solution to fast $\tilde{S}$-switching (Berry's phase analogue of $\tilde{B}$-switching; to be introduced in Section 8.3.3) to suppress uncertainties and systematic effects associated with $\mathcal{E}_z$.

Suppose the axial electric field (ignoring the axial confinement fields here) goes as:

$$\mathcal{E}_z(t) = \mathcal{E}_{\text{dit}} \cos \omega_{\text{dit}} t, \tag{8.16a}$$

where $\mathcal{E}_{\text{dit}}$ is the amplitude of the dithering axial electric field and ω_{dit} is the angular dithering frequency. Also suppose that $\mathcal{E}_{\text{rot}}$ is modulated with fractional amplitude a at angular modulation frequency ω_{dit}:

$$\mathcal{E}_{\text{rot}}(t) = \mathcal{E}_{\text{rot},0}(1 - a \cos \omega_{\text{dit}} t) \tag{8.16b}$$

Then the tangent that the axial electric field makes with $\mathcal{E}_{\rm rot}(t)$ is:

$$\tan\alpha = \frac{\mathcal{E}_{\rm dit}\cos\omega_{\rm dit}t}{\mathcal{E}_{\rm rot,0}(1-a\cos\omega_{\rm dit}t)}. \tag{8.17}$$

For $\mathcal{E}_{\rm dit} \ll \mathcal{E}_{\rm rot,0}$, we use the small angle approximation, and perform a time-average over one full cycle in the dither with the notorious half-tangent substitution to get:

$$\langle\alpha\rangle = \frac{\mathcal{E}_{\rm dit}}{\mathcal{E}_{\rm rot,0}}\frac{1}{a}\left(\frac{1}{\sqrt{1-a^2}}-1\right) = \frac{\mathcal{E}_{\rm dit}}{\mathcal{E}_{\rm rot,0}}\left(\frac{a}{2}+\frac{3a^3}{8}+\mathcal{O}(a^5)\right). \tag{8.18}$$

The ion accumulates the "carrier" Berry's phase by accumulating a lot of it first when it is above the plane, then removing the accumulated phase incompletely below plane. The actual phase evolves as follows:

$$\begin{aligned}
\Delta\phi(t) &= \phi_{m_F=+3/2}(t) - \phi_{m_F=-3/2}(t) \\
&= 3\omega_{\rm rot}\frac{\mathcal{E}_{\rm dit}}{\mathcal{E}_{\rm rot,0}}\left[\frac{\sin\omega_{\rm dit}t}{\omega_{\rm dit}} + a\left(\frac{t}{2}+\frac{\sin 2\omega_{\rm dit}t}{4\omega_{\rm dit}}\right)+\mathcal{O}(a^2)\right] \\
&= \boxed{\frac{3}{2}\frac{\mathcal{E}_{\rm dit}}{\mathcal{E}_{\rm rot,0}}\omega_{\rm rot}a\cdot t+\phi_0(t) \quad , \quad \phi_0(t) = 3\frac{\omega_{\rm rot}}{\omega_{\rm dit}}\frac{\mathcal{E}_{\rm dit}}{\mathcal{E}_{\rm rot,0}}\left[\sin\omega_{\rm dit}t+\frac{a}{4}\sin 2\omega_{\rm dit}t+\mathcal{O}(a^2)\right]}.
\end{aligned} \tag{8.19}$$

8.3.3 New switches for the experiment: $\{\tilde{S},\tilde{T}\}$

There are many switches we can use to reverse the sign of Berry's phase, which can be very helpful in studying systematic effects in our setup. Inferring from Equations 8.17 and 8.18, we have three switches associated with Berry's phase: $\{\tilde{R},\tilde{S},\tilde{T}\}$. The switches can each take on values ±1. The effect of the switches are as follows:

- $\tilde{R}$: Reversing the rotation direction of $\mathcal{E}_{\rm rot}$.
- $\tilde{S}$: Reversing the sign of $\mathcal{E}_{\rm dit}$.
- $\tilde{T}$: Reversing the sign of amplitude modulation.

Formally, the effect of the switches on Berry's phase is given by:

$$\begin{aligned}
\langle\alpha\rangle^{\tilde{R}\tilde{S}\tilde{T}} &= \tilde{R}\cdot\frac{\tilde{S}\cdot\mathcal{E}_{\rm dit}+\mathcal{E}_{\rm nr}}{\mathcal{E}_{\rm rot,0}}\frac{1}{\tilde{T}\cdot a+a_{\rm nr}}\left(\frac{1}{\sqrt{1-a^2-a_{\rm nr}^2-\tilde{T}\cdot 2aa_{\rm nr}}}-1\right)+\alpha_{\rm nr} \\
&\approx \tilde{R}\cdot\frac{\tilde{S}\cdot\mathcal{E}_{\rm dit}+\mathcal{E}_{\rm nr}}{\mathcal{E}_{\rm rot,0}}\frac{\tilde{T}\cdot a+a_{\rm nr}}{2}+\alpha_{\rm nr},
\end{aligned} \tag{8.20}$$

where we introduce the subscript "nr" to indicate the component of the experiment parameter that does not flip with the sign of the switch through imperfections in our experiment like: imperfect potential shimming for the Rings ($\mathcal{E}_{\mathrm{nr}}$), imperfect potential shimming for the Rods (a_{nr}), any asymmetry involved in the switching of the rotation direction of the rotation electric field (α_{nr}).

Note that $\{\tilde{R}, \tilde{T}\}$ are slow switches: the whole Bucket Brigade has to be unloaded before these switches can be flipped. In contrast, $\tilde{S}$ is a fast switch that can have alternating signs for neighbouring buckets.

Once again, to measure the eEDM, we try to measure f^{u} and f^{l} very well, at various configurations of the experiment parameters, and take a smart linear combination of the measured frequencies. Each of the smart linear combinations reveal a certain aspect of our experiment, and one of them tells us about the eEDM. We now attempt to borrow language used in the first two generations of the JILA eEDM experiment (see theses of previous students) to have a glimpse of how using Plan B (Berry's phase) could change the analysis of our data. Each of the linear combinations are called "channels". For the purpose of understanding what the channels will look like in Plan B, we remove the slow switches from Equation 8.20 and keep only the fast $\tilde{S}$ switch in the time-averaged α:

$$\langle\alpha\rangle^{\tilde{S}} = \tilde{S}\langle\alpha\rangle + \alpha_{\mathrm{nr}}. \tag{8.21}$$

8.3.4 $f^{\tilde{D}\tilde{S}}$ channels

8.3.4.1 Introduction

With each repetition of our eEDM experiment, we have the freedom to change the signs of the switches. In a simplified version of Plan B, we have the following switches:

Doublet: $\tilde{D}$. $\tilde{D} = +1$ refers to the upper doublet f^{u}, and $\tilde{D} = -1$ refers to the lower doublet f^{l}.

Sign of $\mathcal{E}_{\mathrm{dit}}$: $\tilde{S}$. We have already introduced this at the start of the Plan B section.

These switches take on values ± 1. We express the frequencies we measured with the various combinations of switches as $f^{\tilde{D}\tilde{S}}$. As an example, frequency $f^{\tilde{D}\tilde{S}} = f^{++}$ corresponds to f^{u} when the experiment was performed with $\tilde{S} = +1$, i.e. when $\mathcal{E}_{\mathrm{dit}}$ has a positive sign. As another example, frequency $f^{\tilde{D}\tilde{S}} = f^{-+}$ corresponds to f^{l} with the same $\tilde{S}$ experiment condition as the above.

To get the frequency "channels", we can then take a switch-weighted average of the above frequencies. For instance:

$$\begin{pmatrix} f^0 \\ f^D \\ f^S \\ f^{DS} \end{pmatrix} := \frac{1}{4} \begin{pmatrix} + & + & + & + \\ + & + & - & - \\ + & - & + & - \\ + & - & - & + \end{pmatrix} \begin{pmatrix} f^{\tilde{D}\tilde{S}} = f^{++} \\ f^{\tilde{D}\tilde{S}} = f^{+-} \\ f^{\tilde{D}\tilde{S}} = f^{-+} \\ f^{\tilde{D}\tilde{S}} = f^{--} \end{pmatrix}.$$

It turns out that each switch-weighted average frequency channel is sensitive to a different systematic effect in the experiment, and we can use these frequencies to compare our experimental results with analytical expressions to learn about our systematic effects. To understand what each frequency channel is sensitive to, we work in a two-level effective Hamiltonian of our system (see Section C.4), and expand out the eigenenergies of our Hamiltonian in powers of the small quantities with the following steps:

(1) Measure the non-inertial-frame coupling term for the upper and lower doublets (Δ^{u} and Δ^{l}), and measure the g-factors for both doublets (g^{u} and g^{l}). Massage them into the following form:

$$\Delta = (\Delta^{\mathrm{u}} + \Delta^{\mathrm{l}})/2 \qquad \Delta^D = (\Delta^{\mathrm{u}} - \Delta^{\mathrm{l}})/2$$

$$g = (g^{\mathrm{u}} + g^{\mathrm{l}})/2 \qquad \delta g = (g^{\mathrm{u}} - g^{\mathrm{l}})/2$$

(2) Perform studies on the two-level Hamiltonian.

(a) Solve for eigenenergies of the two-level Hamiltonian. The frequency $f^{\tilde{D}\tilde{S}}$ is just the difference of the two eigenenergies.

$$\begin{aligned} f^{\tilde{D}\tilde{S}} &= \sqrt{A^2 + B^2} \\ &= 3f_{\mathrm{rot}}\langle\alpha\rangle\sqrt{1 + \tilde{1}(\text{1 term}) + \tilde{D}(\text{D term}) + \tilde{S}(\text{S term}) + \tilde{D}\tilde{S}(\text{DS term})}. \end{aligned}$$

In the above, we identified $3f_{\mathrm{rot}}\langle\alpha\rangle$ to be the biggest term in the square root, so we pull it out. The "1 term" are terms small as compared to $3f_{\mathrm{rot}}\langle\alpha\rangle$, but do not depend on any of the switches. The rest of the terms are terms that depend on the relevant switches. For example, the "D term" include all the terms that depend only on the $\tilde{D}$ switch.

(b) Recognize that the following are small compared to relevant quantities:

- $\{3g\mu_{\mathrm{B}}\mathcal{B}_{\mathrm{nr}}, \Delta, \Delta^D, 2E_{\mathrm{EDM}}\} \ll 3f_{\mathrm{rot}}\langle\alpha\rangle$
- $\delta g \ll g$
- $\alpha_{\mathrm{nr}} \ll \langle\alpha\rangle$

and expand the terms out in the square root of the $f^{\tilde{D}\tilde{S}}$ expression, being consistent in keeping the small terms up to the correct order.

8.3.4.2 Results of the expansion

With the above steps, we get, up to first non-zero correction:

$$f^0 = 3f_{\mathrm{rot}}\langle\alpha\rangle\left[1+\frac{1}{2}\frac{\Delta^2+(\Delta^D)^2}{(3f_{\mathrm{rot}}\langle\alpha\rangle)^2}\right] \tag{8.22a}$$

$$f^D = \frac{\Delta\,\Delta^D}{3f_{\mathrm{rot}}\langle\alpha\rangle}\left[1-\frac{1}{2}\frac{\Delta^2+(\Delta^D)^2}{(3f_{\mathrm{rot}}\langle\alpha\rangle)^2}+\left(\frac{3g\mu_{\mathrm{B}}\mathcal{B}_{\mathrm{nr}}+3f_{\mathrm{rot}}\alpha_{\mathrm{nr}}}{3f_{\mathrm{rot}}\langle\alpha\rangle}\right)^2\right] + 2E_{\mathrm{EDM}}\left[\frac{2E_{\mathrm{EDM}}\Delta\,\Delta^D}{(3f_{\mathrm{rot}}\langle\alpha\rangle)^3}+\frac{\Delta^2+(\Delta^D)^2}{(3f_{\mathrm{rot}}\langle\alpha\rangle)^2}\frac{3g\mu_{\mathrm{B}}\mathcal{B}_{\mathrm{nr}}+3f_{\mathrm{rot}}\alpha_{\mathrm{nr}}}{3f_{\mathrm{rot}}\langle\alpha\rangle}\right] \tag{8.22b}$$

$$f^S = (3g\mu_{\mathrm{B}}\mathcal{B}_{\mathrm{nr}}+3f_{\mathrm{rot}}\alpha_{\mathrm{nr}})\left[1-\frac{1}{2}\frac{\Delta^2+(\Delta^D)^2}{(3f_{\mathrm{rot}}\langle\alpha\rangle)^2}\right]-\frac{2E_{\mathrm{EDM}}\Delta\,\Delta^D}{(3f_{\mathrm{rot}}\langle\alpha\rangle)^2} \tag{8.22c}$$

$$f^{DS} = 2E_{\mathrm{EDM}}\left[1-\frac{1}{2}\frac{\Delta^2+(\Delta^D)^2}{(3f_{\mathrm{rot}}\langle\alpha\rangle)^2}\right]+3\,\delta g\mu_{\mathrm{B}}\mathcal{B}_{\mathrm{nr}}-\frac{\Delta\,\Delta^D}{3f_{\mathrm{rot}}\langle\alpha\rangle}\frac{3g\mu_{\mathrm{B}}\mathcal{B}_{\mathrm{nr}}+3f_{\mathrm{rot}}\alpha_{\mathrm{nr}}}{3f_{\mathrm{rot}}\langle\alpha\rangle} \tag{8.22d}$$

A simple check shows that $f^0 \pm f^D = f^{\mathrm{u/l}}$ with $g^{\mathrm{u/l}} = g \pm \delta g$ and $\Delta^{\mathrm{u/l}} = \Delta \pm \Delta^D$. For future reference, the first non-zero term in the f^0 channel for small $\mathcal{E}_{\mathrm{rot}}$ amplitude modulation ($a \ll 1$) and small dither electric field ($\mathcal{E}_{\mathrm{dit}} \ll \mathcal{E}_{\mathrm{rot},0}$) is:

$$\boxed{f^0 = 3f_{\mathrm{rot}}\langle\alpha\rangle = \frac{3}{2}\frac{\mathcal{E}_{\mathrm{dit}}}{\mathcal{E}_{\mathrm{rot},0}}f_{\mathrm{rot}}a.} \tag{8.23}$$

8.3.4.3 Comparison with Zeeman-dominated f_0 in Plan A

For reference, the channels for a Zeeman-dominated f_0, e.g. in Plan A, can be evaluated in a way similar to the above. The relevant switches are:

Sign of B_{axgrad}: $\tilde{B}$. The sign can be switched by switching the direction of the current in the coils.

Doublet: $\tilde{D}$. $\tilde{D} = +1$ refers to the upper doublet f^{u}, and $\tilde{D} = -1$ refers to the lower doublet f^{l}.

Rotation direction of $\mathcal{E}_{\mathrm{rot}}$: $\tilde{R}$. We conveniently left this out for the Berry's phase $f^{\tilde{D}\tilde{s}}$ suite, but we shall include this here for comparison with previous theses and papers.

The frequency channels are given as follows, to the first non-zero correction term (except for f^R and f^{DR}, where we also include the next non-zero correction term):

$$f^0 = 3g\mu_{\mathrm{B}}\mathcal{B}_{\mathrm{rot}}\left[1+\frac{1}{2}\frac{\Delta^2+(\Delta^D)^2}{(3g\mu_{\mathrm{B}}\mathcal{B}_{\mathrm{rot}})^2}\right], \tag{8.24a}$$

$$f^B = (3g\mu_{\mathrm{B}}\mathcal{B}_{\mathrm{nr}}+3f_{\mathrm{rot}}\alpha_{\mathrm{nr}})\left[1-\frac{1}{2}\frac{\Delta^2+(\Delta^D)^2}{(3g\mu_{\mathrm{B}}\mathcal{B}_{\mathrm{rot}})^2}\right]-\frac{2E_{\mathrm{EDM}}\Delta\,\Delta^D}{(3g\mu_{\mathrm{B}}\mathcal{B}_{\mathrm{rot}})^2}, \tag{8.24b}$$

$$f^D = 3\,\delta g\mu_{\mathrm{B}}\mathcal{B}_{\mathrm{rot}}+\frac{\Delta\,\Delta^D}{3g\mu_{\mathrm{B}}\mathcal{B}_{\mathrm{rot}}}, \tag{8.24c}$$

$$f^R = \frac{3f_{\mathrm{rot}}\langle\alpha\rangle}{(3g\mu_{\mathrm{B}}\mathcal{B}_{\mathrm{rot}})^3}\left[(\Delta^2+(\Delta^D)^2)(3g\mu_{\mathrm{B}}\mathcal{B}_{\mathrm{nr}}+3f_{\mathrm{rot}}\alpha_{\mathrm{nr}})+2E_{\mathrm{EDM}}\cdot 2\Delta\,\Delta^D\right], \tag{8.24d}$$

$$f^{BD} = 2E_{\mathrm{EDM}}\left[1-\frac{1}{2}\frac{\Delta^2+(\Delta^D)^2}{(3g\mu_{\mathrm{B}}\mathcal{B}_{\mathrm{rot}})^2}\right]+3\,\delta g\mu_{\mathrm{B}}\mathcal{B}_{\mathrm{nr}}-\frac{\Delta\,\Delta^D}{3g\mu_{\mathrm{B}}\mathcal{B}_{\mathrm{rot}}}\frac{3g\mu_{\mathrm{B}}\mathcal{B}_{\mathrm{nr}}+3f_{\mathrm{rot}}\alpha_{\mathrm{nr}}}{3g\mu_{\mathrm{B}}\mathcal{B}_{\mathrm{rot}}}, \tag{8.24e}$$

$$f^{BR} = 3f_{\mathrm{rot}}\langle\alpha\rangle\left[1-\frac{1}{2}\frac{\Delta^2+(\Delta^D)^2}{(3g\mu_{\mathrm{B}}\mathcal{B}_{\mathrm{rot}})^2}\right], \tag{8.24f}$$

$$f^{DR} = \frac{3f_{\mathrm{rot}}\langle\alpha\rangle}{(3g\mu_{\mathrm{B}}\mathcal{B}_{\mathrm{rot}})^3}\left[2\Delta\,\Delta^D(3g\mu_{\mathrm{B}}\mathcal{B}_{\mathrm{nr}}+3f_{\mathrm{rot}}\alpha_{\mathrm{nr}})+2E_{\mathrm{EDM}}(\Delta^2+(\Delta^D)^2)\right], \tag{8.24g}$$

$$f^{BDR} = \frac{3f_{\mathrm{rot}}\langle\alpha\rangle}{(3g\mu_{\mathrm{B}}\mathcal{B}_{\mathrm{rot}})^2}\left[-\Delta\,\Delta^D+\frac{\delta g}{g}\left(\Delta^2+(\Delta^D)^2\right)\right]. \tag{8.24h}$$

These are the expressions more familiar to the first two generations of the JILA eEDM experiments. All the terms above have already been introduced in earlier parts of this section.

Here are some observations from comparing $f^{\tilde{D}\tilde{S}}$ and $f^{\tilde{B}\tilde{D}\tilde{R}}$:

(1) f^0 and the eEDM channels $\{f^{DS}, f^{BD}\}$ agree across the Berry's phase $f^{\tilde{D}\tilde{S}}$ and the Zeeman $f^{\tilde{B}\tilde{D}\tilde{R}}$ up to an expansion of this order, where we identify $3f_{\mathrm{rot}}\langle\alpha\rangle$ with $3g\mu_{\mathrm{B}}\mathcal{B}_{\mathrm{rot}}$.

(2) Since there is no $\mathcal{B}_{\mathrm{rot}}$ in $f^{\tilde{D}\tilde{S}}$, the leading term in f^D is the first correction term of that in f^{BDR}. Therefore, we see that $f^D_{\mathrm{Berry}} < f^D_{\mathrm{Zeeman}}$, especially at large f^0. In Gen. II, we expect f^D to increase with f^0, but in the Berry's phase picture, we expect f^D to decrease with f^0 instead.

We shall now move on to the details of how we can implement Plan B in the experiment.

8.3.5 Q-factor & Resonant Circuit

One important ingredient in Plan B is the modulation of the amplitude of $\mathcal{E}_{\mathrm{rot}}$. We plan to charge the Rods with a resonant circuit. One advantage of the resonant circuit is that it stomps on the second harmonic of $\mathcal{E}_{\mathrm{rot}}$ that plagues the systematic effects seen in the first two generations of the JILA eEDM experiment.

One disadvantage, however, is that it stomps on all Fourier components that are not the resonant frequency, thereby suppressing the effects of amplitude modulation. The degree of suppression of the Fourier frequencies in the waveform depends on the Q-factor of the resonant circuit.

For an $f_{\text{rot}} = 150$ kHz, we want to be able to send in sidebands at about 15 kHz away, so we do not want to work with too high a Q-factor. Hence, we aim for a Q-factor of about 20. Figure 8.8 shows the resonance plots at $Q = 20$.

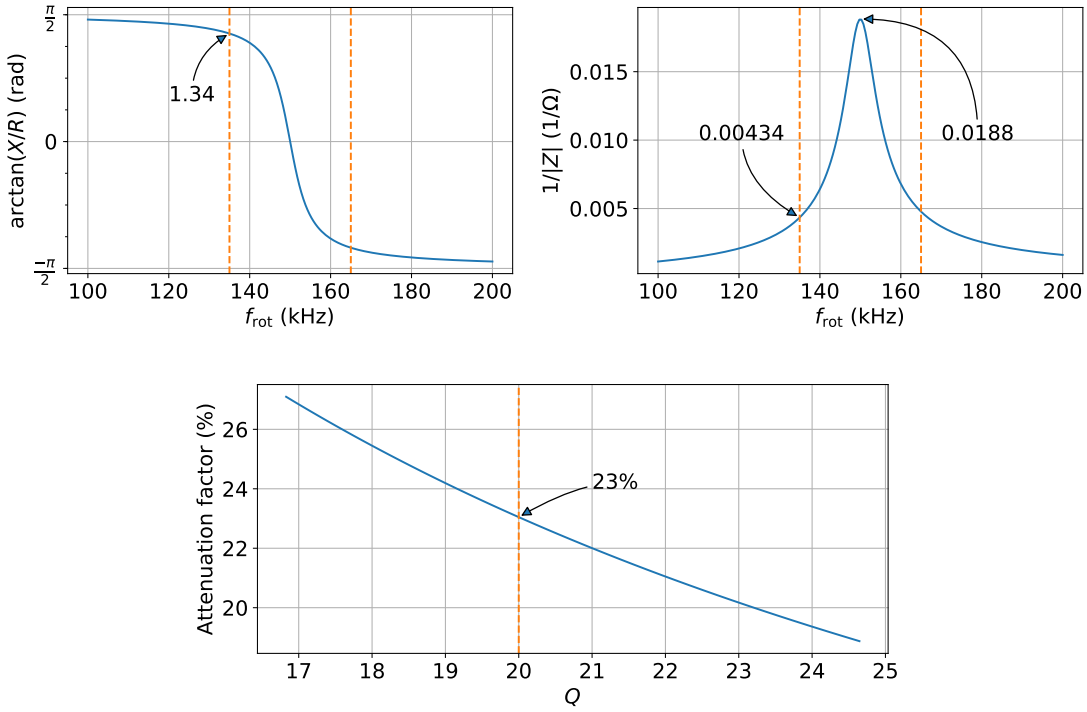

Figure 8.8: **Resonance curves for $Q = 20$.** Top plots: Resonance curves with resonance at 150 kHz. For a $V(t)$ going into the system, the response of $I(t)$ will have a phase shift given by the left plot, and an attenuation given by the right plot. Dashed lines show location of the 15 kHz sidebands. The sidebands are at 23.0% of the maximum on the right plot. Bottom plot: variation of the attenuation factor of the sidebands with a varying Q. The range of Q used corresponds to a change in $R = 53.0\ \Omega$ of $\pm 10\ \Omega$.

We want to have a time modulating $\mathcal{E}_{\text{rot}}$ that looks like:

$$\begin{aligned}\mathcal{E}_{\text{rot}}(t) &= \mathcal{E}_{\text{rot},0}(1 - a\cos\omega_{\text{dit}}t)\begin{pmatrix}\cos\omega_{\text{rot}}t\\ \sin\omega_{\text{rot}}t\\ 0\end{pmatrix}\\ &= \mathcal{E}_{\text{rot},0}\begin{pmatrix}\cos\omega_{\text{rot}}t - \frac{a}{2}\left[\cos(\omega_{\text{rot}}+\omega_{\text{dit}})t + \cos(\omega_{\text{rot}}-\omega_{\text{dit}})t\right]\\ \sin\omega_{\text{rot}}t - \frac{a}{2}\left[\sin(\omega_{\text{rot}}+\omega_{\text{dit}})t + \sin(\omega_{\text{rot}}-\omega_{\text{dit}})t\right]\\ 0\end{pmatrix}\end{aligned}$$

so we reconstruct the input waveform using information in Figure 8.8, and they have the following expression:

$$\mathcal{E}_{\text{rot}}(t) = \mathcal{E}_{\text{rot},0}\left[1 - \frac{a}{23.0\%}\cos(\omega_{\text{dit}}t + 1.34)\right]\begin{pmatrix}\cos\omega_{\text{rot}}t\\ \sin\omega_{\text{rot}}t\\ 0\end{pmatrix}.$$

8.3.6 Spatial homogeneity of the dithering axial electric field

The other crucial ingredient for Plan B is the dithering axial electric field. We shall see if Plan B fulfils Criteria 8.1 and 8.2. Once again, we go back to Equation 7.6 and Table 7.3 and adapt the results for Plan B.

Given the attenuation factors in Table 7.3, it is not practical to work with harmonics of order higher than $n = 3$. Including only up to $n = 3$, the waveform of a potential $V(z,\rho)$ that minimizes spatial inhomogeneity of $\mathcal{E}_{\text{dit}}$ is:

$$\begin{aligned}V(z,\rho) &= V(k,z,\rho) - \frac{1}{27}V(3k,z,\rho),\\ \mathcal{E}_{\text{dit}} &= -\partial_z V(z,\rho) = -V_0\left[\frac{8k}{9} + \frac{k^5}{120}\left(-15\rho^4 + 120\rho^2z^2 - 40z^4\right) + \mathcal{O}\left(\{\rho,z\}^7\right)\right].\end{aligned}$$

Note, once again, that $k = 2\pi/\lambda$, where λ is the wavelength of the fundamental waveform on the Rings. In the case of Plan B, $\lambda = 2\Lambda$. Evidently, the inhomogeneity comes in starting on the fourth power of the size of the ion cloud $2\sigma \sim \{\rho, z\}$. From the coefficients of each inhomogeneity term, we see that the axial inhomogeneity is more stringent than the radial.

The axial inhomogeneity in $\mathcal{E}_{\text{dit}}$ comes in through the first order correction term involving $(kz)^4$. To fulfil Criterion 8.2, we demand that $\frac{3}{8}(kz_{4\sigma})^4 < 0.01\%$, which means that $\lambda > 2\pi\sqrt[4]{\frac{30000}{8}}z_{4\sigma} \approx 49.2z_{4\sigma}$. For

an ion cloud with a 4σ radial extent of 1 cm, we see that each bucket needs to be about 25 cm in length. A spatial plot of such an inhomogeneity is shown in Figure 8.9.

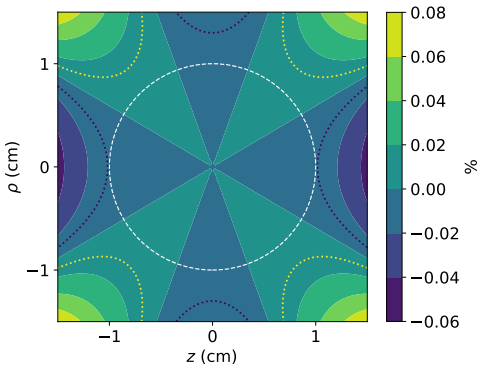

Figure 8.9: **Spatial inhomogeneity of $\mathcal{E}_{\text{dit}}$ w.r.t. point at center of a bucket.** The coordinates ρ and z represent the radial and axial directions, respectively. This plot is generated with $\Lambda = 50$ cm. The white dashed circle indicates a 1 cm radius, corresponding to a 2σ ion cloud radius. The dotted lines indicate contour lines of 0.01%, in line with Criterion 8.2.

8.3.7 Final remarks

Plan B started out looking rather promising, much like Plan A, until we saw the constraints that Criteria 8.1 and 8.2 place on the dimensions of the Bucket Brigade. To this we say, "we should not be sad because it doesn't work, we should be happy because we tried." However, instead of alternating $\tilde{S}$ once every bucket, we could alternate it once every few buckets. This will allow us to have short buckets and homogeneous $\mathcal{E}_{\text{dit}}$ at the same time. This relaxes a lot of design constraints, e.g. λ can even be longer than 50 cm, which improves spatial homogeneity. Having longer λ makes the attenuation factors work less hard (in our favor) so we can add more higher harmonics into the waveform to the potential to make it more triangular. I shall leave the analysis to future generations of students and post-docs.

Much like Plan A, Plan B looks hard, but not impossible. With this, we have looked at examples of how we can introduce a Zeeman frequency offset with Plan A, and Berry's frequency offset with Plan B. The rest of the chapter explores other ingenious ways of introducing Zeeman frequency offsets that do not

require axial quadrupole magnetic fields.

8.4 Plan C: Uniform ambient magnetic field

8.4.1 Working principle

8.4.1.1 History: systematic effect in the Gen. I experiment

Before we talk about Plan C proper, it serves to take a trip back down memory lane to the first two generations of the JILA eEDM experiments, where the inspiration for Plan C is drawn. One of the systematic effects seen in the Gen. I experiment involves the following [14]:

$$f^B \propto \epsilon \left(\mathcal{B}_x X_0 + \mathcal{B}_y Y_0\right), \tag{8.25a}$$

$$f^{BR} \propto \epsilon \left(\mathcal{B}_x Y_0 - \mathcal{B}_y X_0\right), \tag{8.25b}$$

where f^B and f^{BR} are the frequency channels defined in Equation 8.24; $\epsilon = V_{2f}/V_{\text{rot}}$ is the ratio of the amplitude of the second harmonic of $\mathcal{E}_{\text{rot}}$ to the fundamental; $\mathcal{B}_{x,y}$ is the ambient magnetic field strength in the x and y directions, respectively; X_0 and Y_0 are the positions of the ion cloud w.r.t. the trap center in the x and y directions, respectively. The physics behind the above systematic effects is as follows:

(1) The electric potential for $\mathcal{E}_{\text{rot}}$ in the Gen. I experiment was provided by six radial electrodes that are powered by an op-amp each.

(2) Despite receiving a first harmonic low voltage input, the high voltage output from each op-amp also has a component of the second harmonic that is at some phase w.r.t. the first harmonic. This results in an output voltage on the n^{th} electrode of the form: $V_n(\tilde{R}) = V_{\text{rot}}\left[\cos\left(\omega_{\text{rot}}t + \tilde{R}\frac{n\pi}{3}\right) + \epsilon\cos\left(2\omega_{\text{rot}}t + \tilde{R}\frac{2n\pi}{3} + \phi\right)\right]$, where ϕ is the relative phase between the first and the second harmonic, and is determined by the nature of the op-amp; and $\tilde{R}$ is the rotation switch, e.g. $+1$ for $\mathcal{E}_{\text{rot}}$ rotating counter-clockwise, and -1 for clockwise.

(3) Summing the potentials from all the fins, we see that the Lissajous figures that $\overrightarrow{\mathcal{E}_{\text{rot}}}$ traces out as seen by ions at various locations within the ion trap is shown in Figure 8.10.

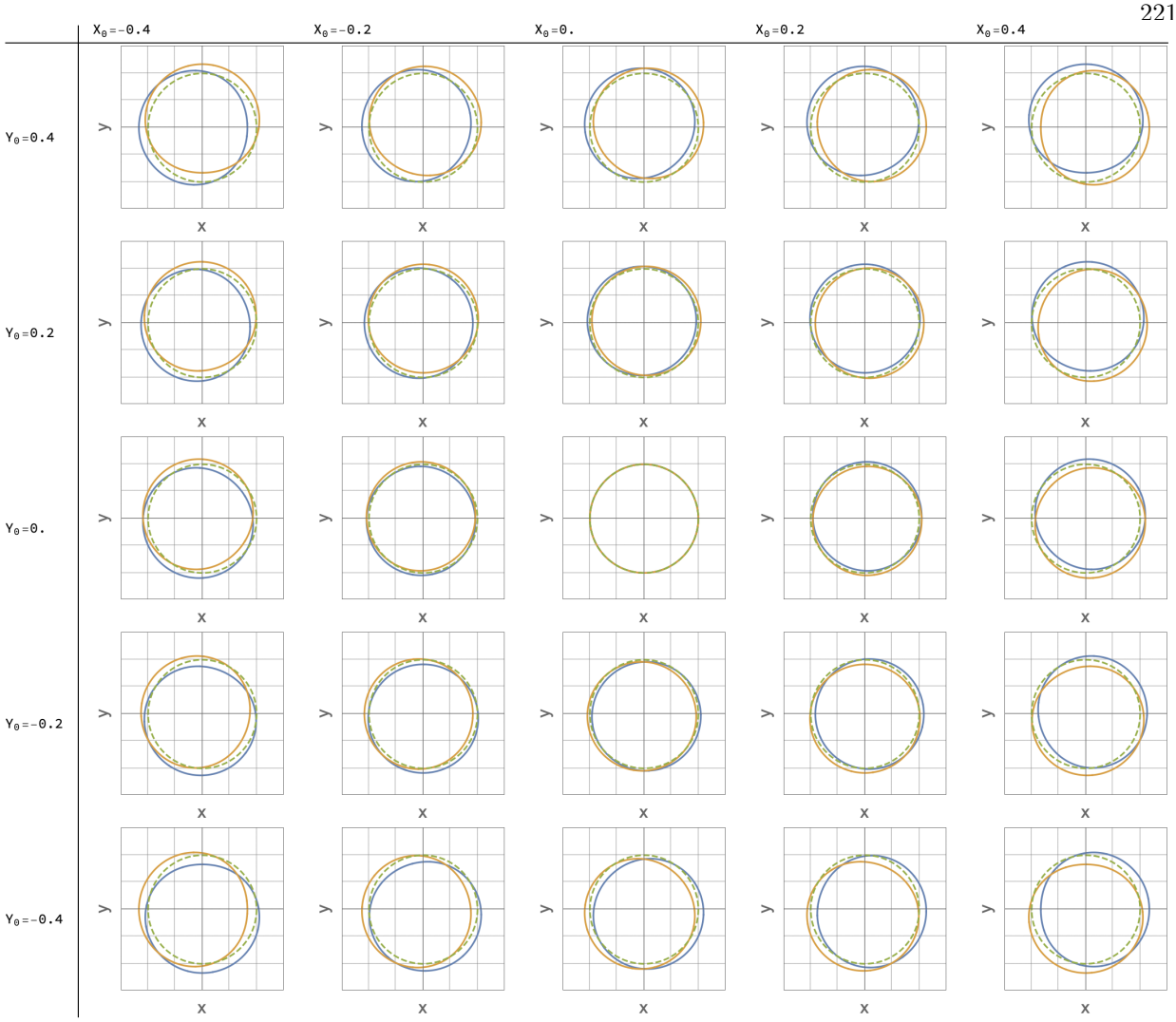

Figure 8.10: **Lissajous figures traced out by $\overrightarrow{\mathcal{E}_{\text{rot}}}$ as seen by ions at various locations within the trap.** X_0 and Y_0 are the mean ion cloud positions w.r.t. the center of the trap, and are expressed in fractions of the radial distance of the electrodes away from the trap center (i.e. ions will be touching the electrodes at, say, $X_0 = 1$). The green dashed circle indicates the Lissajous figure traced out by the $\overrightarrow{\mathcal{E}_{\text{rot}}}$ vector without the second harmonic component as it rotates along the plane. The blue (yellow) circle indicates the corresponding Lissajous figures with the effect of the second harmonic, and when $\tilde{R}$ is $+1$ (-1).

(4) From Figure 8.10, we note the following:

(a) Moving out along the i-axis (where $i \in \{X_0, Y_0\}$) displaces the centroid of the Lissajous figure along the i-direction.

(b) Flipping the sign of $\tilde{R}$ flips the Lissajous figure about the radial axis.

(5) If there is an ambient magnetic field along the plane of the rotating electric field $\mathbf{B} = \mathcal{B}_x\hat{x} + \mathcal{B}_y\hat{y}$, the ions can see a non-zero time-averaged[9] magnetic field in the frame of the rotating electric field:

$$\langle \mathcal{B}_x\hat{x} \cdot \widehat{\mathcal{E}_{\text{rot}}} \rangle \propto \mathcal{B}_x \cdot \epsilon \cdot \Big(X_0 \cos\phi - \tilde{R}\, Y_0 \sin\phi \Big) + \mathcal{O}(\{\epsilon, X_0, Y_0\}^2), \tag{8.26a}$$

$$\langle \mathcal{B}_y\hat{y} \cdot \widehat{\mathcal{E}_{\text{rot}}} \rangle \propto \mathcal{B}_y \cdot \epsilon \cdot \Big(Y_0 \cos\phi + \tilde{R}\, X_0 \sin\phi \Big) + \mathcal{O}(\{\epsilon, X_0, Y_0\}^2). \tag{8.26b}$$

(6) Together with the fact that the ambient magnetic field flips direction w.r.t. the fields introduced by B_{axgrad} under a sign flip of the $\tilde{B}$-switch, we see that:

$$f^B \propto \epsilon \left(\mathcal{B}_x X_0 + \mathcal{B}_y Y_0 \right) \cos\phi + \mathcal{O}(\{\epsilon, X_0, Y_0\}^2), \tag{8.27a}$$

$$f^{BR} \propto \epsilon \left(\mathcal{B}_x Y_0 - \mathcal{B}_y X_0 \right) \sin\phi + \mathcal{O}(\{\epsilon, X_0, Y_0\}^2), \tag{8.27b}$$

which agrees with Equations 8.25 when the phase between the first and second harmonic ϕ is chosen correctly. Evidently, this is a Zeeman effect.

8.4.1.2 Adaptation of the physics behind the systematic effect

From the previous section, we see that we can introduce a bias f_0 if (i) we can disrupt the Lissajous figure of $\mathcal{E}_{\text{rot}}$ such that $\langle \mathbf{B} \cdot \widehat{\mathcal{E}_{\text{rot}}} \rangle \neq 0$, and (ii) introduce a uniform ambient magnetic field parallel to the direction of the displacement. The effect that we saw in the previous section only turns on with a non-zero ion cloud displacement from the trap center, but we do not wish to displace our ions from the trap center because this would introduce additional RF-micromotion and heat up our ion cloud at a much higher rate. Hence, we need to engineer an $\mathcal{E}_{\text{rot}}$ Lissajous figure such that $\mathcal{E}_{\text{rot}}$ such that $\langle \mathbf{B} \cdot \widehat{\mathcal{E}_{\text{rot}}} \rangle \neq 0$ even when the ion cloud is nominally at the trap center. We shall see how this can be done in the next section.

8.4.2 In the Bucket Brigade

It turns out that having an oscillating uniform electric field in the, say, x direction that oscillates at the second harmonic of $\mathcal{E}_{\text{rot}}$ would give $\mathcal{E}_{\text{rot}}$ such that $\langle \mathbf{B} \cdot \widehat{\mathcal{E}_{\text{rot}}} \rangle \neq 0$. The analytical form for such an electric

[9] Important: the averaging must be done over the time domain and not the spatial domain.

field is:

$$\mathbf{E}(t) = \begin{pmatrix} \mathcal{E}_{\text{rot}} \cos \omega_{\text{rot}} t + \mathcal{E}_{\text{2harm}} \cos(2\omega_{\text{rot}} t + \phi) \\ \mathcal{E}_{\text{rot}} \sin \omega_{\text{rot}} t \\ 0 \end{pmatrix}, \tag{8.28}$$

where ϕ is the phase between the first and second harmonic, and $\mathcal{E}_{\text{2harm}}$ is the amplitude of the second harmonic. An example of an Lissajous figure traced out by such a field is shown in Figure 8.11.

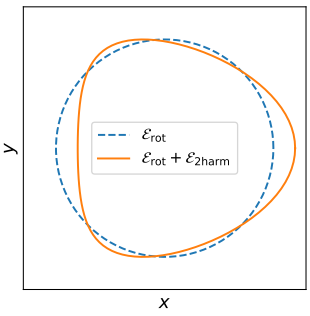

Figure 8.11: **Lissajous figure traced out by $\overrightarrow{\mathcal{E}_{\text{rot}}}$ as seen by ions in the Bucket Brigade.** The dashed line indicates the Lissajous figure in the absence of $\mathcal{E}_{\text{2harm}}$. For illustrative purposes, $\epsilon = \mathcal{E}_{\text{2harm}}/\mathcal{E}_{\text{rot}} = 0.2$, an unrealistically large value, to exaggerate the features.

The Plan C equivalent of Equations 8.26 are:

$$\langle \mathcal{B}_x \hat{x} \cdot \widehat{\mathcal{E}_{\text{rot}}} \rangle \propto -\mathcal{B}_x \cdot \epsilon \cdot \cos\phi, \tag{8.29a}$$

$$\langle \mathcal{B}_y \hat{y} \cdot \widehat{\mathcal{E}_{\text{rot}}} \rangle \propto \mathcal{B}_y \cdot \epsilon \cdot \tilde{R} \sin\phi, \tag{8.29b}$$

which necessarily implies[10] :

$$f^0 \propto \epsilon\, \mathcal{B}_x \cos\phi, \tag{8.30a}$$

$$f^R \propto -\epsilon\, \mathcal{B}_y \sin\phi. \tag{8.30b}$$

In fact, up to second order in $\epsilon = \mathcal{E}_{\text{2harm}}/\mathcal{E}_{\text{rot}}$, we have a frequency offset:

$$f_0 = 3g\mu_{\text{B}}\mathcal{B}_{\text{eff}} \quad , \quad \mathcal{B}_{\text{eff}} = \mathcal{B}_x \left[\frac{\epsilon}{4} + \mathcal{O}(\epsilon^3)\right] \cos\phi. \tag{8.31}$$

[10] Even though "the proportional sign" is used, and frequency is a positive definite value, the relative sign difference between the two expressions shown is included explicitly for future reference.

For typical $f_0 = 50$ Hz and $\epsilon = 0.01$, we just need $\mathcal{B}_x \approx 0.3$ G, which is a doable field that we can apply. The uniform magnetic field will be produced by very wide "Helmholtz coils" running the entire length of the whole Bucket Brigade.

8.4.3 Final remarks

One might think that since $\mathcal{B}_{\text{eff}} \propto \mathcal{B}_x \epsilon$, as long as we choose the values such that they give the $\mathcal{B}_{\text{eff}}$ we want things will be fine. This is not true. Roughly speaking, what the second harmonic does is it accumulates some Zeeman phase for one half of the $\mathcal{E}_{\text{rot}}$ cycle, and removes some of it in the second half to result in a net phase gain. The effect of this is frequency modulation of f_0. From our simulations, when ϵ is too small, the frequency modulation becomes apparent. Since $f_{\text{rot}} = 150$ kHz and $f_0 = 50$ Hz nominally, if we want the modulation index to be less than 0.1, then $\epsilon \gtrsim 0.003$.

One final thing to note is that the rods used to generate $\mathcal{E}_{\text{rot}}$ will be driven by a resonant circuit, which does not like to have a second harmonic component. We will have to drive the second harmonic hard, and we will also need to pay special attention to the stability of the amplitudes of the second harmonic on all the Rods to ensure that we have a homogeneous uniform oscillating second harmonic electric field. This sounds like a hassle, but not impossible. Still, in our quest to get away with being lazy, we came up with Plan D.

8.5 Plan D: Transverse magnetic quadrupole

8.5.1 Working principle

The working principle behind Plan D is similar in spirit to Plans B and C: we allow for an asymmetric phase build-up and subtraction at various parts of the $\mathcal{E}_{\text{rot}}$ cycle. In both Plans B and C, the asymmetry is introduced by modulating the strength of $\mathcal{E}_{\text{rot}}$ at a frequency that is commensurate with the phase-inducing physics (Berry's phase for Plan B, and Zeeman shift for Plan C). Plan D seeks to overcome the problem in Plan C where we will have to drive the second harmonic into the resonant circuit for the rods very hard. To do this, we use the fields of the following form:

$$\overrightarrow{\mathcal{E}_{\text{rot}}} = \mathcal{E}_{\text{rot}} \begin{pmatrix} (1+\varepsilon)\cos\omega_{\text{rot}}t \\ (1-\varepsilon)\sin\omega_{\text{rot}}t \\ 0 \end{pmatrix} \quad , \quad \mathbf{B} = \mathcal{B}_{\text{transgrad}} \begin{pmatrix} \cos 2\phi & \sin 2\phi & 0 \\ -\sin 2\phi & \cos 2\phi & 0 \\ 0 & 0 & 1 \end{pmatrix} \begin{pmatrix} x \\ -y \\ 0 \end{pmatrix}, \tag{8.32}$$

where ϕ is the angle between the x-axis and the principal axis of the transverse magnetic quadrupole that would nominally be aligned with the x-axis; and ε is the ellipticity. Such an $\overrightarrow{\mathcal{E}_{\text{rot}}}$ will give a slightly modified rotational micromotion:

$$\mathbf{r}(t) = \mathbf{r}_{\text{sec}}(t) - r_{\text{rot}} \begin{pmatrix} (1+\varepsilon)\cos\omega_{\text{rot}}t \\ (1-\varepsilon)\sin\omega_{\text{rot}}t \\ 0 \end{pmatrix}, \tag{8.33}$$

where $\mathbf{r}_{\text{sec}}$ is the secular position of the ion; evidently the rotational micromotion is now elliptical.

Employing the same trick used in Plan C, i.e. evaluating $\langle \mathbf{B} \cdot \widehat{\mathcal{E}_{\text{rot}}} \rangle$, the resulting f_0 holds the form:

$$f_0 = 3g\mu_{\text{B}}\mathcal{B}_{\text{eff}} \quad , \quad \mathcal{B}_{\text{eff}} = \frac{3}{2}\varepsilon \cdot B_{\text{transgrad}} r_{\text{rot}} \begin{pmatrix} 0 \\ \sin 2\phi \\ \cos 2\phi \end{pmatrix} + \mathcal{O}(\varepsilon^3), \tag{8.34}$$

where the z-component of $\mathcal{B}_{\text{eff}}$ is the one that goes into f_0, while the y-component is included there to remind ourselves that a non-zero ϕ can induce additional coupling between states of neighboring m_F through the Zeeman term in the Hamiltonian. Fortunately, this additional coupling term ($\sim f_0 = 50$ Hz) is small compared to the rotation term in the Hamiltonian ($\sim f_{\text{rot}} = 150$ kHz), so modifications to $\Delta^{\text{u/l}}$ should be small.

8.5.2 In the Bucket Brigade

The transverse magnetic field gradient will be produced by very wide "anti-Helmholtz coils" running the entire length of the whole Bucket Brigade. For wires at radial distance $R \gtrsim 4''$ away from the trap axis, the magnetic field within the vicinity of the trap axis is:

$$\mathbf{B} = \frac{2\mu_0 I}{\pi R}\left[\left(\frac{x}{R}, -\frac{y}{R}, 0\right) + \mathcal{O}\left(\left(\frac{\{x,y\}}{R}\right)^5\right)\right],$$

and for typical ion cloud radius of $lsim1$ cm, we see that the transverse field will be very homogeneous in the region of interest.

The resonant circuits driving the Rods will be driven only at the resonant frequency. The amplitudes will be tuned such that four of the Rods will operate at $(1+\varepsilon)$ the nominal amplitude, while the other four at $(1-\varepsilon)$. This is easy.

However, to ensure that Criterion 8.1 is fulfilled, we need to ensure that we can maintain the amplitudes of V_{rot} on all the rods down to 0.01% of the desired ellipticity of $\mathcal{E}_{\text{rot}}$. To put things into perspective, the number of significant digits involved for an $\varepsilon = 0.01$ is:

$$1+\varepsilon = 1.010000,$$

$$1-\varepsilon = 0.990000,$$

which is a demand of stability down to 1 ppm on our resonant circuit.

8.5.3 Final remarks

As of the time of writing, we do not know if the above demand is realistic. We currently have a 0.1% amplitude precision for the transformers in the b.B.B., and it is not immediately obvious how we can make this better. To this, our advisors say, "work harder."

8.6 Plan E: Rotating magnetic field with time-oscillating currents

8.6.1 Working Principle

The field generated by a current flowing down a straight infinitely-long wire with current i is given by $\mathbf{B}(\mathbf{r}) = \frac{\mu_0 i}{2\pi r}\hat{\phi}$, as one can easily check with Ampère's law. Suppose in addition to driving the radial electrodes with the RF-trapping potentials and the rotating electric field that polarizes our ions, we drive the electrodes with oscillating currents with phases matched to the rotating electric field. This would give us a net magnetic field along the trap axis that rotates with the electric field — a magnetic field that is truly co-rotating with the polarizing electric field.

8.6.2 In the Bucket Brigade

8.6.2.1 Intentional currents

Suppose we have eight radial electrodes that we number from 1 to 8, these radial electrodes can be long rods that stretch the whole length of the Bucket Brigade. The naïve picture would involve sending oscillating currents *intentionally* and voltages down the rods numbered n with phases like:

$$i_n(t) = -i_0 \sin\left(\omega_{\text{rot}} t + \frac{2\pi(n-1)}{8}\right), \tag{8.35}$$

$$V_n(t) = V_{\text{rot}} \cos\left(\omega_{\text{rot}} t + \frac{2\pi(n-1)}{8}\right). \tag{8.36}$$

This would introduce a $\mathcal{B}_{\text{rot}}$ that is anti-parallel to $\mathcal{E}_{\text{rot}}$. See Figure 8.12 for the same geometry of the setup, but using charging currents instead of intentional currents.

8.6.2.2 Charging currents

The rods have non-zero capacitance, so charging the rods up to V_{rot} would require charging currents to run through the rods. See Figure 8.12 for a schematic of the geometry involved.

The charging currents are to be distinguished from the currents that we *intentionally* want to add to give a rotating $\mathcal{B}_{\text{rot}}$. If the Rods are only being fed the charging currents from one end, there will be a

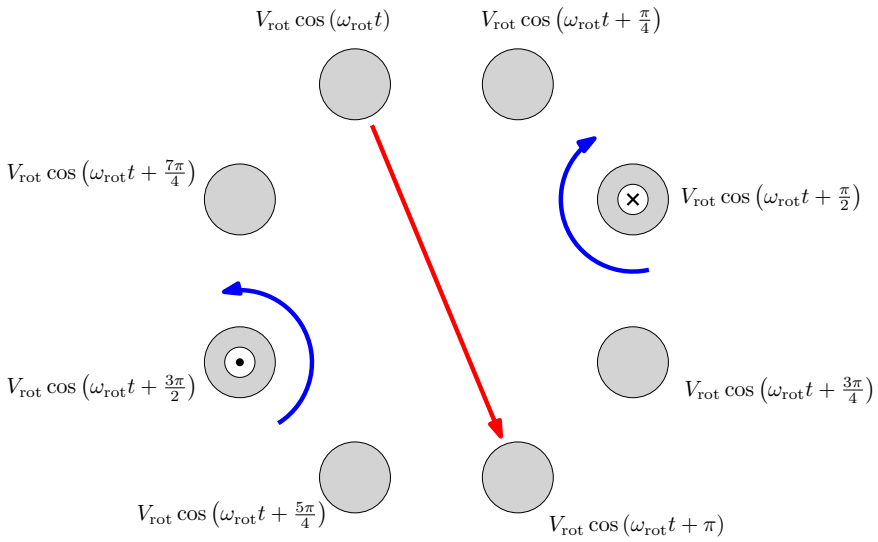

Figure 8.12: **Plan E: geometry of setup with charging currents.** Grey disks represent a cross section of the Rods. The Rods are charged into the page. The red arrow indicates the direction of $\mathcal{E}_{\text{rot}}$ at this instance in time. The blue arrows indicate magnetic field lines generated by the charging currents running through the respective Rods. The arrow head/tail symbols indicate the direction of the current flowing in those Rods. Only the charging currents and magnetic fields for two Rods are shown to prevent clutter. The sum of all the magnetic field contributions give rise to a $\mathcal{B}_{\text{rot,charging}}$ that is anti-parallel to $\mathcal{E}_{\text{rot}}$.

(linear) gradient of charging currents as we move along the Rods. Through the capacitor equation, we have:

$$i_{\text{charging},n}(t) = -C_{\text{Rod}} V_{\text{rot}} \omega_{\text{rot}} \sin\left(\omega_{\text{rot}} t + \frac{2\pi(n-1)}{8}\right), \tag{8.37}$$

where C_{Rod} is the capacitance of each Rod. The above expression incidentally has the same phase as the *intentional* currents that we wish to send. This would be great — we could just use the charging currents as the *intentional* currents — except the gradient of charging currents along the rods would introduce a gradient in the magnitude of $\mathcal{B}_{\text{rot}}$ along the Bucket Brigade. This calls for segmented rods or multiple charging points along the rods[11] to reduce charging current gradients.

8.6.3 Final remarks

Assuming that only the *intentional* current is flowing down the rods[12] , the magnetic field generated by Plan E can be surprisingly uniform in the vicinity of the trap axis with our eight-rod setup. The first

[11] This method would require a current bus along the length of the rod, acting as a highway for current to be fed to multiple points on the rods like highway exits. One would need to shield the fields generated by the currents flowing up and down the bus.

[12] One can also use a separate set of long continuous rods or wires that carry the *intentional* current parallel to the rods supplying the rotating electric field, as this would decouple the wiring for the *intentional* current from the segmented rods.

non-trivial deviation from uniformity comes in as the sixth order in radial coordinates, i.e., $\{x, y\}^6$.

Plan E looks promising in terms of uniformity. The trade off comes in the construction and assembly of parts, especially if we are going to use the segmented rods. Inhomogeneity can come in through the imperfections of the assembly, e.g., if a rod segment is not fully aligned with the rest of the setup, it could introduce deviations in the fields at the homogeneity levels that we care about.

8.7 Further discussion

There are uncertainties associated with all the aforementioned Plans. Spatial field homogeneity requirements also place hard limits on size and geometry of the setup, giving rise to several hard-to-go conclusions. Before we make the big decision to redesign the Bucket Brigade and tailor fit it to a particular Plan, it would be wise to test out some of the Plans in the b.B.B.. This is something that will happen after I am gone from the group, unfortunately.

As of this writing, we are using Plan A in the b.B.B.. There is a pair of circular anti-Helmholtz coils ($8''$ diameter, 10 turns, giving 0.65 Hz/mA at $\mathcal{E}_{\rm rot} = 60$ V/cm with $f_{\rm rot} = 147.5$ kHz) at the Octagon for diagnostics experiments at the Octagon. The wire was wrapped around the Six-way Cross and the Cold Tube on either side of the Octagon. There is another pair of square anti-Helmholtz coils[13] (56 cm each side, 3 turns, giving 21 Hz/A with the same conditions as before) at the Cold Tube where the ions sit, the Science region. When we run experiments at the Science region, we only keep the square anti-Helmholtz coils turned on, and we keep the circular anti-Helmholtz coils at the Octagon turned off.

When we charge up the Rods to give us the rotating electric field, there is enough capacitance per unit length of the Rods with the rest of the world to induce charging currents along the rods. In the current b.B.B. configuration, we charge up the Rods from the warm end (the side closest to the ion detector). At this end of the Rod, the magnitude of the charging current is:

$$I_{\rm charging} = C_{\rm Rod} V_{\rm rot} \omega_{\rm rot},$$

where $C_{\rm Rod}$ is the total capacitance of the Rod-World system, $V_{\rm rot}$ and $\omega_{\rm rot}$ are the voltage amplitudes and

[13] The anti-Helmholtz condition for a square set of coils is for the separation d to be 0.946 times that of the length of each side of the square L, i.e. $d \approx 0.946L$.

angular frequency of the voltage that we send to the Rods to generate the rotating electric fields, respectively. In the same spirit as Plan E (Section 8.6), these charging currents generate a $\mathcal{B}_{\text{rot,charging}}$ aligned with $\mathcal{E}_{\text{rot}}$, giving rise to a net Zeeman shift in our molecules. The magnetic field induced by the charging current decreases in magnitude as we move from the charged (warm) end of the Rods to the unconnected (cold) end of the Rods. Hence, there is a net gradient of Zeeman frequency as we move from the Octagon to the Science region. Figure 8.13 shows a scan of the Zeeman frequency from the charging currents along the length of the b.B.B..

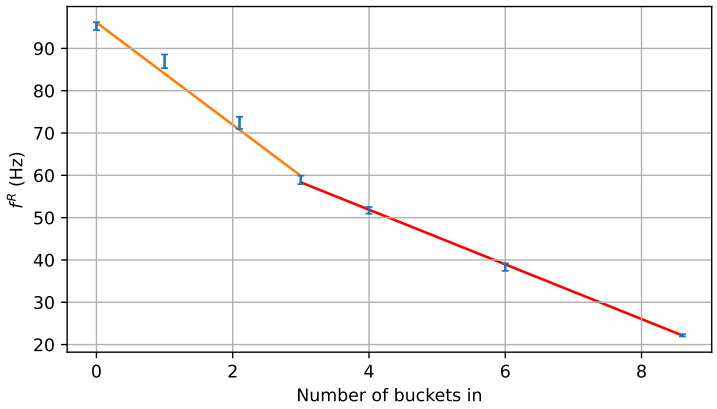

Figure 8.13: **Charging-current–induced Zeeman frequencies in the b.B.B..** Data was taken on 30 April 2023. Steps taken to produce this plot are as follow.

(1) Perform a Ramsey experiment at various locations within the b.B.B. (horizontal axis indicates location into the Cold Tube from the Octagon in units of buckets travelled; one bucket length $\equiv 8$ cm) and extract the Ramsey frequency. Perform all these Ramsey experiments with the rotating electric field rotating in one direction, say, clockwise, corresponding to rotation switch $\tilde{R} = +1$.

(2) Repeat the experiments with the electric field rotating in the other direction, corresponding to rotation switch $\tilde{R} = -1$.

(3) Take the difference between these two frequencies (vertical axis, $f^R = \left[(f^{\tilde{R}} = f^+) - (f^{\tilde{R}} = f^-)\right]/2$), and plot them out for various locations within the b.B.B. (horizontal axis).

At each position, the Zeeman shift measured is a sum of two contributions: (i) ambient axial magnetic field gradient (physics from Plan A), and (ii) magnetic fields from charging currents (Plan E). Reversing the rotation direction of the electric field flips the sign of the Zeeman shift from the charging currents, but keeps the sign of the Zeeman shift from the ambient magnetic field gradients invariant. By taking the difference in frequencies for the two rotation directions, we can extract the component of the Zeeman shift that comes from the charging currents only. We fit two lines to the points. These two lines have different gradients, with a kink connecting them at about three buckets in. This suggests that the capacitance of the Rods per unit length has a sudden change at about three buckets in. It is not immediately clear why the kink happens at three buckets in, but we believe it to come from a combination of extra stray capacitance from the Rods with additional structural support and wiring in the region before three buckets in (see Figure 7.11).

The gradient of Zeeman shift from charging currents is bad for precision metrology with ions in multiple buckets at different axial location within the b.B.B., but it is helpful in preserving the definition of the Zeeman states as we move the ions (that have already gone through state preparation at the Octagon into the $X\,^3\Delta_1(v = 0, J = 1, F = 3/2, m_F = 3/2)$ states) from the Octagon to the Science region.

In the future, there will be additional sets of coils that will suppress the axial gradient introduced by the charging currents so that we can try out multiplexing protocols in the b.B.B. where we will have three or four ion clouds in neighboring buckets inside the b.B.B. for a simultaneous Ramsey spectroscopy.

In the last few chapters, we laid out our ambition to perform a multiplexed ion trap experiment. With so many electrodes to control, so many other instruments to coordinate, and so many ideas we wish to try out, this calls for a robust and scalable control system to govern the operations of the experiment. In the next chapter, we shall look at the brain that holds everything together.

Chapter 9

Control System

9.1 Introduction

We aim to perform a 20 s experiment with nanosecond timing precision on some of our operations, so this requires serious coordination of various components of our hardware. We also need to be able to run our experiment in a programmable and automated way with a user friendly interface, preferably with a system that does not break with operating system or software version updates. The systems used by the first two generations of the JILA eEDM experiments and the ThF spectroscopy experiment use hardware (e.g. ViewPoint DIO64) that are no longer available on the market. It is also not obvious how to implement a pseudo-continuous operation mode that is required for the Bucket Brigade using the old control systems. We decided to take this opportunity to develop a new control system and test it out on the baby Bucket Brigade.

We had a sneak peak at how we will be driving the electrodes with the Rod driver (Section 7.5.1.4) and Ring driver (Section 7.5.2). However, we also need to coordinate the timing of the voltages with the pulses controlling when, say, the nozzle opens, or when the laser fires to perform our eEDM experiment (Section 4.3.3 and Figure 7.9). This requires a control system that knows and controls everything. At some point, we will want to test out some of the Plans that we discussed in Chapter 8. This would require a control system that is scalable and modular. The following sections will briefly touch on the various components of our control system built upon the ARTIQ Sinara systems from M-Labs.

9.2 Hardware

We built upon the wisdom from the Gen. I JILA eEDM experiment to set up our control system. Much of the instruments used in the b.B.B. setup is also inherited from the ThF/ThF^+ spectroscopy setup. There are a few main components:

Master clock (SRS DS345). A master clock at 10 MHz is distributed to all our timing critical components in the experiment. The clock is distributed via a clock distributor (SRS FS735).

Digital delay generator (SRS DG645). A digital delay generator (DDG) generates pulses at 10 Hz repetition rate for our pulsed Nd:YAG lasers. These lasers need to be fired continuously at 10 Hz for optimal performance. The DDG sends out four pulses with well defined delays between them. Two of these pulses go to our SpectraPhysics Lab-190 Nd:YAG laser, and the other two to our SpectraPhysics INDI Nd:YAG laser. The two pulses trigger the flashlamp and the Q-switch of the lasers. The DDG also sends a start pulse to our FPGA controller at the start of each burst of a set of four pulses to synchronize the timing of the DDG with the TTL generator.

FPGA controller. An independent processor that receives commands from the main control computer on when to set off the TTL generator, DACs, and DDSes to run an experiment. Uses the external clock signal from the master clock.

TTL generators. An on-off square pulse generator (referred to as TTL generators, despite not necessarily conforming to TTL standards) triggers the rest of our components, e.g. laser shutters, nozzles, oscilloscope, microwave switches, camera, AOM.

Digital-to-analog converters (DAC). To generate arbitrary voltages that change at low frequencies. This is usually used to add shimming voltages to our electrodes or to act as analog inputs to HV power supplies.

Direct digital synthesizers (DDS). To generate arbitrary voltages that change at higher frequencies. This is used to generate our RF trapping voltages, our rotating electric fields, and our parametric excitation voltages. Uses the external clock signal from the master clock.

Function generators. To strobe our AOMs or to chirp our microwave frequencies. They use the external clock signal from the master clock.

Main control computer. A computer dedicated to talk to the FPGA controller directly.

Auxiliary control computers. Computers throughout the lab that run drivers for other satellite control systems, e.g. wavemeter, fiberswitch, doubling optics servo system, asynchronous camera system, asynchronous oscilloscope system, magnetic field coils driver, and cryocooler control system. These control computers can receive commands from the main control computer, and they can also send information to the main control computer regarding statuses of the systems. Communication is performed with TCP/IP over an intranet system set up in the lab.

In the early days of the ThF spectroscopy, we used "spare parts" from the Gen. I JILA eEDM experiment to set up our control system (Section 9.2.1), but we upgraded to a new system during the pandemic when we switched gears from ThF/ThF^+ spectroscopy to the design and construction of the b.B.B. (Section 9.2.2).

9.2.1 Legacy system

The DDSes used were the part of the trap driver from the Gen. I JILA eEDM experiment. The details of the trap driver can be found in Huanqian Loh's thesis.

The DACs used were from National Instruments. We combined two sets of DACs together in a home-built "consolidator box" to switch between the two sets of voltages quickly.

The main brain of the legacy system uses the ViewPoint DIO64 card, which served both as the FPGA controller and the TTL generator. It boasted 64 TTL output channels, way more than any of its competitors, and it came at a reasonable price. Unfortunately, good things never last, and they were no longer available even at the start of the ThF spectroscopy experiments. We barely made it through the spectroscopy before the DIO64 card started to show signs of failing. This was the main push to search for a new system.

9.2.2 Current system

We were introduced to the ARTIQ control system by our fellow ion trappers from the Ion Storage Group down the street at NIST. ARTIQ was first developed at NIST, and is commercialized by M-Labs, based in Hong Kong. It is a system that is currently used by ion trappers at NIST, Duke, Oxford, and many more. The Thompson Group at JILA is also porting their control system to ARTIQ. Alternatives to ARTIQ includes Quantum Machines (based in Israel) or sticking to the National Instruments suite. We settled for ARTIQ in the end.

We bought two ARTIQ crates (the "cu3 variant") that come with (the datasheets can be found on the M-Labs website, but some of the more critical specifications are listed here):

FPGA controller, the core device (Sinara 1124 Carrier, Kasli). Communicates with the main control computer through ethernet; this is an upgrade over the ViewPoint DIO64 that communicates through GPIB.

64 TTL channels (Sinara 2118 BNC-TTL). There are four channels that can be switched between input and output, and the rest of the sixty channels are output only. We use one of the input channels to receive the start pulse from the DDG to synchronize the TTL outputs with the four pulses for the pulsed Nd:YAG lasers. Outputs a high of 2 V on a 50 Ω load, with a timing jitter of 350 ps. Minimum pulse width of 3 ns.

64 DAC channels (Sinara 5432 Zotino). There are two Sinaro Zotino cards, each with 32 DAC channels. Outputs ±10 V with a 1 MSPS update rate shared across all channels (within each Zotino card). Has a 3 dB bandwidth of 75 kHz, with a 1-99% rise/fall time of about 30 μs.

Figure 9.1 shows a list of how the channels are being used in the current setup.

TTL

0	1	8	9	16	17	24	25	32	33	40	41	48	49	56	57
DDG T0 trigger	Input					43 GHz Switch	30 GHz Switch	Scope1	Scope2	DDS box IO_update	Consolidator TTL		Monkey shutter	Horse shutter	Lion shutter
2	3	10	11	18	19	26	27	34	35	42	43	50	51	58	59
Input	Input					v=0 Doublet select	v=0,1 select	Scope3	Scope4			Dog shutter		Cow shutter	Tiger shutter
4	5	12	13	20	21	28	29	36	37	44	45	52	53	60	61
										Hamster Q-switch	Hamster flashlamp	MCP mesh switch	MCP phosphor switch	Llama shutter	Sheep shutter
6	7	14	15	22	23	30	31	38	39	46	47	54	55	62	63
										Nozzle pulser	Mako camera	Accelerating rings		Goat shutter	Goat AOM

DAC

0	1	8	9	16	17	24	25	32	33	40	41	48	49	56	57
SR1, HV	SR1, LV	SR5, HV	SR5, LV	QR South East, HV	QR South East, LV	QR South West, HV	QR South West, LV	SR9, HV	SR9, LV	Rod 1/2 shim	Rod 3/4 shim				
2	3	10	11	18	19	26	27	34	35	42	43	50	51	58	59
SR2, HV	SR2, LV	QR North Up, HV	QR North Up, LV	QR North Down, HV	QR North Down, LV	SR6, HV	SR6, LV	SR10, HV	SR10, LV	Rod 5/6 shim	Rod 7/8 shim				
4	5	12	13	20	21	28	29	36	37	44	45	52	53	60	61
SR3, HV	SR3, LV	QR South Up, HV	QR South Up, LV	QR South Down, HV	QR South Down, LV	SR7, HV	SR7, LV	TR1	TR2						
6	7	14	15	22	23	30	31	38	39	46	47	54	55	62	63
SR4, HV	SR4, LV	QR North East, HV	QR North East, LV	QR North West, HV	QR North West, LV	SR8, HV	SR8, LV	TR3	TR4						

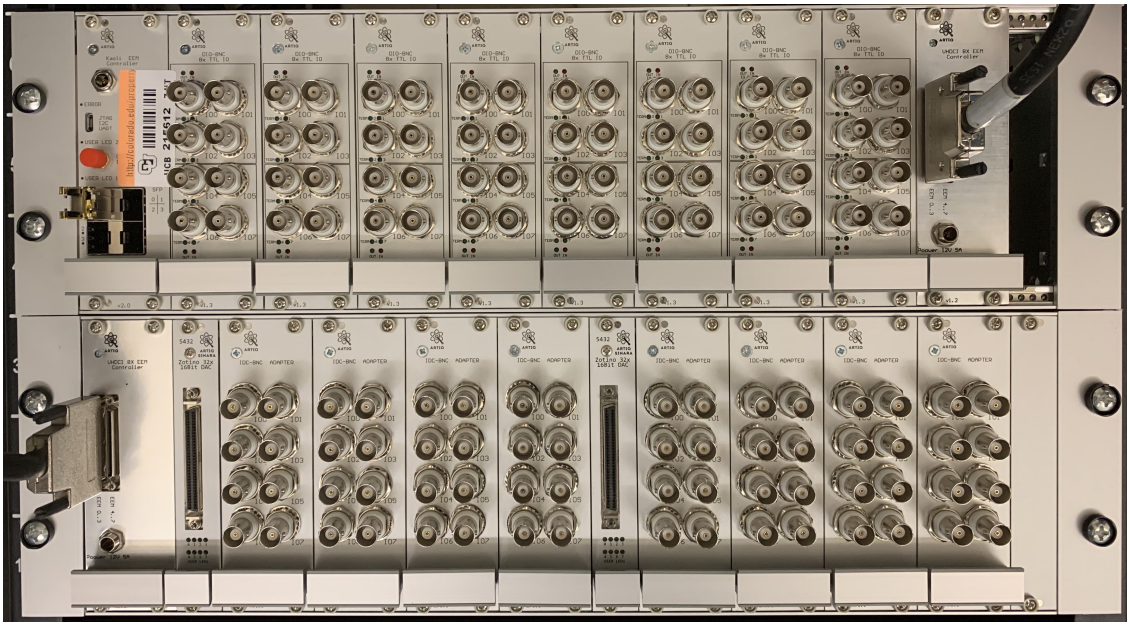

Figure 9.1: **List of things connected to the TTL and DAC channels.** A picture of the hardware is also shown here for a feel of the density of cable connections.

9.3 Software

One of the features of ARTIQ that appealed to us is that it comes with software with built-in graphics user interface (GUI). Despite being students who have had programming experience, programming a GUI is non-trivial, and there is no reason not to use a control system that comes with an in-built GUI. Figure 9.2 shows the ARTIQ dashboard, serving as the GUI frontend.

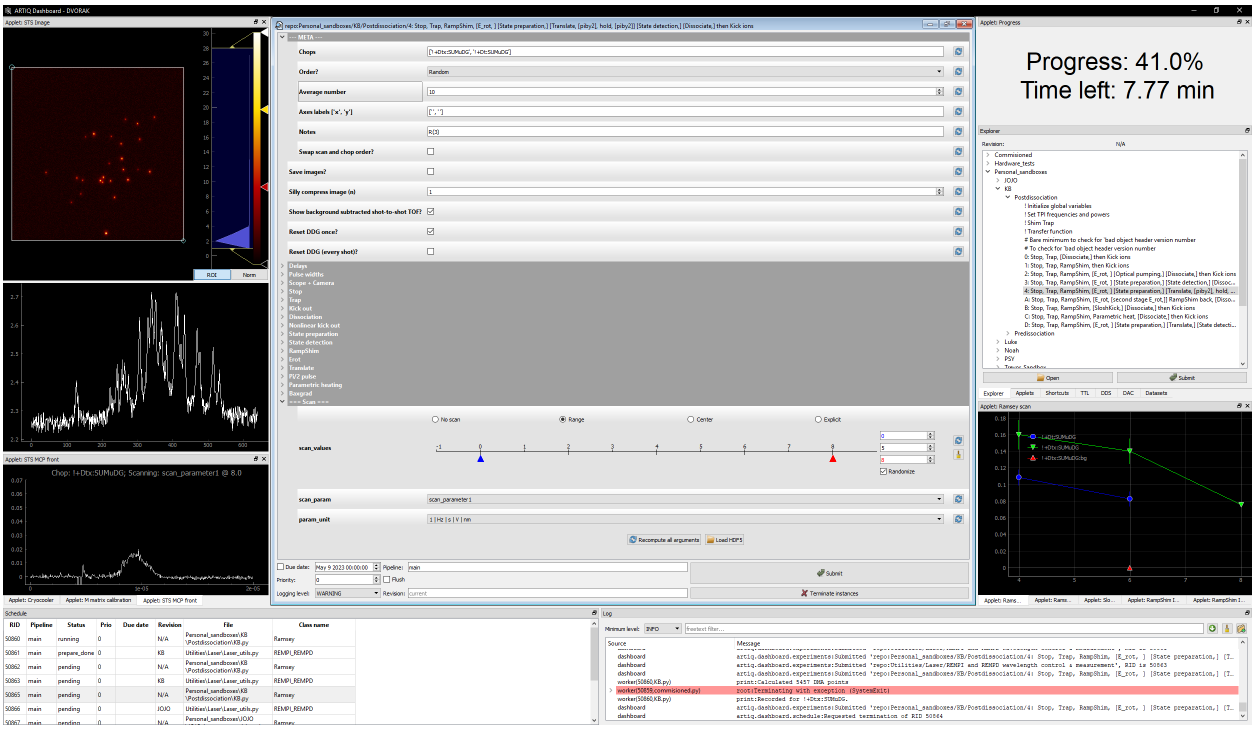

Figure 9.2: **The ARTIQ dashboard.** The panels on the left and right are applets that we can write (using `PyQtGraph`) to show live data streaming in. For example, the top left panel shows the image captured by our camera; each bright spot corresponds to a Th^+ ion hitting our ion detector. The top right panel shows the progress of the experiment that is currently running. The panel in the center allows us to set parameters for an experiment that we wish to use or scan. The bottom left panel shows experiments that are queued to run, and the bottom right panel shows the log. The user is free to move the panels around to suit their tastes.

Upon successful execution of the experiment, the experiment parameters given as user arguments through the dashboard are saved together with the data collected into an HDF5 file on our local server. These saved experimental parameters can be loaded onto the dashboard to rerun the experiment with the exact same conditions as the one saved. The Gens. I and II JILA eEDM experiments' equivalent to this is the `*.ubin` file (see Matt Grau's thesis).

We built our day-to-day experiment runs upon the ARTIQ software platform. I shall go into details for some of the structure that we have built upon the ARTIQ software platform in the following sections.

9.3.1 ARTIQ for the uninitiated

These section is mainly a summary of some key points about the ARTIQ system for the uninitiated. Interested readers can read their more extensive manuals on their website.

The `artiq_master` main control loop handles job scheduling and sends out commands to the FPGA to start the experiment sequence. On the user side, one typically writes code with the typical structure as shown in Figure 9.3. The code is written in `python`.

```
9107  class Ramsey(EnvExperiment):
9108      """ 4: Stop, Trap, RampShim, [E_rot, ] [State preparation,] [Translate, [piby2],
          hold, [piby2]] [State detection,] [Dissociate,] then Kick ions """
9109      def build(self):
9152
9153      def prepare(self):
9157
9158      def _distill_background_chops(self, scan_values, scan_param):
9190
9191      def run_scan_prep(self, scan_param, s, kwargs):
9214
9215      def run_exp(self, scan_param, s, kwargs, chop, mean_intensity_bg, name_cache):
9274
9275      def run(self):
9476
```

Figure 9.3: **Typical code structure.** One would have to write a class for each experiment. The class inherits from `EnvExperiment`, which is defined by ARTIQ, with methods `build`, `prepare`, `run`, and `analyze`. The user then overloads the methods by defining their own version within the user-defined class. In this case, the user defined class is `Ramsey`. The `build` method associates devices and user input arguments as attributes to the class. The `prepare` method runs part of the code that is independent of the actual experiment, e.g. calculating some variables from user specified arguments. The `run` part is where the actual sequences are written. The `analyze` part (not shown in the figure because we do not use it) is where we can perform some post-analysis of the data collected.

Users typically submit jobs to the queue through the ARTIQ dashboard, but can also submit jobs through a command line interface command `artiq_run` or `artiq_client submit`.

Upon a power cycle (from, say, power surges during the summer at JILA), we would need to run the `artiq_master` command on the main control computer once to let the main control loop run. On a day-to-day basis, we would run the `artiq_dashboard` command on our workstations, which will then open up the ARTIQ dashboard GUI, and communicate with the main control computer through our intranet regarding job submission and information.

As alluded to earlier on, the only hardware that the main control computer is connected to is the Sinara

FPGA. The main control computer communicates with the other instruments through remote procedure calls (RPCs). When this happens, the main control computer talks to the instruments through the auxiliary control computers. A list of devices is stored in the `device_db.py` file.

9.3.2 Important folders and files

The folder structure is as follows:

```
artiq_master/
    dataset_db.pyon, last_rid.pyon
    repository/
        device_db.py
        analyses/
            eedm.py, analyze.py, h5_unpack.py
        applets/
        controllers/
        experiments/
            Commissioned/
            Personal_sandboxes/
            Utilities/
        helper/
            gen3_macro.py
            ARTIQ_DAC/driver.py
            TTL_helper/driver.py
    results/
        <YYYY-MM-DD>/<HH>/<RID>_<experiment_name>.h5
```

First we have the home directory `artiq_master/`, not to be confused with the program `artiq_master` mentioned above. It contains two Python JSON files (`*.pyon`). The `dataset_db.pyon` stores a list of

persistent datasets that the users broadcast to the entire system. We use this to broadcast common variables that could change on a day-to-day basis to every connected workstation, e.g. trap shimming voltages. The `last_rid.pyon` file stores the Run ID number of the last run experiment. Within `artiq_master/` there are two folders: `repository/` and `results/`.

Within the `repository/` folder, we have a few important things. The `device_db.py` file stores a list of devices that the main control computer can talk to through the auxiliary control computers, and the addresses and ports of the auxiliary control computers.

The `analyses/` folder contains the suite of analysis tools that we have developed for the experiment (Section 9.3.4.3). `analyze.py` is the main workhorse of the data analysis package. `eedm.py` is the tool that gives all the optical pumping, PQR branch simulations, and ThF^+ Hamiltonian related tools. `h5_unpack.py` is a macro we wrote to unpack the HDF5 files.

The folder `applets/` contain the code for the applets that we saw on the ARTIQ dashboard (Figure 9.2). The folder `controllers/` contains all the drivers that we wrote for our devices. The drivers usually contain a list of important commands in the "programmer's manual" that comes with the device. We try to use VISA communication with the devices whenever possible.

The `experiments/` folder contains all the code with structure mentioned in Figure 9.3 that tells ARTIQ how to run the experiment. We split it up into three main folders: `Commissioned/` for all the code that have been proven to work, `Personal_sandboxes/` for code that each individual would like to mess around with before commissioning, and `Utilities/` for macros to execute small things on devices that are not directly related to an experiment *per se*, e.g. ramping the microchannel plate assembly to the right voltages.

The folder `helper/` consists of macros that we wrote to make our lives easier. `gen3_macro.py` is a dictionary of names that we assign to TTL channels (see Figure 9.1). The `ARTIQ_DAC` and `TTL_helper` driver files parses high-level commands used by the experimentalists into timing and voltage commands that ARTIQ understands. For example, it parses the following:

```
<TTL_helper>.add_pulse(`Trap loading', `Consolidator TTL',\
```

```
pulse_duration = self.pulse_pulser,\
delay_duration = 0)
```

into a series of `<coredevice>.core.seconds_to_mu()` commands to set the time for the next event, and `<coredevice>.ttl.TTLOut.on()` and `<coredevice>.ttl.TTLOut.off()` to turn the TTLs on or off at the corresponding times.

Finally, we have the `results/` folder, which contains all the HDF5 files with the data and user input arguments for all the experiment. This folder is further sorted into the `YYYY-MM-DD/HH/` subfolders based on when the experiment was run.

9.3.3 Communication with auxiliary control computers.

Communication with devices from the main control computer is done through the auxiliary control computers. We used to write our own TCP/IP communication VIs when we were using the LabVIEW system. ARTIQ comes with the Simple Python Communication (SiPyCo) library[1] that allows us to do just that, but in a "pythonic" form that is also fully compatible with ARTIQ.

The communication comes in two parts: (i) the drivers with the relevant commands from the devices' "programmer's manual", and (ii) a controller server loop that opens a connection with the device through the drivers.

Device drivers. The device drivers declare one python class for each device. Upon initiation of the class, communication is established by the auxiliary control computer with the device if the device is connected. Users can call on the methods of the class to ask the device to perform certain tasks. We show an example of a code for a driver in Listing 1.

Controller server loop. The server loop runs on the auxiliary control computer. It runs the drivers and establishes direct communication with the devices. Within the loop, it listens for RPCs from other control computers and runs the relevant RPC commands (involving the methods written in the device drivers). An example of a code for a controller server loop is shown in in Listing 2.

[1] SiPyCo used to be part of ARTIQ, but was split out so that one can use the former without having to install the rest of ARTIQ.

```
class ds30_cryocooler(_visa_comm): # inherit methods from `_visa_comm`
    """ DS30 Cryocooler """
    def __init__(self, visa_resource, baud_rate=None, read_termination=None,\
                 write_termination=None, silent_bool=None):
        ### Inherit `__init__` from `_visa_comm`
        if write_termination==None:
            write_termination = '\r'
        if baud_rate==None:
            baud_rate = 9600
        _visa_comm.__init__(self, visa_resource, baud_rate=baud_rate,\
                            read_termination=read_termination,\
                            write_termination=write_termination,\
                            silent_bool=silent_bool)

    def on(self):
        """ Turns on cryocooler. """
        self.WRITE('COOLER=ON')

    def off(self):
        """ Turns off cryocooler. """
        self.WRITE('COOLER=OFF')

    def set_TTARGET(self,TTARGET):
        """ Sets TTARGET (target temperature). Takes in argument `TTARGET`. """
        self.WRITE('TTARGET={}'.format(TTARGET))
```

Listing 1: **A snippet of the DS30 cryocooler driver.** We communicate with the DS30 cryocooler through VISA. Three methods are shown here: `<ds30_cryocooler>.on()` to turn the cryocooler on, `<ds30_cryocooler>.off()` to turn the cryocooler off, and `<ds30_cryocooler>.set_TTARGET(TTARGET)` to set the target temperature to `TTARGET`.

One can talk to a particular device (e.g. to turn the DS30 cryocooler) on a particular auxiliary control computer connected to the device (e.g. IP address 172.31.1.207, port 7000) from any workstation connected to the intranet with a SiPyCo command (in the terminal or command prompt) of the form:

```
sipyco_rpctool 172.31.1.207 7000 call -t ds30 on
```

where the `-t <device_name>` flag is to indicate which device to talk to in case the auxiliary control computer is connected to multiple devices. I recommend the learning graduate student or post-doc to check the manual on their website (https://m-labs.hk/artiq/sipyco-manual/#remote-procedure-call-tool) for more information on SiPyCo commands.

In general, it is bad practice to connect all the devices to one auxiliary control computer. Doing so

```python
import argparse, sys, asyncio
from camera_vimba.driver import mcp_camera
from current_control.driver import keysight_current
from sipyco.pc_rpc import simple_server_loop
from sipyco import common_args

### To parse argument for controller
def get_argparser():
    """ Argument parser """

    ### Define argument parser object
    parser = argparse.ArgumentParser()

    ### Boilerplate
    common_args.simple_network_args(parser, 7000) # (parser, default_port)
    common_args.verbosity_args(parser)
    return parser

### Main code
def main():
    ### Boilerplate
    args = get_argparser().parse_args() # retrieves dict of arguments
    common_args.init_logger_from_args(args)

    ### Define devices
    connected_dev = {}
    try:
        connected_dev['camera_mako'] = mcp_camera('DEV_000F315C339E')
    try:
        connected_dev['Baxgrad_supply'] = keysight_current()

    ### Open server in a loop
    try:
        simple_server_loop(connected_dev, common_args.bind_address_from_args(args),\
                           args.port)
```

Listing 2: **An example of a controller server loop.** The gist of the code is as follows. We import the classes from the relevant driver files. We then create a `dict` of connected devices, with names of the devices as `keys` and the relevant class as the `values`. Then we execute the server loop with `simple_server_loop`.

will reduce the bandwidth of the computer to work with all the devices simultaneously. In cases where there needs to be simultaneous transfer of information from multiple devices, the computer may make unhappy noises instead.

9.3.4 The JILA eEDM suite

The ARTIQ software framework is very versatile, and in principle one can write code to run any experiment of their liking. We can easily scan experiment parameters by using the for loop in `python`. However, we quickly realized in the early days of getting familiar with ARTIQ that this is not scalable. We would have to write a different for loop each time we wish to scan a different parameter or over a different range. Depending on the order at which we change settings on our devices, changing the order of the for loops could end up being a total disaster. We need a scalable framework.

To address our needs, we introduce a particular structure to our code.[2] We do not claim that this is the best way of doing it. We also encourage users of the code to come up with creative ways to make the code more efficient and more streamlined. The code that we use was written in the land of the free, so free it shall be: free to modify and distribute. This section and the next only serve as a form of documentation of the code structure that we currently have in our lab. The target audience includes incoming students and post-docs, and, of course, people who wish to adopt something similar in their labs.

Like all projects that involve coding, one does not hope to be an expert just from reading the documentation. I certainly do not intend for the content in this section to be fully self explanatory. I highly encourage new students and post-docs to learn by using our system with the guidance of those who have already been using it for some time. Hopefully through a combination of hands-on approach and the summary that I provide here, one would be able to pick up the essence of the JILA eEDM suite, and suit it to their purposes.

9.3.4.1 Experiment code structure

As alluded to in Figure 9.3, to run an experiment, one writes a class with methods `build`, `prepare`, `run`, and `analyze`. Out of the four, only `build` and `run` are the absolutely necessary. The former declares the devices, and the latter is the actual sequence to run for the experiment.

In the JILA eEDM suite, we introduce two types of classes in our attempt to make our code more

[2] We learnt about `ndscan` (see https://github.com/OxfordIonTrapGroup/ndscan) a little too late for us to implement it with minimal effort in our setup.

modular:

The "underscored" class: `class _<experiment>(_edmScan).` We write the "underscored" class to be as general as possible within the framework of a type of experiment. For example, we have a class called `_Ramsey(edmScan)` that performs a Ramsey experiment: (i) create ions and trap them, (ii) perform state preparation, (iii) translate ions into the Science region, (iv) perform the Ramsey sequence, (v) translate ions back into the Octagon, (vi) perform the state detection sequence, and (vii) kick ions out onto detector. Within each stage, all experiment parameters are set to be user input arguments. These user input arguments can be set through ARTIQ dashboard; they also have default values if the user does not wish to change them.

We have a separate "underscored" class for each type of experiment. For example, we also have a class called `_Slosh_Ions(_edmScan)` that kicks the ions in the trap to induce slosh: (i) create ions and trap them, (ii) kick them in a certain direction, (iii) wait for some time, and (iv) kick ions out onto detector. Evidently this type of experiment is very different from that catered by `_Ramsey`.

The "underscored" class inherits from `class _edmScan(HasEnvironment)` that defines all the commonly used user arguments under its `build` method. These user arguments can be shared across multiple types of experiments, e.g. `_Slosh_Ions` and `_Ramsey`. The class `_edmScan` also has a method that consolidates all the user input arguments into a list that can be accessed as an attribute of the class. This list will be used in the non-"underscored" class.

The non-"underscored" class: `class <experiment>(EnvExperiment).` The non-"underscored" class is a wrapper around the "underscored" one, where it sets the user input arguments programmatically. It assigns the "underscored" class as an attribute to itself, and invokes its methods whenever we need to communicate with our devices. The non-"underscored" class allows the user to choose a user argument from the list generated by `_edmScan`, and perform a scan by looping through multiple calls of the "underscored" class. The non-"underscored" class also allows the user to input "chop names" that can be parsed by the "underscored" class to switch between various states of the experiment. This allows lab users to run different variants of the same type of experiment without modifying the

code each time.

We leverage on the class inheritance mechanism to define non-"underscored" classes that inherit from the base non-"underscored" classes to perform a fixed set of routine. For example, we can have `class R_branch(Ramsey)` inheriting from the non-"underscored" `Ramsey`. See Figure 9.4) for more information.

```
3106   # 4.
3107  class _Ramsey(_edmScan):
4329
4330  class Ramsey(EnvExperiment):
4713
4714   ### ========== Daily scans ========== ###
4715
4716   # Pulse Phosphor
4717  class Pulse_Phosphor(Ramsey):
4762
4763
4764   # R branch
4765  class R_Branch(Ramsey):
4811
```

Figure 9.4: **Example of having multiple non-"underscored" classes inheriting from the main non-"underscored" class.** The class `Pulse_Phosphor` is used to scan the timings of when to gate the phosphor off to distinguish phosphorescence signal between Th^+ and ThF^+. The class `R_branch` is used to scan the R branch of the REMPD intermediate state.

9.3.4.2 Parsing the code names

As mentioned in Section 4.3.1.2, we use abbreviated one-character code names to represent each laser and microwave. The JILA eEDM suite turns all the laser and microwaves off by default, but it turns them on instead if it receives the corresponding code name. For example, it the software receives a string "SU", it will turn Sheep and the 43 GHz microwaves on (see Section 4.3.1.1 for the corresponding code names). The user inputs this under the `Chop` section of the ARTIQ dashboard interface.

The code that implements this is a parser written in the "underscored" class. It is just a series of if clauses of the form:

```
if 'S' in chop_name:
    <code to turn Sheep's shutter on>
if 'U' in chop_name:
    <code to turn 43~GHz microwave on>
```

...

To differentiate between having the lasers/microwaves turned on during the state preparation and state detection stages, we use a "+" as a divider. For example, "SU+GL" will turn only Sheep and the 43 GHz microwave on for the state preparation stage, and only Goat and Llama for the state detection stage.

This implementation is just the (upgraded) code version of clicking checkboxes on the LabVIEW GUI in the Gens. I and II experiments to choose which set of lasers/microwaves to turn on. One can easily scale up this protocol to include other "switches" (e.g. whether to translate the ions into the Science region) by encoding the relevant code names into the parser in the JILA eEDM suite.

9.3.4.3 Analysis package

All experiment data and user input variables are saved into HDF5 files after each run. Our analysis suite is contained in the `analyze.py` file mentioned in Section 9.3.2. It consists of `class get_moments()` that takes in an HDF5 file object and an optional dict of keyword arguments. Upon initialization of the class, it extracts (i) the capacitively coupled output from the oscilloscopes, and (ii) phosphorescence as captured by our camera. From here, it massages the data into structured dicts sorted by "chop names" and ascending order of the scan parameter, if any. This forms the basis of our analysis package.

Within `get_moments`, there are methods that can take the structured dicts and perform further analysis, e.g. segregate the detected Th^+ ions into those of the two different doublets depending on which side of the swatch they sit on, and plot out Ramsey fringes for both doublets. One usually writes such analysis code in their personal sandboxes, and only shares it with others by commissioning it into a method in `get_moments` on the demand of others.

There is a wrapper function `edm_analyze(fn)` in `analyze.py`. This wrapper function takes in a filename (of the HDF5 file), analyzes the type of the experiment that was run (saved as metadata in the HDF5 file), and calls the appropriate methods from `get_moments` to generate the plots associated with that type of the experiment.

9.4 Further discussion

We saw how we borrowed wisdom from the Gen. I experiment in setting up our control system. We also listed some of the more critical components of our hardware system. We then discussed how we upgraded our old system to a new one based on the ARTIQ control system. It is mainly an upgrade in the hardware, but the software comes for free. As with all experiments, the control system is mutable. The control system evolves with each stage of the experiment. It is up to the lab users to adapt the tools available to them to their needs.

I led the team in building the control system that we have now. I tried to design it to be as scalable and modular as possible, guided by my limited foresight of the kind of experiments that we wish to perform with the setup. Nevertheless, our experiment is heading in the direction of pseudo-continuous operation with the multiplexed ion trap. This is something that has never been tried in the JILA eEDM labs. Turning an experiment setup that runs one shot of the experiment at a time into one that can coordinate a pseudo-continuous operation is certainly non-trivial. Furthermore, it can also be tricky to correlate the stored HDF5 files with the corresponding bucket of ions. Here, I lay out some extensions to our current system that the group may wish to adopt in their endeavors to get to a fully mature Bucket Brigade experiment.

Idle kernel. The idle kernel is a piece of code that is stored on the core device. It runs whenever the core device is idle. One can possibly use this like a DDG, spitting out pulses continuously with well defined delays between them. I imagine using a version of the idle kernel (or another SRS DG645) to coordinate the pseudo-continuous operations in the Bucket Brigade setup.

Distributed Real Time Input/Output (DRTIO). Verbatim from the ARTIQ website:

> DRTIO is a time and data transfer system that allows ARTIQ RTIO channels to be distributed among several satellite devices synchronized and controlled by a central core device.

Much like how we have on-board FPGAs that control our DDSes in our Rod drivers, we could lessen the burden on our core device and distribute it among several satellite devices. This may come in useful in the future when we find ourselves exceeding 64 TTL channels, or when the core device

cannot keep up with the number of events happening concurrently.

Upgrading to ARTIQ 7+. New versions always come with new features. One of the features in ARTIQ 7 is that one can now configure the number of FIFO lanes in the scalable events dispatcher (SED) directly. One of the problems that we see in our experiment is that when we try to schedule too many events too close in timing, the FIFO lanes (eight of them, by default) fill up and the rest of the events are jammed. This results in events being skipped, and the experiment does not work. When the FIFO lanes are full, sometimes it returns an `RTIO underflow` error (which is already irritating by itself) but sometimes it does not even return an error (a known bug in our system). It turns out that configuring the number of FIFO lanes in the SED in our current ARTIQ 6 system is a real pain. There is a saying that goes, "if it works, do not change it," because there is always a non-zero chance that the thing will break with the change. One will need to have great determination to upgrade our currently working ARTIQ 6 framework into ARTIQ 7+ to get the aforementioned feature. I shall leave this big decision to the diligent, intelligent, and responsible people in the group after I am gone.

Chapter 10

Cryogenics

10.1 Introduction

The Ramsey interrogation time in the HfF^+ experiments are limited by the radiative decay of $^3\Delta_1 \rightarrow X\,^1\Sigma^+$. The radiative lifetime was estimated to be about 2 s [86]. This is sufficient for a Ramsey interrogation time of about 3 s in the Gen. II experiment. As alluded to earlier on, the $^3\Delta_1$ electronic state is the ground state in ThF^+. This means that we will not be limited by decay from $X\,^3\Delta_1$ in ThF^+ to any lower lying states. One limiting factor for our state lifetime (T_1) is the rate at which molecules are excited out of the $X\,^3\Delta_1(v=0)$ manifold through blackbody radiation. We have estimated this to be dominated by the $(v=1) \leftarrow (v=0)$ channel with a lifetime of about 4 s at 300 K (see Table 4.2). We mentioned in Section 4.2.3 that we can suppress this loss by working with cryogenic temperatures. Figure 10.1 shows how quickly we can suppress the blackbody radiation photon numbers by going down to lower temperatures. The relevant

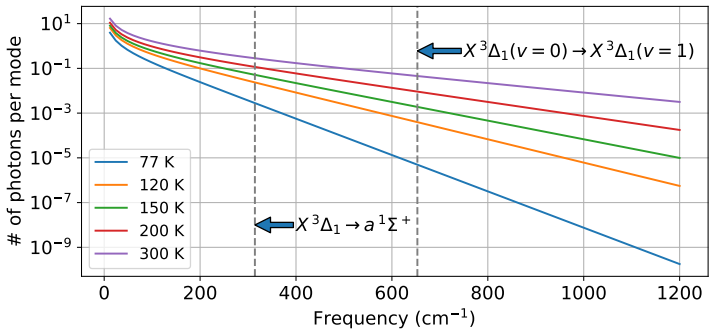

Figure 10.1: **Number of blackbody radiation photons.** Plotted as a function of wavenumbers for easy comparison with Figure 10.2.

energy scales for both molecules are shown in Figure 10.2 for comparison.

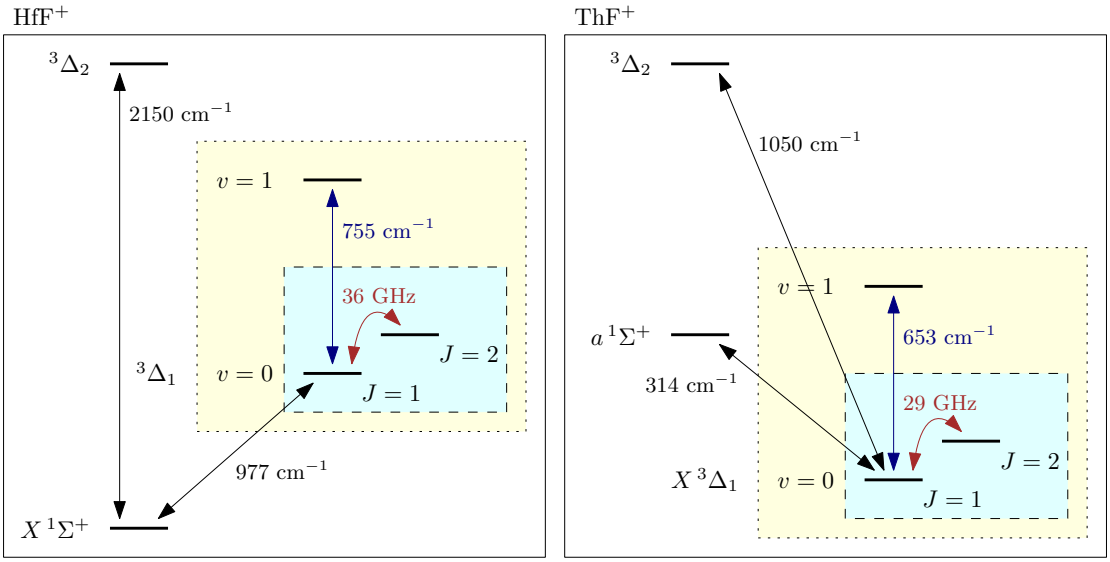

Figure 10.2: **Energy level diagram for the lowest lying states for HfF^+ and ThF^+.** 1 $cm^{-1} \approx$ 30 GHz. Blackbody radiation excitation from the Science state in HfF^+ was never a major concern because the lifetime of the Science state is limited by the radiative decay $^3\Delta_1 \rightarrow X\,^1\Sigma^+$.

In this chapter we shall see how we introduce cryogenics into our setup. We will first look at the design of our cryogenics setup in the context of the Bucket Brigade (Section 10.2). We will then look at the performance of the cryogenics system on our b.B.B. (Seciton 10.3). Finally, we will conclude this chapter with a discussion on possible future upgrades (Section 10.4).

10.2 Design in the context of the Bucket Brigade

The cryogenic temperature that we are aiming for is only about 150 K. This is not serious cryogenics. Here is a list of some common cold stuff for comparison.

- Coldest natural temperature recorded in Boulder: 237 K (17 January 1930, from NOAA)
- Carbon dioxide, sublimation point (dry ice): 195 K
- Coldest natural temperature recorded on Earth: 184 K (21 July 1983, Antarctica [87])
- Bucket Brigade: 150 K
- Methane, boiling point: 112 K
- Oxygen, boiling point: 90 K
- Nitrogen, boiling point (LN2): 77 K
- Helium-4, boiling point: 4.2 K

There are many tried-and-tested solutions to cryogenics (e.g. multi-layer insulation[1] , cold shields[2] , and vacuum jacket[3]), many of these are developed for setup involving serious cryogenics where they want to minimize heat load from the ambient 300 K environment. Although the aforementioned tried-and-tested solutions are established techniques that have been around for some time, they come with intricate problems of their own, which can differ from setup to setup. We explored several options with engineers[4] from NASA, many of those involve using LN2, but the size of our setup makes LN2 an expensive option. In the end we were advised by our in-house Dr. Eric Cornell to try a combination of household insulation foam and a modest cryocooler to get us down to 150 K.

[1] MLIs: multiple layers of thin sheets to suppress radiative heat losses. Commonly used in spacecrafts and cryogenic setup. This was recommended to us by Dr. Eric Silk from NASA.

[2] Cold shields act as heat sinks.

[3] Vacuum jackets are vacuum chambers surrounding the main chamber at cryogenic temperature. The vacuum suppresses conductive and convective heat transfer, so the only mode of heat transport from the cryogenic main chamber to the ambient room temperature environment will be through radiation. Vacuum jackets are typically used in conjunction with MLIs to suppress radiative heat transfer.

[4] Much thanks to Dr. Eric Silk and Dr. Richard Ottens from NASA.

This section proceeds as follows. We will estimate the heat load in the Bucket Brigade at steady state operation (Section 10.2.1). We then look at the effects of (differential) thermal contraction of objects in the Bucket Brigade which can be made of different materials (Section 10.2.3). Finally, we discuss how we want to spread the cold from the cold source (Section 10.2.2).

10.2.1 Heat load

The cryogenic part of the Bucket Brigade setup is shown as the blue part of Figure 5.5. For the purpose of the analysis, we shall work with the schematic diagram shown in Figure 10.3.

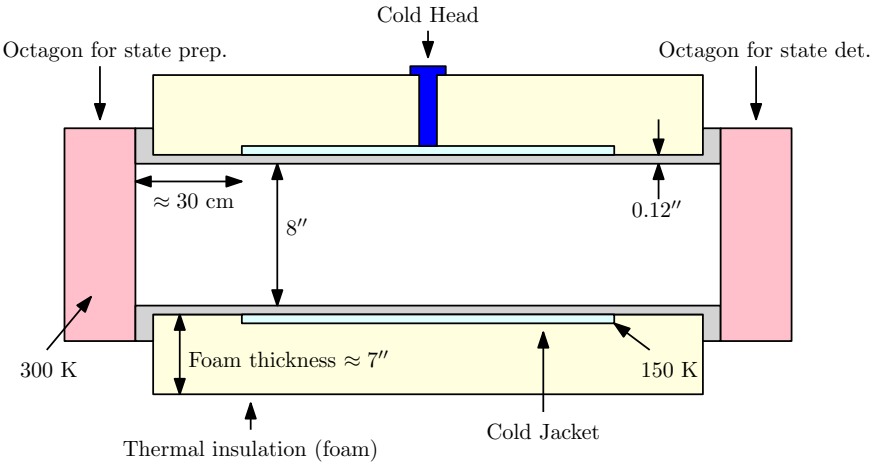

Figure 10.3: **Schematic diagram of a simplified setup for heat load analysis.** There is one Octagon on each side for optics access. These are not temperature controlled, and are nominally at 300 K. A long nipple connects the two Octagon. The dimensions of the nipple are informed by a combination of field homogeneity simulations (Section 7.3) and what can be bought, say, from Kurt Lesker. A Cold Jacket is clamped onto the nipple to spread the cold from the Cold Head. The Cold Head is situated at the center of the setup. The Cold Jacket ends at about 15 cm from each end of the nipple. This provides a natural temperature gradient from the Octagon at 300 K to the Cold Jacket at 150 K. The nipple and the Cold Jacket are enclosed by thermal insulation. The Bucket Brigade is not drawn in the schematic diagram to prevent overclutter.

Heat load in the system comes mainly through three channels: (i) conduction through the nipple, (ii) radiation/conduction from the Bucket Brigade, and (iii) conduction through the thermal insulation. We shall first look at the former.

The rate of heat flow per unit time associated with thermal conduction is given by:

$$P = \kappa(T) A \frac{\mathrm{d}T}{\mathrm{d}x} \implies P = A \frac{\int^{\Delta T} \kappa(T)\,\mathrm{d}T}{\Delta x}. \tag{10.1}$$

Evaluating the above for the nipple with dimensions stated in Figure 10.3, we get a heat load of about 13 and 5.9 W coming in from each side of the nipple for the cases where the nipple is made of 304 SS and Ti-6Al-4V, respectively.[5]

For the Bucket Brigade, we expect to work with eight stainless steel Rods, each 0.5″ in diameter, 1 mm thick. We assume that the Rods come in thermal equilibrium with the nipple along the axial direction. The thermal equilibrium comes from radiative heat transfer along the radial direction.[6] This gives 250 mW per Rod per side, totalling to 4 W. Using titanium would half this amount.

For conduction through the thermal insulation, we estimate it for the case where the foam is cylindrically symmetric, with the outer surface at 300 K, inner surface at 150 K, total length of 3 m, with a conductivity of 60 mW/(m K).[7] A plot of the conduction power at various foam thickness is shown in Figure 10.4.

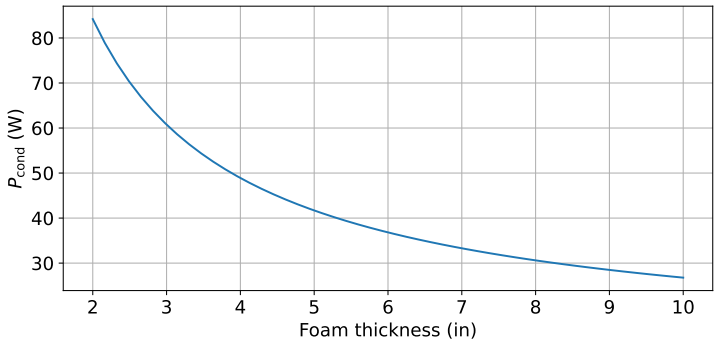

Figure 10.4: **Calculated conduction power through household foam.** Foam thickness is defined in Figure 10.3. The foam is assumed to be cylindrically symmetric, with inner diameter the same as the outer diameter of the nipple. The foam is set to 3 m long, with the outer surface at 300 K and inner surface at 150 K.

We will also have some structural support that will run down the Bucket Brigade. We do not expect to use structures that have huge cross sectional area, or much higher thermal conductivity than stainless steel. The total heat load at steady state from the nipple, Rods, and structural support is estimated to be about 40 W if all of them are made from stainless steel. Using 7″ thick foam will give an additional heat

[5] Thermal conductance of 304 SS and Ti-6Al-4V are obtained from Table 1A (NIST).

[6] There will be some smoothing effect along the axial direction, but we will be ignoring this in our estimation for the heat load budget.

[7] The foam was advertised to have an R-value per inch of 5.48, corresponding to 26 mW/(m K), but we ran tests and found that the net conductivity between a surface at 300 K and the other at 150 K is about 60 mW/(m K); see Section 10.3.1.

load of about 35 W, bringing the total to about 75 W.

Blackbody radiation from the warm ends down the Bucket Brigade contribute to about 30 W (summed from both sides), bringing the total to about 105 W.

Resistive heating from charging currents running up and down the Rods contribute negligibly to the heat load ($\sim$ 100 μW). We do not expect any other significant heat load in the Bucket Brigade. However, one may need to add additional sources of heat from, say, currents flowing in magnet wires used to generate magnetic fields. These could go up to a few watts. They would contribute to the heat load significantly if placed in direct contact with the cold.

105 W is a reasonable heat load at 150 K. As we shall see in a later section, we can buy an off-the-shelf Stirling cryocooler that can operate at around half that heat load, so we just need two of those. It certainly looks like our modest cryogenic temperature allows us to get away with using a simple cryocooler and household insulating foam. However, the above only holds if we can spread the cold effectively. We shall look at how we do this in the next section.

10.2.2 Spreading the cold with the Cold Jacket

The Cold Head is a local heat sink, and we need to spread the cold to the rest of the Bucket Brigade setup. This requires a Cold Jacket made from a material with high thermal conductivity, like copper or aluminum. We went through a few iterations for this design, including (see Figure 10.5):

Slab + copper braids. Cold Head attached to the middle of an aluminum slab on the top of the nipple to spread the cold axially along the top of the nipple. Copper braids wrap around the nipple to spread the cold azimuthally.

Backbone + ribs. A rib-like structure that hugs the nipple. It comes in two halves, one for the top half, and one for the bottom. The "backbone" of the rib-like structure will be on the top part of the nipple, and the Cold Head will be at the center of the backbone. The ribs spread the cold azimuthally, and replace the copper braids in the previous design.

Clamshells. Two clamshells of half-cylinders. This spreads cold in the same way as the rib-like struture,

except that we fill in the gaps of the ribs to simplify the geometry.

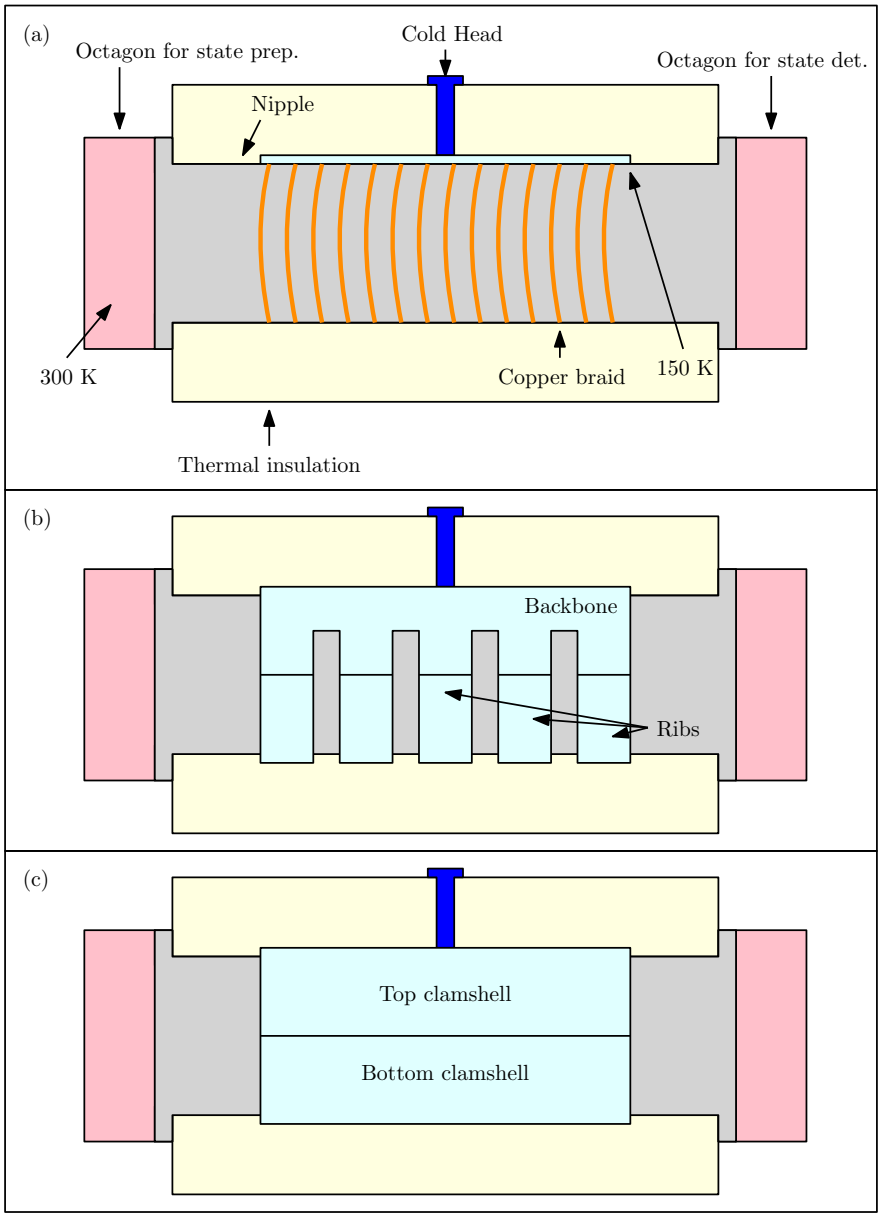

Figure 10.5: **Early plans for Cold Jacket.** (a) Slab + copper braids. (b) Backbone + ribs. (c) Clamshells.

Some design constraints include:

- Being able to fit the Cold Jacket onto the nipple. The copper braid design just involves wrapping the braids around. The other two designs involve clamping the two halves onto the nipple. Since we want good thermal contact between the Cold Jacket and the nipple, it could be a little tricky to get

the machining tolerances right for the latter two.

- Having high thermal conductivity. This means that we would want to use copper or aluminum. Aluminum is lighter (and cheaper) than copper, so the former is the preferred choice.

To get efficient thermal conduction, though, we would need to have big cross sectional areas. We first stumbled upon the rib design to save on some materials (and thermal mass). However, we realized that it complicated the machining process and did not save us that much time and money, so we ended up going with the clamshell of half-cylinders. Having a big cross sectional area means high thermal mass for the Cold Jacket. The question now is: will the high thermal mass result in a longer cool down time?

Here I present a simple model for us to understand how the cool down time constant depends on the design parameters of the Cold Jacket. We make a few simplifying assumptions:

(1) We assume that the thermal mass of the Bucket Brigade system is dominated by the thermal mass of the Cold Jacket. This is true for a Cold Jacket with large cross section area. This ensures that the main route of axial thermal transfer is through the Cold Jacket.

(2) We assume that there is no additional heat load. We just want to know how long it takes for us to extract all the thermal energy from the Cold Jacket.

(3) We simplify the geometry and model the Cold Jacket as a long slab with cross-sectional area A and length $L = 3$ m.

This slab is being cooled from the center ($x = 0$) with a cold thermal bath held at T_{cold} (skip ahead to Figure 10.7 for the geometry of this toy model). We discretize the slab into chunks of length Δx to study the time required to cool the slab down to some temperature of interest from room temperature. A schematic is shown in Figure 10.6.

In a short time Δt, the net energy going into the discrete chunk at x is given by:

$$\begin{aligned}(P_{\text{in}} - P_{\text{out}})\,\Delta t &= \left[\kappa A\,\frac{T(x-\Delta x) - T(x)}{\Delta x} - \kappa A\,\frac{T(x) - T(x+\Delta x)}{\Delta x}\right]\Delta t \\ &= \kappa A\,\Delta t\,\frac{T(x+\Delta x) - 2T(x) + T(x-\Delta x)}{\Delta x}.\end{aligned} \tag{10.2}$$

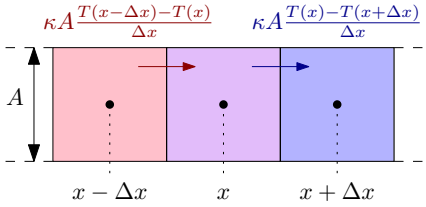

Figure 10.6: **Schematic of model used to study cool down time of cold plate.**

The change in the thermal energy stored in the chunk at x in this time is given by:

$$U(t+\Delta t)-U(t)=mc[T(t+\Delta t)-T(t)]=\rho\,\Delta x A c[T(t+\Delta t)-T(t)].$$

We equate the two equations above and work in the limits $\{\Delta x\to 0,\Delta t\to 0\}$ to get:

$$\partial_x^2 T(x,t)=\frac{\rho c}{\kappa}\partial_t T(x,t), \tag{10.3}$$

where $T(x,t)$ is the time-varying temperature profile of the slab, ρ is the mass density of the slab, c is the specific heat capacity of the slab, and κ is the conductivity of the slab. Note that the cross sectional area drops out.

Using the separation of variables, we demand that $T(x,t)=\mathbb{X}(x)\mathbb{T}(t)$ to get:

$$\frac{1}{\mathbb{X}}\partial_x^2\mathbb{X}=\frac{1}{\mathbb{T}}\frac{\rho c}{\kappa}\partial_t\mathbb{T}=-K^2,$$

where K is some real positive constant to be determined. The solution to the above is as follows:

$$\mathbb{X}(x)=A_K\sin Kx+B_K\cos Kx, \tag{10.4a}$$

$$\mathbb{T}(t)=e^{-\frac{K^2\kappa}{\rho c}\cdot t}, \tag{10.4b}$$

where we conveniently define $\mathbb{T}(0)=1$. To determine the constants $\{A_K,B_K\}$, first we note by symmetry of the setup about $x=0$, $\mathbb{X}(x)$ has to be an even function, so $A_K=0$. Next, we note that there are two boundary conditions:

(1) From the cryocooler: $T(x=0,t)=T_{\text{cold}}$.

(2) There is no heat flow into the ends (by assumption), so $\partial_x T(x=\pm L/2,t)=0$.

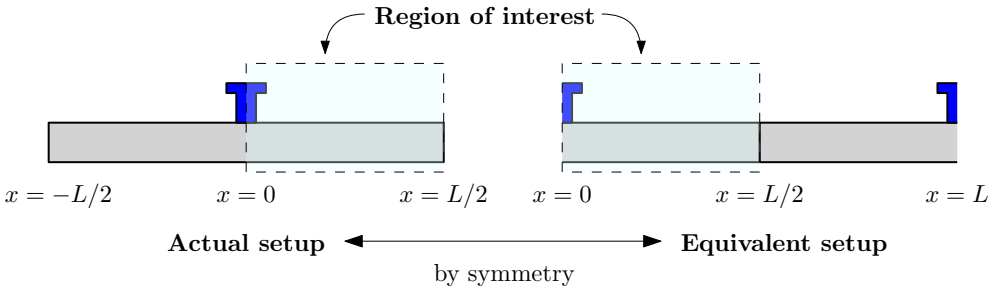

Figure 10.7: **Equivalent mathematical model for the actual setup.** Blue and grey areas denote the cryocooler and the cold-transmitting slab, respectively.

By the symmetry of the second boundary condition above, we recast the problem into an equivalent setup shown in Figure 10.7.

Also important to note is that we can always add or subtract a constant from $T(x,t)$ from Equation 10.3, so the quantity that matters is the temperature difference. Hence, we demand the following:

(1) $\mathbb{X}(x=0) = \mathbb{X}(x=L) = 0 \implies B_K = 0$ and $K = n\pi/L$.

(2) $\mathbb{X}(x)$ is to be an even function about $x = L/2$.

(3) $\mathbb{X}(x = L/2) = T_{\text{start}} - T_{\text{cold}}$.

The above gives:

$$A_n = (T_{\text{start}} - T_{\text{cold}}) \cdot \frac{4\sin^2(n\pi/2)}{n\pi} \quad , \quad B_n = 0 \quad , \quad n \in \mathbb{Z}^+,$$

and so our final solution is

$$T(x,t) = T_{\text{cold}} + \sum_{n=1}^{\infty} (T_{\text{start}} - T_{\text{cold}}) \cdot \frac{4\sin^2(n\pi/2)}{n\pi} \cdot \sin\frac{n\pi x}{L} \cdot e^{-\frac{n^2\pi^2\kappa}{\rho c L^2} \cdot t}. \tag{10.5}$$

One important thing to note from the above analysis is that we assumed that κ and c have no temperature dependence. In the following results, we use values $\kappa = \min[\kappa(T = 150\text{ K}), \kappa(T = 300\text{ K})]$ and $c = \max[c(T = 150\text{ K}), c(T = 300\text{ K})]$ to get the upper bound on cooling time required. The plots below assume $T_{\text{start}} = 300$ K and $T_{\text{cold}} = 120$ K. We also show plots for the cases where the slab is made of aluminum and copper.

Time constant We can define the time constant as the following:

$$\tau := \frac{\rho c L^2}{\pi^2 \kappa}, \tag{10.6}$$

which is the decay time constant for the $n = 1$ mode. Since the higher harmonics decay at rates $\sim e^{n^2}$ faster than the fundamental, this time constant gives us a good idea of how fast the system cools down. Figure 10.8 shows the temperature profile of the cold slab at various times.

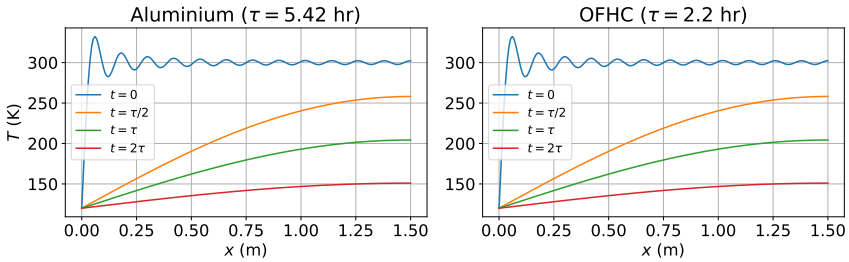

Figure 10.8: **Temperature profile along cold slab at various times.** Ringing in the $t = 0$ plot is attributed to taking a finite sum of Equation 10.5 to $n = 50$ for the numerical plot.

Not surprisingly, copper (OFHC) gives a shorter cooldown time constant than aluminum for the same dimensions of the slab. Nevertheless, the time constant of about 5 hours for the case of aluminum is already a very friendly time scale to work with.

Temperature drop Figure 10.9 shows the temperature drop at various parts of the cold slab with time. We see that the whole setup is cooled down to 150 K in about 10 hours. This means that one can turn

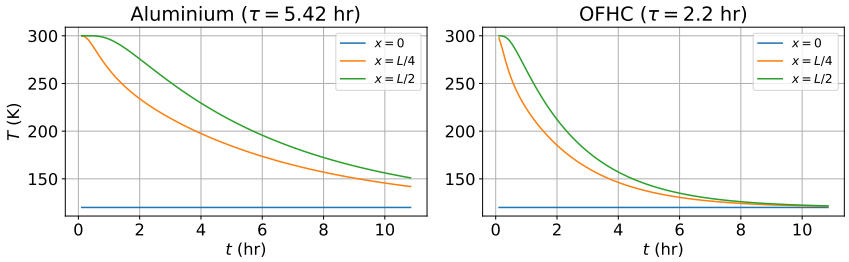

Figure 10.9: **Plots of temperature drop at various positions with time.**

the cryocooler on before they leave for the day, and come back the next morning to a nice and cool setup to begin experiments with.

Cooling power Figure 10.10 shows the cooling power required for the above cooling process. Note that the powers plotted are those required to cool one half of the slab. This requires us to have two cryocoolers with cooling power at 80 W at 150 K (or actually 120 K at the Cold Head) placed on both sides of the slab.

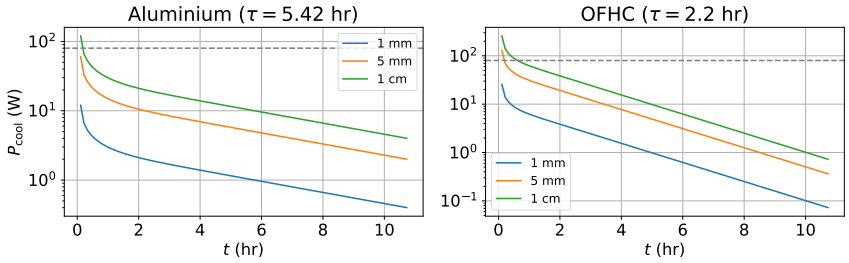

Figure 10.10: **Plot of cooling power required versus time.** The cooling power here only accounts for the thermal mass of the slab, and neglects that of the Bucket Brigade. Width of slab is assumed to be 10 cm. Grey dashed line shows the 80 W mark. Legend shows the thickness of the slab. We need more cooling power to cool off the extra thermal mass of the cooling slab. Note that the thermal mass of the nipple (and the Bucket Brigade) is assumed to be small compared to the slab in this (overly) simplified model.

One is actually enough if we are willing to wait a little while more. There are a few places to get cryocoolers with the cooling power that we need: RIX, Cryomech, and Sunpower.

In this section we simplified the geometry of the cylindrical Cold Jacket to a planar slab. We also ignored the thermal mass of the nipple and the Bucket Brigade. One can easily show with COMSOL simulations that making the geometry and thermal masses more faithful only increases the time constants by order unity. Equation 10.6 still captures the characteristic time scale involved. The time scales are reasonable time scales that one can be comfortable working with. The cooling power at steady state is also manageable by cryocoolers that we can buy off the shelf. We believe we have spreading of the cold under control. In the next section, we shall look at what happens to the system during the cool down.

10.2.3 Thermal contraction

We learn in kindergarten that objects contract when cooled. Even though we are not ambitious in our cryogenic temperatures, thermal contraction will still be a noticeable effect in our setup. This effect comes in twice: (i) change in the length of the setup at steady state, and (ii) differential changes in length for different parts of the setup during the cooldown. We shall look at the former first.

Thermal contraction at steady state. Using temperature-dependent thermal expansion coefficients from NIST, the absolute changes in length (of the 300-cm apparatus) during the temperature change from 300 K to 150 K and 300 K to 120 K were calculated for 304 SS and Ti (Table 10.1). For a setup made

	150 K	120 K
ΔL 304 SS (cm)	-0.648	-0.756
ΔL Titanium (cm)	-0.348	-0.393

Table 10.1: **Thermal contraction of a 3 m long setup.** We calculate for stainless steel because it is very strong (and cheap), so having the Bucket Brigade made from stainless steel will be strong. Titanium is also strong. Furthermore, it is non-magnetic. However, it is much more expensive than steel. Our current setup uses 304 SS and the "non-magnetic" 316LN SS, but we have plans to upgrade to titanium in the future to suppress spatial magnetic field noise coming from the material.

fully from stainless steel, we expect the whole setup to contract by slightly more than 5 mm. This implies a few things:

(1) We will need to install expansion tubes on at least one side of the nipple so that the thermal contraction does not result in strain on the structural support of our setup.

(2) If the Bucket Brigade is one continuous structure, it will not end up aligned both with the Octagon for state preparation and the other Octagon for state detection after cooling down. We will either have to (i) break up the Bucket Brigade into smaller sections so that the thermal contraction does not manifest all on one end, or (ii) be comfortable with realigning optics and reoptimizing the ion ejection protocol every time we warm up or cool down the Bucket Brigade setup. We may have field homogeneity concerns if we do the former. We have to ensure that the graduate students are well fed if we want to go with the latter.

Differential thermal contraction during cool down. In the above, we discussed the problem at steady states, i.e. comparing the setup when it is warm and when it is cool. There could also be problems during the cool down. Different parts of the Bucket Brigade setup will not be at the same temperature during the cool down. The parts closer (thermally) to the cryocooler will be colder than the rest, and so they will thermally contract first. The Bucket Brigade sits in the nipple, and is supported by the structural support which makes points of contact with the nipple. When the cool down happens, the Bucket Brigade will cool down slower than the nipple, and the nipple will contract first. This will result in strain between the nipple and the contact points of the Bucket Brigade. This strain could deform the Bucket Brigade, albeit so slightly, and change the positioning of our electrodes. Given that we care about field inhomogeneity down

to a level of 0.01%, and that position tolerances of the Rods are only on the order of 100 μm, we will need to ensure that the structural support is strong enough to withstand strains from the differential thermal contraction.

Caterpillar action from differential thermal contraction during cool down. Furthermore, even if the structural support is strong enough to ensure that our electrodes do not move, there could be another problem. If the differential thermal contraction between the nipple and the Bucket Brigade is large enough to cause the contact points to slip and stick at a new place, the Bucket Brigade may end up moving along the nipple like a caterpillar after a few warm-up–cool-down cycles unless we secure the Bucket Brigade. Securing one structure is still relatively easy, but if we wish to break up the Bucket Brigade to ensure that the thermal contraction does not manifest all on one end, then we will have to secure all those structures to the nipple. It is not immediately obvious at the point of this writing how we want to do this inside the nipple.

We are testing the cryogenics out in the b.B.B., and we are learning as we go along. We are not seeing any major issues with this 1/3-scale prototype yet, but we are cautious in our design of the full scale Bucket Brigade. Let us now look at the state of cryogenics in the b.B.B..

10.3 Current status in the baby Bucket Brigade

The short version of the current status of the cryogenic system in the b.B.B. is that it works. We have already seen in Figure 4.13 all the way back in Chapter 4 showing the effect of cryogenics on increasing our T_1 time. We shall go into a little bit more detail in the next few sections, partly to serve as documentation.[8]

We will first look at characterization of the properties of the household insulation foam (Section 10.3.1). We then look at the specifications of our cryocooler (Section 10.3.2). Finally, we shall discuss the effective temperature that the ions see at the Science region (Section 10.3.3).

[8] Or, looking ahead into Section 10.4, an obituary of using household insulation foam for insulation in the Bucket Brigade setup, documenting all the fun times we had with foam. Spoiler alert: we have plans to move away from household insulation foam.

10.3.1 Household insulation foam

10.3.1.1 Foam versus aerogel

Before we dive into the fun we had with foam proper, we should first address the debate the group had early on in the cryogenics design. Having given up on vacuum jackets and MLIs, we were still presented with two choices for thermal insulation: household insulation foam and aerogel. There were many uncertainties back then, and I will list some of them here:

Foam.
- How does foam perform at 150 K? Will it crumble at low temperatures?
- Can we spray it evenly enough that there are no air pockets?
- Are the foam kits from Home Depot going to work? If not, where should we get them?
- How does foam react to condensation and frost?
- Is it safe for us to spray it ourselves?

Aerogel.
- The datasheet (for Cryogel Z) includes 150 K, but how much can we trust it, especially given our inexperienced skills in wrapping it?
- How hard is it to wrap it? How do we wrap it?
- Aerogel feels powdery to the touch between the layers. This is bad for optics. How bad will it be for optics in the long run?
- How does aerogel react to condensation and frost?
- How bad will it be for us when we cut and wrap it? Is it going to be like asbestos?

Just looking at the datasheets, we see that aerogel boasts a thermal conductivity of only 14 mW/(m K) at 150 K. Aerogel is also the tried-and-tested insulating material used in many cryogenic applications. Aerogel can also withstand baking temperatures of up to 125 °C, whereas foam starts to degrade at around 70 °C. A lot can be said for using aerogel. However, we know for a fact that aerogel is bad for optics. We will have to wrap the nipple up with aerogel with all the surrounding optics covered. It can be a pain if we need to remove or replace the aerogel when all the optics are in place. Once again, advised by our in-house

Dr. Eric Cornell, "where's the fun if we just use standard techniques," he asked, so we decided to give foam a try.

10.3.1.2 Recipe for working with household insulation foam

Now that we are committed to foam, we ordered some spray foam kits from Home Depot and started spraying. We made a container with a 1/30-scale Bucket Brigade (just a half-cylinder) and filled it with spray foam. Figure 10.11 shows the disaster from our first try.

(a) We thought the foam has cured.

(b) It had not.

Figure 10.11: **First attempt at spraying foam into a container.** A total disaster. We sprayed the foam in a fume hood, and let it cure for about an hour. The top layer has cured completely, but this forms a seal preventing the lower layers from curing. The mess was absolutely disgusting. It was very hard to clean. The uncured part was sticky and left stains. The stains either had to be scrapped off through mechanical means, or dissolved with acetone (recommended by the internet) which left even stickier stains if not done thoroughly.

We got smarter with each attempt, and eventually we came up with a recipe:

- Keep the spray foam at room temperature before using it. If not, it will not cure well.
- Spray foam at a distance of about half a meter away at least.
- With a sweeping action, spray a thin layer of foam each time. Allow the newly sprayed foam to expand and fill gaps naturally. When the foam has stopped expanding, apply the next layer if desired.

- Aim for the corners first when spraying, otherwise air pockets will form around the corners.
- When making the mold, line the surfaces with aluminum foil. The foam will stick to the foil, but one can easily slide the foam that is set out of the mold by detaching the aluminum foil from the mold.
- After the foam has cured, surfaces that are exposed to air or the aluminum foil will have a nice finish. However, if one cuts the foam (to shape it into something more convenient), the cut surface will turn powdery. This is bad for optics. Paint these surfaces with acrylic paint to stop the powder from coming off the surfaces.
- Outgassing from the spray foam stinks. Do it in a ventilated area.

A photo montage of the whole process is shown in Figure 10.12. This whole process happened at a random garage that was available to us.[9]

Before we end this section, we have some closing remarks on foam. The manual says that the thermal conductivity of the foam will degrade after about 90 days. We have not seen significant degradation of insulating properties. The current set of foam on the b.B.B. setup is still those that we made on 25 May 2021 (from the photo montage in Figure 10.12). We tried several brands of foam, and we find that HandiFoam has a better after-feel: less powdery.

Now that we know how to make foam blocks, it is time to characterize the performance of the foam.

10.3.1.3 Characterizing the thermal conductivity

The thermal conductivity of household insulation foam is typically reported as an R-value.[10] The R-value is related to the thermal conductivity through:

$$\kappa = \Delta x/\text{R-value},$$

[9] Prior to this, the author has never seen a garage before. Having grown up in Singapore reading books written by American authors who write about elves, forests, and garages, the author is happy to have finally seen at least two out of the three during his Ph.D..

[10] There is a closely related quantity called the RSI-value, and it is the SI version of the R-value, but people in the industry call the RSI-value the R-value nonetheless. The units have to be determined from context. This is the thermal insulation version of kilocalories, Calories, and calories. The R-value (inch-Pound system) is expressed in units of $^\circ\text{F} \cdot \text{ft}^2 \cdot \text{h/BTU}$. The RSI-value is expressed in units of $\text{K} \cdot \text{m}^2/\text{W}$. The conversion factor between the two is given by: $\text{RSI-value}[\text{K} \cdot \text{m}^2/\text{W}] \approx 0.176 \times \text{R-value}[^\circ\text{F} \cdot \text{ft}^2 \cdot \text{h/BTU}]$. You are welcome.

Figure 10.12: **Photo montage of the process of making the foam blocks.** Top row: (i) mold for one half of the foam, lined with aluminum sheets; (ii) applied first layer of foam; (iii) end product after spraying. Bottom row: (i) painting the surfaces of the foam blocks with acrylic paint; (ii) cutting the top surface of the foam block, because it is easier to clamp the two halves together with flat surfaces; (iii) end products. Shown in this picture are also fellow graduate students Sun Yool Park and Noah Schlossberger; one can also make out undergraduate Gustavo Santaella cleaning up in the garage; the extra pair of hands holding on to the foam being cut belongs to JILA instrument maker James Uhrich. James helped us make the big saw to cut the foam, also shown in that picture.

where Δx is the thickness of the sample used to determine the R-value. One needs to be careful to ensure consistency of units (see Footnote 10 below).

Thermal conductivity of foam could be very different at 150 K than at room temperature or normal winter temperatures. We constructed a simple setup that is a 1/20-scale version of the Bucket Brigade to test the insulation properties of the foam. Figure 10.13 shows some pictures of the setup.

The idea behind the experiment is simple. We want to measure the thermal conductivity of the foam. To do this, we need to know (i) the temperature on the inner and outer surfaces of the foam, and (ii) the heat flux flowing through it. We can measure the temperatures with thermometers. We can also deduce the heat flux through the foam with conservation of energy flow:

(1) Referring to the top right diagram in Figure 10.13, we see that heat is flowing from the warm outer

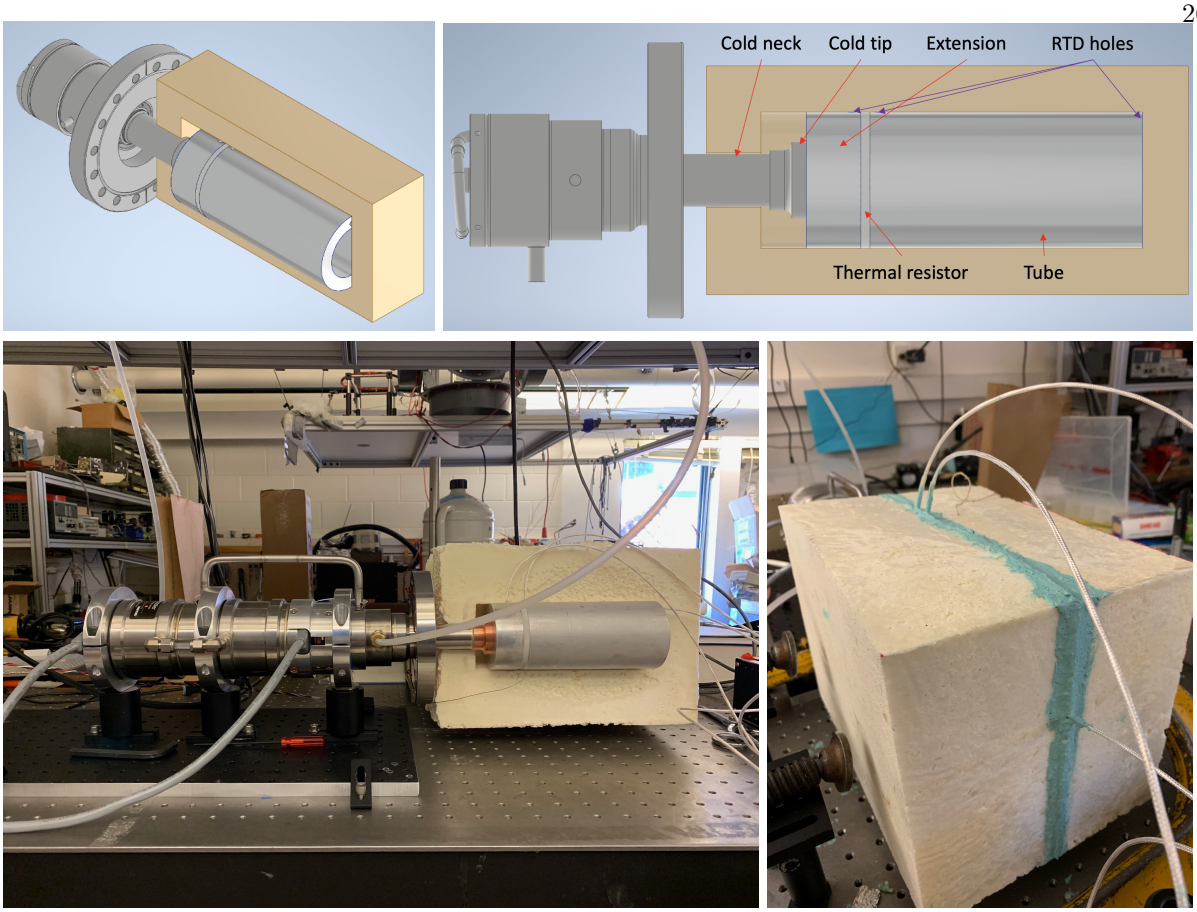

Figure 10.13: **Schematic diagrams and pictures of the setup used to test thermal conductivity of foam.** Upper left: setup viewed from an angle. Upper right: parts of the setup. Lower left: the setup with half of the foam block removed. Lower right: setup with viewing angle of upper left. The teal colored goop is the sealant used to seal the gap between the two halves of the foam blocks. The *tube* is hollowed out in the center to allow access for screws that secure the *extension*, thermal resistor, and the *tube* to the Cold Head. Several holes for resistance temperature devices (RTDs) can also be seen in the left figure. The *extension* and *tube* are made from aluminum, while the thermal resistor is made from Teflon.

surfaces of the foam to the cold inner surfaces of the foam (in contact with the *tube*).

(2) All the heat flux going through the foam between the thermal resistor and the far right end of the foam has to go into the *tube*.

(3) This heat flux has to go through the thermal resistor to get to the heat sink on the Cold Head. This results in a temperature difference across the thermal resistor.

(4) By using a thermal resistor with a well characterized thermal conductivity, and measuring the temperature difference across the thermal resistor, we can deduce the heat flux through the foam.

As a result, there are several key aspects to this setup: (i) foam blocks, (ii) thermal resistor, (iii) resistance temperature devices (RTDs), (iv) *extension*,(v) *tube*, (vi) power resistors, and (vii) sealant. A table of dimensions and important parameters of the above are summarized in Table 10.2. Before we dive

Part	**Parameters**
Foam	Product: Handi-Foam model #P10625 Cross sectional dimensions: 21 cm by 21 cm Bottom thickness: 2″ thickness on far end from Cold Head Top thickness: 3 cm thickness on for cold neck side Inner diameter (tube part): 76 mm Inner diameter (cold neck part): 30 mm
Thermal resistor	Material: Teflon (McMaster item #9266K82) Thickness: 1.62 mm (measured) Diameter: 76 mm Thermal conductivity at 150 K: 26 mW/(m K)
RTD	Model: PT100, DigiKey #1528-2090-ND
Thermal grease	Model: Apiezon N Cryogenic Heat-Transfer Greases
Extension	Material: aluminum Length: 30 mm Diameter: 76 mm
Tube	Material: aluminum Length: 15 cm Outer diameter: 76 mm Inner diameter: 51 mm Base thickness: 1 cm

Table 10.2: **Some important parameters of setup used.**

into the results, we shall cover a little bit more detail of the setup. We have already seen our recipe for making foam blocks in Section 10.3.1.2. We shall go through the remainder on the list in the following paragraphs.

Thermal resistor Using a thermal resistor with known thermal conductivity at 150 K, we can deduce the amount of heat flowing through it by measuring the temperature difference across the thermal resistor. We then attribute the heat flowing through the thermal resistor at steady state with the conduction heat flux through the foam into the *tube*.

We use Teflon for the thermal resistor because it has a well known thermal conductivity[11] at 150 K of 260 mW/(m K), which allows for a measurable temperature drop (∼10 K) across a piece of reasonable

[11] https://trc.nist.gov/cryogenics/materials/Teflon/Teflon_rev.htm

thickness (∼2 mm) for an expected conduction heat flux through the foam at steady state (∼10 W) simulated with COMSOL.

Resistance temperature devices (RTDs) The RTDs used in this experiment are PT100 (DigiKey #1528-2090-ND). These RTDs have a temperature dependent resistance of the form:

$$R(T) = R_0 \left[1 + A \cdot T + B \cdot T^2 + C \cdot T^3(T - 100)\right],$$

where T is temperature in Celsius, $A = 3.9083 \times 10^{-3}$, $B = -5.775 \times 10^{-7}$ and $C = -4.138 \times 10^{-12}$ if $T < 0$ and $C = 0$ otherwise, and $R_0 = 100\ \Omega$ for the PT100.

We send in about 2 mA of current into each RTD[12] and read out the potential difference across each of them to deduce the temperature of the environment that the RTDs are exposed to. The RTDs are slotted into machined holes on the *extention* and the *tube* of very similar dimensions to the RTDs, and thermal grease (Apiezon N Cryogenic Heat-Transfer Grease) is applied to the RTDs to ensure good thermal contact with the surroundings.

Extension The *extension* is a cylindrical block of aluminum in direct contact with the Cold Head. Its purposes are (i) to spread the temperature of the Cold Head to a bigger cross-sectional surface area, and (ii) to act as a holder for an RTD to measure the temperature on one side of the thermal resistor.

Tube The *tube* is a cylindrical block of aluminum that conducts the conduction heat flux from the foam to the Cold Head. It has two holes for RTDs on both of its ends. The RTD on the side of the thermal resistor is used to measure the temperature difference across the thermal resistor, while the RTD on the far side is there to ensure that things are making sense. We bored the *tube* out so that we can screw the whole assembly to the Cold Head from the far end.

Power resistors It turns out that the cryocooler that we have has a minimum cooling power[13] . The working range of the cryocooler is shown in Figure 10.14.

At steady state, our COMSOL simulation suggests a heat load of about 10 W at 150 K. Hence, we need to introduce active heating elements into the setup to bring the total heat load into the grey region (about 35 W in total at 150 K).

[12] Each RTD is in series with a 2 kΩ resistor, and a total potential of 5 V is applied across the setup.

[13] The compressors use air bearing sliders to reduce friction between moving parts, so there is a minimum power that has to be sent into the compressors to maintain the air flow, which results in a minimum cooling power.

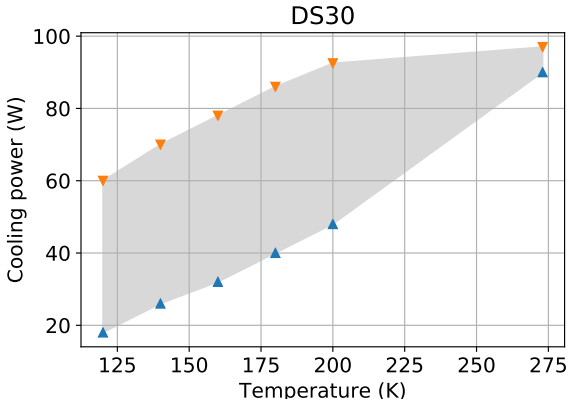

Figure 10.14: **Working range for the Ametek CryoTel DS30 cryocooler.** The blue points are the quoted minimum cooling power, while the orange points are the maximum cooling power that the cryocooler can deliver. The grey region is a visual aid to the working region of the cryocooler.

The power resistors we use are Ohmite HS10 100R, which are 100 Ω resistors rated for 10 W each. Three such power resistors are mounted on the Cold Head side of the *extension* as shown in Figure 10.15. The power resistors are connected in series, and hooked up to a Variac. The nominal voltage applied on them at steady state is $V_{\mathrm{rms}} = 72.5$ V, corresponding to about 17.5 W of additional heat load into the system.

Sealant The sealant's only function is to seal the small gaps between the two halves of the foam blocks to prevent convection. We tried two types of sealant: (i) Molykote Valve Lubricant and Sealant, and (ii) Gasoila Soft-Set Thread Sealant with PTFE.

We noticed that the Gasoila sealant freezes at low temperatures, and it also dries up when exposed to air in Boulder and turns into a strong glue that holds the two halves together. It is also quite messy to deal with, so our preferred choice is the Molykote sealant for areas close to delicate parts.

Discussion and Results The results of an instance of an experimental run is shown in Figure 10.16. We performed the experiment with two different runs using two different sets of foam blocks, and also an additional run to estimate additional heat load from the RTD cables[14] . The final result is an effective conductivity of the foam at about 60 mW/(m K), which is not far away from that of closed-cell foam at room temperature as quoted in literature[15] .

[14] This run involves having additional RTDs attached to the tube, and having their cables come out between the two halves of the foam blocks like the RTDs that are used to measure the temperatures. Each cable brings in an additional 1 W.

[15] COMSOL has data on closed-cell foam between 293 K and 373 K. The conductivity quoted at 293 K is 49 mW/(m K).

Figure 10.15: **Power resistors mounted onto the *extension*.**

Note that the value of the measured conductivity is an effective thermal conductivity, because the calculations assume that the foam blocks have a isotropic thermal conductivity throughout. However, there is a huge temperature gradient along the thickness of the foam, and we expect the thermal conductivity to change along the thickness of the foam because of the temperature gradient. So this effective thermal conductivity is a weighted average of a case with a specific boundary condition. We put the words above into an equation: approximating the foam blocks as cylinders instead of cuboids, we have for the conduction power through the foam:

$$\begin{aligned} P = \kappa(T) A(r) \frac{\mathrm{d}T}{\mathrm{d}r} \quad \Longrightarrow \quad P \int_{R_1}^{R_2} \frac{1}{2\pi L r}\,\mathrm{d}r &= \int_{T_1}^{T_2} \kappa(T)\,\mathrm{d}T \\ \frac{P}{2\pi L} \log\frac{R_2}{R_1} &= \bar{\kappa}_{T_1,T_2}(T_2 - T_1) \\ P &= 2\pi L \cdot \frac{\bar{\kappa}_{T_1,T_2}(T_2 - T_1)}{\log(R_2/R_1)}, \end{aligned}$$

where L is the length of the setup, $\{R_1, T_1\}$ are the inner radius of the foam and the temperature there, $\{R_2, T_2\}$ are the outer radius and the temperature there, and $\bar{\kappa}_{T_1,T_2}$ is the effective thermal conductivity. We see that as long as T_1 and T_2 do not change, the effective thermal conductivity will remain unchanged even if there are changes to the radii.

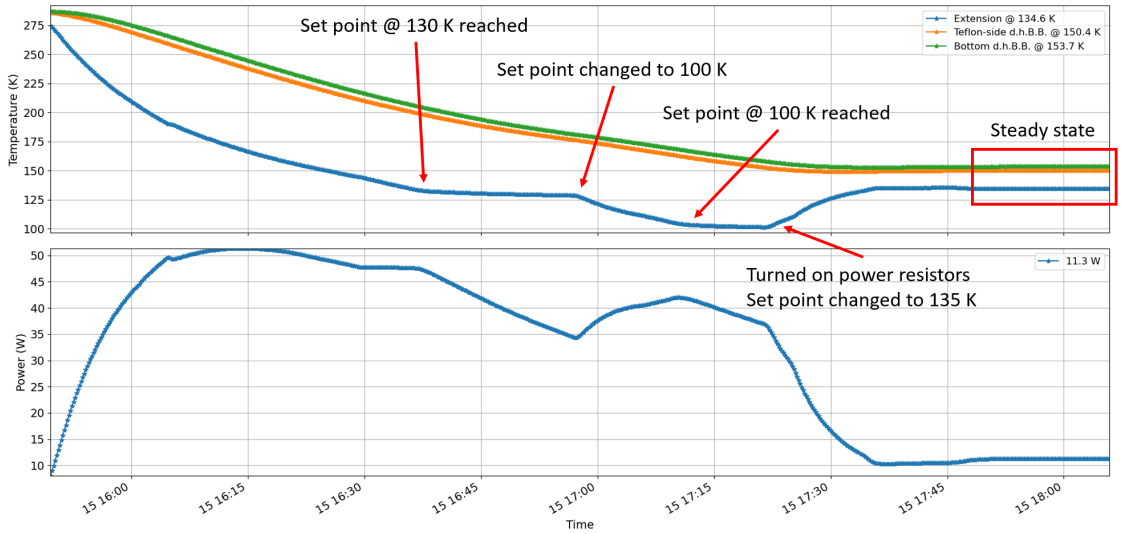

Figure 10.16: **Temperature readings of RTDs in one experimental run.** Points of interest are noted in the figure. The lower plot of power vs time is obtained from the difference between the values of the blue and orange lines in the upper plot, i.e., the temperature difference across the thermal resistor.

10.3.1.4 In the baby Bucket Brigade

We now understand the thermal properties of the foam. It is time to scale up the experiment and test this on the b.B.B.. Figure 10.17 shows the results of using foam as thermal insulation in the b.B.B..

The test shows that the design is a great success. The cold can be maintained by the foam, the cool down time is acceptable, and the cryocooler has enough cooling power to sustain the cold. Subsequently with the full setup, including the b.B.B. trap (and ThF^+ ions), we demonstrated no problem maintaining 170 K at where the ions sit with a Cold Head temperature of 150 K. The b.B.B. trap also stomped on the "smoothing out" of the hot and cold sides of the Cold Tube seen in part (d) of Figure 10.17 by restricting the reach of blackbody radiation from the hotter surfaces. This works using the same principle behind how MLIs work.

10.3.2 Cryocooler

We now know how to make foam blocks. We also know its thermal insulation properties. It is time to move on to the next big thing in our cryogenic system: the cryocooler. There are two main things to discuss here: (i) cooling power of the cryocooler, and (ii) magnetic fields from the cryocooler.

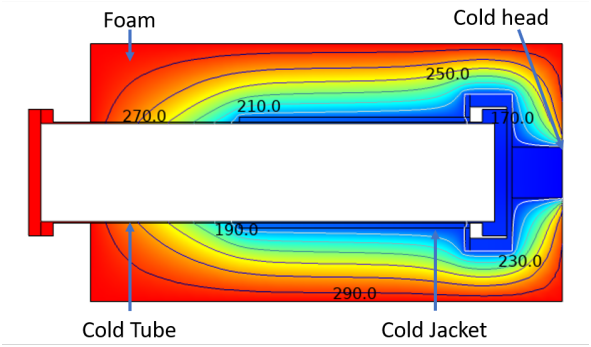

(a) Simulation of the steady state temperature profile. Numbers shown are temperature contour lines in kelvins.

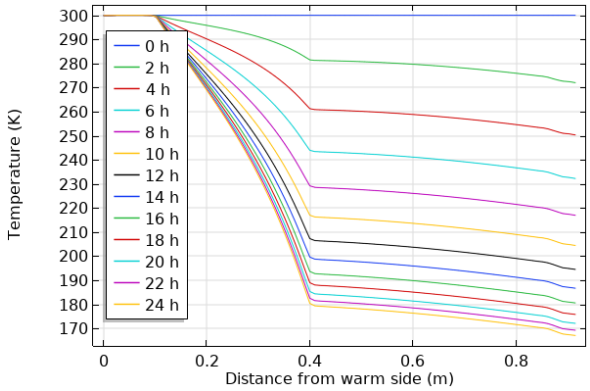

(b) Time evolution of the simulated temperature profile along the inner surface of the Cold Tube.

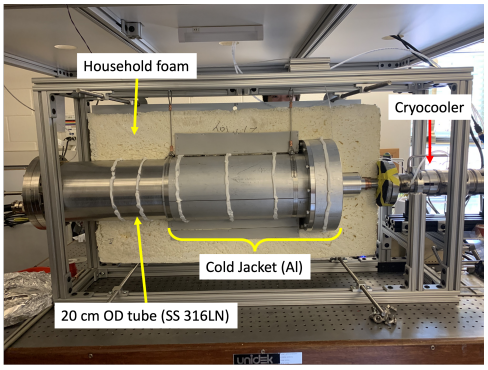

(c) Test setup.

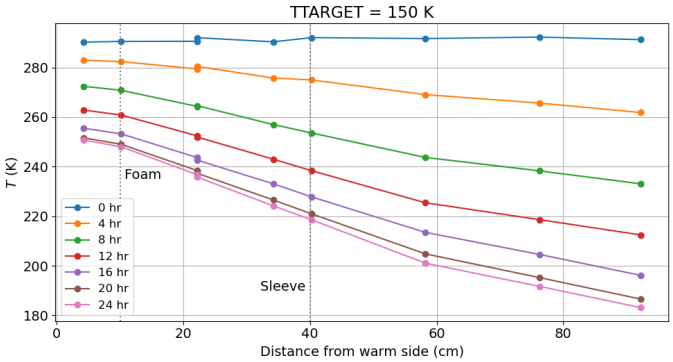

(d) Measured temperature profile with time.

Figure 10.17: **Testing the cryogenics out in the b.B.B. setup.** In all the simulations and experiment, we did not include the effect of the b.B.B. trap, i.e. the Cold Tube is empty inside (except for the thermometers).

(a) The Cold Head is set to 120 K, while the exterior surfaces of the foam and the exposed parts of the Cold Tube are set to 300 K. The Cold Jacket starts at the 40 cm mark.

(b) The Cold Head is set to 150 K for this simulation. The Cold Jacket (40 cm mark) falls below 200 K in about 14 hours. Bounds are not set on the cooling power in the simulation. Thermal radiation within the Cold Tube is not included in the simulation.

(c) One half of the foam block is removed to show the insides. The white goop is the Molykote sealant used to break convective flow along the axial direction of the Cold Tube between the Cold Tube and the foam. One can also see the Cold Jacket for the b.B.B. here. The Cold Jacket was machined by the JILA instrument makers.

(d) We placed RTDs along the bottom of the Cold Tube. The Cold Tube was pumped down to about 1 mTorr with a scroll pump. The time constant is longer than those in (b), but it is still within an acceptable range. The temperature profiles have smoother kinks than in (b) probably because (i) the temperature on the surfaces are "smoothed out" by blackbody radiation within the inner surface, and (ii) there is imperfect thermal contact between the Cold Jacket and the Cold Tube.

10.3.2.1 Cooling power

We had a sneak peak at the cooling power of our cryocooler in Figure 10.14. It has a minimum cooling power to run smoothly. The consequence is that if the heat load is smaller than the minimum cooling power, the cryocooler will cool the sample to temperatures below the set point. This is only a problem if the setup has a small heat load. We expect a heat load of about 80 W on the Bucket Brigade, so this is not a problem.

From Figure 10.14, we also see that the total cooling power at 150 K is also slightly lower than 80 W. If we find ourselves liking the cryocooler, we could buy another one for a total of two in the Bucket Brigade setup.

10.3.2.2 Magnetic fields

The cryocooler we have is a Stirling refrigerator. It has two counter-moving magnetic pistons that are moved by the 60 Hz AC current from the wall. The counter-movement reduces vibration in the setup by making making use of the symmetry to keep the center of mass stationary.

The magnetic fields from the pistons decay with distance away from the cryocooler. Associated with the decaying field is a magnetic field with gradients. We saw in Section 8.2 that having an axial magnetic field gradient gives rise to a non-zero f_0. We also saw in Section 6.3 that any spatial inhomogeneity of the axial magnetic field gradient within the spatial extent of the ion cloud gives rise to decoherence. We can mitigate these effects by parking our ions far away from the cryocooler. However, the cooling power of the cryocooler decreases with distance because of the additional heat load that comes with the distance. We want to park our ions far enough that the fields are homogeneous enough, but close enough that the ions are still bathed in a 150 K thermal environment. The question now is where should we park our ions?

We measure the magnetic fields of the cryocooler with a setup shown in Figure 10.18. The cryocooler sits on a movable platform some distance away from an array of magnetometers. The Cold Head points towards the magnetometer array. The magnetometer array consists of seven magnetometers, one on each end of the (3D) cross, and one at the center. The magnetometers are Adafruit LSM303 three-axes magnetometers, connected to an Arduino Uno with I2C communication. The arms of the cross are 9 cm in length, and the axes are defined to be $\{x, y, z\}$ in the directions { up, towards the measuring tape, the direction that the

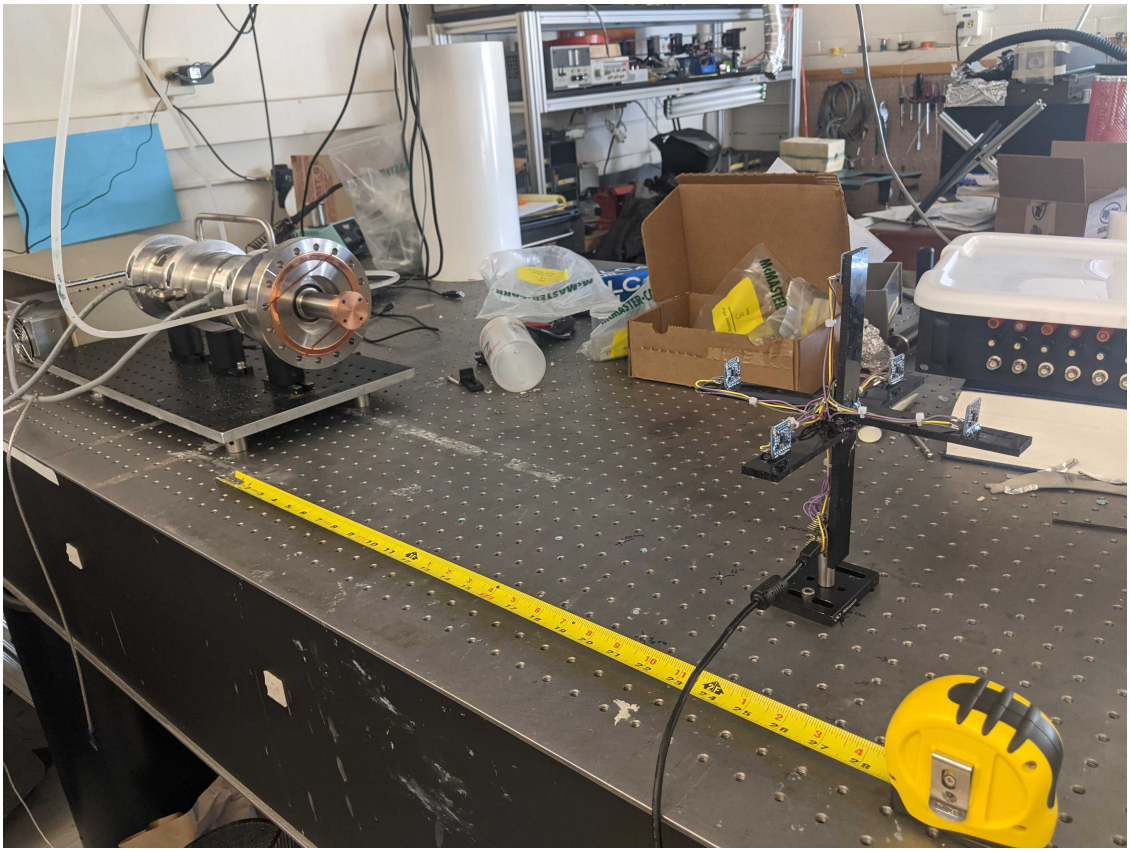

Figure 10.18: **Setup used to measure the magnetic fields from the cryocooler.** An array of magnetometers arranged in the shape of a cross is shown in the bottom right of the picture.

Cold Head is facing } in a right-handed convention, respectively.

We measure the magnetic field strengths at varying distances between the center of the magnetometer cross and the Cold Head. We first do this with the cryocooler turned off, i.e. no moving parts in the cryocooler.

Axial direction We assume that the local magnetic field can be expressed as an expansion up to first order derivatives:

$$\mathbf{B}(x,y,z) = \mathbf{B}_0 + B_{\text{axgrad}} \begin{pmatrix} x \\ y \\ -2z \end{pmatrix} + B_{\text{transgrad}} \begin{pmatrix} x \\ -y \\ 0 \end{pmatrix} + B_1 \begin{pmatrix} y \\ x \\ 0 \end{pmatrix} + B_2 \begin{pmatrix} z \\ 0 \\ x \end{pmatrix} + B_3 \begin{pmatrix} 0 \\ z \\ y \end{pmatrix}. \tag{10.7}$$

Using the parameters that we got from performing a least squares fit of Equation 10.7 onto the data points acquired, we obtain the variation of B_{axgrad} with axial distance from the Cold Head, as shown in Figure 10.19. The fit of the form $f(d) = ae^{-bd} + c$, where a, b, and c are fit parameters, seems to work very well,

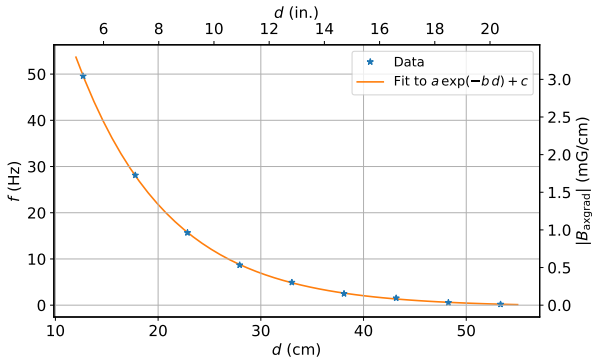

Figure 10.19: **Plot of B_{axgrad} vs d, the distance between the Cold Head and the center of the magnetometer cross.** The fit of the form $ae^{-bd} + c$, where a, b, and c are fit parameters, seems to work very well. A B_{axgrad} of 3.07 mG/cm corresponds to an f_0 of 50 Hz for ThF^+ at an $f_{\text{rot}} = 150$ kHz and $\mathcal{E}_{\text{rot}} = 60$ V/cm.

with d in units of cm, and $a = 206(2)$, $b = 0.1116(8)$, $c = -0.33(8)$. The fit is done after converting the B_{axgrad} values to the Ramsey frequency as seen by ThF^+ at an $f_{\text{rot}} = 150$ kHz and $\mathcal{E}_{\text{rot}} = 60$ V/cm. Taylor expanding $f(d) = a\,\exp(-b\,d) + c$ about $d = d_0$, we get:

$$f(d) = f(d_0) - b\,f(d_0)\cdot(d - d_0) + \frac{1}{2}b^2\,f(d_0)\cdot(d - d_0)^2 + \mathcal{O}[(d - d_0)^3].$$

The constant term is the base frequency as seen by all ions. The linear term is averaged out by ions in their secular motion in the trap. Evidently, the third term is the first non-trivial term that is responsible for decoherence within the ion cloud. We see that it scales with the distance between the Cold Head and the center of the magnetometer cross (d_0) as a decreasing exponential, and it scales with the size of the ion cloud ($d - d_0$) with the second power. For an ion cloud of 1 cm radius at 40 cm away from the Cold Head, this term corresponds to $\Delta f = 0.015$ Hz, which is 0.03% of $f = 50$ Hz, not that far away from our desired 0.01%.

Radial direction In the radial direction, the variations are much smaller than the radial direction at $d_0 = 40$ cm. We did not measure anything significant down to the precision of our magnetometers within the spatial extent of ion cloud.

Cryocooler turned on Turning on the cryocooler and repeating the experiment gives similar results down to the precision of our magnetometers.

Summary To suppress decoherence effects coming from gradients of axial magnetic field gradients from the cryocooler, we just need to park our ions at least 40 cm away from the Cold Head.

10.3.3 Effective temperature and lifetime

Cryogenics is only applied to part of the b.B.B. setup. This means that the ions will see a non-zero solid angle of 300 K blackbody radiation photons coming at them. However, as we shall see later on, this solid angle decreases very quickly as the ions translate into the cold region. The effective rate is then the rate given by Equation 4.1 weighted by the solid angle of the temperature involved:

$$\overline{\Gamma}_{\text{b.B.B.}}(f, \mu_{12}) = \frac{|\mu_{v,v+1}|^2}{6\epsilon_0 \hbar^2} \int \rho\Big(f, T(\Omega)\Big)\, \mathrm{d}\Omega,$$

where $\mu_{v,v+1}$ is given by Equation 4.3.

We estimate the effective lifetime for the full 3 m long Bucket Brigade, with both ends open to 300 K, and Cold Tube cooled to 150 K.[16] The results shown in Figure 10.20 are very reassuring. We do not have to be worried about the ends exposed to 300 K.

10.4 Further discussion

10.4.1 Vacuum

One can see from our design (see, for instance, Figures 10.5 and 10.17) that we do not have access ports in the cryogenic part of the Cold Tube to install vacuum pumps. Our cryogenic temperature is cold enough to suppress some outgassing, but it is not cold enough to act as a cryopump, except for water vapor and some organic molecules. Even without the cryopump action on water and organic molecules, the partial pressures are already very low in our vacuum chamber after a bake at around 150 °C for a few days.

There are currently no vacuum pumps inside the Cold Tube in the b.B.B. setup. The pressure reading from our ion gauge at the Six-way Cross is at 1×10^{-9} Torr. The pressure is maintained by a 500 L/s turbomolecular pump and a non-evaporable getter pump at the Six-way Cross (see Figure 7.9). We are currently limited by T_1 losses from ion-ion collisions. We are not seeing signs that we are being limited

[16] The b.B.B. has one end open to 300 K, so the estimate for the blackbody radiation excitation lifetime for the Bucket Brigade will be a lower bound for the b.B.B..

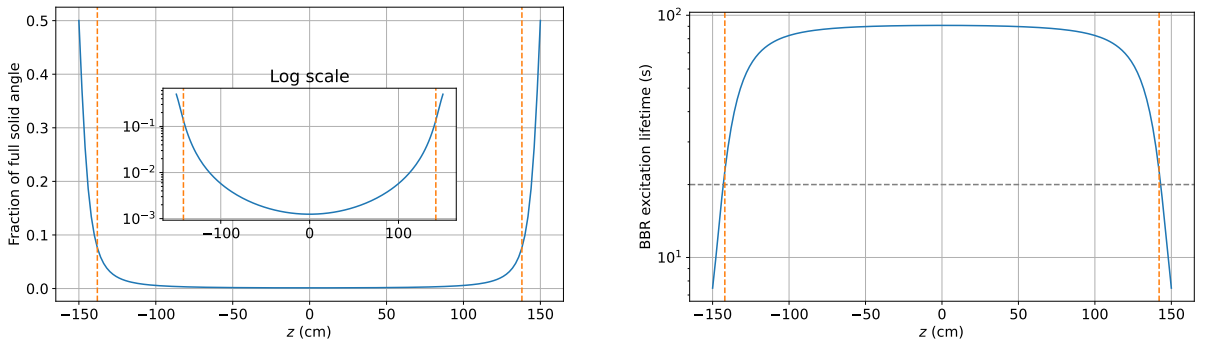

(a) Solid angle of 300 K seen by the ion packet.

(b) Effective blackbody radiation excitation lifetime.

Figure 10.20: **Effective blackbody radiation excitation lifetime in the Bucket Brigade.** We simplified the geometry such the walls of the Bucket Brigade are at 150 K within -150 cm $\leq z \geq 150$ cm and 300 K beyond that. We assume that the radial direction is bound by the inner radii of the Rings at 7.5 cm.

(a) The inset shows the same plot, but in log scale. The yellow dashed lines indicate one bucket in (8 cm). One can see that the solid angle of 300 K drops to below 10% just one bucket into the cold region.

(b) The lifetime is evaluated for the transition $(v = 0) \rightarrow (v = 1)$. The vertical dashed lines indicate one bucket in (8 cm). The horizontal dashed line indicates 20 s. One can see that once we are one bucket into the Bucket Brigade, blackbody radiation excitation limits our T_1 lifetime to only about 20 s.

by ion-neutral collisions, yet. We believe the vacuum in the b.B.B. is good enough for now. If we need to improve the vacuum, we could put some getters inside the Cold Tube at strategically chosen locations to act as passive pumps.

10.4.2 Liquid nitrogen, LN2

Liquid nitrogen (LN2) costs about \$160 per dewar (240 L) at JILA (circa 2020). LN2 has a latent heat of vaporization of about 1.6×10^6 J/L. This means LN2 costs about \$0.40 per watt-day. One would naïvely think that with 80 W of heat load (Section 10.2.1), this would total to only \$32 per day. However, if we bathe the Bucket Brigade setup in LN2, the temperature would be lower (77 K instead of 150 K), and there would be additional heat load. So the correct cost would be around \$50 per day, still cheap compared to graduate students[17] (accounting only for additional heat load from the increased temperature gradient between the cold region at 77 K and warm at 300 K). Furthermore, dewars can be magnetic, so we want to put them far away from the Bucket Brigade, but in doing so the LN2 needs to travel a longer path before getting to the

[17] And we know graduate students are only slight more expensive than fresh air in Boulder.

cold region. Having a longer path means more heat load. Depending on how we do the thermal insulation and LN2 transport, using LN2 on our setup could easily be just as expensive as a graduate student.

Instead of bathing the Bucket Brigade setup in LN2, we could instead use a temperature regulated thermostat with LN2 as the cryogen. This has already been demonstrated in the Ye group downstairs, so we just need to copy the technology over and scale it up. This is highly non-trivial though, but if the magnetic fields from our cryocooler turns out to be a huge source of decoherence, we have to seek alternative sources of cold.

10.4.3 Raining cryogen

An alternative cooling method that is being pursued in the group right now is to bridge the cryocooler and the Bucket Brigade with a cryogen. Much of the cooling power is lost in the long thermal conduction path between the b.B.B. setup and the Cold Head in the current setup. We could place the cryocooler far above the b.B.B. setup, where its magnetic fields are small at the region where ions are. We then use the cryocooler to cool a gaseous cryogen, whereupon it condenses (at the temperature we want) and rains upon the b.B.B. setup. The cryogen then absorbs heat from the b.B.B. setup and evaporates back up to the cryocooler. The condensation point of the cryogen can be controlled by choosing a suitable cryogen and working pressure. This work was started by undergraduate Gustavo Santaella, and is currently being pursued by graduate student Trevor Wright. The source of the cold need not be the cryocooler, it can be a pool of LN2. I am excited as to how this will turn out.

10.4.4 Cold shield

One disadvantage of using foam for thermal insulation is that it is bulky. We learnt from the systematics studies in the Gen. II experiment that magnetic field gradients can be a huge source of systematic errors. Furthermore, our ions are going to be translating inside the Bucket Brigade, so we do not have the option to park them at a spot where the fields are the most homogeneous; we need the fields to be homogeneous and well controlled throughout the Bucket Brigade. This requires some form of magnetic shielding.

Magnetic shielding with μ-metal (or other metals with high permeability) works by concentrating the

field lines into itself. A nicely sealed enclosure made from μ-metal can give a very nice field-free region inside it. However, our Bucket Brigade extends in the axial direction to Octagons and Six-way Crosses, so there is no easy way for us to enclose only the Cold Tube inside the magnetic shielding. Fortunately, if the shield is a long cylinder, the fields inside the cylinder (with distance inside z greater than the diameter of the cylinder d, i.e. $z \gtrsim d$) can still be suppressed.

The above would work if we can put magnetic shielding right outside the Cold Tube. Leaving the cryogenic behaviors of the shield aside, we see that the bulky foam is in the way of the shield. The shield will have to be big to enclose the foam, but it would also lose its effectiveness in shielding external magnetic fields. The solution is to (i) make the whole cryogenic setup smaller by moving away from foam, or (ii) come up with a design where the magnetic shield is sandwiched between the Cold Tube and foam blocks, or even within an inner and outer layer of foam.

Whatever we end up doing in the full Bucket Brigade setup will likely look quite different from what we have now. Much of what I have described in this chapter will become outdated. I seek solace in that this chapter has been fun, with many pretty looking pictures of the setup.

Chapter 11

Conclusion

This thesis has been a rather extensive investigation on the prospects of performing a multiplexed ion trap eEDM experiment with ThF^+. The group is currently working on suppressing ion-ion collisions hoping to demonstrate 20 s coherence time. These collisions can be reduced by working with a weaker confining trap, but we first need to reduce the spatial gradients of the ponderomotive potentials from the rotating electric fields; the trap was ramped up to retain ions with the deconfining ponderomotive potentials.

The group is also branching out into many exciting new directions, and I shall list some here:

REMPD 1+(532 nm) (Section 3.4.2). I foresee in the near term performing the survey spectroscopy will be a now-or-never experiment. We would like to settle down on the beam directions and polarizations so that we can design the rest of the setup around the constraints imposed upon us by the two-state detection protocol.

New ion detector (Figure 7.13). We believe that the current setup introduces substantial lensing effects because the microchannel plates are recessed from the flange into the assembly. We could upgrade to a better designed ion detector system after we settle on the REMPD protocol. If we found a protocol such that $KE_{dissoc.}$ is much larger than what we have now, we may need to get a larger ion detector to capture all the ions; or we need to introduce ion optics to focus them down (still in the velocity mapping regime).

Using $\Omega = 0^+$ for depletion (Section 4.3.1.1). This would allow for a cleaner depletion from $X\,^3\Delta_1(v = 0, J = 1)$ instead of using Goat.

Multiple buckets. What is the point of having a prototype of a multiplexed ion trap if we are not using it multiplexed? Multiplexing the experiment in the b.B.B. will be slightly different from that in the Bucket Brigade in the sense that operations in the b.B.B. will not be pseudo-continuous, but will still be a single shot experiment. Nevertheless, it will still be meaningful to try preparing multiple buckets of ions and performing a simultaneous Ramsey experiment on all of them, first-in-last-out.

Magnetic shielding (Section 10.4). The JILA eEDM group has not experimented with magnetic shielding yet. We managed to get away with this because of our rotating quantization axis behaves like a lock-in detector, making us very insensitive to uniform ambient fields. Unfortunately, the g-factor in ThF^+ is larger than HfF^+, and the rotation micromotion is also larger because we are using a smaller f_{rot} in Gen. III than II. These two combine to make us about thirty times more sensitive to magnetic field effects than the Gen. II experiment. Aiming to break our Gen. II record, we need magnetic shielding.

New cryogenic scheme (Section 10.4). This will help with the design for magnetic shielding by making the cryogenic setup more compact. It will also move the magnetic cryocooler further away from the ions (or remove it totally).

Catching ions with $\mathcal{E}_{\mathrm{rot}}$. We ramp $\mathcal{E}_{\mathrm{rot}}$ up after we caught our ions in the trap in the b.B.B.. However, the Bucket Brigade requires pseudo-continuous operation. It would be great if we can catch our ions with $\mathcal{E}_{\mathrm{rot}}$ always turned on. We would match the phase of $\mathcal{E}_{\mathrm{rot}}$ with when the molecular beam enters the trap. Since the molecular beam goes into the trap at a speed lower than the rotation micromotion, we will have to accelerate the ions instead of stopping them.

More DAC channels (Section 7.5.2). We now have two sets of DAC channels that allow us to switch the voltages on the Rings between a short pulse (e.g. stop pulse to stop the ions) and a steady state (e.g. usual trapping conditions). Much can be said for having a third channel so that we can, say, switch from stop pulse (to stop the ions) to kick pulse (to eject the ions from the trap) to ground (so that the ions see no fields for the rest of the flight to the ion detector). This will involve upgrades to the current Ring driver.

Testing out various f_0-generating Plans (Chapter 8). As we learn about the decohering mechanisms and possible new systematic effects in the b.B.B. we may want to explore various plans of introducing f_0.

New $\pi/2$ pulse. Depending on the Plan we decide to use in the end, there could be more novel $\pi/2$ pulses that we can use. The current $\pi/2$ pulse involves ramping $\mathcal{E}_{\mathrm{rot}}$, but this would be bad for ions in neighboring buckets in the Bucket Brigade. We could, instead, sweep through $f_0 = 0$ in some kind of an adiabatic rapid passage in some way that would only affect this local bucket and not the neighboring ones.

Travelator. The state preparation and detection stages of the experiment are quite destructive to the quantum states: they move population around the Hilbert space. When we perform these operations to the relevant buckets, we do not want ions in the neighboring buckets to be affected. One way to do this is to keep the buckets undergoing these operations well separated in space from the next bucket. Once state preparation is done, we move the bucket quickly into the cold region and match the translation speed with the rest of the buckets. On the far end, we also pull it out quickly to do the state detection sequence. We call this problem the travelator: it is like matching one's walking speed when hopping on or off a travelator at the Denver International Airport. One could try this out in the b.B.B..

Fighting against aging flashlamps, thinking about whether vacuum is broken during summer when power surges at JILA are common, and with so many things to try, the JILA eEDM group will stay busy for quite some time. With that, I present you an incomplete guide on using ThF^+ for an eEDM experiment, the first of its series, with many more to follow.

Bibliography

[1] E. A. Hinds. Testing time reversal symmetry using molecules. Physica Scripta, 1997(T70):34, 1997.

[2] Iosif B. Khriplovich and Steve K. Lamoreaux. CP violation without strangeness: electric dipole moments of particles, atoms, and molecules. Springer Science & Business Media, 2012.

[3] Timothy Chupp and Michael Ramsey-Musolf. Electric dipole moments: A global analysis. Physical Review C - Nuclear Physics, 91(3):1–11, 2015.

[4] Y. V. Stadnik, V. A. Dzuba, and V. V. Flambaum. Improved Limits on Axionlike-Particle-Mediated P, T -Violating Interactions between Electrons and Nucleons from Electric Dipole Moments of Atoms and Molecules. Physical Review Letters, 120(1):13202, 2018.

[5] Subir Sarkar. Big bang nucleosynthesis and physics beyond the standard model. Reports on Progress in Physics, 59(12):1493, 1996.

[6] John Ellis. Beyond the standard model with the LHC. Nature, 448(7151):297, 2007.

[7] M. E. Pospelov and I. B. Khriplovich. Electric dipole moment of the W boson and the electron in the Kobayashi-Maskawa model. Yadernaya Fizika, 53(4):1030–1033, 1991.

[8] Stephen M. Barr and A. Zee. Electric dipole moment of the electron and of the neutron. Physical Review Letters, 65(1):21, 1990.

[9] Werner Bernreuther and Mahiko Suzuki. The electric dipole moment of the electron. Reviews of Modern Physics, 63(2):313, 1991.

[10] Stephen M. Barr. A review of CP violation in atoms. International Journal of Modern Physics A, 8 (02):209–236, 1993.

[11] Maxim Pospelov and Adam Ritz. Electric dipole moments as probes of new physics. Annals of physics, 318(1):119–169, 2005.

[12] Eugene D. Commins. Electric dipole moments of leptons. In Advances in Atomic, Molecular, and Optical Physics, volume 40, pages 1–55. Elsevier, 1999.

[13] Jonathan J. Hudson, Dhiren M. Kara, I. J. Smallman, Ben E. Sauer, Michael R. Tarbutt, and E. A. Hinds. Improved measurement of the shape of the electron. Nature, 473(7348):493–496, 2011.

[14] William B. Cairncross, Daniel N. Gresh, Matt Grau, Kevin C. Cossel, Tanya S. Roussy, Yiqi Ni, Yan Zhou, Jun Ye, and Eric A. Cornell. Precision measurement of the electron's electric dipole moment using trapped molecular ions. Physical Review Letters, 119(15):153001, 2017.

[15] V. Andreev, D. G. Ang, D. DeMille, J. M. Doyle, G. Gabrielse, J. Haefner, N. R. Hutzler, Z. Lasner, C. Meisenhelder, B. R. O'Leary, C. D. Panda, A. D. West, E. P. West, and X. Wu. Improved limit on the electric dipole moment of the electron. Nature, 562:355–360, 2018.

[16] Brent Graner, Y. Chen, E. G. Lindahl, and B. R. Heckel. Reduced limit on the permanent electric dipole moment of Hg-199. Physical review letters, 116(16):161601, 2016.

[17] Michael Bishof, Richard H. Parker, Kevin G. Bailey, John P. Greene, Roy J. Holt, Mukut R. Kalita, Wolfgang Korsch, Nathan D. Lemke, Zheng-Tian Lu, Peter Mueller, Thomas P. O'Connor, Jaideep T. Singh, and Matthew R. Dietrich. Improved limit on the Ra 225 electric dipole moment. Physical Review C, 94(2):025501, 2016.

[18] F. Kuchler, E. Babcock, M. Burghoff, T. Chupp, S. Degenkolb, I. Fan, P. Fierlinger, F. Gong, E. Kraegeloh, W. Kilian, et al. A new search for the atomic EDM of ^{129}Xe at FRM-II. Hyperfine interactions, 237(1):95, 2016.

[19] E. R. Tardiff, E. T. Rand, G. C. Ball, T. E. Chupp, A. B. Garnsworthy, P. Garrett, M. E. Hayden, C. A. Kierans, W. Lorenzon, M. R. Pearson, et al. The radon EDM apparatus. Hyperfine Interactions, 225(1-3):197–206, 2014.

[20] Eric Norrgard, Eustace Edwards, Daniel McCarron, Matthew Steinecker, David DeMille, Shah Alam, Stephen Peck, Neha Wadia, and Larry Hunter. Hyperfine structure of the B state and predictions of optical cycling behavior of the XB transition in TlF. Bulletin of the American Physical Society, 62, 2017.

[21] S. Eckel, P. Hamilton, E Kirilov, H. W. Smith, and D. DeMille. Search for the electron electric dipole moment using Ω-doublet levels in PbO. Physical Review A, 87(5):052130, 2013.

[22] L. V. Skripnikov and A. V. Titov. Theoretical study of ThF^+ in the search for T, P-violation effects: Effective state of a Th atom in ThF^+ and ThO compounds. Physical Review A, 91(4):042504, 2015.

[23] L. V. Skripnikov and A. V. Titov. Theoretical study of thorium monoxide for the electron electric dipole moment search: Electronic properties of H $^3\Delta_1$ in ThO. The Journal of chemical physics, 142 (2):024301, 2015.

[24] A. N. Petrov, NS Mosyagin, T. A. Isaev, and A. V. Titov. Theoretical study of HfF^+ in search of the electron electric dipole moment. Physical Review A, 76(3):030501, 2007.

[25] Aaron E. Leanhardt, John L. Bohn, Huanqian Loh, Patrick Maletinsky, Edmund R. Meyer, Laura C. Sinclair, Russell P. Stutz, and Eric A. Cornell. High-resolution spectroscopy on trapped molecular ions in rotating electric fields: A new approach for measuring the electron electric dipole moment. Journal of Molecular Spectroscopy, 270(1):1–25, 2011.

[26] M. S. Safronova, D. Budker, D. DeMille, Derek F. Jackson Kimball, A. Derevianko, and Charles W. Clark. Search for new physics with atoms and molecules. Reviews of Modern Physics, 90(2):025008, 2018.

[27] T. E. Chupp, Peter Fierlinger, M. J. Ramsey-Musolf, and J. T. Singh. Electric dipole moments of atoms, molecules, nuclei, and particles. Reviews of Modern Physics, 91(1):015001, 2019.

[28] Mohit Verma, Andrew M. Jayich, and Amar C. Vutha. Electron electric dipole moment searches using clock transitions in ultracold molecules. Physical Review Letters, 125(15):153201, 2020.

[29] Yuiki Takahashi, Chi Zhang, Arian Jadbabaie, and Nicholas R. Hutzler. Engineering field-insensitive molecular clock transitions for symmetry violation searches. arXiv preprint arXiv:2304.13817, 2023.

[30] Ivan Kozyryev and Nicholas R. Hutzler. Precision measurement of time-reversal symmetry violation with laser-cooled polyatomic molecules. Physical Review Letters, 119(13):133002, 2017.

[31] Christian Hallas, Nathaniel B. Vilas, Loïc Anderegg, Paige Robichaud, Andrew Winnicki, Chaoqun Zhang, Lan Cheng, and John M. Doyle. Optical trapping of a polyatomic molecule in an l-type parity doublet state. Physical Review Letters, 130(15):153202, 2023.

[32] Benjamin L Augenbraun, Loic Anderegg, Christian Hallas, Zack D. Lasner, Nathaniel B. Vilas, and John M. Doyle. Direct laser cooling of polyatomic molecules. arXiv preprint arXiv:2302.10161, 2023.

[33] Benjamin L. Augenbraun, Zack D. Lasner, Alexander Frenett, Hiromitsu Sawaoka, Calder Miller, Timothy C. Steimle, and John M. Doyle. Laser-cooled polyatomic molecules for improved electron electric dipole moment searches. New Journal of Physics, 2020.

[34] Loïc Anderegg, Nathaniel B. Vilas, Christian Hallas, Paige Robichaud, Arian Jadbabaie, John M. Doyle, and Nicholas R. Hutzler. Quantum control of trapped polyatomic molecules for eedm searches. arXiv preprint arXiv:2301.08656, 2023.

[35] Tanya S. Roussy, Luke Caldwell, Trevor Wright, William B. Cairncross, Yuval Shagam, Kia Boon Ng, Noah Schlossberger, Sun Yool Park, Anzhou Wang, Jun Ye, and Eric A. Cornell. An improved bound on the electron’s electric dipole moment. Science, 381(6653):46–50, 2023. doi: 10.1126/science.adg4084. URL https://www.science.org/doi/abs/10.1126/science.adg4084.

[36] Luke Caldwell, Tanya S. Roussy, Trevor Wright, William B. Cairncross, Yuval Shagam, Kia Boon Ng, Noah Schlossberger, Sun Yool Park, Anzhou Wang, Jun Ye, and Eric A. Cornell. Systematic and statistical uncertainty evaluation of the hff$^+$ electron electric dipole moment experiment. Phys. Rev. A, 108:012804, Jul 2023. doi: 10.1103/PhysRevA.108.012804. URL https://link.aps.org/doi/10.1103/PhysRevA.108.012804.

[37] J. Baron, W. C. Campbell, D. DeMille, J. M. Doyle, G. Gabrielse, Y. V. Gurevich, P. W. Hess, N. R. Hutzler, E. Kirilov, I. Kozyryev, et al. Order of magnitude smaller limit on the electric dipole moment of the electron. Science, 343(6168):269–272, 2014.

[38] Yan Zhou, Yuval Shagam, William B. Cairncross, Kia Boon Ng, Tanya S. Roussy, Tanner Grogan, Kevin Boyce, Antonio Vigil, Madeline Pettine, Tanya Zelevinsky, Jun Ye, and Eric A. Cornell. Second-scale coherence measured at the quantum projection noise limit with hundreds of molecular ions. Physical Review Letters, 124(5):053201, 2020.

[39] Yuval Shagam, William B. Cairncross, Tanya S. Roussy, Yan Zhou, Kia Boon Ng, Daniel N. Gresh, Tanner Grogan, Jun Ye, and Eric A. Cornell. Continuous temporal ion detection combined with time-gated imaging: normalization over a large dynamic range. Journal of Molecular Spectroscopy, page 111257, 2020.

[40] Edmund R. Meyer and John L. Bohn. Prospects for an electron electric-dipole moment search in metastable ThO and ThF$^+$. Physical Review A, 78(1):010502, 2008.

[41] M. Denis, M. S. Nørby, H. J. A. Jensen, A. S. P. Gomes, M. K. Nayak, S. Knecht, and T. Fleig. Theoretical study on ThF$^+$, a prospective system in search of time-reversal violation. New Journal of Physics, 17(4):043005, 2015.

[42] L. V. Skripnikov and A. V. Titov. Theoretical study of ThF$^+$ in the search for T,P-violation effects: Effective state of a Th atom in ThF$^+$ and ThO compounds. Physical Review A, 91(4):042504, 2015.

[43] Daniel N. Gresh, Kevin C. Cossel, Yan Zhou, Jun Ye, and Eric A. Cornell. Broadband velocity modulation spectroscopy of ThF$^+$ for use in a measurement of the electron electric dipole moment. Journal of Molecular Spectroscopy, 319:1–9, 2016.

[44] Beau J. Barker, Ivan O. Antonov, Michael C. Heaven, and Kirk A. Peterson. Spectroscopic investigations of ThF and ThF$^+$. The Journal of Chemical Physics, 136(10):104305, 2012.

[45] Michael C. Heaven, Beau J. Barker, and Ivan O. Antonov. Spectroscopy and structure of the simplest actinide bonds. The Journal of Physical Chemistry A, 118(46):10867–10881, 2014.

[46] Yan Zhou, Kia Boon Ng, Lan Cheng, Daniel N. Gresh, Robert W. Field, Jun Ye, and Eric A. Cornell. Visible and ultraviolet laser spectroscopy of ThF. Journal of Molecular Spectroscopy, 358:1–16, 2019.

[47] John Michael Brown, John M. Brown, and Alan Carrington. Rotational spectroscopy of diatomic molecules. Cambridge University Press, 2003.

[48] Huanqian Loh, Russell P. Stutz, Tyler S. Yahn, Herbert Looser, Robert W. Field, and Eric A. Cornell. Rempi spectroscopy of HfF^+. Journal of Molecular Spectroscopy, 276:49–56, 2012.

[49] A. Kramida, Yu. Ralchenko, J. Reader, and NIST ASD Team. NIST Atomic Spectra Database (version 5.10), [Online]. Available: https://physics.nist.gov/asd [Wed May 24 2023]. National Institute of Standards and Technology, Gaithersburg, MD. DOI: https://doi.org/10.18434/T4W30F. 2022.

[50] Jinchun Xie and Richard N. Zare. Selection rules for the photoionization of diatomic molecules. Journal of Chemical Physics, 93(5):3033, 1990.

[51] I. Majewska, S. S. Kondov, C-H Lee, M. McDonald, BH McGuyer, R. Moszynski, and T. Zelevinsky. Experimental and theoretical investigation of the crossover from the ultracold to the quasiclassical regime of photodissociation. Physical Review A, 98(4):043404, 2018.

[52] M. McDonald, B. H. McGuyer, F. Apfelbeck, C-H Lee, I. Majewska, R. Moszynski, and T. Zelevinsky. Photodissociation of ultracold diatomic strontium molecules with quantum state control. Nature, 535 (7610):122, 2016.

[53] J. Alberto Beswick and Richard N. Zare. On the quantum and quasiclassical angular distributions of photofragments. The Journal of chemical physics, 129(16):164315, 2008.

[54] Kia Boon Ng, Yan Zhou, Lan Cheng, Noah Schlossberger, Sun Yool Park, Tanya S. Roussy, Luke Caldwell, Yuval Shagam, Antonio J. Vigil, Eric A. Cornell, et al. Spectroscopy on the electron-electric-dipole-moment–sensitive states of ThF^+. Physical Review A, 105(2):022823, 2022.

[55] Kang-Kuen Ni, Huanqian Loh, Matt Grau, Kevin C. Cossel, Jun Ye, and Eric A. Cornell. State-specific detection of trapped HfF^+ by photodissociation. Journal of Molecular Spectroscopy, 300:12–15, 2014.

[56] Huanqian Loh, Kevin C. Cossel, Matt C. Grau, Kang-Kuen Ni, Edmund R. Meyer, John L. Bohn, Jun Ye, and Eric A. Cornell. Precision spectroscopy of polarized molecules in an ion trap. Science, 342 (6163):1220–1222, 2013.

[57] David J. Griffiths. Introduction to Quantum Mechanics. Pearson Education, second edition, 2005.

[58] Nicolas Vanhaecke and Olivier Dulieu. Precision measurements with polar molecules: the role of the black body radiation. Molecular Physics, 105(11-12):1723–1731, 2007.

[59] R. W. Nicholls. Approximate formulas for franck–condon factors. The Journal of Chemical Physics, 74 (12):6980–6981, 1981.

[60] James K. G. Watson. Hönl–london factors for multiplet transitions in hund's case a or b. Journal of Molecular Spectroscopy, 252(1):5–8, 2008.

[61] D. DeMille, F. Bay, S. Bickman, D. Kawall, L. Hunter, D. Krause Jr, S. Maxwell, and K. Ulmer. Search for the electric dipole moment of the electron using metastable PbO. In AIP Conference Proceedings, volume 596, pages 72–83. AIP, 2001.

[62] Jun Ye, H. J. Kimble, and Hidetoshi Katori. Quantum state engineering and precision metrology using state-insensitive light traps. science, 320(5884):1734–1738, 2008.

[63] D. T. C. Allcock, W. C. Campbell, J. Chiaverini, I. L. Chuang, E. R. Hudson, I. D. Moore, A. Ransford, C. Roman, J. M. Sage, and D. J. Wineland. Omg blueprint for trapped ion quantum computing with metastable states. Applied Physics Letters, 119(21):214002, 2021.

[64] Bernd André Jung and Matthias Weigel. Spin echo magnetic resonance imaging. Journal of Magnetic Resonance Imaging, 37(4):805–817, 2013.

[65] T. H. Taminiau, J. J. T. Wagenaar, T. Van der Sar, Fedor Jelezko, Viatcheslav V. Dobrovitski, and R. Hanson. Detection and control of individual nuclear spins using a weakly coupled electron spin. Physical review letters, 109(13):137602, 2012.

[66] Steve Plimpton. Fast parallel algorithms for short-range molecular dynamics. Technical report, Sandia National Labs., Albuquerque, NM (United States), 1993.

[67] Florian Kranzl, Manoj K. Joshi, Christine Maier, Tiff Brydges, Johannes Franke, Rainer Blatt, and Christian F. Roos. Controlling long ion strings for quantum simulation and precision measurements. Physical Review A, 105(5):052426, 2022.

[68] Dominik Kiesenhofer, Helene Hainzer, Artem Zhdanov, Philip C. Holz, Matthias Bock, Tuomas Ollikainen, and Christian F. Roos. Controlling two-dimensional coulomb crystals of more than 100 ions in a monolithic radio-frequency trap. PRX Quantum, 4(2):020317, 2023.

[69] L. Spitzer. Physics of Fully Ionized Gases. John Wiley & Sons, New York, 1962.

[70] James D. Callen. Coulomb collisions. Fundamentals of Plasma Physics, 2006.

[71] Kuang Chen, Scott T. Sullivan, Wade G. Rellergert, and Eric R. Hudson. Measurement of the coulomb logarithm in a radio-frequency paul trap. Physical review letters, 110(17):173003, 2013.

[72] R. Blatt, P. Zoller, G. Holzmüller, and I. Siemers. Brownian motion of a parametric oscillator: A model for ion confinement in radio frequency traps. Zeitschrift für Physik D Atoms, Molecules and Clusters, 4(2):121–126, 1986.

[73] Yoshiki Moriwaki, Maki Tachikawa, Yoshiharu Maeno, and Tadao Shimizu. Collision cooling of ions stored in quadrupole radio-frequency trap. Japanese journal of applied physics, 31(11B):L1640, 1992.

[74] R. Blümel, C. Kappler, W. Quint, and H. Walther. Chaos and order of laser-cooled ions in a paul trap. Physical Review A, 40(2):808, 1989.

[75] F. G. Major and H. G. Dehmelt. Exchange-collision technique for the rf spectroscopy of stored ions. Physical Review, 170(1):91, 1968.

[76] Chaobo B. Zhang, D. Offenberg, B. Roth, M. A. Wilson, and S. Schiller. Molecular-dynamics simulations of cold single-species and multispecies ion ensembles in a linear paul trap. Physical Review A, 76(1): 012719, 2007.

[77] D. J. Berkeland, J. D. Miller, James C. Bergquist, Wayne M. Itano, and David J. Wineland. Minimization of ion micromotion in a paul trap. Journal of applied physics, 83(10):5025–5033, 1998.

[78] David Kielpinski, Chris Monroe, and David J. Wineland. Architecture for a large-scale ion-trap quantum computer. Nature, 417(6890):709, 2002.

[79] Juan M. Pino, Jennifer M. Dreiling, Caroline Figgatt, John P. Gaebler, Steven A. Moses, M. S. Allman, C. H. Baldwin, M. Foss-Feig, D. Hayes, K. Mayer, et al. Demonstration of the trapped-ion quantum ccd computer architecture. Nature, 592(7853):209–213, 2021.

[80] S. A. Moses, C. H. Baldwin, M. S. Allman, R. Ancona, L. Ascarrunz, C. Barnes, J. Bartolotta, B. Bjork, P. Blanchard, M. Bohn, J. G. Bohnet, N. C. Brown, N. Q. Burdick, W. C. Burton, S. L. Campbell, J. P. Campora III, C. Carron, J. Chambers, J. W. Chan, Y. H. Chen, A. Chernoguzov, E. Chertkov, J. Colina, J. P. Curtis, R. Daniel, M. DeCross, D. Deen, C. Delaney, J. M. Dreiling, C. T. Ertsgaard, J. Esposito, B. Estey, M. Fabrikant, C. Figgatt, C. Foltz, M. Foss-Feig, D. Francois, J. P. Gaebler, T. M. Gatterman, C. N. Gilbreth, J. Giles, E. Glynn, A. Hall, A. M. Hankin, A. Hansen, D. Hayes, B. Higashi, I. M. Hoffman, B. Horning, J. J. Hout, R. Jacobs, J. Johansen, L. Jones, J. Karcz, T. Klein, P. Lauria, P. Lee, D. Liefer, C. Lytle, S. T. Lu, D. Lucchetti, A. Malm, M. Matheny, B. Mathewson, K. Mayer, D. B. Miller, M. Mills, B. Neyenhuis, L. Nugent, S. Olson, J. Parks, G. N. Price, Z. Price,

M. Pugh, A. Ransford, A. P. Reed, C. Roman, M. Rowe, C. Ryan-Anderson, S. Sanders, J. Sedlacek, P. Shevchuk, P. Siegfried, T. Skripka, B. Spaun, R. T. Sprenkle, R. P. Stutz, M. Swallows, R. I. Tobey, A. Tran, T. Tran, E. Vogt, C. Volin, J. Walker, A. M. Zolot, and J. M. Pino. A race track trapped-ion quantum processor. arXiv preprint arXiv:2305.03828, 2023.

[81] Wolfgang Paul. Electromagnetic traps for charged and neutral particles. Reviews of modern physics, 62(3):531, 1990.

[82] Hendrick L. Bethlem, Giel Berden, Floris M. H. Crompvoets, Rienk T. Jongma, André J. A. Van Roij, and Gerard Meijer. Electrostatic trapping of ammonia molecules. Nature, 406(6795):491–494, 2000.

[83] R. Alheit, C. Hennig, R. Morgenstern, F. Vedel, and G. Werth. Observation of instabilities in a paul trap with higher-order anharmonicities. Applied Physics B, 61:277–283, 1995.

[84] Julian Schmidt, Daniel Hönig, Pascal Weckesser, Fabian Thielemann, Tobias Schaetz, and Leon Karpa. Mass-selective removal of ions from paul traps using parametric excitation. Applied Physics B, 126(11): 176, 2020.

[85] M. A. N. Razvi, X. Z. Chu, R. Alheit, G. Werth, and R. Blümel. Fractional frequency collective parametric resonances of an ion cloud in a paul trap. Physical Review A, 58(1):R34, 1998.

[86] Kevin C. Cossel, Daniel N. Gresh, Laura C. Sinclair, Tyler Coffey, Leonid V. Skripnikov, Alexander N. Petrov, Nikolai S. Mosyagin, Anatoly V. Titov, Robert W Field, Edmund R. Meyer, et al. Broadband velocity modulation spectroscopy of HfF^+: Towards a measurement of the electron electric dipole moment. Chemical Physics Letters, 546:1–11, 2012.

[87] John Turner, Phil Anderson, Tom Lachlan-Cope, Steve Colwell, Tony Phillips, Amélie Kirchgaessner, Gareth J. Marshall, John C. King, Tom Bracegirdle, David G. Vaughan, et al. Record low surface air temperature at vostok station, antarctica. Journal of Geophysical Research: Atmospheres, 114(D24), 2009.

[88] Dmitry Budker, Derek Kimball, Derek F. Kimball, and David P. DeMille. Atomic physics: an exploration through problems and solutions. Oxford University Press, USA, 2004.

[89] A. N. Petrov, L. V. Skripnikov, and A. V. Titov. Zeeman interaction in the $^3\delta_1$ state of HfF^+ to search for the electron electric dipole moment. Physical Review A, 96(2):022508, 2017.

[90] J. Robert Johansson, P. D. Nation, and Franco Nori. Qutip: An open-source python framework for the dynamics of open quantum systems. Computer Physics Communications, 183(8):1760–1772, 2012.

Appendix A

Paul Trap and Mathieu Equations

A.1 Introduction

Paul traps come in various geometries, and I will just list two here:[1]

3D Paul trap. The original Paul trap. The electrodes consist of a ring shaped like a hyperboloid, and two hyperbolic cylindrically symmetric caps placed on either side of the ring. An electric field oscillating at an RF frequency is applied between the ring and caps for radial confinement. A DC potential is applied on the caps w.r.t. the ring for axial confinement. See, for example, Figure 6 of Ref. [81]. The electrodes are shaped like hyperboloids because the equipotential surfaces for a quadrupolar potential are hyperboloids.

2D/linear Paul trap. Originally used as a quadrupole mass filter; only charged particles with the right charge-mass ratio can stay within the "trap" (see Figure 4 of Ref. [81]). The electrodes consist of two sets of radial electrodes, and end caps on either end of the radial electrodes. An electric field oscillating at an RF frequency is applied between the two sets of radial electrodes for radial confinement. A DC potential is applied on the end caps w.r.t. the radial electrodes for axial confinement. See, for example, Figure 1 of Ref. [77]. The electrodes are sometimes shaped like hyperboloids, but usually they are of the shape of more convenient geometries, e.g. rods for radial electrodes, plates for end caps. The potentials generated by these electrodes will not be of a pure quadrupolar form, but the quadrupolar potential is the most dominant one at the trap center.

[1] Check out R. Bradford Blakestad's thesis from the Wineland group for a compilation of common geometries not mentioned here (e.g. surface trap, wafer traps, wire trap).

The equations of motion have the form of a Mathieu's differential equations (see Section A.4), so the motion of the ions in a Paul trap are described by the Mathieu functions. Hence, the working of Paul traps are usually parameterized in terms of the Mathieu parameters (a, q) to be defined below. One thing to note is that the relation between the Mathieu parameters to the trap configuration depends on whether it is a 3D or 2D Paul trap. Here, I summarize the expressions for a 2D Paul trap, our Paul trap.

A.2 Definition of variables

There are quite a number of variables used throughout this appendix, so here I present a list of all the parameters.

Spatial coordinates, x, y, z**.** The spatial coordinates in the Cartesian system. The trap center is defined to be at $x = y = z = 0$. The z axis is defined to be along the axial direction.

RF voltage amplitude, $V_{\mathrm{rf},0}$**.** The amplitude (peak) of the RF voltage on the radial electrodes.

Effective radial distance, R_0**.** The effective radial distance of the radial electrodes from the trap axis. This would be the radial distance of the hyperboloid surface of the radial electrode from the trap axis if it were shaped like a hyperboloid.

RF angular frequency, ω_{rf}**.** The angular frequency of the RF oscillation.

DC axial voltage, $U_{\mathrm{ec},0}$**.** The potential difference between the $z = 0$ plane and the end cap. Usually this is just the voltage applied on the end caps, because the radial electrodes are at DC ground. However, in our Bucket Brigade, we apply a sinusoidal spatial modulation on the voltages on the Rings, so $U_{\mathrm{ec},0}$ would correspond to the peak-to-peak voltage applied on the Rings. See Figure A.1 for a comparison between the definitions for linear Paul traps and the Bucket Brigade.

Effective axial distance, Z_0**.** The effective axial distance of the axial electrodes from the $z = 0$ plane. This would be the axial distance of the hyperboloid surface of the caps from the $z = 0$ plane if it were shaped like a hyperboloid. In the Bucket Brigade, this parameter is just there to parameterize

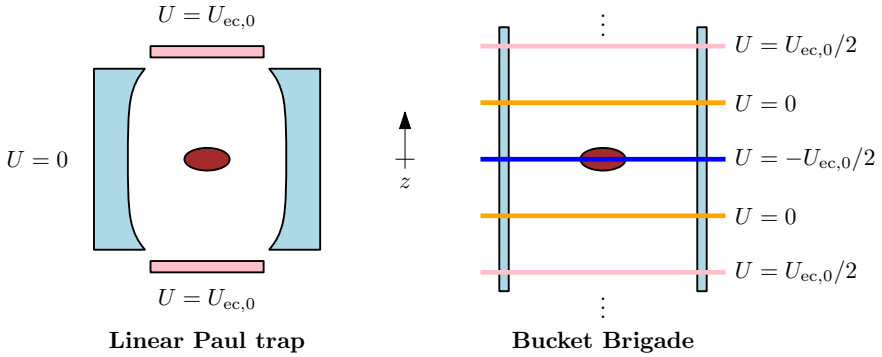

Figure A.1: **Comparing definition of $U_{\mathrm{ec},0}$ between conventional linear Paul traps and the Bucket Brigade.** The red blob represents the ion cloud. Left: a linear Paul trap. The red boxes indicate end caps, while the blue fins indicate radial electrodes. The radial electrodes are held at DC ground. Right: the Bucket Brigade with Rings and Rods. Rods are colored blue. The Rings are represented by colored horizontal lines.

the curvature of the axial trapping potentials as a "length"; it does not correspond to the distance from the ion cloud center to any Ring.

DC radial quadrupole voltage, $V_{\mathrm{DC},0}$. Half of the DC potential difference between the two sets of radial electrodes, defined to be positive for the set of radial electrodes along the x direction. This DC voltage will introduce a DC quadrupole potential in the radial direction, making the trap more confining in x and deconfining in y for a positive $V_{\mathrm{DC},0}$. We turn this on sometimes to filter away the heavier species from our trap, e.g. ThF_2^+. Some non-zero effective $V_{\mathrm{DC},0}$ may be present due to patch charges on Rods.

Mathieu a parameter. Contains all the information of the DC voltages. Typically $a \approx -0.0027$.

Mathieu q parameter. Contains all the information of the RF voltages. Typically $q \approx 0.14$.

Angular secular trap frequency, Ω. To flash out the secular frequencies from the rest of the frequencies in this appendix, we use Ω instead of ω to represent angular secular trap frequencies for the rest of this appendix.

Electric charge, e. The charge of our singly charged ion.

Ion mass, m. The mass of our ion.

The rest of the sections will just list the equations involved with minimal elaboration.

A.3 Potentials

RF potential

$$V_{\mathrm{rf}} = V_{\mathrm{rf},0}\left(\frac{x^2-y^2}{R_0^2}\right)\cos\omega_{\mathrm{rf}}t. \tag{A.1}$$

DC end caps

$$U_{\mathrm{ec}} = \frac{U_{\mathrm{ec},0}}{Z_0^2}\left(z^2-\frac{x^2+y^2}{2}\right), \text{ where } U_{\mathrm{ec},0} \text{ is the peak-to-peak voltage on Rings.} \tag{A.2}$$

DC electrodes

$$V_{\mathrm{DC}} = \frac{V_{\mathrm{DC},0}}{R_0^2}(x^2-y^2).$$

Total electric potential

$$V_{\mathrm{tot}} = \left[-\left(\frac{U_{\mathrm{ec},0}}{2Z_0^2}-\frac{V_{\mathrm{DC},0}}{R_0^2}\right)+\frac{V_{\mathrm{rf},0}}{R_0^2}\cos\omega_{\mathrm{rf}}t\right]x^2+\left[-\left(\frac{U_{\mathrm{ec},0}}{2Z_0^2}+\frac{V_{\mathrm{DC},0}}{R_0^2}\right)-\frac{V_{\mathrm{rf},0}}{R_0^2}\cos\omega_{\mathrm{rf}}t\right]y^2+\frac{U_{\mathrm{ec},0}}{Z_0^2}z^2.$$

A.4 Equations of motion

Total force

$$\begin{pmatrix}\ddot{x}\\ \ddot{y}\\ \ddot{z}\end{pmatrix} = \begin{pmatrix}\left[-\left(\frac{U_{\mathrm{ec},0}}{2Z_0^2}-\frac{V_{\mathrm{DC},0}}{R_0^2}\right)+\frac{V_{\mathrm{rf},0}}{R_0^2}\cos\omega_{\mathrm{rf}}t\right]\frac{-2e}{m}x\\ \left[-\left(\frac{U_{\mathrm{ec},0}}{2Z_0^2}+\frac{V_{\mathrm{DC},0}}{R_0^2}\right)-\frac{V_{\mathrm{rf},0}}{R_0^2}\cos\omega_{\mathrm{rf}}t\right]\frac{-2e}{m}y\\ \frac{U_{\mathrm{ec},0}}{Z_0^2}\frac{-2e}{m}z\end{pmatrix}. \tag{A.3}$$

Form of Mathieu equations

$$\ddot{\lambda}(\tau) = (-a+2q\cos 2\tau)\lambda(\tau).$$

Our Mathieu equations Performing the transformations $2\tau := \omega_{\mathrm{rf}}t$ and $\partial_t = \frac{\omega_{\mathrm{rf}}}{2}\partial_\tau$ on Equation (A.3) gives:

$$\begin{pmatrix}\ddot{x}\\ \ddot{y}\\ \ddot{z}\end{pmatrix} = \begin{pmatrix}\left[-\left(\frac{U_{\mathrm{ec},0}}{2Z_0^2}-\frac{V_{\mathrm{DC},0}}{R_0^2}\right)+\frac{V_{\mathrm{rf},0}}{R_0^2}\cos 2\tau\right]\frac{-8e}{m\omega_{\mathrm{rf}}^2}x\\ \left[-\left(\frac{U_{\mathrm{ec},0}}{2Z_0^2}+\frac{V_{\mathrm{DC},0}}{R_0^2}\right)-\frac{V_{\mathrm{rf},0}}{R_0^2}\cos 2\tau\right]\frac{-8e}{m\omega_{\mathrm{rf}}^2}y\\ \frac{U_{\mathrm{ec},0}}{Z_0^2}\frac{-8e}{m\omega_{\mathrm{rf}}^2}z\end{pmatrix},$$

where we can define the following:

$$a_x = -\frac{8e}{m\omega_{\mathrm{rf}}^2}\left(\frac{U_{\mathrm{ec},0}}{2Z_0^2} - \frac{V_{\mathrm{DC},0}}{R_0^2}\right) \qquad q_x = -\frac{4e}{m\omega_{\mathrm{rf}}^2}\frac{V_{\mathrm{rf},0}}{R_0^2}$$
$$a_y = -\frac{8e}{m\omega_{\mathrm{rf}}^2}\left(\frac{U_{\mathrm{ec},0}}{2Z_0^2} + \frac{V_{\mathrm{DC},0}}{R_0^2}\right) \qquad q_y = \frac{4e}{m\omega_{\mathrm{rf}}^2}\frac{V_{\mathrm{rf},0}}{R_0^2}$$
$$a_z = \frac{8e}{m\omega_{\mathrm{rf}}^2}\frac{U_{\mathrm{ec},0}}{Z_0^2} \qquad q_z = 0,$$

and relate to the more familiar forms:

$$a_0 = -\frac{4e}{m\omega_{\mathrm{rf}}^2}\frac{U_{\mathrm{ec},0}}{Z_0^2} < 0 \qquad a_x = -|a_0| + a' \qquad q_x = -q_0$$
$$a' = \frac{8e}{m\omega_{\mathrm{rf}}^2}\frac{V_{\mathrm{DC},0}}{R_0^2} > 0 \qquad a_y = -|a_0| - a' \qquad q_y = q_0$$
$$q_0 = \frac{4e}{m\omega_{\mathrm{rf}}^2}\frac{V_{\mathrm{rf},0}}{R_0^2} > 0 \qquad a_z = 2|a_0| \qquad q_z = 0$$

Secular frequencies

$$\Omega_z = \frac{\omega_{\mathrm{rf}}}{2}\sqrt{a_z} \quad , \quad \Omega_{x,y} = \frac{\omega_{\mathrm{rf}}}{2}\sqrt{a_{x,y} + q_0^2/2}. \tag{A.4}$$

Appendix B

Typical Parameters for the Bucket Brigade

In this part of the appendix, we present (i) the typical trap parameters of the baby Bucket Brigade for quick reference to ion dynamic quantities, and (ii) typical experiment and molecular parameters that could go into the study of possible systematic effects in Gen. III.

B.1 Trap parameters

Parameter	Value	Comments
Ring inner radius	7.5 cm $\times$90%	Scaled down to make space for structural support.
Ring outer radius	8.5 cm $\times$90%	Scaled down to make space for structural support.
Inter-ring spacing	2 cm	4 Rings per bucket.
Rod outer diameter	$0.5''$	Stock dimension.
Rod radial distance	6.5 cm $\times$90%	Center-to-center. Scaled down to make space for structural support.
$\mathcal{E}_{\mathrm{rot}}$ per V_{rot}	14.0 (V/m)/V	From COMSOL simulations.
V_{rot}	430 V	For $\mathcal{E}_{\mathrm{rot}} = 60$ V/cm.
R_0	5.36 cm	From COMSOL. Effective radial distance of radial electrodes.
$V_{\mathrm{rf},0}$	25.6 V	RF voltage for radial secular frequency of 2 kHz, $V_{\mathrm{rf},0} \sim f_{\mathrm{sec,radial}}$.
Z_0	33.8 cm	From COMSOL. Effective axial distance of "end caps".
$U_{\mathrm{ec},0}$	19.9 V_{pp}	"End cap" voltage for axial secular frequency of 2 kHz, $U_{\mathrm{ec},0} \propto f^2_{\mathrm{sec,axial}}$.
ω_{rf}	$2\pi \times 50$ kHz	RF frequency.

Table B.1: **Table of typical parameters for the (Baby) Bucket Brigade.** Refer to Appendix A for the definition of the variables. R_0 is obtained from a fit to the potential within 2 cm of the trap axis.

B.2 Internal state and trapping field parameters

Parameter	Value (to 3 s.f.)	Notes
$d_e\mathcal{E}_{\text{eff}}$	$2\pi \times 0.851$ μHz	Assuming $d_e = 10^{-31} e \cdot$ cm.
$A_{\|\|}$	$2\pi \times -20.1$ MHz	Hyperfine splitting constant.
E_{hf}	$2\pi \times -15.1$ MHz	Hyperfine splitting.
ω_{ef}	$2\pi \times 5.29$ MHz	Ω-doubling splitting constant.
d_{mf}	3.37 D	$2\pi \times 1.70$ MHz/(V/cm).
$\mathcal{E}_{\text{rot}}$	60 V/cm	.
$\mathcal{E}_{\text{capture}}$	18.8 V/cm	Supersonic expansion speed for Neon is 780 m/s.
ω_{rot}	$2\pi \times 147.5$ kHz	.
E_{rot}	93500 K	Kinetic energy of rotational micromotion.
r_{rot}	2.69 mm	Radius of rotational circular motion.
r_{capture}	0.842 mm	Radius of capture circular motion.
$d_{\text{mf}}\mathcal{E}_{\text{rot}}$	$2\pi \times 102$ MHz	.
$\frac{3}{2}\gamma_{F=3/2} d_{\text{mf}}\mathcal{E}_{\text{rot}}$	$2\pi \times 50.9$ MHz	Stark shift of $m_F = \pm 3/2$ states in $J = 1$.
$g_{F=3/2}$	-0.0149	Sign not measured.
$g_{F=1/2}$	-	-
$\mathcal{B}_{\text{axgrad}}$	2.97 mG/cm	-
$\mathcal{B}_{\text{rot}}$	799 μG	-
$3g_F\mu_{\text{B}}\mathcal{B}_{\text{rot}}$	$2\pi \times 50$ Hz	Zeeman splitting.
$\delta g_F / g_F$	-2.55×10^{-3}	At $\mathcal{E}_{\text{rot}} == 60$ V/cm.
Δ^{u}	$2\pi \times 0.511$ Hz	.
Δ^{l}	$2\pi \times 1.43$ Hz	.
$\mathcal{B}_{\perp}$	-	-
$\omega_{x,y,z}$	$2\pi \times 2$ kHz	Trap secular frequencies.
$r_{1\sigma}$	0.251 cm	1σ radius of ion cloud.
T	30 K	Temperature of ion cloud.
$\mathcal{E}_z$	20.6 mV/cm	Axial electric field for confinement at 2σ radius.
$\mathcal{E}_{\text{rf}}$	0.447 V/cm	RF field strength at 1σ radius.
ω_{rf}	$2\pi \times 50$ kHz	RF frequency
$\langle\mathcal{E}_{\text{rf}}\rangle$	15.5 mV/cm	Averaged over one Paul cycle.
E_{rf}	22.6 K	Kinetic energy of RF micromotion over one Paul cycle.
$T_{\text{trap},z}$	1000 K	Trap depth along the z direction.
$T_{\text{trap},\rho}$	2100 K	Trap depth along the radial direction.

Table B.2: **Table of typical parameters for the Gen. III experiment.** Additional notes:

- $\mathcal{E}_z = m\omega_z^2 z/e$.
- $\mathcal{E}_{\text{rf}} = V_{\text{rf,pp}} r_{1\sigma}/R_0^2$, where R_0 is given in Table B.1.
- $\langle\mathcal{E}_{\text{rf}}\rangle = \frac{e\mathcal{E}_{\text{rf}}^2}{2m\omega_{\text{rf}}^2 r_{1\sigma}}$ (Huanqian's thesis Equation 4.7) and is lightly larger than $\mathcal{E}_z$ because of deconfining potential from rings.
- $E_{\text{rf}} = \frac{e^2\mathcal{E}_{\text{rf}}^2}{4m\omega_{\text{rf}}^2}$ (Huanqian's thesis Equation 4.8).

Appendix C

Hamiltonian

C.1 Introduction

Writing out the full Hamiltonian is highly non-trivial. The details of the Hamiltonian are scattered across many papers [14, 25] and theses of previous group members. This chapter seeks to (i) consolidate information pertaining to ThF^+, (ii) address common pitfalls in understanding[1] , and (iii) serve as a reference for the previous chapters.

Before we go into the details of the Hamiltonian, it serves to address the first common pitfall in understanding: frames of reference. Two frames of reference are used in the evaluation of the Hamiltonian: (i) frame defining the quantization axis, and (ii) frame of the molecule. The former is defined to be a frame of reference that is rotating with $\mathcal{E}_{\text{rot}}$, and we define quantum numbers like F, m_F, and J in this frame of reference. The latter has quantization axis defined along the internuclear axis, pointing towards thorium, and we define the quantum number Ω in this frame of reference.

C.2 Terms in the Hamiltonian

The Hamiltonian has this simple form:

$$H = H_{\text{hyperfine}} + H_{\Omega\text{-doub.}} + H_{\text{rot.}} + H_{\text{Stark}} + H_{\text{Zeeman}} + H_{\text{offset}}(v, J) + H_{\text{eEDM}}. \tag{C.1}$$

The following sections go into the details of each term in order.

[1] Mainly to do justice to the insane amount of time I put into understanding and writing legible code to solve the Schrödinger's equation, and to lessen the burden on whoever the new Hamiltonian custodian is.

C.2.1 Hyperfine

The hyperfine splitting arises from the interaction between the total angular momentum $\mathbf{J}$ and the total nuclear spin $\mathbf{I}$. Since ^{232}Th has no nuclear spin, the nuclear spin comes solely from the spin-1/2 ^{19}F nucleus. Since the angular momenta precesses around the internuclear axis $\mathbf{n}$, the interaction energy has the form: $E_{\text{hyperfine}} \sim (\mathbf{I}\cdot\mathbf{n})(\mathbf{J}\cdot\mathbf{n})$. Using the projection theorem (e.g. Sakurai Equation 3.10.40), we have:

$$H_{\text{hyperfine}} = A_{||}\frac{\mathbf{F}^2-\mathbf{I}^2-\mathbf{J}^2}{2\mathbf{J}^2}, \tag{C.2}$$

where $A_{||}$ is the hyperfine splitting constant; $\mathbf{F}=\mathbf{I}+\mathbf{J}$, $\mathbf{I}$, and $\mathbf{J}$ are the hyperfine states, nuclear spin, and total angular momentum, respectively.

For ThF^+ in the $X\,^3\Delta_1(v=0)$ manifold where $I=1/2$, we have the ratio

$$\Delta E_{\text{hyperfine},J=1}/\Delta E_{\text{hyperfine},J=2} = 9/5,$$

which says that the hyperfine splitting in the $J=1$ state is larger than that in $J=2$.

C.2.2 Ω-doubling

The Ω-doubling splitting arises from the interaction between electronic and rotational motions that splits the energy degeneracy of $\Omega=\mathbf{J}\cdot\mathbf{n}$ of opposite signs[2] . This Hamiltonian only couples $|\Omega\rangle$ to $|-\Omega\rangle$ with the same J, F, and m_F. In our group, we defined it as:

$$H_{\Omega\text{-doub.}} = \bigoplus_{J\geq\Omega}\frac{(-1)^J}{2}\hbar\omega_{\text{ef}}\Omega_x^{(J)}, \tag{C.3}$$

where $\bigoplus$ is the direct sum, ω_{ef} is the energy splitting between the two Ω levels for $J=1$, and $\Omega_x^{(J)}$ connects states of Ω with opposite signs within the same J subspace:

$$\Omega_x^{(J)} = \frac{J(J+1)}{2}\Big[|J,\Omega=+1\rangle\langle J,\Omega=-1| + |J,\Omega=-1\rangle\langle J,\Omega=+1|\Big].$$

The Ω states are connected to the parity states $|\pm\rangle$ through:

$$|\Omega=\pm1\rangle = \frac{|+\rangle\pm|-\rangle}{\sqrt{2}}.$$

The factor $(-1)^J$ is there to account for the alternating parity with J.

[2] For more details see Chapter 7.9 of Dave DeMille's book [88].

C.2.3 Rotation

Since we are operating in a rotating reference frame defined by $\mathcal{E}_{\text{rot}}$, there is a non-inertial-frame term in the Hamiltonian. This is the part of the Hamiltonian that is responsible for Berry's phase. This Hamiltonian couples states with $\Delta m_F = \pm 1$ with the same F, J, and Ω. We define the z-axis to be pointing in the direction of $\mathcal{E}_{\text{rot}}$, and the x-axis to be anti-parallel to the (counter-clockwise) rotation vector. Hence, we have:

$$H_{\text{rot.}} = \hbar \omega_{\text{rot.}} F_x, \tag{C.4}$$

where $F_x = \frac{F_+ + F_-}{2}$, $F_\pm |F, m_F\rangle = \sqrt{(F \mp m_F)(F \pm m_F + 1)} |F, m_F \pm 1\rangle$, and $\omega_{\text{rot.}}$ is the angular frequency of $\mathcal{E}_{\text{rot}}$.

C.2.4 Stark

In the presence of external electric fields, states of opposite parities are mixed to give us states of good Ω. The mixing happens across states of different J and F, but share the same Ω and m_F. Hence, states between $J = 1$ and $J = 2$ can couple to each other, and depending on the exact energy difference between the coupling states, properties like the magnetic g-factor can be different between the upper and lower doublets. Expressing the Hamiltonian in element-form, we have:

$$\begin{aligned} H_{\text{Stark}} = -d_{\text{mf}} \mathbf{n} \cdot \mathcal{E} = -d_{\text{mf}} \sum_{p \in \{0, \pm 1\}} \mathcal{E}_p \times (-1)^{F + J' + 1 + I} \begin{Bmatrix} J & F & I \\ F' & J' & 1 \end{Bmatrix} \\ \times (-1)^{F' - m'_F} \sqrt{(2F+1)(2F'+1)} \begin{pmatrix} F' & 1 & F \\ -m'_F & p & m_F \end{pmatrix} \\ \times (-1)^{J' - \Omega'} \sqrt{(2J+1)(2J'+1)} \begin{pmatrix} J' & 1 & J \\ -\Omega' & q = 0 & \Omega \end{pmatrix}. \end{aligned} \tag{C.5}$$

We have chosen $q = 0$ because the dipole is aligned along the internuclear axis, and $p = 0, \pm 1$, which correspond to the spherical tensor components. The derivation is long, so I recommend interested readers to start from page 167 in Brown and Carrington [47].

C.2.5 Zeeman

In the presence of external magnetic fields, states of different F are mixed. Since the magnetic g-factor depends on F, we get different extents of mixing of g_F depending on the exact energy difference between the coupling states. This is the other reason for a differential g-factor δg. In the presence of weak external magnetic fields, $\mathbf{J}$ couples more strongly to the internuclear axis than the external magnetic field, and the Hamiltonian can be expressed in the following form:

$$H_{\text{Zeeman}} = -G_{||}\mu_{\text{B}}(\mathbf{J}\cdot\mathbf{n})\,(\mathbf{n}\cdot\mathcal{B}) - g_{\text{N}}\mu_{\text{N}}\mathbf{I}\cdot\mathcal{B}, \tag{C.6}$$

where g_{N} is the nuclear g-factor of ^{19}F, and $G_{||}$ is related to the hyperfine g-factor through the following [89]:

$$g_F = -G_{||}\frac{F(F+1)+J(J+1)-3/4}{2F(F+1)J(J+1)} + g_{\text{N}}\frac{\mu_{\text{N}}}{\mu_{\text{B}}}\frac{F(F+1)-J(J+1)+3/4}{2F(F+1)},$$

which evaluates to $\frac{1}{3}\left(-G_{||}+g_{\text{N}}\frac{\mu_{\text{N}}}{\mu_{\text{B}}}\right)$ for $F=3/2$, $J=1$. Evaluating the dot products in the Hamiltonian give:

$$\begin{aligned}(\mathbf{J}\cdot\mathbf{n})\,(\mathbf{n}\cdot\mathcal{B}) = \Omega\sum_{p\in\{0,\pm1\}}\mathcal{B}_p \times (-1)^{F+J'+I+1}\begin{Bmatrix} J & F & I \\ F' & J' & 1\end{Bmatrix} \\ \times (-1)^{F'-m'_F}\sqrt{(2F+1)(2F'+1)}\begin{pmatrix} F' & 1 & F \\ -m'_F & p & m_F\end{pmatrix} \\ \times (-1)^{J'-\Omega'}\sqrt{(2J+1)(2J'+1)}\begin{pmatrix} J' & 1 & J \\ -\Omega' & q=0 & \Omega\end{pmatrix}.\end{aligned}$$

$$\begin{aligned}\mathbf{I}\cdot\mathcal{B} = \sum_{p\in\{0,\pm1\}}\mathcal{B}_p \times (-1)^{F'+J'+I+1}\sqrt{I(I+1)(2I+1)}\begin{Bmatrix} I & F' & J' \\ F & I & 1\end{Bmatrix} \\ \times (-1)^{F'-m'_F}\sqrt{(2F+1)(2F'+1)}\begin{pmatrix} F' & 1 & F \\ -m'_F & p & m_F\end{pmatrix}.\end{aligned}$$

The astute reader will recognize that the first form above is similar to Equation (C.5). Once again, the derivation is long, so I recommend interested readers to start from page 606 in Brown and Carrington [47].

C.2.6 Offset

While all the Hamiltonians above deal with energy scales $\lesssim 2\pi \times 100$ MHz, this last term is on the order of 10 GHz and above. For the numbers relevant to ThF^+ [43], the energy levels within the same electronic level hold the approximate form:

$$H_{\text{offset}} = G(v) + E(v, J), \tag{C.7a}$$

$$G(v) = \hbar\omega_e \left(v + \frac{1}{2}\right) - \hbar\omega_e\chi_e \left(v + \frac{1}{2}\right)^2, \tag{C.7b}$$

$$E(v, J) = B_e J(J+1) - D\left[J(J+1)\right]^2 - \alpha_e \left(v + \frac{1}{2}\right) J(J+1). \tag{C.7c}$$

$$= B_v J(J+1) - D\left[J(J+1)\right]^2. \tag{C.7d}$$

$G(v)$ accounts for vibrational levels, and the energy spacing is on the order of about 600 cm^{-1} (1 $\text{cm}^{-1} \approx$ 30 GHz), while $E(v, J)$ accounts for the rotational levels, with energy spacing on the order of 15 GHz. The spectroscopic constants are the vibrational constant ω_e, anharmonicity constant $\omega_e\chi_e$, equilibrium rotational constant B_e, centrifugal distortion constant D_e, and rotational-vibrational coupling constant α_e. The terms involving B_e and α_e are often grouped together to give a v-dependent $B = B_e - \alpha_e(v + 1/2)$.

C.2.7 eEDM

For completeness, the effective Hamiltonian responsible for the shift in the energy levels due to the eEDM is [25][3] :

$$H_{\text{eEDM}} = -d_e \mathcal{E}_{\text{eff}} \frac{\Omega}{|\Omega|}, \tag{C.8}$$

where $\mathcal{E}_{\text{eff}} \approx 35$ GV/cm is the effective electric field within ThF^+ that is seen by the unpaired electron in the $X\,^3\Delta_1$ state [22, 40, 41].

Since the Stark shifts go as $m_F\Omega$ while the eEDM term goes as Ω, we see that states that are energetically degenerate under Stark shifts (e.g. $|m_F = +3/2, \Omega = +1\rangle$ and $|m_F = -3/2, \Omega = -1\rangle$) have eEDM shifts of different signs.

[3] There is an extra factor of 1/2 in the cited paper [25], which uses a different convention for how $\mathcal{E}_{\text{eff}}$ is defined in papers that calculate the value [22, 40, 41]. The factor of 1/2 is removed for consistency with the cited value of $\mathcal{E}_{\text{eff}}$.

In principle, all we need to do to determine the eEDM is to measure the energy difference between degenerate Stark pairs. In practice, we choose to do so with the outer-most stretched Stark pairs, because these stretched states are the easiest to prepare. There are two such pairs, and we call the pair that is more (less) energetic the "upper doublet" ("lower doublet").

C.3 Solving the Schrödinger's Equation

C.3.1 Time-independent

Solving the time-independent Schrödinger's Equation is as easy as diagonalizing the full 12- (for $J = 1$ only) or 32-state (for $J = 1\&2$) Hamiltonian. In general, the eigenstates are superposition states of our basis set $\{|J, \Omega, F, m_F\rangle\}$ because of the mixing induced by $H_{\text{rot.}}$, H_{Stark}, and H_{Zeeman}. Nevertheless, one can still distill out the dominant component of the basis set from each eigenstate, and draw meaningful descriptions of the system. Figure 4.7 shows an example of diagonalizing the 32-state Hamiltonian at $\mathcal{E}_{\text{rot}} = 60$ V/cm for ThF^+.

C.3.2 Time-dependent

Propagating the quantum state with time is not cheap computationally. Unless one wishes to investigate the effects of the $J = 2$ states coupling to the $J = 1$ states, it is highly advisable to use the 12-state Hamiltonian instead of the 32-state Hamiltonian. Unfortunately, many systematics involve contribution from coupling between the $J = 1\&2$ states. We can speed up the computation by propagating the quantum state of different $\tilde{R}$ and $\tilde{B}$ switches in parallel. The `python` package QuTip [90] allows for such parallel computation, and has been used for simulation works in this thesis.

C.4 Two-level effective Hamiltonian

For a more intuitive understanding of the relevant parameters involved in studies of systematics, it is helpful to work with a two-level effective Hamiltonian that captures all the physics in newly defined effective parameters. There are two of such two-level Hamiltonians, corresponding to the upper (states 8 and 9 in Figure 4.7) and the lower doublets (states 0 and 1 in Figure 4.7). The effective parameters are defined as such:

Magnetic g-factor, g, δg. The mean magnetic g-factor of the upper and lower doublets is defined as $g = (g^{\mathrm{u}} + g^{\mathrm{l}})/2$, while the difference in magnetic g-factor between the upper and lower doublets is defined as $\delta g = (g^{\mathrm{u}} - g^{\mathrm{l}})/2$, where "u" and "l" refer to the upper and lower doublets, respectively. Typically $\delta g \ll g$.

Non-reversing magnetic field, $\mathcal{B}_{\mathrm{nr}}$. In the eEDM experiments with HfF^+, we switch the direction of the applied magnetic field to search for systematics. In the event of an imperfect switch, the magnetic field can be decomposed into a part that reverses, and a part that does not, i.e. $\mathcal{B}(\tilde{B}) = \tilde{B}\mathcal{B} + \mathcal{B}_{\mathrm{nr}}$, where $\tilde{B} = \pm 1$ is the sign of the switch. In the Bucket Brigade experiment, we do not plan to apply Zeeman shifts to our eEDM sensitive states, so $\mathcal{B} = 0$ and $\mathcal{B}_{\mathrm{nr}}$ corresponds to the ambient magnetic field.

Berry's frequency, $3f_{\mathrm{rot}}(\tilde{S}\langle\alpha\rangle + \alpha_{\mathrm{nr}})$. This term (integrated with time) is the Berry's phase accumulated by the states. Much like the case for magnetic fields in the second generation experiment, we can also switch the sign of Berry's phase in our experiment by switching the direction of the relevant fields. In the case of an imperfect switch, Berry's phase can also be decomposed into a reversing part $\langle\alpha\rangle$ and a non-reversing part α_{nr}. We aim for $\alpha_{\mathrm{nr}} \ll \langle\alpha\rangle$. The switch is defined as $\tilde{S} = \pm 1$.

Energy splitting at avoided crossing, Δ, Δ^D. Rotation coupling from Equation C.4 splits the degeneracy of the eEDM sensitive states within each doublet into those with avoided crossings Δ^{u} and Δ^{l} for the upper and lower doublets, respectively. The mean and the difference are defined as $\Delta = (\Delta^{\mathrm{u}} + \Delta^{\mathrm{l}})/2$ and $\Delta^D = (\Delta^{\mathrm{u}} - \Delta^{\mathrm{l}})/2$, respectively. Typically $\Delta^D \approx \Delta$. We also define a

convenient "doublet switch" $\tilde{D}$ such that $\Delta^{\mathrm{u,l}} = \Delta + \tilde{D}\,\Delta^{D}$, $\tilde{D} = \pm 1$.

Using the eEDM experiment with ThF^+ in the Bucket Brigade using Berry's phase as the dominant frequency as an example, the steps involved are detailed in Section 8.3.4.